TECHNISCHE
UNIVERSITÄT
WIEN
Vienna University of Technology

GEOWISSENSCHAFTLICHE MITTEILUNGEN

Heft Nr. 96, 2014

Atmosphere-induced short period variations of Earth rotation

Michael Schindelegger

Veröffentlichung des Departments für Geodäsie und Geoinformation
ISSN 1811-8380

Schriftenreihe der Studienrichtung VERMESSUNG UND GEOINFORMATION

TECHNISCHE
UNIVERSITÄT
WIEN
Vienna University of Technology

GEOWISSENSCHAFTLICHE MITTEILUNGEN

Heft Nr. 96, 2014

Atmosphere-induced short period variations of Earth rotation

Michael Schindelegger

Veröffentlichung des Departments für Geodäsie und Geoinformation
ISSN 1811-8380

Schriftenreihe der Studienrichtung VERMESSUNG UND GEOINFORMATION

2014
Published by the Department of Geodesy and Geoinformation
of the Vienna University of Technology
Gußhausstraße 27-29
1040 Vienna, Austria

Responsible for this issue: Prof. Dr. Johannes Böhm
Printed by: Grafisches Zentrum HTU GmbH

The digital version of the full document with colored figures is available online:
http://www.hg.tuwien.ac.at/Bibl_Docs/Theses_phd/phd_full/2014_phd_mschind.pdf

Die Kosten für den Druck wurden vom Department für Geodäsie und Geoinformation übernommen.

Diese Arbeit wurde an der Fakultät für Mathematik und Geoinformation der Technischen Universität Wien zur Erlangung des akademischen Grades eines Doktors der technischen Wissenschaften eingereicht.

Begutachter:

Prof. Dr. Harald Schuh
Department für Geodäsie und Geoinformation der Technischen Universität Wien
Gußhausstraße 27-29, 1040 Wien, Österreich
Department 1 „Geodäsie und Fernerkundung“, Deutsches Geoforschungszentrum GFZ
Telegrafenberg, 14473 Potsdam, Deutschland

Prof. Dr.-Ing. Florian Seitz
Institut für Astronomische und Physikalische Geodäsie der Technischen Universität München
Arcisstraße 21, 80333 München, Deutschland

Tag der mündlichen Prüfung: 24.01.2014

Auflage: 60 Stück

ISSN 1811-8380

Prüfungssenat:

Prof. Dr. Robert Weber
Technische Universität Wien

Prof. Dr. Harald Schuh
Deutsches Geoforschungszentrum Potsdam

Prof. Dr.-Ing. Florian Seitz
Technische Universität München

Prof. Dr. Johannes Böhm
Technische Universität Wien

Prof. Dr. Aleksander Brzeziński
Technische Universität Warschau

Acknowledgments

Accomplishing the research and writing of this thesis would not have been possible without the support of many people. First and foremost, I sincerely appreciate the guidance and foresight of my supervisor Harald Schuh, who elicited my enthusiasm for higher geodesy from the very first minute but also granted me the right amount of liberty in developing my own ideas. His encouragement to promote my work at numerous international meetings and to get involved with the Earth rotation community are held in high esteem. Living up to the inquiring mind of my co-supervisor, Florian Seitz, was a great motivation throughout, and I am obliged to him for igniting insightful discussions and establishing a smooth, cross-border collaboration.

Special thanks goes to David Salstein, whose interest in the progress of this work was second to none from the outset. His persistent efforts to enlighten me on the subtleties of the English language have hopefully found expression in one way or another hereinafter. The advice of further international colleagues, most notably Aleksander Brzeziński, Olivier de Viron, Steve Dickman, Henryk Dobslaw, and Richard Ray, was substantial for mastering several critical issues, and their efforts are greatly acknowledged.

I take particular pleasure in thanking my dear colleague Johannes Böhm, who provided the technical assistance for the realization of this thesis and also supplied the eventually decisive literature at my first day as a graduate student. His pragmatic approach in solving the little problems of a researcher's everyday life was a real asset to my development. All other colleagues at the research group of Advanced Geodesy shall be appreciated, with the solace offered by Banoub Akladious and the scientific advice provided by Sigrid Böhm and Tobias Nilsson being especially invaluable.

On a very personal note, I would like to express my heartfelt gratitude to my parents and my grandmother for being the bedrock of stability and encouragement throughout my life. Only under their faith and sacrifices I was able to receive the education this thesis is resting upon. I am equally indebted to my wife for her unwavering patience and caring love, and for reminding me time and again of what is also important in life.

Financial support of my work was made available both by the Austrian Science Fund (FWF) within projects P20902-N10 and P23143-N21 as well as the Vienna University of Technology. I also kindly acknowledge the diverse sources of geophysical fluid data blended in this thesis, amongst them the European Centre for Medium-Range Weather Forecasts (UK), the Global Modeling and Assimilation Office (US), the Research Data Archive at the National Center for Atmospheric Research (US), and the Centre National d'Études Spatiales (FR).

Michael Schindelegger, November 2013

Abstract

Thorough investigation of Earth rotation irregularities plays a key role in advancing the quality and accuracy of space geodetic products, which have become truly indispensable to global positioning and navigation tasks. To the same extent, dissecting the observed variability of the rotation magnitude and the spin axis' equatorial motion in terms of its geophysical origin is a rewarding endeavor in favor of promoting insight into Earth system dynamics on a broad range of time scales. Much of the modern-day interest in those effects pertains to short periods, encompassing also a minute but measurable influence of diurnal and semi-diurnal atmospheric tides on Earth rotation parameters (ERP), which describe polar motion and changes in length of day (LOD). The physical character of this forcing is known to be twofold—the atmosphere exchanges angular momentum with the solid Earth both directly through boundary layer stresses and indirectly through the oceans—but existing quantifications of the elicited rotational perturbations at those high frequencies are still at discord and thus a source of uncertainty in the analysis and interpretation of space geodetic data.

The present dissertation aspires to redress this shortcoming by examining atmosphere-induced (semi-)diurnal ERP signals with a comprehensiveness that is especially devoted to the validity of the underlying dynamical quantities computed from atmospheric models. Based upon a carefully selected pool of meteorological data from three state-of-the-art atmospheric analysis and assimilation systems, a range of numerical tests peruses both groups of valid excitation measures, that is, atmospheric angular momentum (AAM) terms, involving pressure and wind contributions, and Earth-atmosphere interaction torques, composed of ellipsoidal, mountain, and friction effects. A mutual comparison of individual quantities among all models indicates their reliability for describing short period ERP signals, and this inquiry is augmented by a numerical verification of the analytical balance existing between the time derivative of AAM and the total atmospheric torque at diurnal and higher frequencies. Further inadequacies impacting pressure terms and ellipsoidal torques are potentially detected by a newly-proposed cross-check against a mean atmospheric mass-field variability dataset derived from frequent surface barometer recordings at land stations and marine platforms. These investigations form the foundation for the thesis' final goal of advancing the agreement between modeled and observed ERP variations in selected components.

As a first major qualitative finding, the inspection of the AAM balance in the equatorial and axial directions demonstrates a wholesale improvement with respect to comparative efforts in the literature. This result partly relates to the increased quality of atmosphere analysis systems over the last decade, but it also owes to the availability of high-resolution (3-hourly) meteorological fields and their consistent treatment when determining AAM and torque quantities. Remaining deficiencies in the diurnal and semi-diurnal AAM balance appear to be inflicted by either pressure or wind terms rather than by mountain and friction torques, and this suspicion is additionally reinforced by the comparatively inferior match of AAM components in contrast to the general

inter-analysis agreement of torque terms in a component-wise comparison. The sensitivity to small secondary modes in the spherical harmonic development of atmospheric tides emerges as a particular vulnerability of the angular momentum modeling route. In-situ barometric data prove to be only a partial remedy in this respect, impaired also by a massive analysis effort necessary to derive global pressure tide grids. Nevertheless, the semi-diurnal equatorial pressure term phasors of one specific atmospheric model can be identified as erroneous quantities in this vein.

The host of validity tests allows for a plausible argumentation with regard to Earth's diurnal and semi-diurnal excitation budget after fully accounting for the substantial influence of ocean tidal angular momentum, which originates either from gravitational or meteorological forces. Semi-diurnal polar motion and LOD solutions from the most recently analyzed space geodetic data accommodate an effectively negligible direct atmospheric contribution and rather await the prospective improvement of ocean model predictions to mitigate the discrepancies between geodetic measurements and the geophysical quantities that excite them. Persisting leakage in the diurnal polar motion budget pinpoints remaining errors in the observed wobble series as the geodetic solutions themselves disagree on a level exceeding the supposed magnitude of atmosphere-induced signals. However, the budget inquiry for diurnal LOD variations testifies a hitherto unmatched closure, and this key result is established by resorting to atmospheric torque terms instead of the customary but less credible axial AAM measures. Projected onto Earth's surface, the successfully explained LOD variation might not exceed 0.3 mm, but this effect nonetheless constitutes one piece of the puzzle that allows for refining the models of Earth's variable rotation.

Kurzfassung

Die umfassende und exakte Beschreibung des Rotationsverhaltens der Erde ist ein integraler Bestandteil weltraumgestützer Messverfahren, die heute sowohl zur Bestimmung globaler Referenzrahmen als auch für vielzählige Positionierungsaufgaben unerlässlich geworden sind. In einem äußerst interdisziplinären Ansatz ermöglicht die Studie beobachteter Erdrotationsschwankungen aber auch Rückschlüsse auf die zugrundeliegenden geodynamischen Prozesse und die manigfaltigen Wechselwirkungen im System Erde. Ein nicht unwesentlicher Anteil des diesbezüglichen Forschungsinteresses gilt täglichen und halbtäglichen Effekten, welche neben gravitativ bedingten Ozeangezeiten in geringfügigem Maße durch thermische Gezeiten in der Atmosphäre hervorgerufen werden. Während die physikalische Ausprägung dieses Einflusses auf die Erdrotationsparameter (ERP) offenkundig in einem Drehimpulsaustausch zwischen Atmosphäre und rotierender fester Erde besteht, herrscht zwischen entsprechenden quantitativen Abschätzungen deutliche Dissonanz, was wiederum eine Fehlerquelle in der Interpretation der Resultate geodätischer Weltraumverfahren darstellt.

Die vorliegende Dissertation liefert einen entscheidenden Beitrag zur Behebung dieses Defizits anhand einer detaillierten Analyse der aus Atmosphärenmodellen abgeleiteten täglichen und halbtäglichen Anregungsgrößen, wobei besonderes Augenmerk auf deren Zuverlässigkeit gelegt wird. Auf Basis von meteorologischen Daten dreier modernster Analyse- und Assimilationssysteme werden sämtliche Komponenten der zwei verfügbaren Modellierungsansätze über atmosphärische Drehimpulsvariationen (AAM, Atmospheric Angular Momentum) bzw. atmosphärische Drehmomente eingehend numerisch geprüft. Eine erstmalige Verifikation der Gleichgewichtsbeziehung zwischen AAM-Tendenz und Drehmomentkomponenten auf subtäglichen Zeitskalen (AAM-Bilanz) dient dabei als zentrales Instrument zur Klärung der Validität von geophysikalisch modellierten Erdrotationssignalen. Unterstützt wird dieser Ansatz von einem modellübergreifenden Vergleich hinsichtlich jeder einzelnen Anregungsgröße—sprich Massen- und Bewegungsterme im Falle von AAM bzw. integrierte Druck- und Reibungseffekte im Falle von Drehmomenten. Des Weiteren erlaubt eine eigens konzipierte Gegenüberstellung zu AAM-Signalen basierend auf global verteilten, hochaufgelösten Barometermessungen die Detektion von Unzulänglichkeiten atmosphärischer Massenterme. Die Summe dieser Untersuchungen bildet das Fundament auf dem eine engere Übereinstimmung zwischen beobachteten und modellierten ERP (Polbewegung und Tageslängenschwankungen) erzielt werden soll.

Die umfassende Verbesserung in der Verifikation der AAM-Bilanz gegenüber Vorgängerstudien stellt ein erstes Kernresultat der Arbeit dar, welches offenbar durch die gesteigerte Qualität von Atmosphärenmodellen über das letzte Jahrzehnt, aber auch durch die konsistente Verwendung und Prozessierung von 3-stündlichen Vorhersagedaten zustande kommt. Verbleibende Mängel in den täglichen und halbtäglichen Bilanzvergleichen ergeben sich augenscheinlich weniger aus unrealistischen Drehmomentgrößen als aus fehlerhaften Massen- oder Bewegungstermen. Dieser

Verdacht verstärkt sich im Zuge der Gegenüberstellung jeweils gleicher Anregungskomponenten aus allen verwendeten Modelle, innerhalb welcher die AAM-Reihen verhältnismäßig schlecht abschneiden. Als physikalische Erklärung dieses Umstandes ist die Sensitivität von Drehimpulsgrößen auf nur sehr schwache Moden im Spektrum atmosphärischer Gezeiten naheliegend. Die aus lokalen Barometerdaten erstellten Drucktiden ermöglichen in begrenztem Maße die Aussortierung mangelhafter Massenterme. Letzteres gelingt insbesondere für die halbtäglichen Komponenten einer der drei atmosphärischen Analysesysteme.

Nachdem dem Effekt der gravitativ und meteorologisch bedingten Ozeangezeiten Rechnung getragen wird, lassen die angestellten Zuverlässigkeitsbetrachtungen eine plausbile Argumentation in Hinblick auf das residuale Budget von beobachteten ERP zu. Halbtägliche Polbewegungs- und Tageslängenschwankungen aus aktuellen Lösungen geodätischer Weltraumverfahren beinhalten nur einen äußerst geringen atmosphärischen Beitrag, der vor allem angesichts der bestehenden Unstimmigkeiten zwischen verschiedenen Abschätzugen des Ozeangezeitensignals faktisch vernachlässigbar ist. Demgegenüber suggeriert das unzureichend geschlossene Budget der täglichen Polbewegung verbleibende Fehlereinflüsse in den beobachtungsbasierten Variationen, da diese Lösungen Diskrepanzen aufweisen die quantitativ den mutmaßlichen Effekt der atmosphärischen Anregung klar übersteigen. Die Beurteilung des täglichen Rotationsbudgets für die Tageslänge fällt mit einer bislang unerreichten Übereinstimmung zwischen geodätischen und geophysikalischen Größen allerdings sehr positiv aus, wobei das Ergebnis in erster Linie durch eine Vermeidung der wenig glaubwürdigen AAM Werte zugunsten der weitaus stabileren atmosphärischen Druck- und Reibungsdrehomente erreicht wird. Trotz der geringen Größe dieses hochfrequenten Signals—0.3 mm in einer Projektion auf den Äquator—ist seine Berücksichtigung für ein zukünftiges, verfeinertes Modell der Erdrotation ein potentiell wertvoller Beitrag.

Contents

Chapter 1

Introduction

Much of the fascination of higher geodesy emanates from the dynamic nature of the Earth system. The spatial and temporal scales on which our planet exhibits changes of its geometric composition, its gravitational field, and its rotary motion are unbounded—as is the aspiration to give an accurate account of those phenomena. Knowledge of Earth rotation irregularities in particular is substantial for any positioning task involving spaceborne observations, but beyond that it is also invaluable for foundational research aiming to probe the structure of the core and mantle as well as the interactions between Earth's solid and fluid components. Atmosphere and ocean dynamics, capable of inducing significant mass displacements and particle flow, have been recognized as pivotal sources for fluctuations of Earth's rotation vector on time scales from hours to several years; and inferring these perturbations from such marvelous tools as global geophysical fluid models has become an intriguing branch of science that is decisive in improving both the results of space geodesy and our understanding of the Earth as a complex dynamical system.

1.1 Earth's variable rotation

Geodetic devices sensing our planet's rotary motion are placed at the surface of the solid Earth, which is encased by an atmosphere, partly covered by water masses, and moving in the gravitational fields of extraterrestrial bodies. The forcing associated with these internal and external agents engenders manifold spatio-temporal variations of the Earth rotation vector, both in terms of its planar movement and its actual magnitude. Specifically, changes in the rotation speed can be stated as excess values over the nominal length of one day (LOD for short), whereas axis movement with respect to the crust refers to *polar motion* (or *wobbles*) and direction changes with respect to stable celestial objects are labeled as *precession* and *nutation*. A few signal components in those parameters are so prominent that they deserve special mention in advance. Specifically, precession constitutes the gravest deviation from rotational uniformity and arises as a result of Earth's gyroscopic response to the gravitational torques exerted by Moon and Sun on our oblate planet. The corresponding circular revolution of the spin axis around the ecliptic pole has an approximate period of 25800 yr at aperture $2 \cdot 23.5^\circ$, corresponding to a velocity of around

600 m yr^{-1} if projected onto the Earth surface. The paramount characteristic of polar motion is a beat-like oscillation of up to 9 m in consequence of an annual wobble (that is mainly caused by the seesawing of atmospheric mass between hemispheres) interfering with the free mode known as *Chandler Wobble*. While the misalignment of the rotation and figure axes of the Earth has long been identified as the basic mechanical catalyst for this free oscillation, its definite excitation sources are still the matter of some debate, see Seitz & Schuh (2010) for more details.

The ambition to discover the geophysical origin of periodic or more irregular Earth rotation variations may extend to even the faintest signals found at *short periods*, i.e. time scales of one day or less in the context of this thesis. Partly concealed by the substantial effect of water mass displacements in the wake of lunisolar gravitational attraction, thermal *tides in the atmosphere* at the principal diurnal and semi-diurnal frequencies of one and two cycles per solar day (cpd) perturb nutation at a fully measurable level and likewise elicit minute wobbles and LOD variations. This specific forcing on the rotation of the solid Earth embraces both a direct influence due to pure atmosphere dynamics as well as a non-direct fraction attributed to the oceans' response to the meteorological tidal cycle. In order to quantify such fluid layer effects in general, two distinct but closely connected approaches have been conceptualized (Munk & Groves, 1952). The first, traditionally used method capitalizes on the angular momentum conservation property of a whole Earth system, thus allowing for a diagnosis of the solid Earth's rotational behavior from the sole knowledge of the change in fluid *angular momentum*. Equivalently, the normal and tangential interaction forces at the subsystems' interfaces (Schindelegger *et al.*, 2013c) can be integrated to global *torque* measures that are capable of unveiling the physical interplay between solid and fluid portions. Both methods originate from the same analytical statement and should therefore yield identical rotational predictions.

Amidst the devotion to geophysical modeling, one must not lose sight of the subject's geodetic basis, which eventually bears assets for applied research and global society alike. The frequently cited example of spacecraft navigation is a flagship application that critically depends on an utmost accurate knowledge of Earth rotation variability in the form of nowcast and forecast models. More to the point, reliable Earth observations, e.g. that of the global sea level, are rendered possible by the establishment of stable coordinate frames. This geodetic reference derives almost entirely from the measurements of space geodetic techniques, such as VLBI (*Very Long Baseline Interferometry*) or GNSS (*Global Navigation Satellite Systems*), amassed on multiple time scales. The post-processing of these observations toward a robust coordinate frame profits decidedly from precise functional models of Earth's motion in space, in particular in cases where not all rotational parameters can be estimated but instead have to be fixed to a priori values (Böhm, 2012).

1.2 Motivation and objectives of the study

The present dissertation is conceived as a comprehensive treatise on the nature and scope of atmosphere-induced diurnal and semi-diurnal excitation of polar motion and changes in LOD from the viewpoint of geophysical modeling. The cardinal necessity of such an effort arises from the fact that current determinations of the effect are still without consensus (e.g. Brzeziński, 2008; Brzeziński *et al.*, 2012; de Viron *et al.*, 2005b), thereby introducing a considerable amount of uncertainty to any discussion of the observed but unexplained portion of short period Earth rotation. On the face of it, the minute size of the sought-for perturbations—less than 0.5 mm when projected at the Earth's surface—might attenuate the interest in them to a rather scholarly level, but then again, modern space geodetic techniques pursue ambitious objectives for the accuracy and quality of Earth rotation products (Schlüter & Behrend, 2007). As a matter of fact, the short period spectra of polar motion and changes in LOD as observed by VLBI or GNSS have reached a noise level that positively warrants a detailed account of atmosphere-induced signals at diurnal and semi-diurnal frequencies (Artz *et al.*, 2012). Determining comprehensive and reliable estimates of those effects will eliminate parts of the ambiguities within future considerations of the short period excitation budget, thereby facilitating the assessment of the remaining inadequacies inherent to both space geodetic results and models of the dominant influence due to ocean tides.

The central theme for the majority of the thesis is to scrutinize the validity of atmospheric excitation measures at (semi-)diurnal periodicities by several conclusive numerical tests. This strategy goes beyond the customary, mere diagnosis of rotational corrections via the angular momentum approach and grounds on the incorporation of Earth-atmosphere interaction torques as legitimate proxy in studies of Earth system dynamics. Caveats on the use of the torque approach are usually strong, though, pointing to uncertainties in the mathematical formalism, a detrimental vulnerability to errors in the geophysical fluid data, and high quality requirements on the underlying model. While most of these statements have been inferred by considerations at long periods (de Viron & Dehant, 2003), and might therefore not necessarily hold for excitation signals associated with atmospheric tides, recent substantial advances of atmospheric analysis and assimilation systems in terms of model physics, actual observations, spatial resolution, and output parameters are themselves capable of mitigating some of the drawbacks of the torque method, see Schindelegger *et al.* (2013c). Hence, a sensibly selected assembly of meteorological data from established atmospheric models operated by the ECMWF (*European Centre for Medium-Range Weather Forecasts*) and GMAO (*Global Modeling and Assimilation Office*) of NASA (*National Aeronautics and Space Administration*) represents the numerical backbone of this thesis. Much the same care has to be exercised when adapting the mathematical formalism of the torque approach to the high frequencies of interest. While the study is not targeting a major overhaul of theoretical concepts, a recently proposed alternative excitation scheme for equatorial torques (Schindelegger *et al.*, 2013c) shall be further investigated and extended to the axial component.

Both angular momentum and torque quantities for the atmosphere are computed with utmost consistency and with an unprecedented 3-hour temporal resolution in all models, evading aliasing effects and enabling an unambiguous examination of semi-diurnal signals. On that basis, the analytical equivalence between the time rate of change in AAM (atmospheric angular momentum) and the sum of interaction torques on the atmosphere shall be successfully verified for the first time at sub-daily periodicities. This inquiry on the global *AAM balance* fosters insight into the validity of atmospheric analysis systems for accurately describing Earth rotation variability and can be complemented by a mutual comparison of the utilized datasets in terms of individual torque and AAM quantities. Both tests serve to single out deficiencies and weaknesses of the two respective modeling approaches, which is a great asset when deciding on the probable amplitude and phase values of atmospheric contributions to polar motion and LOD variations.

The simplified notion of time-invariant, harmonic geophysical phenomena represents a common thread throughout the study and one must abide by that methodology when probing atmospheric excitation quantities by yet another approach. Globally distributed barometer recordings convey the most reliable knowledge of the pressure portion of atmospheric tides (Ray, 2001) and can be subject to a fit of low-degree spherical harmonics in the quest for an independent validation of the mass-field signal in the AAM vector. Being a novel approach, its subtleties and overall feasibility are not less interesting than the eventual results in the context of Earth rotation. Once more, the analysis effort profits from a recent, reliable compilation of geophysical data—in this case an extensive, quality-controlled surface pressure databank.

1.3 Thesis outline

Following this preface, Chapter 2 elucidates the study's geodetic framework in a very brief manner. The concepts underlying the realization of celestial and terrestrial reference systems are supplemented by a description of the rotational elements that transform from one reference frame to the other. The reader is equipped with some rudimentary information on how VLBI and GNSS operate and derive Earth rotation data, before being given a spectral decomposition of the major geophysical effects on the equatorial and axial components of the Earth rotation vector.

Chapter 3 assembles the mathematical tools for modeling geophysical—and specifically atmospheric—excitation of polar motion and changes in LOD on the basis of both angular momentum and torque methods. Rather than recapitulating established equations that are mostly valid at low frequencies, the derivations interlace short period formalisms with some theoretical advances of recent publications. Particular emphasis is placed on the nature of the AAM balance and its intricacies at diurnal and semi-diurnal periodicities.

Knowledge of the characteristics of atmospheric tides, as essential for argumentation throughout the thesis, is nurtured in the first section of Chapter 4, including a short sketch of the phenomenon's analytical treatment. Targeting a preliminary comparison of atmospheric models in terms of selected tidal variables, the features of the utilized assimilation systems as well as their analysis and forecast fields are portrayed thoroughly. The closing section reports on the scientific value of barometric in-situ observations as extracted from a global surface pressure archive.

On the back of a detailed spectral examination of the torque and angular momentum contributions to their respective approaches, the sought-for reliability assessment of (semi-)diurnal excitation quantities is accomplished in Chapter 5 within a three-step procedure. The first two analyses derive from the AAM balance constraint and are realized by means of correlation and regression tests in the frequency domain as well as a component-wise breakdown into complex phasors at both tidal bands. A term-by-term comparison across all atmospheric models rounds off this chapter and leads to an interesting intermediate conclusion.

Chapter 6 illustrates the journey from point observations of surface pressure to the global measure embodied by the mass portion of the AAM vector. Considerable space is devoted to the description of processing strategies for continental and marine barometric measurements and the adjustment of globally gridded pressure tide harmonics. The resultant AAM variations facilitate the validation of model-based phasors for selected components.

Observed Earth rotation variations from most recent VLBI analyses and a stand-alone reprocessing of a global GPS network are finally ingested in Chapter 7, which also gives an accurate account of the role and magnitude of oceanic angular momentum at diurnal and semi-diurnal frequencies. Blended with estimates of the atmosphere-related rotational corrections from both the angular momentum and torque approaches, the geophysical excitation terms are examined for their agreement with geodetic observations of short period polar motion and changes in LOD.

A compact summary of this study's findings and the conclusions thereof can be found in Chapter 8.

Chapter 2

Parametrization and observation of Earth rotation variations

Describing and monitoring the rotational behavior of the Earth are intricate challenges and provide the geodetic foundation of the present study. A very concise outline of these concepts is given in the following, encompassing observation techniques as well as the definition of geodetic reference systems and their interlinking parameters. A broad band look on the spectrum of geophysical fluid effects in Earth rotation allows the reader to capture the relevance of atmosphere-induced excitation signals on all time scales.

2.1 Geodetic reference systems and frames

The orientation of the Earth axis has variations in space as well as with respect to the Earth surface. Precise monitoring of these effects thus relies on the definition and establishment of both space-fixed and body-fixed coordinate systems. Their respective realizations, commonly referred to as Celestial Reference Frame (CRF) and Terrestrial Reference Frame (TRF), are maintained and constituted under the auspices of the *International Earth Rotation and Reference Systems Service* (IERS), the *International Astronomical Union* (IAU), and the *International Union of Geodesy and Geophysics* (IUGG). Each reference frame is characterized by a set of physical and mathematical properties (Altamimi *et al.*, 2011), comprising origin, scale, orientation, and temporal evolution.

Celestial Reference Frame

The *International Celestial Reference Frame 2* (ICRF2, Fey *et al.*, 2009) represents the current conventional space-fixed coordinate frame, realized based upon the concept of the ICRS (*International Celestial Reference System*, Arias *et al.*, 1995) by virtue of precise equatorial coordinates of 3414 extragalactic radio sources observed in VLBI programs. In accordance with the recommendations of the IAU, the ICRS is an equatorial system, its origin placed at the barycenter of the solar system, and its pole aligned with the J2000.0 (standard epoch) direction as deduced from

VLBI corrections to previous IAU standard models of precession and nutation. The origin of right ascensions is defined in close proximity to the dynamical equinox at J2000.0 (Arias *et al.*, 1995), and the positions of all 295 axes-defining sources are independent of the observation epoch, see Fey *et al.* (2009) for further details.

Terrestrial Reference Frame

Present-day TRF specifications are constructed based on the theoretical concept of the ITRS (*International Terrestrial Reference System*), which is stipulated as a geocentric Cartesian coordinate system co-rotating with the Earth in its diurnal motion and having its origin defined at the center of mass of the whole Earth (including atmosphere and oceans, Petit & Luzum, 2010). By convention, the ITRS orientation coincides with that of the previous BIH (*Bureau International de l'Heure*) system at the epoch 1984.0, implying that the origin of longitudes roughly corresponds to the Greenwich meridian, while the ITRS pole is located in vicinity of the mean rotation pole at the beginning of the 20th century (Böhm, 2012). In order to define the datum of the ITRS and represent velocities without referring to a particular plate, a no-net-rotation condition is imposed on the horizontal lithospheric motions over the whole Earth. This also ensures the time evolution of the ITRS orientation (Petit & Luzum, 2010).

The materialization of the ITRS consists of estimated coordinates and velocities of globally distributed, crust-bound stations that are observed by four space geodetic techniques: VLBI, GNSS, SLR (*Satellite Laser Ranging*), and DORIS (*Doppler Orbitography Radiopositioning Integrated by Satellite*). 934 stations at 580 different sites contribute to the current ITRS realization, called ITRF2008 (Altamimi *et al.*, 2011), which is believed to hold origin and scale accuracies at the level of 1 cm and 1.2 ppb (8 mm at the equator), respectively. The ITRF2008 positions are referred to the epoch 2005.0 and can be formulated with respect to other TRF versions by a similarity transformation involving seven parameters (three rotations, three translations and a scale) as well as their first-order time derivatives.

2.2 The Earth orientation parameters[1]

Changes in the orientation of the terrestrial reference system relative to a geocentric celestial reference system are unambiguously described by three time-dependent Euler angles. However, owing to tradition and convenience, astronomy accomplishes this transformation via an intermediate reference system and five rotational elements, called *Earth orientation parameters* (EOP). The three EOP categories are: *precession* and *nutation*, comprising long-periodic motions of a preassigned reference axis (e.g. the rotation axis) in the CRF; *polar motion*, representing direction changes of the reference axis in the TRF; and an angular quantity describing the actual phase of the TRF rotation with respect to the CRF. The non-uniform part of this diurnal rotation can be

---

[1] Parts of this section are taken from Schindelegger *et al.* (2013b) and Böhm (2012).

reckoned in changes in *length of day* (LOD) or, alternatively, in dUT1 = UT1 − UTC, i.e. the deviation of UT1 (*Universal Time 1*) from the uniform atomic time UTC (*Universal Time Coordinated*). The choice of the above reference axis for both the calculation of the precession-nutation models and the accordingly defined polar motion is not forced by observation conditions (Böhm, 2012) but purely conventional. Following resolution B1.7 adopted by the IAU in the year 2000, the reference direction is the axis of the *Celestial Intermediate Pole* (CIP), the definition of which is further discussed at the end of this section. In practice, all space geodetic techniques utilize the conventional, currently recommended precession-nutation model (IAU 2006/2000 precession-nutation model, see Petit & Luzum, 2010), and their observations therefore refer to the CIP.

The actual transformation procedure according to present IAU resolutions is specified between the ITRS and the so-called *Geocentric Celestial Reference System* (GCRS), which conforms to the ICRS in its orientation but has been moved from the barycenter to the geocenter. For any position vector $\boldsymbol{r}$ at date t, the transition ITRS → GCRS (or vice versa) can be expressed as a series of time-dependent rotation matrices (Petit & Luzum, 2010)

$$\boldsymbol{r}_{GCRS}(t) = \mathbf{Q}(t) \cdot \mathbf{R}(t) \cdot \mathbf{W}(t) \cdot \boldsymbol{r}_{ITRS}(t) . \tag{2.1}$$

Herein, $\mathbf{W}(t)$ describes the terrestrial motion of the intermediate system's reference pole, the CIP, through the pole coordinates x_p and y_p. The argument of the spin component matrix $\mathbf{R}(t)$ is named *Earth Rotation Angle* (ERA) and directly relates to UT1. Precession and nutation are accounted for via $\mathbf{Q}(t)$ based on the angles X and Y that signify the coordinates of the CIP with respect to the GCRS. Within the framework of this transformation (see Petit & Luzum, 2010, for notes on the erstwhile, equinox-based transformation), the set of $\{x_p, y_p, \mathrm{dUT1}, X, Y\}$ constitutes the EOP. The nutation angles occupy a special position amongst those parameters, as their major portion due to lunisolar, planetary and geophysical (ocean tidal) effects is well predictable and thus covered by the conventional nutation model. Residual motions of the CIP in the GCRS are measured by means of VLBI and denominated *celestial pole offsets*. The terrestrial EOP subset of

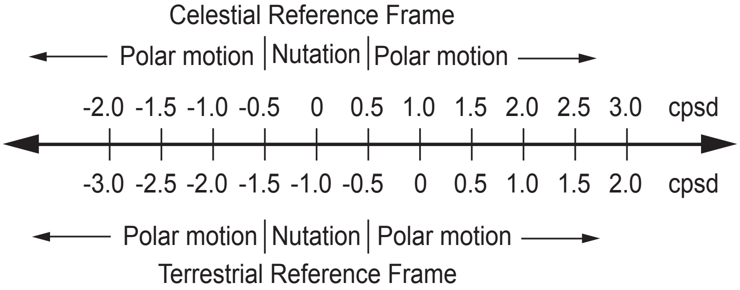

Figure 2.1: Relationship between the frequency of some motion as viewed from the celestial reference frame (top half of figure) and the corresponding frequency of the same motion as observed from the terrestrial reference frame (bottom half) (Gross, 2007; Schindelegger *et al.*, 2013b).

polar motion and dUT1, or also LOD, represents the *Earth rotation parameters* (ERP). Continuous time series of ERP and celestial pole offsets are published by the IERS at daily intervals.

As a consequence of utilizing an intermediate reference system, each motion of the CIP in the ITRS implicates a corresponding positional change of the CIP in the GCRS, i.e. polar motion and nutation are kinematically connected (Gross, 2007). To resolve this ambiguity, the definition of the CIP has been equipped with a conventional frequency separation. Specifically, all long-periodic celestial CIP variations within the frequency range $\sigma_c \in (-0.5, 0.5)$ cpsd (cycles per sidereal day) are assigned to precession and nutation. When viewed from the ITRS, σ_c is shifted by the frequency of diurnal rotation (1 cpsd) to $\sigma_t \in (-1.5, -0.5)$ cpsd. Terrestrial CIP variations outside this retrograde diurnal band are thus allocated to polar motion, see Figure 2.1. Note that retrograde frequency (minus sign) reckons motion opposite to the sense of Earth rotation, while prograde terms (plus sign) accommodate CIP variations in the sense of Earth rotation. Refer to Petit & Luzum (2010) or Seitz & Schuh (2010) for further details on the presented transformation procedure and the CIP frequency convention.

2.3 Space geodetic observations of Earth rotation

Modern-day space geodetic techniques grant access to the full spectrum of Earth rotation, covering in particular irregular fluctuations that are not predictable through theoretical or semi-empirical models but have to be monitored instead. The sensitivity of those techniques to precession-nutation, polar motion, and changes in rotation speed emanates from the transition between space-fixed and Earth-fixed reference systems being an integral part of the evoked observation equations. Sub-daily Earth rotation variations, as scrutinized from a geophysical modeling point of view in the present thesis, are measured with peerless accuracy by means of VLBI or GNSS, and for that reason a brief outline of both observing systems shall be given.

2.3.1 Very Long Baseline Interferometry

VLBI measures the delay in arrival times of microwave signals from extragalactic radio sources (e.g. *quasars*) across intercontinental baselines. In its most elementary configuration, the technique consists of two simultaneously operating large dish antennas (telescopes), detecting the plane wavefront signal of the distant emitter at observation instants separated by the *time delay* τ, see the schematic diagram in Figure 2.2. τ is measured through wave interference in post-processing mode, which necessitates the use of precise on-site atomic clocks that render the time, frequency, and phase information of the digitalized radiation signals on magnetic disks (Schuh & Behrend, 2012). Within geodetic VLBI, the traditionally probed frequencies are 2.3 GHz and 8.4 GHz, and routine experiments (labeled as *sessions*) comprise networks of four to eight globally distributed stations on average (Böhm, 2012). Rapid sequential observations of multiple radio sources in the course of a session allow for the determination of basically all quantities affecting the delay measurements, in particular station positions, quasar coordinates and Earth

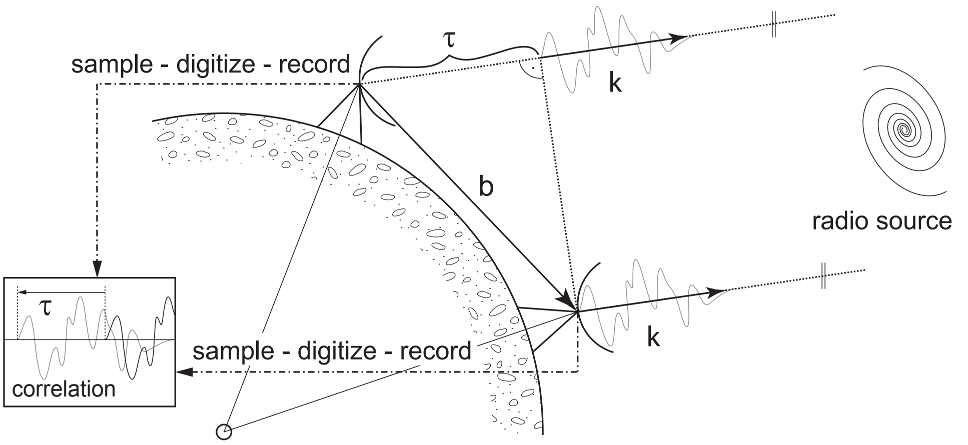

Figure 2.2: Basic concept of VLBI observation after Sovers *et al.* (1998) and Böhm (2012). Two antennas separated by the baseline b receive plane wave forms which are emitted by a radio source located in the direction k. After digital sampling and time-tagging, a correlator determines the difference in arrival time τ between the two telescopes.

orientation data.

VLBI analysis essentially boils down to a least-squares adjustment procedure minimizing the differences between the actual observations and that recreated from an utmost accurate *delay model*. Following Schuh & Böhm (2013), the raw observations have to be cleaned from all instrumental effects (systematic clock instabilities, electronic delays, thermal deformation) and atmospheric ray path distortions (dispersive ionospheric effects and the predictable part of non-dispersive tropospheric effects) prior to adjustment. Theoretical delays are computed from the basic geometric constellation as seen from the barycentric solar system, requiring initial station-dependent corrections (plate motion, tidal displacements, loading from geophysical fluids) before the baseline vector is transfered to the geocentric CRF and subject to adaptations in the framework of general and special relativity. In-depth discussions of these and further supplemental effects as well as implementation details can be found in Sovers *et al.* (1998), Schuh & Böhm (2013) or Petit & Luzum (2010).

VLBI is an exceptional technique in that it allows the observation of all EOP, including dUT1 and celestial pole offsets, without resorting to hypotheses. Typically, the ERP subset follows from estimating one offset and one rate per session, whereas sub-diurnal variations are routinely inferred as time-invariant harmonic coefficients from a so-called *global solution*, i.e. an inversion of the normal equations accumulated over a sufficiently long time span. Within such a rigorous approach, the partial derivatives of ERP are introduced already on the level of observed delays. Alternative strategies comprise the recovery of harmonic terms from unequally-spaced, highly resolved time series at the solution level, the transformation of normal equation systems from epoch-wise ERP derivatives toward a representation in terms of harmonics at specific frequencies (Artz *et al.*, 2011), or the extraction of time-variable sub-diurnal ERP amplitudes via demodulation to low frequencies within the global solution (Böhm *et al.*, 2012b). On average, the noise level (precision) of VLBI-derived diurnal and semi-diurnal polar motion terms is in the range of 1–2 µas (microseconds of arc) and below 0.2 µs for the dUT1 components, see Artz *et al.* (2012).

2.3.2 Global Navigation Satellite Systems

Diverse high-precision geodetic and geodynamic applications as well as civil positioning tasks build on satellite-based radio navigation systems that are nowadays summarized under the hypernym GNSS. Both the US-American GPS (*Global Positioning System*) and its Russian counterpart GLONASS (*Global'naya Navigatsionnaya Sputnikowaya Sistema*) rank among the GNSS systems, which represent microwave techniques measuring the signal travel time from artificial satellites at about 20000 km altitude to terrestrial receivers. On-board atomic clocks generate carrier phase signals of at least two frequencies (1575.42 and 1227.60 MHz in the case of GPS), which are modulated by predefined codes and can be correlated with time-tagged signal replicates in the receiver to obtain precise range estimates. In its most elementary application, GNSS positioning involves range measurements to four satellites that determine the receiver's absolute coordinates and its clock error.

The abundance of observations and the well-developed network of both satellites and permanent tracking stations fuel the significance of GNSS for realizing the ITRS, sensing the ionosphere and neutral atmosphere, or monitoring Earth rotation alike (Steigenberger, 2009). Least squares adjustment and Kalman filter procedures have become the typical tools within the post-processing analysis of GNSS data, which has to make allowance for a host of effects in the observation equation, in particular instrumental corrections (clock errors, phase biases, antenna phase center variations), surcharges due to signal propagation (atmospheric delay, multipath), the unknown number of full phase cycles, relativistic corrections, or station-dependent deformation effects, see Seeber (2003) for more explicit information.

As opposed to VLBI, the space segment of GNSS realizes a dynamical rather than an inertial reference frame by virtue of the revolving satellites, and the quality of the orbit determination thus limits the accuracy of the EOP. Both parameter species (orbits and EOP) are typically adjusted in parallel, but one needs to bear in mind the virtual one-to-one correspondence between orbital elements and nutation angles as well as dUT1 (Rothacher *et al.*, 1999). Yet, the estimation of nutation rates and LOD provides a makeshift solution at high frequencies. Remaining orbit modeling biases for GPS satellites entail possible additional artifacts in diurnal and semi-diurnal ERP signals owing to the 2:1 resonance of the revolution period with Earth rotation. Nonetheless, the dense GNSS observing network is well suited for the precise estimation of polar motion (Böhm, 2012). Analogous to VLBI analysis, sub-daily ERP harmonics can be set up as global parameters across the assembled normal equations, or may be derived from the highly-resolved time series of daily or weekly solutions. The approximate accuracy of such short period ERP models is quoted to be in the range of 4–7 µas for polar motion and 0.3–0.6 µs for dUT1, see the stability analysis and intercomparison of different techniques of Steigenberger (2009).

2.4 Major geophysical effects on Earth rotation

The proven causes of Earth rotation variations are classically divided into the effects of external gravitational torques exerted by other celestial bodies on the Earth and the forcing associated with geophysical fluid dynamics (Eubanks, 1993). This section gives a brief compilation of the latter phenomena in order to assess the role and relevance of diurnal and semi-diurnal excitation signals, which are the subject matter of the present thesis. Two common subcategories of geophysical fluid motion must be distinguished: *tidal* effects, associated with the periodic and well predictable displacements of Earth's solid and fluid masses; and *non-tidal* effects that encompass the remaining, more irregular excitation signals from atmosphere, oceans, land hydrology and Earth's liquid core due to various types of forcing (radiational, thermohaline, hydrodynamic, electromagnetic, gravitational, etc.) on time scales of a few hours up to years or decades in individual cases. Besides rotational variations induced by fluid dynamics and lunisolar torques, Earth's single most important free modes, the Chandler Wobble (CW) and the *Free Core Nutation* (FCN) are the primary features of the broad band excitation spectrum in the equatorial direction. Their nature depends solely on Earth's shape and physical properties instead of any energy source, but both modes are consistently excited by geophysical effects. For an extended treatment of observed and modeled Earth rotation variations, see Gross (2007) or Seitz & Schuh (2010).

2.4.1 Equatorial signal components

The CIP frequency convention separating the motion of the ITRS pole in the GCRS into celestial and terrestrial parts (Section 2.2) entails the peculiarity of geophysical signals being present in both polar motion *and* precession-nutation. Effectively harmonic influences with retrograde diurnal periodicity (such as that of the ocean tides on a level of 1 mas, milliseconds of arc, see Mathews *et al.*, 2002) are considered in the conventional nutation model, whereas the more irregular atmospheric and non-tidal oceanic variability alongside the effect of the FCN must be monitored by means of VLBI in terms of celestial pole offsets at the size of 100–300 µas. Figure 2.3 illustrates these residual nutational motions from the viewpoint of the TRS and also presages the amplification of geophysical signals in the vicinity of the FCN resonance frequency. However, the dominant portion of the celestial CIP variability is caused by lunisolar and planetary torques acting upon Earth's equatorial bulge and engendering precession as well as periodical nutational motions (not included in Figure 2.3) with peak amplitudes found at cycles of 18.6 yr (9.2 as or 280 m if projected at the Earth's surface), 182.6 d (550 mas), and 13.7 d (94 mas).

Maintained by irregular processes in the atmosphere-ocean-system (Gross, 2000; Seitz & Schmidt, 2005), the free mode of the Chandler Wobble interferes with a stable but forced annual oscillation to produce the well-known beat-like pole curve. The mean amplitudes of those wobbles amount to 160 mas and 90 mas, respectively, both of which are merged to one peak in Figure 2.3 as a result of spectral smoothing. Pro- and retrograde annual frequencies aside, continental hydrology plays a rather subordinate role to atmospheric and

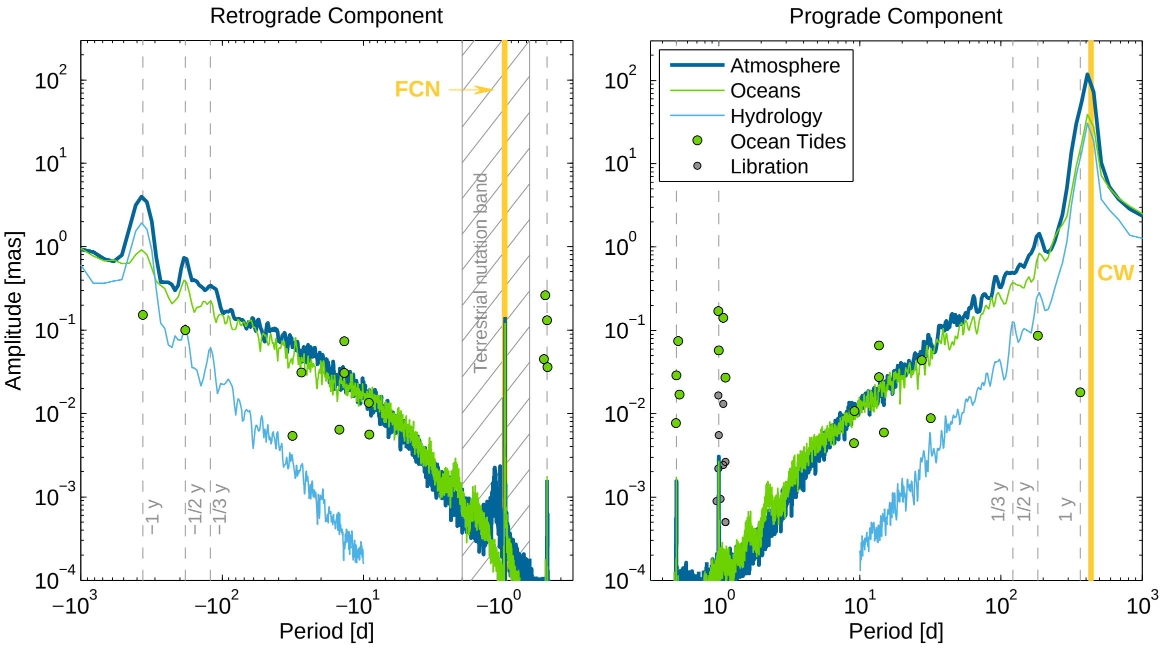

Figure 2.3: Approximate amplitude spectrum of geophysical effects on polar motion. Atmospheric excitation series (1991–2010, taken from Schindelegger *et al.*, 2013b) as well as oceanic and hydrological excitation functions (retrieved from `ftp://ftp.gfz-potsdam.de/pub/home/ig/ops/IERS_ERAinterim/`, see Dobslaw *et al.*, 2010) have been interpolated to 3-hourly values by spline interpolation. Libration harmonics, long period ocean tidal terms, and eight major diurnal/semi-diurnal tides are that of the IERS Conventions (Petit & Luzum, 2010, Chapter 5 and Chapter 8, respectively). Both CW and FCN eigenfrequencies are indicated.

oceanic processes in inducing polar motion variability. On those intraseasonal time scales, large-scale surface pressure variations over mid-latitude landmasses have been found to be the main driving agents of Earth's wobbles (Gross *et al.*, 2003; Nastula & Salstein, 1999), surpassing the influence of oceanic mass-field variability, ocean currents, and winds. Strictly harmonic phenomena embodied by long period ocean tides are capable of exceeding the non-tidal geophysical effects merely at fortnightly and monthly frequency bands.

Diurnal and semi-diurnal periodicities offer a somewhat reversed picture, which is shaped by the dominance of ocean tidal excitation at the level of 100–200 µas and only marginally affected in the order of 2–3 µas (0.1 mm at the Earth' surface) by atmosphere dynamics related to radiational tides. Additionally, near-diurnal wobbles termed *libration* are engendered by the effect of the external (mainly lunisolar) torque on the non-axisymmetric figure of the Earth (Petit & Luzum, 2010). Much the same as in the case of ocean tides, such gravitationally forced terms do not necessarily appear at the exact frequencies of atmospheric tides (1 and 2 cpd), and thereby leave enough warrant for the interest in wobbling motion as elicited by radiational tides (including their indirect effect through the oceans).

Further equatorial perturbations of the CIP, not shown in Figure 2.3, are a secular drift of the

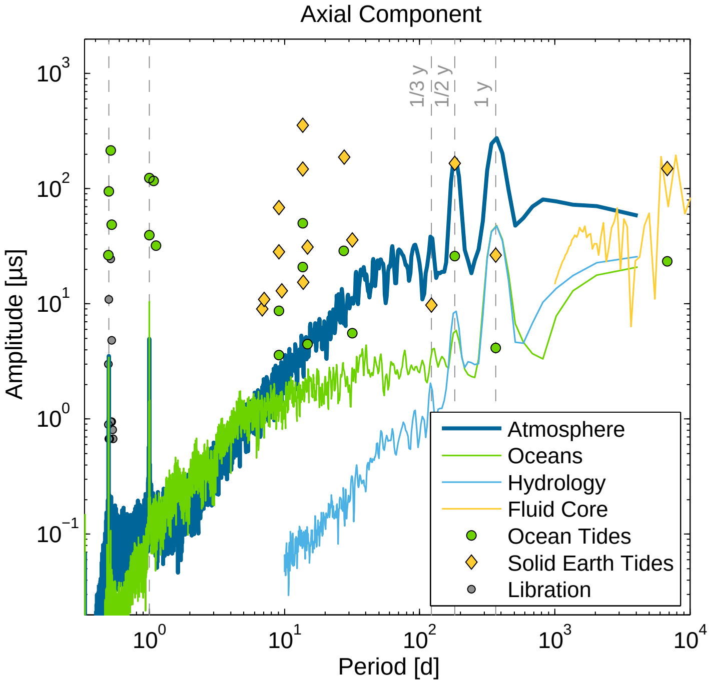

Figure 2.4: Approximate amplitude spectrum of geophysical effects on changes in length of day. Atmospheric, oceanic, and hydrological excitation series are the axial counterparts of those in Figure 2.3, while core angular momentum data have been downloaded from `http://sbc.oma.be/` (Jackson, 1997). The LOD amplitudes of libration effects, eight major diurnal/semi-diurnal ocean tides (both from Petit & Luzum, 2010), long period dynamic ocean tides (Table 4 of Dickman & Gross, 2010), and largest 'solid Earth' (elastic solid body/equilibrium ocean) tides (Table 5 of Gross, 2007) are represented by their respective markers.

pole at a rate of 3.3 mas yr^{-1} toward 76–78° W (Schuh *et al.*, 2001), interannual fluctuations due to atmospheric and oceanic excitation, and the 30-year *Markowitz* wobble, which is possibly driven by core-mantle interactions and/or mass changes in the cryosphere (Gross, 2007).

2.4.2 Axial signal components

Partly because of the absence of resonance effects and the convenience in dealing with one-sided spectral phenomena, decomposition of variations in Earth's rotation speed has been a fruitful geophysical industry for decades. Some of the very well-known signals in LOD are a secular increase by 1.8 ms per century (Morrison & Stephenson, 2001), primarily caused by the loss of angular momentum to the Earth-Moon system in the wake of tidal dissipation, significant (> 100 µs) elastic solid body/equilibrium ocean tidal harmonics at fortnightly, monthly, seasonal or longer periods, as well as the effect of (semi-)diurnal dynamic ocean tides as large as 200 µs, see Ray *et al.* (1994) and the approximate power spectrum in Figure 2.4.

In between the tidal lines, measured LOD variations are almost entirely accounted for by geophysical fluid processes, with their spectral appearance being that of 'red noise' (i.e. an increase in power is noted with decreasing frequency, Eubanks, 1993). Amongst those influences, angular momentum changes in the core dominate on decadal time scales, but elsewhere atmosphere dynamics are of paramount importance. Specifically, the pronounced annual LOD cycle of approximately 0.3 ms is associated with the yearly but asymmetric seesawing of hemispheric jet streams (Schindelegger *et al.*, 2013b), amplified interannually both by large-scale climate anomalies every 4–6 yr (El Niño-Southern Oscillation phenomenon) and a quasi-biennial oscillation from stratospheric zonal winds. Oceans and continental hydrology provide small but non-negligible contributions to the seasonal variability of the rotation rate. At diurnal and semi-diurnal periodicities, Figure 2.4 offers a constellation fairly similar to the high-frequency part of the equatorial excitation spectrum, with the influence of radiational tides in the atmosphere (also that through the oceans) being outnumbered by dynamic ocean tides and the largest libration terms. However, for the same reasons as cited in Section 2.4.1 and in face of a noteworthy magnitude level (diurnal LOD variations of 7 μs correspond to 0.5 mm at the equator), non-tidal geophysical effects at 1 and 2 cpd cannot be overlooked in closing the Earth's axial excitation budget.

Chapter 3

Modeling geophysical excitation of Earth rotation

The theoretical framework of Earth's rotational dynamics builds on the equations of gyroscopic motion applied to a multi-layered, deformable physical model of our planet. In this analytical setting, small perturbations of Earth rotation associated with motion and mass redistribution effects in the atmosphere, the oceans, the hydrosphere, etc. can be studied by utilizing either angular momentum or torque quantities. Connected via the simple statement of angular momentum balance within a fluid layer, both approaches are fundamentally equivalent but differ conceptually in their notion of the Earth system (Seitz & Schuh, 2010). The following paragraphs portray the formalisms inherent to both methods and outline how these model quantities can be related to observed ERP at diurnal and sub-diurnal periodicities.

3.1 Equations of motion

Detailed descriptions on the set-up and solution of the equations governing non-rigid body rotation are abundant in the literature (Lambeck, 1980; Munk & MacDonald, 1960; Seitz & Schuh, 2010; Wahr, 1982) and do not need to be fully recapitulated for the purpose of this thesis. The core statement is that changes in the Earth angular momentum $\boldsymbol{H} = \boldsymbol{H}(t)$ perfectly balance the external torques $\boldsymbol{L} = \boldsymbol{L}(t)$ acting upon the system. If the Earth is viewed as a deformable body composed of solid and fluid portions, $\boldsymbol{H}$ depends on (1) the time-variable mass distribution as expressed in the tensor of inertia $\boldsymbol{I} = \boldsymbol{I}(t)$; (2) the relative angular momentum $\boldsymbol{h} = \boldsymbol{h}(t)$ caused by particle motion with respect to the rotating coordinate system; and (3) variations in the angular velocity vector of the Earth $\boldsymbol{\omega} = \boldsymbol{\omega}(t)$. Hence, Earth's rotational behavior obeys

$$\boldsymbol{L} = \underbrace{\frac{\mathrm{d}}{\mathrm{d}t}(\boldsymbol{I}\boldsymbol{\omega} + \boldsymbol{h})}_{\frac{\mathrm{d}}{\mathrm{d}t}\boldsymbol{H}} + \boldsymbol{\omega} \times \underbrace{(\boldsymbol{I}\boldsymbol{\omega} + \boldsymbol{h})}_{\boldsymbol{H}}, \tag{3.1}$$

which represents the well-known *Liouville equation* (Munk & MacDonald, 1960) in a body-fixed reference frame. By convention, the latter is defined in the manner of a *Tisserand mean-mantle* frame (Tisserand, 1891), minimizing the integral of relative motion in the mantle (m) ($\boldsymbol{h}^{(m)} \overset{!}{=} 0$) while atmospheric, oceanic, and core-related contributions to $\boldsymbol{h}$ are allowed for. The validity of such a hypothetical definition has been recently addressed by Schindelegger *et al.* (2013b).

With rotational disturbances being small in size with respect to Earth's nominal sidereal angular velocity $\Omega = 2\pi/86164$ s, Eq. (3.1) can be linearized on the basis of an equilibrium state in which the entire, undeformed system is rotating around the polar axis of the body-fixed reference system. Mass redistributions perturb this initial state, generating both relative angular momentum $\boldsymbol{h} = \left(h_x, h_y, h_z\right)^T$ in the Tisserand mean-mantle frame and small, time-variable surcharges on an inertia tensor of diagonal structure

$$\boldsymbol{I} = \begin{pmatrix} A' & 0 & 0 \\ 0 & A' & 0 \\ 0 & 0 & C \end{pmatrix} + \begin{pmatrix} \Delta I_{xx} & \Delta I_{xy} & \Delta I_{xz} \\ \Delta I_{xy} & \Delta I_{yy} & \Delta I_{yz} \\ \Delta I_{xz} & \Delta I_{yz} & \Delta I_{zz} \end{pmatrix}. \tag{3.2}$$

A' and C denote the mean equatorial and polar principal moments of inertia of a dynamically axisymmetric Earth. Excursions of the instantaneous rotation vector from uniform rotation are specified by the dimensionless elements $\left(m_x, m_y, m_z\right)$, representing both the angular offsets of polar motion and the changes in the rate of rotation (also called *spin*)

$$\boldsymbol{\omega} = \Omega \begin{pmatrix} 0 \\ 0 \\ 1 \end{pmatrix} + \Omega \begin{pmatrix} m_x \\ m_y \\ m_z \end{pmatrix}. \tag{3.3}$$

Substituting Eqs. (3.2) and (3.3) into the Liouville equation and omitting products as well as derivatives of small quantities (details see Seitz & Schuh, 2010), the equations relating changes in Earth rotation to mass displacements, relative angular momenta, and external torques read

$$\hat{m} + \frac{\mathrm{i}}{\sigma_r}\dot{\hat{m}} = \frac{\Omega^2 \Delta\hat{I} - \mathrm{i}\Omega\Delta\dot{\hat{I}} + \Omega\hat{h} - \mathrm{i}\dot{\hat{h}} + \mathrm{i}\hat{L}}{\Omega^2 (C - A')} \tag{3.4}$$

$$m_z = \frac{-\Omega\Delta I_{zz} - h_z + \int L_z \mathrm{d}t}{\Omega C} + \text{const.}, \tag{3.5}$$

where $\hat{m} = m_x + \mathrm{i}m_y$, $\hat{h} = h_x + \mathrm{i}h_y$, $\Delta\hat{I} = \Delta I_{xz} + \mathrm{i}\Delta I_{yz}$, $\hat{L} = L_x + \mathrm{i}L_y$ are written in complex notation ($\mathrm{i} \equiv \sqrt{-1}$) and for once here, the time derivative in the rotating frame has been abbreviated by a dot above the character. The axial differential equation in integrated form (Eq. 3.5) is decoupled from the horizontal component (Eq. 3.4), which governs the variations of polar motion. The homogeneous solution in the equatorial direction consists of a circular motion characterized by the Euler frequency $\sigma_r = \frac{(C-A')}{A'}\Omega$ (period $T = 304$ d) of a rigid axisymmetric Earth. All factors that may perturb this rigid body rotation are contained in the *excitation functions* (Munk & Mac-

Donald, 1960) on the right-hand side of the system, including time-variable external torques, incremental inertia elements and relative angular momenta associated with, e.g., atmospheric and oceanic circulation, as well as Earth's elastic deformation due to centrifugal and tidal forces (see also next section). Their cumulative effect needs to balance the geodetic evidence of Earth rotation variations on the left-hand side of the system. Equations (3.4) and (3.5) are common to the angular momentum and the torque approaches, but are henceforth refined in a different way since both methods diverge in their partition of the Earth system (de Viron *et al.*, 2005a).

3.2 Angular momentum approach

3.2.1 First-order solution

In the classical approach for modeling geophysical excitation of Earth rotation, the rotating body encompasses both solid and fluid portions and, as such, is isolated in space, conserving its total angular momentum (Munk & MacDonald, 1960). Hence, exterior lunisolar torques $\boldsymbol{L}$ are omitted from the Liouville equation, and a net change of fluid angular momentum in the atmosphere, the oceans, and land hydrology must be budgeted by a mirror image change of angular momentum of the solid Earth (Schindelegger *et al.*, 2013c). Note the generally accepted but curious terminology in which the crust, the mantle, and the core are together known as 'solid Earth' (Dickman, 2005).

In order to quantify angular momentum variations and obtain a practical phrasing of Eqs. (3.4) and (3.5), the excitation functions are rewritten in terms of (dimensionless) equatorial and axial *angular momentum functions* $\hat{\chi}$, χ_z following Barnes *et al.* (1983)

$$\hat{\chi} = \chi_x + \mathrm{i}\chi_y = \frac{1}{\Omega(C-A')}\underbrace{\Omega\Delta\hat{I}}_{\hat{H}^p} + \frac{1}{\Omega(C-A')}\underbrace{\hat{h}}_{\hat{H}^w} = \hat{\chi}^p + \hat{\chi}^w \tag{3.6}$$

$$\chi_z = \frac{1}{\Omega C}\underbrace{\Omega\Delta I_{zz}}_{H_z^p} + \frac{1}{\Omega C}\underbrace{h_z}_{H_z^w} = \chi_z^p + \chi_z^w\,, \tag{3.7}$$

where the inertia-related parts are conventionally called *mass* or *matter* term and the relative angular momenta form the *motion* term. With reference to the underlying parameters for the case of the atmosphere, the notation of *pressure* (superscript p) and *wind* (superscript w) terms is also widely used. In fact, Chapters 5 and 6 are almost entirely devoted to $\hat{H}^p, \hat{H}^w$ and H_z^p, H_z^w respectively, i.e. the pressure and wind portions of atmospheric angular momentum (AAM). The equations of motion, formulated for the instantaneous rotation axis $\boldsymbol{\omega}$ in the Tisserand mean-mantle frame, reduce to

$$\hat{m} + \frac{\mathrm{i}}{\sigma_r}\frac{\mathrm{d}}{\mathrm{d}t}\hat{m} = \hat{\chi} - \frac{\mathrm{i}}{\Omega}\frac{\mathrm{d}}{\mathrm{d}t}\hat{\chi} \tag{3.8}$$

$$m_z = -\chi_z + \mathrm{const.}\,, \tag{3.9}$$

and need to be modified for the fact that space geodetic techniques do not observe $\boldsymbol{\omega}$ but instead, by convention, sense the motion of the CIP axis in the ITRF (Section 2.2). The prerequisite relationship between the reported polar motion of the CIP $\hat{p} = x_p - \mathrm{i} y_p$ and the location of the instantaneous rotation axis follows from considering the properties of transformation matrices (e.g. Gross, 1992)

$$\hat{m} = \hat{p} - \frac{\mathrm{i}}{\Omega} \frac{\mathrm{d}}{\mathrm{d}t} \hat{p} \, . \tag{3.10}$$

By virtue of $\hat{m}$, this kinematical equation can be connected to the dynamical theory (Eq. 3.8)

$$\hat{p} + \frac{\mathrm{i}}{\sigma_r} \frac{\mathrm{d}}{\mathrm{d}t} \hat{p} = \hat{\chi} \tag{3.11}$$

after acknowledging that the two reference frames involved (the Tisserand mean-mantle frame and the ITRF) sufficiently agree with each other. Specifically, current realizations of the ITRS provide valid approximations to the Tisserand frame of the mantle as they incorporate the concept of the mean crust (Altamimi *et al.*, 2003) and mass movements in the mantle on time scales up to decades prevail in the uppermost layer of the astenosphere (see also Schindelegger *et al.*, 2013b). While being applicable to polar motion variations at periods much longer than 1 d (Gross, 2007), Eq. (3.11) is inappropriate for the study of diurnal and sub-diurnal effects. The eventual equatorial excitation scheme will be introduced in Section 3.2.3. For the axial component, the relationship between excitation measures and published LOD or dUT1 values is straightforward (Barnes *et al.*, 1983)

$$\chi_z = \frac{\partial \Lambda}{\Lambda_0} + \text{const.} = \frac{\text{LOD[s]}}{86400\,[\text{s}]} + \text{const.} = -\frac{\mathrm{d}}{\mathrm{d}t} \text{dUT1} + \text{const.} \, , \tag{3.12}$$

where $\partial \Lambda$ (in seconds) designates the minute excess of the actual length of the solar day from its nominal length $\Lambda_0 = 86400$ s. Numerically, LOD conforms to $\partial \Lambda$ but is usually reported as seconds per nominal day, though not explicitly stated. In accordance with that custom, LOD variations are understood as time units (s, ms, or µs) per nominal day in the remainder of this work but labeled without a *per day* suffix, cf. the above equation.

3.2.2 A complication: the deformable Earth and its spin-wobble response

Hitherto the notion of deformability has been realized by accounting for mass redistributions in Earth's fluid layers, while perfect rigidity has been assumed for the mantle and the core. Allowance must be made for secondary effects that relate to the elastic properties of the solid Earth and the response of the whole system to changes in rotation. In brief, the corrections toward a more realistic Earth model comprise contributions to $\Delta \boldsymbol{I}$ and $\boldsymbol{h}$ induced by the dislocation of $\boldsymbol{\omega}$ or, equivalently, changes in the centrifugal force. Despite being evoked in every subsystem, the only non-negligible relative angular momentum surcharges arise in the core (Smith & Dahlen, 1981).

Increments to the inertia tensor as a result of the solid Earth's reaction to the body force of a varying centrifugal potential are known as *rotational deformation* (Munk & MacDonald, 1960) and augmented by the oceanic spin-wobble response in the form of an equilibrium *pole tide* (Dahlen, 1976). Moreover, surficial loads associated with the mass term of geophysical excitation are partly compensated by solid Earth deformations, and small anelasticity effects in the mantle might be taken into account as well. Considering those refinements introduces scaling factors to the mass and motion terms of Eqs. (3.8) and (3.9) but also migrates the period of the free mode from its rigid-Earth value of 304 d ($2\pi/\sigma_r$) to the theoretical Chandler period of about 425.6 d (Gross, 2007), which is in close vicinity to the actually observed period. A standard estimate from optical and space geodetic data is $T_c = 433.1$ d with a quality (dampening) factor of $Q_c = 179$ (Vicente & Wilson, 1997), yielding a complex frequency

$$\hat{\sigma}_c = \frac{2\pi}{T_c}\left(1 + \frac{\mathrm{i}}{2Q_c}\right) . \tag{3.13}$$

The corresponding modifications to the angular momentum functions are well established, with different formulations agreeing within 2%, see Schindelegger *et al.* (2013b) and references therein. Nonetheless, most of the suggested numerical schemes have been developed with the aid of a few approximations that are inadequate at near-diurnal frequencies, such as the pole tide model. Additionally, none of the formulations treats the amount of core participation in the rotational fluctuations in a fully consistent way (Dickman, 2003). This shortcoming shall be rectified in the present thesis by closely following the expressions furnished by Dickman (2005), which allow for variable degrees of core-mantle coupling during geophysical excitation. Using the example of the axial component and omitting the so-called *oceanic Love number* of the pole tide response (Dahlen, 1976), Eq. (2) of Dickman (2005) reads

$$\left\{1 + \frac{4}{3}\alpha_2 k_2 \frac{a^5\Omega^2}{3G}\frac{\alpha_1}{C}\right\} m_z = -\left\{\left(1 + \alpha_3 k_2'\right) H_z^p + H_z^w\right\} \frac{\alpha_1}{\Omega C} , \tag{3.14}$$

where a is Earth's mean radius and G represents the Newtonian gravitational constant. Both the load Love number k_2' (Farrell, 1972) and the second-degree body tide Love number k_2, describing the impact of rotational deformation, apply to an atmosphere-less, ocean-less Earth system comprising mantle and core. The fraction of this solid Earth model that responds to rotational, tidal, and load perturbations is reflected by the α_j ($j = 1, 2, 3$) coefficients. For a fully decoupled core their values reduce to

$$\alpha_1 = C/C_m, \quad \alpha_2 = k_{2,m}/k_2, \quad \alpha_3 = k_{2,m}'/k_2' ,$$

by virtue of which the mantle-only (subscript m) versions of both Love numbers and the polar moment of inertia are introduced into Eq. (3.14). Since the liquid parts of the outer core cannot follow rotational fluctuations on short time scales such as those treated here, the complete absence of core-mantle coupling is a valid assumption (Dickman, 2003). Moreover, anelastic relaxation of Earth's mantle in the wake of variable surface loads is practically negligible at daily periodicities (S. Dickman, 2013, personal communication) and has been excluded from Eq. (3.14). Using the numerical constants and parameters specified in Appendix A.5, the axial angular momentum function reads

$$\chi_z = \frac{0.757 H_z^p + 0.999 H_z^w}{\Omega C_m}, \tag{3.15}$$

which conforms to the solution proposed in Schindelegger *et al.* (2011). Despite the omission of feedback effects in the oceans (that is, the pole tide at long periodicities), the cited scaling factors deviate by only about 1% from those of Gross (2007), portending the numerical stability of axial excitation functions across different frequency bands. On the back of this positive result, Eqs. (3.12) and (3.15) can be combined without issuing a caveat on the analytical inadequacy of the axial excitation formalism[1].

Similar considerations in the equatorial component based on core decoupling during the wobble have been conducted by Schindelegger *et al.* (2011) and lead to angular momentum function prefactors that differ up to 5% (pressure term) and 13% (wind term) with respect to conventionally applied schemes (Barnes *et al.*, 1983; Gross, 2007). A discussion of those discrepancies and the underlying theoretical uncertainties is however dispensable in light of the alternative modeling route taken in the next section.

3.2.3 Broad band Liouville equation

Studies of long period polar motion variability at terrestrial frequencies $|\sigma| \ll \Omega$ are grounded on Eq. (3.11) after replacing σ_r by the CW eigenfrequency $\hat{\sigma}_c$ and allowing for the effects of deformability in $\hat{\chi}$. At near-diurnal periodicities, in particular those expressing nutational motion in the celestial reference frame, this simple model becomes inapplicable, because the geophysical forcing is close to the terrestrial frequency of the FCN normal mode. The existence of the FCN relates to the fact that the liquid outer core is of ellipsoidal shape and does not necessarily rotate in unison with the surrounding mantle. Specific excitation mechanisms, such as the deformation associated with the second-order tesseral harmonic of the surface load distribution (Sasao & Wahr, 1981), are capable of perturbing the rotation of the fluid core relative to the mantle, thus creating a strong inertial (hydrodynamic pressure) torque at the core-mantle-boundary (Eubanks, 1993). Earth's reaction to this torque is the space-referred FCN, or equivalently, a retrograde diurnal

---

[1] Given the highly rigid and viscous properties of Earth's mantle as well as the rapidity at which (semi-)diurnal mass redistributions try to perturb the solid body rotation, one might be tempted to question the realism of the rotational and load deformation models in Eq. (3.14). Yet, those concepts are definitely valid on the time scales considered here. The particular fraction of Earth's mantle that is capable of an elastic, instantaneous response to surface fluctuations is exactly conveyed by the body tide and load Love numbers, which have been designed as response factors at tidal frequencies in the first place (S. Dickman, 2013, personal communication). Observational evidence confirming those theoretical predictions can be found, e.g., in the field of ocean tidal loading (Thomas *et al.*, 2007).

oscillation of the rotation axis in the terrestrial frame at frequency

$$\hat{\sigma}_f = 2\pi\left(\frac{1}{T'_f} - \frac{1}{T_{sid}}\right)\left(1 - \frac{\mathrm{i}}{2Q_f}\right), \tag{3.16}$$

where $T_{sid} = 0.9973$ d signifies the length of the sidereal day, and $T'_f = -430.2$ d (space-referred FCN period) as well as $Q_f = 20000$ (Earth-referred quality factor) are taken from Mathews *et al.* (2002), yielding a frequency of resonance at $\sigma/2\pi = -1.00232$ cpsd or -1.00506 cpd (cycles per mean solar day), cf. Schindelegger *et al.* (2013b).

The mathematical treatment of the fluid core effect upon nutation and (sub-)diurnal polar motion necessitates the partitioning of the Liouville equation (Eq. 3.1) and the expressions of elasticity for a multi-layer Earth (mantle and liquid core at least), see Sasao & Wahr (1981) and references therein. If external gravitational torques and hypothetical, irregular core-mantle torques other than that due to the CMB deformation are neglected, the frequency domain equation of motion in a very general form reads

$$\hat{p}(\sigma) = \underbrace{\left(\frac{a_c^p}{\hat{\sigma}_c - \sigma} + \frac{a_f^p}{\hat{\sigma}_f - \sigma}\right)}_{\hat{T}^p(\sigma)}\hat{H}^p(\sigma) + \underbrace{\left(\frac{a_c^w}{\hat{\sigma}_c - \sigma} + \frac{a_f^w}{\hat{\sigma}_f - \sigma}\right)}_{\hat{T}^w(\sigma)}\hat{H}^w(\sigma)\,. \tag{3.17}$$

Earth's response to the mass and motion effects of the perturbing fluid is described via the *transfer functions* $\hat{T}^p(\sigma)$ and $\hat{T}^w(\sigma)$, which in turn depend on the coefficients $a^p_{c,f}$ and $a^w_{c,f}$ that characterize the strengths of the CW and FCN resonances upon pressure and wind excitation. All information on the underlying core-mantle model, its interior structure, elastic properties and the amount of rotational and load deformation is condensed in those coefficients. Their small imaginary parts ($<$ 0.3% of the absolute value) are virtually negligible. For the case of the CW, $a_c^{p,w}$ must be of order $\hat{\sigma}_c/\Omega\left(C - A'\right) \approx 10^{-38}$, cf. the frequency domain transform of Eq. (3.11). Three commonly applied versions of the above *broad band Liouville equation* have emerged in literature[1]: (1) Gross (1993), who rewrites the theoretical result of Sasao & Wahr (1981) (*ibid.*, Eq. 4.18) in terms of observed resonance frequencies; (2) Brzeziński (1994), who proceeds likewise but also incorporates the angular momentum function formalism of Barnes *et al.* (1983); (3) Koot & de Viron (2011), who provide a reconsideration of Sasao & Wahr (1981)'s seminal work in light of up-to-date geophysical models and the theoretical advances made by Mathews *et al.* (2002). After noting each of those schemes in the fashion of Eq. (3.17) and inserting the inherent parameter values (theoretical and/or observation-based), the CW/FCN strength coefficients of (1)–(3) can be numerically intercompared, see Table 3.1. Probably owing to the common origin given by Sasao & Wahr (1981)'s pilot equations, the overall agreement for each parameter type is on the level of 1–2%. The sole significant deviation appears for a_f^w as predicted by Koot & de Viron

---

[1] See also Dickman (1993) for an interesting but less cited study on that subject as well as Chen *et al.* (2013) for a recent, semi-analytical update on the wobble excitation functions at frequencies between -0.5 and 1 cpd.

Table 3.1: Numerical comparison of the different strength coefficients of CW ($a_c^{p,w}$) and FCN ($a_f^{p,w}$) resonances as proposed in literature. Units are 10^{-38} kg^{-1}m^{-2}.

Source	a_c^p	a_c^w	a_f^p	a_f^w
Gross (1993)	0.972	1.389	0.092	$7.626 \cdot 10^{-4}$
Brzeziński (1994)	0.963	1.403	0.092	$7.700 \cdot 10^{-4}$
Koot & de Viron (2011)	0.979	1.415	0.090	$3.718 \cdot 10^{-4}$

(2011). Yet, due to the smallness of the wind term forcing of the FCN with respect to the pressure effect, this difference is unlikely to have practical implications. On another note, the magnitude difference between a_f^p and the CW coefficients portends the irrelevance of the FCN term at long periods (though, its contribution in the retrograde semi-diurnal and the prograde diurnal band amounts to 19% and 5% of the total transfer function, see Brzeziński, 1994).

The close match amongst the existing polar motion broad band schemes at the periods of interest (±0.5 d and +1 d) is further confirmed in Figure 3.1, which displays the frequency-dependent deviations in $\hat{T}^p(\sigma)$ and $\hat{T}^w(\sigma)$ of Brzeziński (1994) and Koot & de Viron (2011) with respect to the formulation of Gross (1993). This reference study and Brzeziński (1994) apparently agree within 1% on all time scales, as both sources share exactly the same mathematical expressions and differ only due to numerical adaptations. Koot & de Viron (2011)'s update and their use of a theoretical $\hat{\sigma}_f$ value instead of the observed resonance frequency induce larger discrepancies near $-\Omega$, but do not affect the semi-diurnal and prograde diurnal bands of the terrestrial CIP motion above a level of 1.5%. Hence, the polar motion excitation results of this thesis will not critically depend on the choice of the kind of broad band Liouville equation. Ocean tidal investigations commonly employ the version of Gross (1993), and Chapter 7 will abide by that custom.

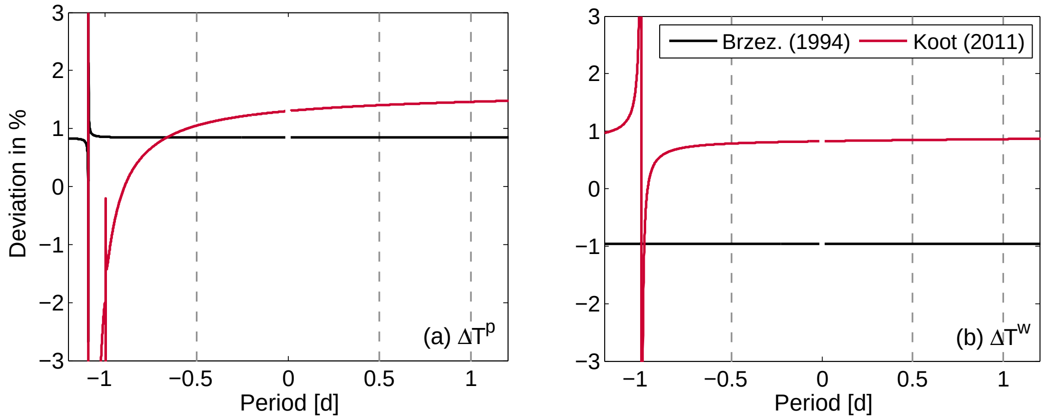

Figure 3.1: Pressure and wind term transfer functions $\hat{T}^p(\sigma)$ (a) and $\hat{T}^w(\sigma)$ (b) of Brzeziński (1994) and Koot & de Viron (2011) expressed as deviations in percent with respect to the formulation of Gross (1993). Only real parts are shown.

With regard to the geophysical discussion of Section 3.2.2, it is worth noting that the equatorial transfer function conforms with the LOD excitation scheme in its omission of anelasticity effects and the oceanic spin-wobble response. However, the strong inertial coupling associated with the FCN resonance casts doubt over the afore-going assumption of a decoupled core that cannot follow perturbations of the mantle's rotation. Also, the FCN normal mode is possibly driven by the loading deformation of the CMB (Sasao & Wahr, 1981), which contradicts the use of $k'_{2,m}$ instead of the whole-Earth value k'_2. We thus might adopt the notion of a fluid core which is decoupled from the mantle in the axial direction alone, cf. also Gross (2007).

3.2.4 Evaluation of atmospheric angular momentum

Pressure and wind term vectors $\boldsymbol{H}^p$ and $\boldsymbol{H}^w$ still need to be casted in terms of parameters that are issued with the standard output from atmospheric models and analysis systems. Starting from Cartesian coordinates, $\boldsymbol{\Delta I}$ and $\boldsymbol{h}$ are written as volume integrals over the atmosphere (Munk & MacDonald, 1960) and subsequently transfered to spherical coordinates. Thereupon, different computation methods can be formulated (see Schindelegger *et al.*, 2013b, for much more details), amongst which the thin layer approximation yields the usually preferred pressure term formulae ($\iint(.)\mathrm{d}\theta\mathrm{d}\lambda = \int_0^{2\pi}\int_0^{\pi}(.)\mathrm{d}\theta\mathrm{d}\lambda$)

$$\hat{H}^p = -\frac{\Omega a^4}{g}\iint p_s \cos\theta \sin^2\theta \mathrm{e}^{\mathrm{i}\lambda}\mathrm{d}\theta\mathrm{d}\lambda \tag{3.18}$$

$$H_z^p = \frac{\Omega a^4}{g}\iint p_s \sin^3\theta \mathrm{d}\theta\mathrm{d}\lambda\ , \tag{3.19}$$

where the atmosphere is modeled as a spherical shell (radius approximated by a) and constant gravity acceleration g. The instantaneous surface pressure $p_s = p_s(\theta,\lambda)$ at geocentric co-latitude θ and longitude λ is an accurate measure of the mass in the atmospheric column aloft. For the case of the wind term, the full three-dimensional velocity field must be taken into account

$$\hat{H}^w = -\frac{a^3}{g}\iiint (u\cos\theta + \mathrm{i}v)\sin\theta \mathrm{e}^{\mathrm{i}\lambda}\mathrm{d}\theta\mathrm{d}\lambda\mathrm{d}p \tag{3.20}$$

$$H_z^w = \frac{a^3}{g}\iiint u\sin^2\theta \mathrm{d}\theta\mathrm{d}\lambda\mathrm{d}p\ , \tag{3.21}$$

with $u = u(\theta,\lambda,p)$ and $v = v(\theta,\lambda,p)$ denoting eastward and northward wind speeds. Analytically, the vertical integration over pressure increments dp extends from the very top of the atmosphere (zero pressure) to the surface point of each column (p_s).

3.3 Torque approach

An analytical equivalent but computational alternative to the angular momentum approach can be constructed by phrasing Euler's dynamical equation of rigid body rotation (equation 3.1.1

in Lambeck, 1980) for a mechanical system in which Earth's fluids are external layers to the solid body (Munk & Groves, 1952). In this setting, the fluid (assumed to be the atmosphere (a) in the following without loss of generality) exerts an interaction torque on the solid Earth (s)

$$\boldsymbol{L}^{(a)\to(s)} = \frac{\mathrm{D}\boldsymbol{H}^{(s)}}{\mathrm{D}t} \,. \tag{3.22}$$

$\mathrm{D}/\mathrm{D}t$ signifies the time rate of change in the celestial frame as opposed to $\mathrm{d}/\mathrm{d}t$, which is the time derivative in the rotating frame. In the absence of lunisolar torques, angular momentum variations within the mechanical system are exactly balanced

$$\frac{\mathrm{D}\boldsymbol{H}^{(s)}}{\mathrm{D}t} = -\frac{\mathrm{D}\boldsymbol{H}^{(a)}}{\mathrm{D}t} \tag{3.23}$$

$$\boldsymbol{L}^{(a)\to(s)} = -\boldsymbol{L}^{(s)\to(a)} \tag{3.24}$$

$$\Longrightarrow \boldsymbol{L}^{(s)\to(a)} = \frac{\mathrm{D}\boldsymbol{H}^{(a)}}{\mathrm{D}t} \,, \tag{3.25}$$

where the last expression describes the instantaneous angular momentum budget of the atmospheric layer in inertial space (de Viron & Dehant, 1999). For use of Eq. (3.22) as a forcing term in the Liouville equations the constituents of the total torque acting on the solid Earth (or vice versa, on the atmosphere) have to be known. Those components can be derived from the classical equations of fluid motion around a rigid, rotating body (de Viron *et al.*, 1999; Wahr, 1982) and usually comprise global integrals of pressure forces on the topography (superscript p), friction drag due to surface winds (superscript f), and gravitational forces corresponding to the attraction of air masses by Earth's irregular mass distribution (superscript g)

$$\boldsymbol{L}^{(s)\to(a)} = \boldsymbol{L}^{p} + \boldsymbol{L}^{g} + \boldsymbol{L}^{f} \,. \tag{3.26}$$

The actually computed torque terms derive from this assembly after a few small modifications and a separation of equatorial and axial components as presented below. (Note that the interface signified by $(s) \to (a)$ strictly refers to the atmospheric boundary layer over the entire globe, and the surface of the 'solid Earth' therefore comprises both oceanic and continental points. This imprecise notation does not restrain the physical validity of the present equations, though.)

3.3.1 Equatorial torque components

Ellipsoidal torque

Earth's oblateness in both surface topography and the gravitational equipotential surface represents the gravest deviation from spherical symmetry, capable of producing large global pressure and gravitational torques acting on the atmosphere. As demonstrated by Marcus *et al.* (2004) for a thin, hydrostatic atmosphere, the combination of both pressure and gravitational bulge torques is subject to a distinct cancellation. Their residual effect emanates from the difference between the geopotential surface (represented by the geoid, including only the zonal spherical harmonic of degree 2) and the gravitational potential surface. The resulting contribution to $\hat{L}^{(s)\to(a)}$ thus relates to the topography of the centrifugal equipotential surface (see also Hughes, 2002), and is commonly labeled as *ellipsoidal* or *equatorial bulge torque*. Its one-to-one correspondence to the mass component of equatorial angular momentum has been deduced by Wahr (1982)

$$\hat{L}^e = \mathrm{i}\Omega\hat{H}^p \ . \tag{3.27}$$

Consequently, as seen from the Laplace spherical harmonics in Eq. (3.18), only a degree 2/order 1 pattern of the global surface pressure field produces a net signal in the ellipsoidal torque. (de Viron & Dehant, 1999).

Local torques

Local pressure forces across non-bulge topographic features are accounted for in the *mountain torque* $\hat{L}^m$ by multiplication of p_s with co-latitudinal and longitudinal gradients of the elevation above the geoid (Hughes, 2002). Given this height reference, $\hat{L}^m$ also contains a minute contribution from the local gravitational torque (O. de Viron, 2013, personal communication). The globally integrated effect of tangential wind stress at the atmospheric boundary layer is represented by the friction torque $\hat{L}^f$. Besides, a few selected studies (de Viron *et al.*, 2005b; Huang *et al.*, 1999) have considered an additional torque quantity which is usually designated *gravity wave drag torque* and captures the interchange of AAM on spatial scales smaller than the grid size of the utilized model. However, as the prerequisite *parametrization* (see Section 4.2.5) of subgrid-scale surface stresses is still not fully solved and the associated torque signal is very small for all periods (< 0.5–1.5% of the total torque depending on the model), the gravity wave drag torque will not be addressed any further. The mathematical expressions of mountain and friction torques in complex notation read (cf. Egger & Hoinka, 2002)

$$\hat{L}^m = a^2 \iint p_s \mathrm{e}^{\mathrm{i}\lambda} \left(\frac{\partial h}{\partial \lambda} \cos\theta - \mathrm{i} \frac{\partial h}{\partial \theta} \sin\theta \right) \mathrm{d}\theta \mathrm{d}\lambda \tag{3.28}$$

$$\hat{L}^f = -a^3 \iint \mathrm{e}^{\mathrm{i}\lambda} (-\tau_\lambda \cos\theta + \mathrm{i}\tau_\theta) \sin\theta \mathrm{d}\theta \mathrm{d}\lambda \ , \tag{3.29}$$

where the sign of each torque term is consistent with the total torque acting on the atmosphere ($\hat{L}^{(s)\to(a)}$). $h = h(\theta, \lambda)$ represents the orthometric height of the topography, and $\{\tau_\lambda, \tau_\theta\}$ are the longitudinal (eastward) and co-latitudinal (southward) components of frictional surface traction *on* the solid Earth[1] (orientated in the direction of the surface wind). In Eq. (3.28), integration by parts leads to an alternative rephrasing of the mountain torque in terms of pressure gradients (de Viron & Dehant, 1999; Schindelegger *et al.*, 2013c).

---

[1] This convention conforms to the orientation of stress variables as available from numerical weather models, cf. also Wahr & Oort (1984)

3.3.2 Axial torque components

Since Earth's flattening has no direct impact on axial torques, only local pressure and friction effects need to be considered in the zonal dynamical coupling between the atmosphere and the underlying solid Earth. The relevance of these axial forcing functions L_z^m and L_z^f for atmospheric circulation and/or excitation of changes in LOD is a well-studied problem on various time scales (e.g. Boer, 1990; Iskenderian & Salstein, 1998; Lott *et al.*, 2008; Wahr & Oort, 1984, etc.). Estimates of L_z^m and L_z^f derive from

$$L_z^m = -a^2 \iint p_s \frac{\partial h}{\partial \lambda} \sin\theta \mathrm{d}\theta \mathrm{d}\lambda \tag{3.30}$$

$$L_z^f = -a^3 \iint \tau_\lambda \sin^2\theta \mathrm{d}\theta \mathrm{d}\lambda \,, \tag{3.31}$$

where positive friction torque anomalies in the sense $(s) \rightarrow (a)$ relate to $\tau_\lambda < 0$ (that is, east–west orientated wind stress vectors acting on the solid Earth) as a result of easterly surface winds. In this constellation, L_z^f tends to increase AAM (Eq. 3.22), whereas the angular momentum of the solid Earth is reduced, see Figure 3.2. Positive mountain torque anomalies—likewise increasing AAM—are typically engendered at north-south-orientated mountain ranges. Higher pressure on the eastern slopes ($\partial h/\partial\lambda < 0$) relative to the western slopes ($\partial h/\partial\lambda > 0$) leads to a negative

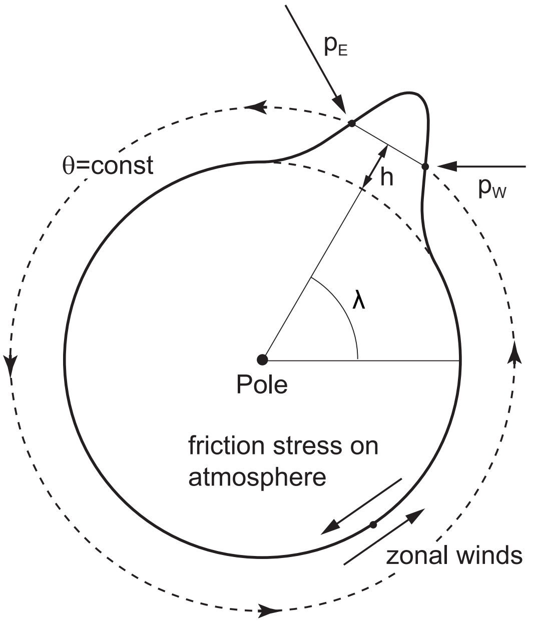

Figure 3.2: Schematic diagram of axial mountain and friction torques after Peixoto & Oort (1992) and Schindelegger *et al.* (2013b). A north-south-orientated topographic feature at co-latitude θ is subject to a zonal pressure gradient force of magnitude $p_E - p_W$. Local surface winds engender frictional stresses on the atmosphere, which in turn counter and reduce the depicted easterlies, i.e. the atmosphere gains angular momentum from the solid Earth.

integrand in Eq. (3.30) and thus a positive net effect in L_z^m (Iskenderian & Salstein, 1998).

3.3.3 The AAM budget equation

The angular momentum budget (or balance) equation of the atmosphere is a straightforward statement of the time rate of change in global AAM being equal to the sum of interaction torques on the atmosphere. Owing to a very simple formulation, the zonal AAM budget has been examined by a host of studies on a wide range of time scales, see e.g. the partially successful efforts of Swinbank (1985), Huang *et al.* (1999), or de Viron & Dehant (2003). Larger quantitative departures from an exact AAM balance have however been documented at the frequency bands of atmospheric tides (de Viron *et al.*, 2001, 2005b), with the exception of results from dedicated simulations (Lott *et al.*, 2008; Madden *et al.*, 1998). Similar conclusions can be drawn for the much less addressed equatorial part of the budget, see de Viron & Dehant (2003) and de Viron *et al.* (2001, 2005b) for a tentative numerical verification at atmospheric tidal bands. Observed disparities between the AAM derivative and the total interaction torque are typically ascribed to deficiencies in the utilized atmospheric models, in particular imperfect analysis data (e.g. vertical wind profiles) or parameterized fields (e.g. surface stress vectors). Lott *et al.* (2008) additionally emphasize on numerical instabilities inflicted by large canceling AAM terms. Nonetheless, a recent study on intraseasonal polar motion variability (Schindelegger *et al.*, 2013c) suggests that the quality of current atmospheric models can mitigate those difficulties (see Chapter 1.2), thus warranting a renewed interest in the budget verification at (sub-)diurnal frequencies.

Equation (3.25) displays the AAM balance in a vector-based form with respect to the celestial reference frame. The practical application on angular momentum time series given in the terrestrial frame (Eq. 3.18–3.21) is thus based upon (de Viron *et al.*, 1999)

$$\frac{\mathrm{d}\boldsymbol{H}^{(a)}}{\mathrm{d}t} + \boldsymbol{\Omega} \times \boldsymbol{H}^{(a)} = \boldsymbol{L}^{(s)\to(a)} , \tag{3.32}$$

where the angular velocity vector of the Earth has been approximated by $\boldsymbol{\omega} \approx \boldsymbol{\Omega} = (0, 0, \Omega)^T$. All terms in Eq. (3.32) are conceived as instantaneous physical quantities (Seiler, 1991), and this notion is of particular relevance for both the AAM derivative (usually determined from numerical differentiation of time series at 3-hourly or longer intervals) and the friction torque as a conventionally time-averaged or accumulated variable within atmospheric model runs. Moreover, an instantaneous budget equation implicates that the damping and/or accentuation of AAM through torques occurs without phase lag. Equatorial and axial components of the AAM balance can be considered in separate equations, i.e.

$$\begin{aligned} \frac{\mathrm{d}\hat{H}^{(a)}}{\mathrm{d}t} + \mathrm{i}\Omega\hat{H}^{(a)} &= \hat{L}^{(s)\to(a)} && (3.33)\\ \frac{\mathrm{d}H_z^{(a)}}{\mathrm{d}t} &= L_z^{(s)\to(a)} , && (3.34) \end{aligned}$$

both of which play a recurring theme throughout this thesis. Their spectral equivalents at terrestrial frequency σ (in rad/s) are of particular computational use

$$\mathrm{i}(\sigma+\Omega)\hat{H}(\sigma)=\hat{L}(\sigma) \tag{3.35}$$

$$\mathrm{i}\sigma\hat{H}_z(\sigma) \qquad =\hat{L}_z(\sigma)\,, \tag{3.36}$$

wherein $\hat{H}(\sigma)=\hat{H}^{(a)}(\sigma)$, $\hat{H}_z(\sigma)=\hat{H}_z^{(a)}(\sigma)$, $\hat{L}(\sigma)=\hat{L}^{(s)\to(a)}(\sigma)$, and $\hat{L}_z(\sigma)=\hat{L}_z^{(s)\to(a)}(\sigma)$ denote the Fourier coefficients of equatorial and axial AAM and torque terms. The underlying frequency domain transform reads, by taking the example of equatorial AAM, $\hat{H}(t)=\sum_\sigma \hat{H}(\sigma)\mathrm{e}^{\mathrm{i}\sigma t}$ (Jenkins & Watts, 1968). Consistent with the standard polar motion/nutation conventions, $\sigma<0$ conforms to retrograde circular motion.

Particular attention must be paid to the nature of the equatorial budget equation (Eq. 3.33). Expanded into its individual constituents in the time domain

$$\frac{\mathrm{d}\left(\hat{H}^p+\hat{H}^w\right)}{\mathrm{d}t}+\mathrm{i}\Omega\left(\hat{H}^p+\hat{H}^w\right)=\hat{L}^f+\hat{L}^m+\hat{L}^e\,, \tag{3.37}$$

the left- and right-hand sides of the equation have a common term, $\hat{L}^e=\mathrm{i}\Omega\hat{H}^p$, which explains up to 90% of the torque variability on seasonal time scales (Schindelegger *et al.*, 2013c) and about 60% at sub-daily periods. Provided that neither local torques nor the wind term introduce grave erroneous signals, Eq. (3.37) will thus innately provide an approximately closed AAM budget at the frequencies of atmospheric tides. If this is the case, a second, even more sensitive validation can be conducted based on the residual budget equation after removal of the ellipsoidal effect

$$\frac{\mathrm{d}\left(\hat{H}^p+\hat{H}^w\right)}{\mathrm{d}t}+\mathrm{i}\Omega\hat{H}^w=\hat{L}^f+\hat{L}^m\,. \tag{3.38}$$

Although the present thesis does not attempt to model nutational motions via the torque approach (cf. Gegout *et al.*, 1998), the above-noted budget relationships shall be also investigated at the retrograde diurnal frequency $\sigma_s=-2\pi/86400$ rad/s, corresponding to a period of one solar day. With $\Omega=2\pi/86164$ rad/s being the absolute value of Earth's angular velocity defined on a sidereal scale, one may write $\sigma_s=-\Omega(1-\epsilon)$, where $\epsilon\approx 1/366$ (see also Marcus *et al.*, 2004, despite a different frequency convention). The frequency domain budget equation for retrograde diurnal AAM variations thus reads

$$\mathrm{i}\epsilon\Omega\hat{H}(\sigma_s)=\hat{L}(\sigma_s)\,, \tag{3.39}$$

implying that the left-hand side of the relationship drops to a magnitude level about 300 times smaller than that at prograde frequencies. As a result, successful verification of the AAM budget at the retrograde diurnal frequency requires $\hat{L}(\sigma_s)$ to effectively vanish, i.e. the individual torque terms must approximately cancel out each other. By combining Eqs. (3.37)–(3.39) in spectral domain, Marcus *et al.* (2004) arrived at the specific prerequisite of an almost exact counterbalance between the retrograde diurnal bulge torque and the sum of local mountain and friction torques. This constraint has been noted as *ill-conditioning* of the AAM budget equation, prescribing the total torque to be only a minute residual of two much larger but opposite components. The inherent numerical instability of such a constellation clearly impairs the further use of torque quantities for examining atmospheric excitation of nutation.

3.3.4 Connection between torques and observed variations of Earth rotation

If the torque method is to be a legitimate alternative to the angular momentum approach, it should impart an akin mathematical framework to relate globally integrated bulge, mountain, and friction effects to observed variations in Earth rotation. Unfortunately, the theoretical advances in this respect have been limited, and the present thesis does not provide a direct remedy, either. Recalling the existing concepts might be instructive nonetheless.

In the first-order approximation, a one-layer Earth is embraced by a single fluid shell (the atmosphere) that affects the rotary motion of the body by means of an external torque $\boldsymbol{L}$. The Liouville equation can be adapted accordingly, but as the dynamical system is separated from the mobile fluid, neither mass redistribution terms nor relative angular momentum need to be accommodated. Surcharges on the inertia tensor of the solid Earth are solely caused by the deformation response to the atmospheric mass load. Applying the standard load Love number formalism on both $\Delta\hat{I}, \Delta I_{zz}$ and their time derivatives, Eqs. (3.4) and (3.5) translate into

$$\hat{m} + \frac{\mathrm{i}}{\sigma_r}\dot{\hat{m}} = \frac{1}{\Omega^2(C-A')}\left\{\mathrm{i}\hat{L}^{(a)\to(s)} + k_2'\Omega^2\left(\Delta\hat{I} - \frac{\mathrm{i}}{\Omega}\Delta\dot{\hat{I}}\right)\right\} \tag{3.40}$$

$$\dot{m}_z = \frac{1}{\Omega C}\left\{L_z^{(a)\to(s)} - k_2'\Omega\Delta I_{zz}\right\}\ , \tag{3.41}$$

see de Viron *et al.* (2005a). Present-day numerical applications (Fujita *et al.*, 2002; Schindelegger *et al.*, 2013a) of these expressions for a single-fluid system with a decoupled core for wobbling motion still follow Wahr (1982)

$$\hat{m} + \frac{\mathrm{i}}{\sigma_{cw}}\dot{\hat{m}} = \frac{1}{\Omega^2(C-A')}\left\{\mathrm{i}1.61\hat{L}^{(a)\to(s)} - 0.49\Omega\hat{H}^p\right\} \tag{3.42}$$

$$-\frac{\mathrm{d}}{\mathrm{d}t}\frac{\mathrm{LOD}}{86400\,\mathrm{s}} = \frac{1}{\Omega C}\left\{L_z^{(a)\to(s)} + 0.31\dot{H}_z^p\right\}\ , \tag{3.43}$$

where the rigid Earth eigenmode σ_r has been replaced by the Chandler frequency σ_{cw} and the loading effect is conveyed by the pressure term of AAM. While the axial solution offers a usable though approximate alternative to its angular momentum counterpart (Eq. 3.15) on all time scales, the validity of Eq. (3.42) is restricted to seasonal periodicities through the assumption of slow geophysical processes ($\mathrm{d}/\mathrm{d}t \ll \Omega$, p. 357 of Wahr, 1982) and, to a lesser extent, through the omission of the FCN rotational mode. Gegout *et al.* (1998) rectified the latter shortcoming, but the presentation of their theoretical body rather impedes a replicate numerical implementation.

More to the point, the oceans provide an equally potent source of geophysically-driven Earth rotation variability at short periods although this influence has been left out of any previous considerations. Within the angular momentum framework a simple superposition of atmospheric and oceanic excitation terms is legitimate, whereas for the torque approach the methodology is less straightforward. From a physical point of view, the determination of the assembly of interaction torques in a coupled three-component system (Earth-atmosphere-ocean) would be the route of choice (de Viron *et al.*, 2001a; Wahr, 1982), but such a complex effort is beyond the scope of this study. Fujita *et al.* (2002)'s suggestion of introducing OAM (oceanic angular momentum) values in Eq. (3.42) represents an alternative at long periods only and also requires a careful apportionment of the forcing terms to the atmospheric and oceanic model components. In order to circumvent those conceptual difficulties, Schindelegger *et al.* (2013c) recently proposed to integrate Earth-atmosphere interaction torques to the corresponding changes in AAM. This efficient workaround is summarized in the following and will eventually be deployed in Chapter 7.

Equatorial torques and polar motion

The spectral version of the equatorial AAM balance in Eq. (3.35) presents a practicable one-to-one correspondence between $\hat{L} = \hat{L}^{(s)\to(a)}$ and the angular momentum of the atmosphere or, more precisely, its deviation from a global mean value. In terms of Fourier coefficients the transfer function at arbitrary frequency σ reads

$$\hat{H}(\sigma) = \frac{-\mathrm{i}}{\sigma + \Omega}\hat{L}(\sigma)\,, \tag{3.44}$$

the retrograde diurnal resonance of which has already been detailed in the previous section. For applications that involve torque series sampled at intervals coarser than 12 h, a proper inverse transform of $\hat{H}(\sigma)$ to the time domain yields a viable $\hat{H}(t)$ estimate (Schindelegger *et al.*, 2013c). Yet, the resonance at $-\Omega$ impairs an analogous procedure if diurnal and sub-diurnal effects are involved, and one might either limit subsequent considerations to the frequency domain or remove spectral content in the vicinity of $-\Omega$ before converting the filtered coefficient series to its time domain equivalent. Moreover, as $\hat{H}^p = -\mathrm{i}/\Omega\hat{L}^e$, the method can be reduced to a solitary discussion of the wind term driving from mountain, friction, and ellipsoidal torques, which is reminiscent of early studies on the general circulation of the atmosphere (e.g. Starr, 1948). By expanding Eq. (3.44) into its components and by rewriting the pressure term as bulge torque, the spectral representation of the wind term becomes

$$\hat{H}^w(\sigma) = \frac{-\mathrm{i}}{\sigma + \Omega}\hat{L}^f(\sigma) + \frac{-\mathrm{i}}{\sigma + \Omega}\hat{L}^m(\sigma) + \frac{\mathrm{i}\sigma}{\sigma\Omega + \Omega^2}\hat{L}^e(\sigma)\,. \tag{3.45}$$

The prefactors on the right-hand side may be perceived as frequency-dependent weights regulating the influence of each torque term on $\hat{H}^w$, as plotted in Figure 3.3. Irrespective of their actual magnitude, local torques (mountain + friction) appear to be the single most significant source of the equatorial AAM wind term on time scales of a few days or longer, (cf. also Eq. 5.11 of Wahr, 1982), whereas at higher frequencies their contribution is increasingly attenuated.

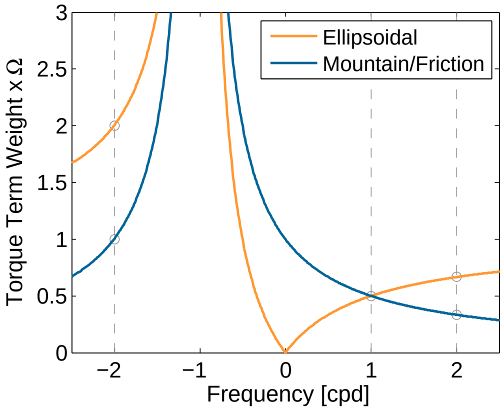

Figure 3.3: Absolute weights of the ellipsoidal and mountain/friction torque contributions to the equatorial wind term.

At semi-diurnal periods in particular, the ellipsoidal torque's weight exceeds that of mountain and friction effects by a factor of two, and if σ approaches even larger values, Eq. (3.45) yields $\hat{H}^w(\sigma) \approx -\hat{H}^p(\sigma)$. This counterbalance relation conforms with Eubanks (1993)'s statement on the diminished power of high-frequency geophysical excitation processes and will reappear to a certain extent in Chapter 5.

Coming back to Earth rotation, the genuine advantage of translating torque quantities to the evoked variations of angular momentum consists in the possibility of capitalizing on the advanced broad band formalism of Section 3.2.3. OAM values can be incorporated (added) in the usual way, and if the original AAM values (that of the wind term, to be exact) are deficient, an immediate crosscheck via atmospheric torques is possible. Admittedly, this hybrid version of a torque approach blurs some of the potential of the original torque method for physical interpretation of induced polar motion variations. It is also restricted to pure post-processing applications, see Schindelegger *et al.* (2013c).

Axial torques and changes in LOD

Equation (3.43) represents a valid expression of how axial mountain and friction torques can be connected to the time derivative of changes in LOD. In order to once more bypass the subtleties of a consistent treatment of OAM values and atmospheric torques, a slightly different path is taken in this study. Much the same as for the equatorial case, the basic idea is to integrate the AAM budget equation to deviatoric, torque-induced AAM values (Wolf & Smith, 1987). Accepting some minor numerical approximations, Eq. (3.15) may be rewritten as

$$\frac{\mathrm{LOD}}{86400\,\mathrm{s}} = \chi_z = \frac{\left(H_z^p + H_z^w\right) - 0.243 H_z^p}{\Omega C_m} = \frac{1}{\Omega C_m}\left\{\int L_z^{(s)\to(a)}\mathrm{d}t - 0.243 H_z^p\right\}\,, \tag{3.46}$$

with the pressure loading effect on a mantle-only solid Earth being conveyed by $-0.243H_z^p \approx \alpha_3 k_2' H_z^p$, cf. the respective values in Appendix A.5. A spectral equivalent of Eq. (3.46) reads

$$\frac{\hat{\mathrm{LOD}}(\sigma)}{86400\,\mathrm{s}} = -\frac{1}{\Omega C_m} \left\{ \frac{\mathrm{i}}{\sigma} \hat{L}_z^f(\sigma) + \frac{\mathrm{i}}{\sigma} \hat{L}_z^m(\sigma) + 0.243 \hat{H}_z^p(\sigma) \right\} . \tag{3.47}$$

Apparently, only the sum of pressure and wind terms may be apportioned to the action of mountain and friction torques. It should be noted, though, that by introducing an additional *Coriolis conversion* term, the exchanges between both AAM portions as well as the impact of mountain and friction torques on H_z^w can be examined in more detail (e.g. Lott *et al.*, 2008).

3.3.5 Pros and cons of the angular momentum and torque approaches

The assets and drawbacks of the presented modeling approaches have already partially surfaced. They are briefly compiled at this place, while for a more detailed discussion the reader is referred to de Viron *et al.* (2005a) or Seitz & Schuh (2010).

Angular momentum approach, pros:

- AAM values can be computed directly from surface pressure and three-dimensional wind data, which are standard output fields of atmospheric analysis systems and determined in large parts by direct observations.
- The method involves largely robust quantities from an ‘average-like’ computation procedure (de Viron *et al.*, 2005a).
- Sophisticated schemes for angular momentum considerations exist both at short and long periods, and the superposition of oceanic excitation is a straightforward measure.

Angular momentum approach, cons:

- Changes of solid Earth angular momentum can only be ‘diagnosed’, without involving knowledge on the specific processes causing those rotational perturbation.
- The integration of wind velocities at vertical increments might be a laborious task.

Torque approach, pros:

- A clear understanding of the physical interaction between the Earth’s subsystems, in particular the spatial location and origin of angular momentum exchanges, is conveyed.
- The evaluation of mere surface integrals requires fewer computational resources.

Torque approach, cons:

- An accurate computation of all torque quantities imposes strong quality requirements on the underlying model, e.g. a high spatial resolution as well as a precise knowledge of local interaction forces—such as pressure variations across large altitude features—surface properties, and variables that are not directly observed. These prerequisites represent severe obstacles to the torque approach for the oceans, too.
- Formalisms relating torque terms to geodetic observations are generally less advanced and comprise approximations that are insufficient at intraseasonal or shorter periodicities (cf. Section 3.3.4 and Wahr, 1982).
- The method is virtually inappropriate for modeling atmospheric excitation of nutation.

Chapter 4

A short excursion to meteorology: tides in the atmosphere

The physical phenomena providing impetus to the effects considered in this thesis are atmospheric tides, which refer to global-scale oscillations in the atmosphere at periods that divide evenly into a solar or lunar day (Lindzen, 1979). The primary and by far the largest tides are found at diurnal and semi-diurnal frequencies, corresponding to one and two cycles per solar day. While most of the early interest in these phenomena has been attached to the small but regular variations of air pressure at the Earth's surface, the modern understanding of atmospheric tides encompasses temperature, wind, pressure, and even geomagnetic oscillations from the troposphere up to the thermosphere and ionosphere, see e.g. Pancheva *et al.* (2012). In the first place, this chapter strives to give a general overview of the physics and characteristics of solar tides in the atmosphere. The second part portrays the ensemble of models and datasets from which atmospheric angular momentum and torques at tidal frequencies are deduced.

4.1 Review of solar tides

The full scope of tides in the atmosphere is caused by the rotation of the Earth within (1) gravitational tidal fields, in particular that of the Moon, and (2) the radiational field of the Sun (Chapman & Lindzen, 1970). As early as Newton (1687), gravitational forces have been recognized as paramount causes for the case of ocean tides, primarily produced by the attraction of water masses through the Moon. Although the Sun exerts an important secondary effect, at most locations ocean tides peak at the overhead transit of the Moon and thus occur at the harmonics of a lunar day, $\sim$24.8 h. Analogous to the oceans, atmospheric masses are free to move in response to the gravitational attraction of the Moon (Whiteman & Bian, 1996), implying that lunar tides can be recognized in the atmosphere as well. Newton (1687) correctly anticipated the smallness of such gravitational effects in the atmosphere, of which the observational evidence was provided at the end of the 19$^{\text{th}}$ century. Lunar tidal amplitudes in surface pressure range between 0.5 and 8 Pa with a clear dependency on latitude (Haurwitz & Cowley, 1970). However, a much more effective source for exciting atmospheric tides is offered by periodic solar radiation, its absorption at different levels in the atmosphere and the associated heating. Additional contributions to the various tidal components originate from latent and sensible heat release near the ground. The obvious departures from a strictly sinusoidal heating pattern at 1 cpd and near-surface effects related to topography, ocean-continent distribution, cloudiness, or ice coverage (Brzeziński *et al.*, 2002) are commonly considered as the catalysts for the rich harmonic spectrum of atmospheric tides in addition to the principal diurnal component.

A possible mathematical expression for any tidal oscillation S of an arbitrary atmospheric parameter at the n-th harmonic frequency of the solar day has been given by Haurwitz & Cowley (1973) in the form of

$$S_n = \sum_s \left[a_n^s \cos(nt + s\lambda) + b_n^s \sin(nt + s\lambda) \right] , \tag{4.1}$$

where n is usually either 1 (diurnal tide, S_1) or 2 (semi-diurnal tide, S_2), a_n^s and b_n^s represent the harmonic coefficients of the expansion, and t designates Greenwich mean time (GMT) expressed as radians (i.e. $t = 2\pi t_h/24$, with t_h being GMT in hours). The pivotal parameter distinguishing different tidal modes in Eq. (4.1) is the *wave number* s, of which the magnitude indicates the number of wave crests on each latitude circle and the sign reveals the zonal direction of propagation (Hagan *et al.*, 2003). In the present notation, $s > 0$ signifies waves traveling westward, and $s < 0$ corresponds to eastward propagation. The components for which s is equal to the frequency n of the oscillation represent waves that travel westward at the speed of the mean Sun. Such waves are known as *migrating solar tides* and have the same local time variation at all longitudes (Hagan *et al.*, 2003), as can be seen from Eq. (4.1) when using $s = n$ and introducing the mean local time t_l via $t = t_l - \lambda$. For the case of surface pressure, both diurnal and semi-diurnal tides are largely affected by their respective migrating components, $s = n = 1$ and $s = n = 2$. Waves with $s \neq n$ are called *non-migrating tides* and depend on local time as well as on longitude. This subset of atmospheric tides comprises waves that move eastward, travel westward faster or slower than the Sun, or are standing waves.

Given that tidal variations are excited at numerous altitudes in the lower atmosphere, the concept of vertical wave propagation needs to be considered in the evaluation of atmospheric tides at specific layers. Downward-propagating tidal components influence surface fields, whereas upward propagation is essential for the dynamics of the mesosphere and lower thermosphere (Pancheva *et al.*, 2012). Characteristically, tidal waves tend to grow in amplitude with decreasing density owing to energy conservation. This accounts for the fact that atmospheric tides, which constitute only a small fraction of the meteorologically interesting variations at the Earth's surface, are dominant features in upper atmospheric wind and temperature fields, in particular at altitudes between 80 and 100 km (Chapman & Lindzen, 1970).

4.1.1 Migrating and non-migrating radiational tides

The absorption of insolation by the atmosphere has been identified as primary source of migrating solar tides by studies published in the 1960s (Butler & Small, 1963; Siebert, 1961). The resultant heating is periodic with respect to the rotating reference frame and produces migrating tidal oscillations throughout the Earth's atmosphere. Atomic and molecular oxygen (O and O_2) absorb the shortest wavelengths of incoming solar radiation at about 100–150 km above ground level. Peak heating associated with absorption of solar ultraviolet radiation by ozone (O_3) occurs in middle atmospheric altitudes between 30 and 70 km, and thus, mostly in the stratosphere. Water vapor (H_2O) in the troposphere provides another significant portion of thermal excitation by absorbing solar infrared radiation (Hagan *et al.*, 2003).

Those heating cycles are not evenly distributed among the migrating diurnal and semi-diurnal tides. More than 60% of the semi-diurnal forcing is caused by ozone absorption in the stratosphere and is capable of propagating to the ground effectively, at wavelengths greater than 300 km (Covey *et al.*, 2011). On the contrary, migrating diurnal tides have vertical wavelengths smaller than 30 km and mainly originate in the troposphere. Stratospheric diurnal excitation caused by ozone heating is still significant, but, to a large measure, cannot propagate down to the surface due to *energy trapping*, see Chapman & Lindzen (1970). These findings resolve the apparent paradox of the semi-diurnal cycle dominating day-to-night variations of surface pressure p_s despite the obvious diurnal periodicity of solar radiation (Covey *et al.*, 2011). Figure 4.1 illustrates this discrepancy based on amplitude plots of the (a) diurnal and (b) semi-diurnal surface pressure oscillations, denoted as $S_1(p_s)$ and $S_2(p_s)$. Both sinusoids were calculated from 1 yr of gridded ECMWF data by fitting

$$S_n(p_s) = A_n \cos(nt - \varphi_n) = a_n \cos(nt) + b_n \sin(nt) \ , \ n = 1,2 \tag{4.2}$$

at each geographic location. Here, t denotes GMT in radians, A_n is the amplitude, and φ_n a *Greenwich phase lag* that derives from the inverse tangent of b_n/a_n, i.e. the harmonic coefficients in Eq. (4.1). Both migrating and non-migrating tides are retained in this representation. Figure 4.1 depicts maximum amplitudes at low latitudes where insolation and its subsequent absorption are greatest. The prominent longitudinal uniformity of $S_2(p_s)$ is related to its migrating component, which, if considered separately, produces contours that are parallel to lines of constant latitude (Hagan *et al.*, 2003). In contrast, $S_1(p_s)$ is weak over the oceans but matches the amplitudes of $S_2(p_s)$ over land areas ($\sim$180 Pa), reflecting the influence of non-migrating tides. This kind of tidal signals are of regional or local origin, generated i.a. by the sensible heat flux from the ground (Dai & Wang, 1999), differential heating of adjacent land and water surfaces (perceptible as land and sea breezes, Dai & Deser, 1999) or other surface interactions. The phase lag plots in Figure 4.1 confirm the noted amplitude characteristics. Zero phase values mark the location of high pressures at GMT = 0 when the Sun is over the 180° meridian. Hence, peak pressures in $S_2(p_s)$ lead the Sun by roughly 60° or 2 h (Ray, 2001), which can be seen from the phase difference at

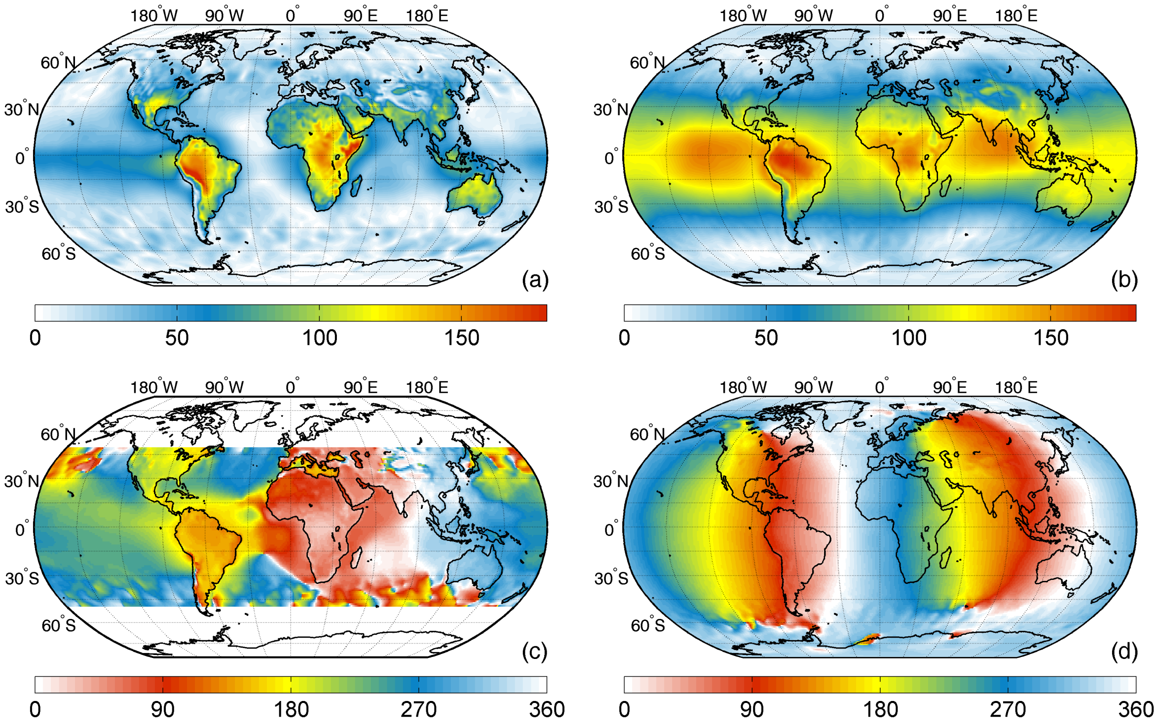

Figure 4.1: Diurnal (a) and semi-diurnal (b) surface pressure amplitudes [Pa], and the corresponding diurnal (c) and semi-diurnal (d) Greenwich phase lags [deg] as deduced from 3-hourly ECMWF pressure fields for the year 2011.

the 180° meridian and the zero phase contour in the western Pacific. The clear-cut, monotonic westward increase in phase values relates to the dominance of the semi-diurnal migrating tide up to the polar circles. At the diurnal frequency, as a result of the strong non-migrating tides, the phase behavior is largely ragged, in particular at latitudes above 50° which are not depicted. Over the tropical oceans, the diurnal migrating component is more pronounced, leading the Sun by about 110° or 7 h (Ray & Ponte, 2003).

A complementary analysis for 1 yr of ECMWF eastward surface stress fields τ_λ at 1 and 2 cpd is presented in Figure 4.2. Those variations are closely related to daily wind oscillations, of which the diurnal cycle is substantially larger than the semi-diurnal one, in particular over land and high terrain (Dai & Deser, 1999). Accordingly, the associated stresses peak over the western Unites States, the Andes, and the Tibetan Plateau, where the resistance of the surface to atmospheric flow leads to high drag coefficients (Garratt, 1977). Amplitudes in $S_1(\tau_\lambda)$ are twice as large as those of $S_2(\tau_\lambda)$. The phase values of both harmonics are characterized by data noise at high latitudes and strong non-migrating components (see e.g. the west coast of the United States), although a generally resemblance to the phase behavior of the diurnal and semi-diurnal surface pressure tides is seen. Specifically, $S_2(\tau_\lambda)$ displays a clear westward propagation, with positive maxima (0° phase) located over those meridians where the semi-diurnal pressure tide exhibits negative maxima (180° phase) at GMT $= 0$, cf. Figures 4.1d and 4.2d. This out-of-phase relation

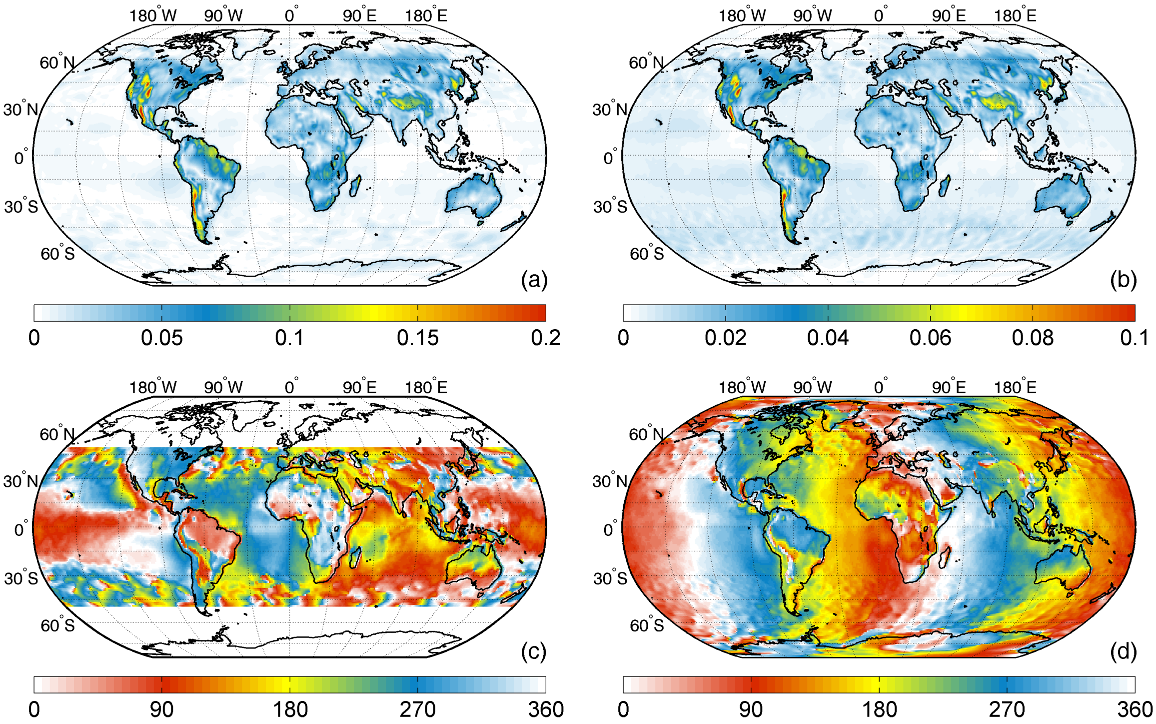

Figure 4.2: Diurnal (a) and semi-diurnal (b) eastward surface stress amplitudes $\left[\mathrm{Nm}^{-2}\right]$, and the corresponding diurnal (c) and semi-diurnal (d) Greenwich phase lags [deg] as deduced from 3-hourly ECMWF surface fields for the year 2011.

between the semi-diurnal tides of pressure and zonal wind (or eastward stress, equivalently) is an important observation with implications for Earth rotation studies deploying the angular momentum approach, see Section 5.1. Such an overall phase difference between pressure and wind (or stress) variables is more difficult to establish for the diurnal tide, even though an approximate 180° discrepancy can be noted in the tropical Atlantic Ocean.

4.1.2 Tidal theory

This section shall complete the general portrayal of atmospheric tides by a brief look at the main pillars of tidal theory, which attempts to explain measured tidal oscillations in the atmosphere and offer predictions that go beyond existing observations (Lindzen, 1990). Although such a portrayal is not of immediate importance for the present thesis, study of the theoretical framework sharpens the understanding of the physics behind tidal phenomena in the atmosphere.

In the classical theory of atmospheric tides of Chapman & Lindzen (1970), the Earth is assumed to be a smooth, topography-less sphere, enclosed by the atmosphere as a shallow, compressible, hydrostatic and perfect gas. As the considered oscillations travel at phase speeds in the vicinity of Ω, the background flow at much smaller velocities is treated as a basic state on which the equations of motion can be linearized. Specifically, the evoked equations are that of horizontal and vertical momentum (Forbes & Garrett, 1979), hydrostatic equilibrium, continuity and thermodynamic energy, incorporating the effect of external heating. The momentum equations are phrased without friction terms but consider Coriolis and pressure gradient forces as well as gravitational forces associated with the Earth's potential and the external lunisolar potential, see Randall (2007). Linearization yields a single equation, which can be separated into two parts, the first portion depending only on latitude and called *Laplace's tidal equation*, the second portion depending only on altitude and called *vertical structure equation*. Laplace's tidal equation is an eigenvector-eigenvalue problem, defining the free surface oscillations of a fluid envelope on an arbitrarily chosen sphere (Chapman & Lindzen, 1970). Its solution consists in a combination of *Hough functions* (representing the eigenvectors) and the associated eigenvalues, which are called *equivalent depths*. Capable of representing very general classes of oscillations, Hough functions play a major role in meteorology and geophysics (Lindzen, 1990). For a given frequency n and wave number s, the set of Hough functions and equivalent depths can be determined and used in order to expand the radiational and/or gravitational forcing. Introduced into the vertical structure equation, this strategy allows solving for the perturbations of all meteorological parameters (temperature, wind, etc.) associated with each Hough function. The totality of these perturbations constitute a *Hough* or *tidal mode*, see Lindzen (1979). In particular, the equivalent depths determine the vertical structure of each mode and indicate whether vertical wave propagation is possible or the energy is trapped in the region of excitation. To apply this procedure and quantitatively assess e.g. the discrepancy between diurnal and semi-diurnal surface pressure, the radiational forcing must be specified in a realistic manner. Such theoretical profiles of the heating caused by water vapor and ozone absorption can be found in Forbes & Garrett (1978).

Classical tidal theory appears to explain the major characteristics of diurnal and semi-diurnal oscillations throughout the atmosphere. Yet, the significant contributions of additional physical processes have been investigated. Among them are the interaction with background winds, the effects of molecular viscosity and thermal conductivity on tidal dissipation, or electrodynamic forces (Forbes & Garrett, 1979). At lower altitudes, the influence of oscillations in condensation (and thus latent heat release) must be considered in order to account for the phase of the S_2 surface pressure as well as the 180° phase shift in horizontal winds at about 28 km above ground (Lindzen, 1979). Furthermore, tidal theory has been modified for differential heating between land and sea (Giwa & Hussain, 1978) and the effects of surface elevation have been assessed. With regard to the signals of relevance for Earth rotation, the semi-theoretical investigations of Lott *et al.* (2008) are of particular interest. Closely related to Laplace's tidal equations, this study formulates the equations of a spherical shallow water model including zonal mean dynamical forcing, i.e. a body force that can mimic the action of mountain and friction torques. Large portions of the standing ($s = 0$) diurnal and semi-diurnal surface pressure tides are found to be produced during the geostrophic adjustment (Blumen, 1972) of the model to mid-latitude mountain forcing.

4.2 Representation of radiational tides in atmospheric models and data-assimilation systems

Parallel to the advances in the analytical description of atmospheric tides, science has also taken great interest in accounting for tidal fluctuations in global numeric models of the atmosphere. Early efforts (Hunt & Manabe, 1968) have been restricted to general circulation models (GCM), which are explicit mathematical simulations of the various processes occurring in Earth's fluids (Peixoto & Oort, 1992). Yet, atmospheric GCMs are frequently incorporated in the analysis and forecast systems of the world's leading numerical weather prediction centers, which are strongly constrained by meteorological observations. Major developments of these analysis and forecast systems since the mid-1980s in terms of model physics, temporal and spatial resolution, computer capacities, assimilation techniques, etc. have allowed for a detailed documentation of tidal fluctuations in the global troposphere and stratosphere (e.g. Hsu & Hoskins, 1989).

However, models and methods within forecast systems are subject to frequent modifications, introducing jumps, gaps, or systematic errors in the issued data, which in turn impair reliable long-term analyses of retrieved products such as excitation signals due to atmospheric tides. For that reason, weather centers like ECMWF, NCEP (*National Centers for Environmental Prediction*) or JMA (*Japan Meteorological Agency*) have conceived so-called *reanalyses* based on a single, pre-defined model and an unchanged analysis method, usually spanning the historical data record (Rienecker *et al.*, 2011). Within this configuration, reanalyses estimate global fields of the main atmospheric parameters and account for consistency between the laws of physics and the observations given their range of uncertainty (Dee *et al.*, 2011). The core components of any reanalysis are thus a realistic forecast model and a data assimilation procedure, the combination of which propagates information forward both in time and space. Two reanalysis systems, one from the ECMWF and one from NASA's GMAO, are deployed in this study and portrayed in the following.

4.2.1 ECMWF Reanalysis Interim

ERA-Interim represents the latest global atmospheric reanalysis of the ECMWF, designed to prepare for an even more comprehensive reanalysis effort in the future and to elaborate on specific difficulties of its predecessor ERA-40 (Uppala *et al.*, 2005). The strengths and improvements of ERA-Interim are well-documented (see Dee *et al.*, 2011, and references therein), so that a brief reprise of its main interacting components can be given.

Data assimilation

The assimilation scheme incorporates all suitable observations to estimate the state of the atmosphere on a global scale. 12-hourly variational analyses are performed sequentially, combining the prior information from the previous analysis cycle with valid observations as well as with the error covariances of both background estimates and observations. The deduced analyses of

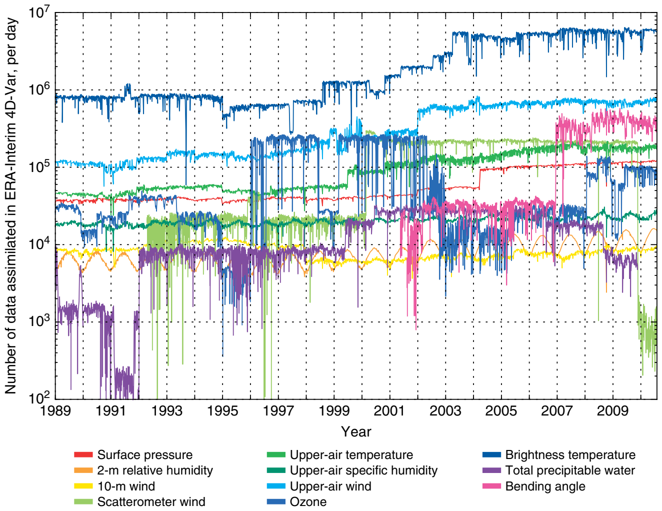

Figure 4.3: Daily average and types of observations assimilated into ERA-Interim from 1989 to 2009. Figure extracted from Dee *et al.* (2011).

near-surface fields and upper-air atmospheric parameters then enter the forecast system to obtain the prior state required for the next 12-hourly cycle (Dee *et al.*, 2011).

Forecast model

The physical coherence and dynamical evolution of the described procedure is guaranteed by the forecast model, which in ERA-Interim is represented by release Cy31r2 of the IFS (*Integrated Forecast System*). The IFS consists of three fully coupled models for the atmospheric circulation, the land surface and ocean waves (Persson, 2011). Specifically, the atmospheric component is realized in spectral space by a spherical harmonic expansion of degree 255 (approximately 79 km grid spacing), 60 vertical layers up to 0.1 hPa and a 30 min time-stepping scheme. In this configuration, the model equations are discretized and solved numerically, considering clouds, convection, moisture, orographic effects on the atmospheric flow, as well as absorption and scattering of solar radiation. (Note that this ensemble of equations basically covers all effects considered in the classical analytical approach of atmospheric tides.) During the assimilation procedure, the forecast model generates updated global fields of temperature, wind, humidity, and pressure, but also physical parameters (such as precipitation, moisture, or turbulent fluxes) which cannot be observed directly (Dee *et al.*, 2011).

Within the IFS, a land surface model is adopted to describe the heat, water, and momentum exchange based on the area and vegetation properties of differential tiles, while the ocean general circulation model describes the influence of ocean waves and sea surface temperature on the airflow aloft (or vice versa). This ocean-atmosphere forcing implies energy and momentum transfer and is discretized at weekly intervals.

Observations

The real-time constraint on atmospheric models is imposed by the ensemble of assimilated data, which can be roughly categorized into *conventional*, in-situ observations and *non-conventional*, remotely-sensed parameters originating from satellites (Persson, 2011). Non-conventional observations compose the vast majority of daily data counts, which approach an average number of 10^7 per day in the last decade of ERA-Interim, see Figure 4.3. Satellite-borne observations mainly include measurements of clear-sky radiances (quantified as *brightness temperature*, that is the temperature of a hypothetical black body emitting the observed amount of radiation at the same wavelength) from a diversity of polar-orbiting and geostationary satellites. Vertical wind profiles over the oceans can be retrieved from the backscatter of radar sensors of low Earth orbit satellites, which are called *scatterometers*. Geostationary satellite imagery of clouds allows for an estimation of upper atmospheric motion vectors. A great variety of ozone and water vapor retrievals has been considered for ERA-Interim as well. The particularly high volume of assimilated refractivity data or *bending angle* profiles originate from GPS radio occultation measurements (Kursinski *et al.*, 1997) taken with the six-satellite constellation COSMIC (*Constellation Observing System for Meteorology, Ionsosphere, and Climate*) since 2007. The derived temperature profiles at high spatial and vertical resolution are perceived as beneficial for the study of atmospheric tides at altitudes lower than 30–40 km (Pirscher *et al.*, 2010), i.e. the high-mass atmospheric regions accounting for excitation signals in Earth rotation.

Conventional observations are likewise essential constraints to the reanalysis system, despite their comparatively small number. This includes globally well-distributed surface reports of pressure, temperature, relative humidity, and winds just above ground level, available from ships, buoys, and land stations. Additional temperature, wind, and humidity profiles are obtained from radiosondes, dropsondes, aircrafts, and vertically pointing radar wind systems. Both conventional and non-conventional observations undergo a thorough quality control before and during the actual assimilation, see Dee *et al.* (2011).

4.2.2 GEOS-5 Modern Era-Retrospective Analysis for Research and Applications

MERRA has been conducted by NASA's GMAO to create a climate context for long-term observations from NASA's satellite missions and to advance the representation of the hydrological cycle with respect to earlier reanalyses (Rienecker *et al.*, 2011). The latter objective certainly has implications on the field of Earth rotation, as precipitation and water vapor signals connect to latent heat release that in turn generates non-migrating atmospheric tides.

Like ERA-Interim, MERRA builds on the interaction of an atmospheric general circulation model with a sophisticated data assimilation system. Both components in MERRA are taken from version 5.2.0 of the *Goddard Earth Observing System Model* (GEOS-5 for short), which uses a horizontal resolution of 1/2° in latitude and 2/3° in longitude with 72 vertical levels up to 0.01 hPa. The atmospheric model, bounded by a land surface and ocean wave representation, is based on finite volume dynamics that describe moist and radiative processes as well as the effects of turbulent mixing (e.g. gravity wave drag) and surface processes (e.g. the exchange of linear momentum via stresses). All state variables of the model are propagated in time under the constraint of meteorological observations by the assimilation system. The required variational analysis is performed at 6-hourly intervals and provides the correction to the background information by the aid of recursive filters in grid space (Rienecker *et al.*, 2008). Data streams and procedures for quality control and data thinning are basically comparable to ERA-Interim, with about $2 \cdot 10^6$ observations assimilated per 6-hourly analysis cycle, see Rienecker *et al.* (2011). However, no radio occultation measurements were considered for MERRA prior to 2011. Further differences between the two reanalyses definitely exist in the numerical evaluation of the model's physics, the assimilation scheme, and the realization of the variational analysis. Substantial discrepancies are anticipated for weakly constrained parameters such as surface fluxes and precipitation.

Conservation of angular momentum, which is addressed in this study in the context of Earth rotation, has not been implemented in MERRA, whereas a full accounting for various mass and energy budgets is produced (Lucchesi, 2012). On the contrary, the data assimilation of ERA-Interim is not designed to conserve any of the mass, energy, and angular momentum quantities. These global properties are instead perceived as useful diagnostics of the reanalysis' quality.

4.2.3 ECMWF operational model (delayed cut-off)

Weather prediction on a daily basis relies on the operational, near real-time output of atmospheric models. The basic configuration of such operational systems is equivalent to that described in the previous sections, but in face of the increasing quality demands of weather forecast applications, continuous developments and updates are being implemented to all components of both the assimilation and analysis technique as well as the model itself. During 2007–2011 (i.e. the time span considered for this study) 13 updates of the ECMWF's IFS can be noted, e.g. a change in horizontal resolution from T799 (25 km grid spacing) to T1279 (16 km grid spacing) in January 2010. Furthermore, the ECMWF offers two different versions of its operational model dependent on the delivery time of the issued products. Rapid delivery is achieved within the standard atmospheric model by an early cut-off of incoming observations in the analysis procedure. If timeliness of the model output is regarded as secondary to the quality of the analysis fields, data from the *delayed cut-off* (DC) scheme can be used (Persson, 2011). The essential feature of the DC suite consists in waiting about 5 h after each 12-hourly variational analysis cycle in order to ensure all observations allocated to the cycle have arrived. From this complete set of observations, the variational analysis produces a forecast that yields both the initial conditions and background information for the next 12-hourly cycle. The distinction between the two delivery suites has been implemented in the ECMWF's operational data assimilation system commencing June 29, 2004.

4.2.4 Meteorological forecast and analysis fields for Earth rotation studies

Registered users can download global or regional meteorological data from the presented models as gridded output of both the intrinsic analysis and forecast runs. In order to meet the requirements of specific applications, a variety of horizontal and vertical discretization options exist, while the offered temporal intervals are usually 3-hourly, 6-hourly, daily or monthly. Given the strong observational constraints and control procedures, analysis products are considered to be of high quality and accuracy. However, their availability at only four synoptic times (0, 6, 12, 18 UTC) is inadequate for investigating tidal phenomena at frequencies $\sigma \geq 2$ cpd. Sampling rates of 3 h are usually achieved for auxiliary fields within the variational analysis cycles, e.g. forecasts for ERA-Interim and the ECMWF operational DC model or so-called *assimilated states* in the case of MERRA. The difference between forecasts and assimilated states is subtle but may have implications for the diagnosis of diurnal and sub-diurnal signals. Forecasts use a free-running model initialized from an analyzed state at the end of a 12-hourly cycle and typically extend over 10 d in the future. When the next analysis cycle finishes, a new, more accurate 10-day forecast is available to supersede the previous one. Extracting the first 12 h of each of those forecasts yields an equidistant dataset that is characterized by small discontinuities at the transition epochs. Such effects can impede the representation of atmospheric tides in the downloaded data and have been addressed by Schindelegger *et al.* (2011). (Refer also to Dobslaw, 2007, for a validation of the short-term forecasts against analysis fields at the synoptic times.) On the contrary, GMAO does not provide pure forecasts from MERRA but instead issues assimilated states, which originate from the combination of analysis fields and forecasts. A predictor-corrector scheme called *incremental analysis update* (IAU, Bloom *et al.*, 1996) gradually distributes the difference between the background estimate and the analyzed state over all epochs of the current assimilation window. This technique guarantees smooth transition between all 6-hourly cycles and minimizes spurious periodic perturbations (Rienecker *et al.*, 2008).

Table 4.1: Grid specifications of the utilized data streams during 01/2007–12/2011.

Data stream	Level type	levels	Δt [h]	1^{st} epoch [UTC]	horiz. grid
ERA-Interim forecasts	pressure	25	3	3:00	$2.0° \times 2.0°$
	surface	-	3	3:00	$0.5° \times 0.5°$
ECMWF DC forecasts	pressure	21	3	9:00	$1.0° \times 1.0°$
	surface	-	3	9:00	$0.5° \times 0.5°$
MERRA assimilation	pressure	25	3	0:00	$1.25° \times 1.25°$
	surface	-	1	0:30	$0.5° \times 0.\dot{6}°$

Grid specifications and temporal resolutions of the actually used data streams are summarized in Table 4.1. Additional information for each product shall be noted:

- **ERA-Interim**: both pressure level data and surface fields at 3-hourly intervals are available under the path *ERA-Interim>Atmospheric Model(1)>Forecast*; from successive 10-day forecasts, initialized either at 0 or 12 UTC, the first four time steps (3, 6, 9, and 12 h) were extracted.
- **ECMWF DC**: the full path of this stream reads *Operational>Atmospheric Model (delayed cut-off)>Atmospheric Model(1)>Forecast*; initialization epochs are located at 6 and 18 UTC,

and data from the forecast intervals 3, 6, 9, and 12 h were extracted.

- **MERRA**: the data holdings[1] of MERRA offer 3-hourly pressure level grids and hourly surface flux data under the product names *3D assimilated state on pressure* and *IAU 2D surface-turbulent flux diagnostics*, respectively.

In order to calculate angular momentum and torque quantities in a consistent way, the output of each model has to comprise all necessary parameters, given either on all vertical layers (geopotential Φ, specific humidity s, absolute temperature T, eastward and northward wind speeds) or as surface fields (pressure, eastward and northward wind stresses). See Table 4.2 for the availability of those parameters within each data stream. Stress variables are instantaneous fields in both ECMWF models, but are time-averaged over 1 h in the MERRA flux data. Moreover, the geopotential parameter, determining the altitude grid of each pressure level at 1–1000 hPa, can be downloaded as real potential value (ECMWF) or its derivate, the geopotential height $\overline{g}\Phi$, after multiplication with a constant gravity acceleration $\overline{g}$ (MERRA). Both reanalyses have their well-defined, static surface potential field (orography), of which the deduced topography is instrumental in the computation of AAM wind terms and mountain torques. Starting from January 2007, the orography retrieved for ECMWF's operational DC model was kept constant until June 21, 2010. The influence of the subsequent orography change on AAM and torque quantities was briefly investigated and was found to be negligible.

Table 4.2: Availability of parameters within the utilized data streams.

Data stream	Level type	Φ $[\frac{\mathrm{m}^2}{\mathrm{s}^2}]$	s [ ]	T [K]	u, v $[\frac{\mathrm{m}}{\mathrm{s}}]$	p_s [Pa]	$\tau_\lambda, -\tau_\theta$ $[\frac{N}{\mathrm{m}^2}]$
ERA-Interim	pressure	×	×	×	×		
	surface					×	×
ECMWF DC	pressure	×	×	×	×		
	surface					×	×
MERRA	pressure	×	×	×	×	×	
	surface						×

Processing strategies

A documentation on how to optimally deal with the coordinate systems of atmospheric models when using meteorological data for computations in a geodetic reference frame is currently being developed (Hobiger *et al.*, 2012). Here, partly due to the treatment of globally integrated quantities instead of more sensitive local applications (e.g. ray-tracing or loading), an approximate method for preparing the data was adopted. The first of essentially three main issues consisted in the determination of orthometric heights from geopotential values Φ at the point locations of all surface and vertical grids. This step was accomplished by scaling Φ with a gravity acceleration

---

[1] `http://disc.sci.gsfc.nasa.gov/mdisc/data-holdings`

estimate at half height to the geoid (Nafisi *et al.*, 2012). Second, the model data at each location are point measurements (Persson, 2011) and need to be averaged to cell midpoint values in order to conform the method of numerical integration (used in evaluating the analytical expressions of all excitation terms). Both surface and pressure level data were rearranged according to this principle. Non-negligible mass and particle motion between the topography and the nearest pressure level aloft were accounted for in the final processing step by interpolation or extrapolation of the parameters $\{p, g, u, v\}$ at height h to resampled versions of the surface topography field (2.0° × 2.0° for ERA-Interim, 1.0° × 1.0° for ECMWF DC, 1.25° × 1.25° for MERRA). Exponential height dependence was assumed for the pressure, whereas the remaining parameters were interpolated by a linear scheme.

Evaluation of torque and AAM formulae

Discretized versions of the analytical expressions for pressure and wind terms as well as mountain and friction torques can be found in Appendix A.2. Both horizontal and vertical integrals were approximated by the trapezoidal rule, whereas a second-order centered difference scheme was used to evaluate the topography gradients in the longitudinal and co-latitudinal directions. Note that the partial objections of Huang & Weickmann (2008) to second-order differences can be neglected in light of the dense spatial sampling ($0.5^\circ \times 0.5^\circ$). Repeated application of the discretized integrals yielded 5-year time series of each excitation term at a unified temporal resolution of 3 h, where the hourly friction torque from MERRA had to be interpolated to the aforementioned eight synoptic hours.

4.2.5 Preliminary model comparison in terms of selected tidal variables

Tidal fluctuations at diurnal and higher frequencies are readily detectable in all invoked datasets, particularly in that valid at the Earth's surface. In order to assess the discrepancies in the representation of atmospheric tides within the three circulation models, their gridded surface pressure and tangential stress signals at $n = 1, 2$ cpd can be intercompared. Following Eq. (4.2), the sinusoids of p_s and τ_λ at frequency n were determined by a least squares fit for each grid point based on 1 yr of data from each of the three models, ERA-Interim, MERRA and ECMWF DC. After evaluating S_1 and S_2 harmonics at eight discrete epochs of a mean day (0, 3, 6, etc. UTC) on a unified 1° grid, root mean square (RMS) values were deduced, e.g. for the surface pressure differences between ERA-Interim and MERRA via

$$\mathrm{RMS}(\theta, \lambda) = \sqrt{\frac{1}{8} \sum_{i=1}^{8} \left(p_{s,i}^{ERA}(\theta, \lambda) - p_{s,i}^{MERRA}(\theta, \lambda) \right)^2} \, . \tag{4.3}$$

The resulting global RMS grids are depicted in Figure 4.4. Overall, the largest disparities at both diurnal and semi-diurnal frequencies exist between the two reanalysis datasets, ERA-Interim and MERRA, while the two models operated by the ECMWF agree well as one would expect.

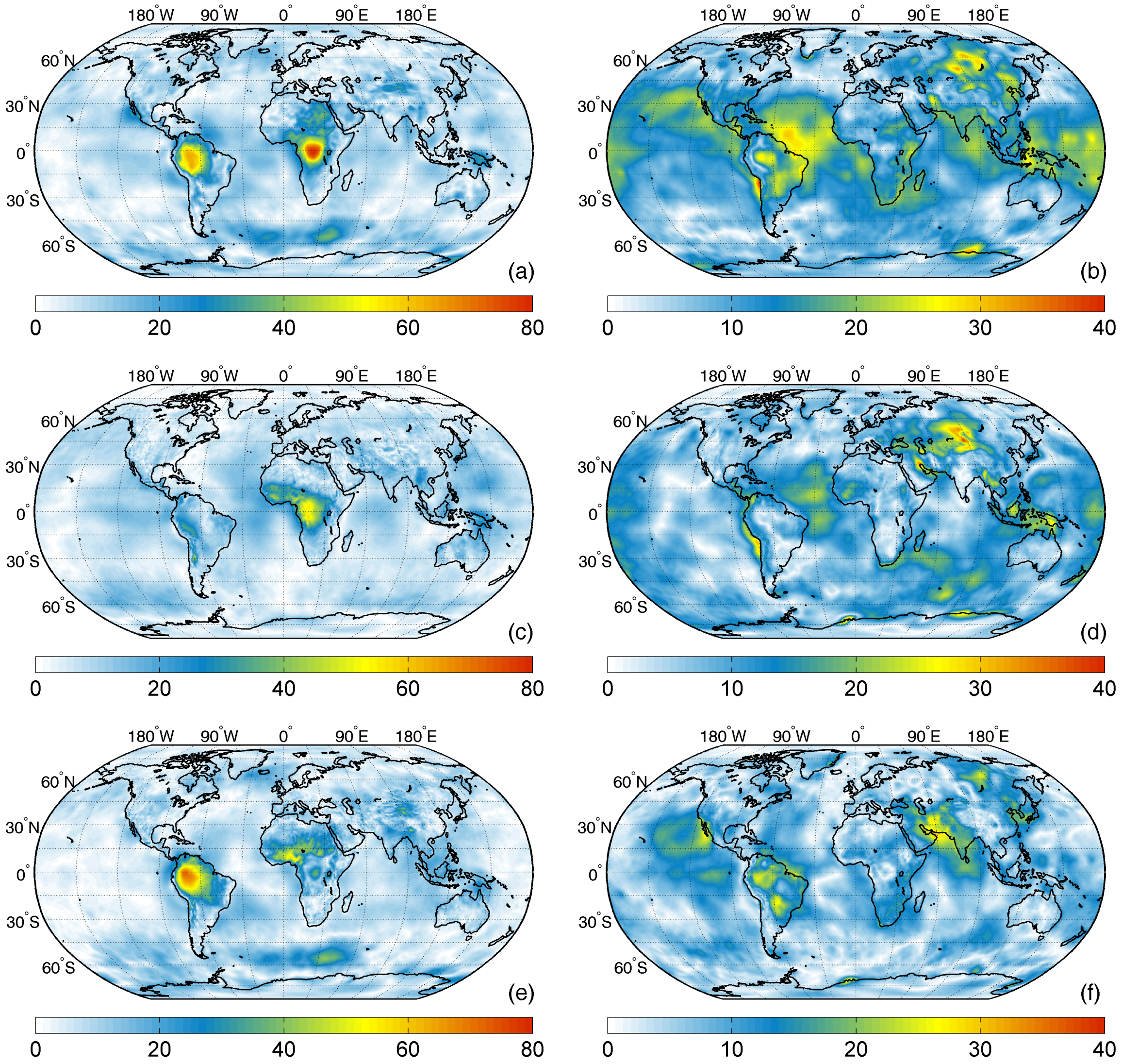

Figure 4.4: Grid point-wise RMS values deduced from the differences in surface pressure [Pa] between two atmospheric models at frequencies 1 and 2 cpd. (a,b) ERA-Interim – MERRA at S_1 (left) and S_2 (right). (c,d) ERA-Interim – ECMWF DC at S_1 (left) and S_2 (right). (e,f) ECMWF DC – MERRA at S_1 (left) and S_2 (right). Analyzed time span: 2011.

RMS values for the S_2 tide (right column of Figure 4.4) appear equally over landmasses and the oceans due to the dominance of the migrating tidal component, and do not exceed 40 Pa, which corresponds to about 25% of the full semi-diurnal signal in surface pressure. For the diurnal tide (left column of Figure 4.4), RMS values between ERA and MERRA reach 80 Pa and thus almost 50% of the values shown in Figure 4.1a. The location of those discrepancies concurs with the maxima of the diurnal surface pressure tide over the Amazon rain forest and Central Africa (Congo River basin rain forest). Figure 4.4 therefore illustrates the incoherence of current coupled atmosphere-land analysis systems in precisely accounting for regional and local effects

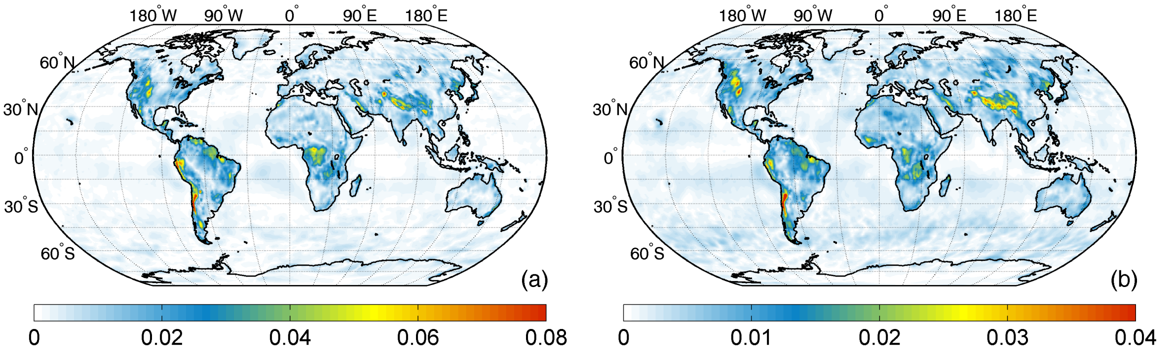

Figure 4.5: Grid point-wise RMS values $\left[\mathrm{Nm}^{-2}\right]$ deduced from the differences in eastward instantaneous surface stress between ERA-Interim and MERRA at S_1 (a) and S_2 (b). Analyzed time span: 2011.

in the daily hydrological cycle (Dee *et al.*, 2011). Condensation, latent heat release, and cloud amounts are key features governing water vapor heating rates in the troposphere, which in turn are key features for the accurate representation of atmospheric tides.

In the case of eastward surface stresses (Figure 4.5), the largest discrepancies between ERA-Interim and MERRA at diurnal and sub-diurnal periodicities are naturally found for terrain that is subject to strong tangential forces, such as the Rocky Mountains, the southern Andes, the Congo River basin, as well as the Himalaya and the Karakorum. Considerable RMS values up to 50% of the total signal in τ_λ over those regions demonstrate how sparse observational constraints and deficiencies in quantifying vegetation type or surface roughness complicate the estimation of stress variables. Significantly lower differences were obtained for the comparison of stress tides from both ECMWF data streams (not depicted). This good agreement arises from both models' native similarities in their physics and parametrization schemes, which are a statistical description of sub-grid scale effects such as turbulence and convection (Peixoto & Oort, 1992; Persson, 2011). It remains to be seen if the model disparities in τ_λ will bear any effect on the estimates of the global friction torque.

4.3 Land and ocean in-situ observations of barometric solar tides

Prior to the advent of general circulation models and data assimilation systems, global estimates of pressure tides $S_1(p_s)$ and $S_2(p_s)$ were usually constructed by harmonic analyses of barometric measurements from widely distributed meteorological stations (Ray & Ponte, 2003). Provided careful analysis and the use of multi-year time series, these 'ground truth' compilations are still one of the most reliable representations of surface pressure tides (Ray, 2001). Their capability in revealing inadequacies of the $S_1(p_s)$ and $S_2(p_s)$ signatures in recent climate model simulations has been demonstrated by Covey *et al.* (2011). The surface pressure output of operational and reanalysis systems can be tested in a similar manner, although such a crosscheck is not fully independent since considerable volumes of barometer data are assimilated in those models. However, the ingested samples of in-situ observations in each analysis cycle certainly depart from an optimal global coverage, allowing other observations, the model physics, the assimilation technique, etc. to affect the representation of barometric tides in the model output. Significant systematic amplitude and phase differences between analyzed fields and 'ground truth' tides have thus been noted by Ray (2001) or Ray & Ponte (2003) and illustrate the sustained scientific value of in-situ observations.

4.3.1 Existing spherical harmonic expansions

The use of global barometric measurements for the purpose of validating diurnal and semi-diurnal AAM pressure term estimates is a novel approach that imposes high requirements on the underlying data and their analysis. This is due to the mere fact that the dominant, migrating components of $S_1(p_s)$ and $S_2(p_s)$—which are the $\{1,1\}$-term (corresponding to degree or wave number $s = 1$ and order 1) in an expansion of the diurnal tide and the $\{2,2\}$-term in an expansion of the semi-diurnal tide—produce a zero net effect when inserted in the AAM integrals of Eqs. (3.18)–(3.21) as a result of the orthogonality properties of spherical harmonics. All remaining terms are of reduced amplitude, among them those which actually couple to variations in Earth rotation: the $\{2,1\}$-term for the equatorial component and the two zonal terms $\{0,0\}$ and $\{2,0\}$ for changes in LOD. Inclusion of the $\{0,0\}$-term in spherical harmonic expansions of the pressure tide is a formal necessity that improves the overall fit of Legendre polynomials to the data (Haurwitz & Cowley, 1973). The physical equivalent of such a component would be a periodic oscillation of the mean global pressure, which is unlikely to exist on diurnal time scales. On the contrary, the $\{2,0\}$-term, corresponding to a standing wave with two nodes between the poles, can be definitely observed in polar regions where the amplitudes of all other tidal terms decrease toward zero. For the semi-diurnal tide, its magnitude is thought to be about 15% of that of the main migrating wave (Ray, 2001).

Early harmonic analyses of both the diurnal and semi-diurnal surface pressure oscillations were conducted by Haurwitz & Cowley (1973) based on data collected at 264 stations. While all afore-noted terms are included in their expansion, the applicability of the retrieved fields is clearly impaired by vast data gaps and the omission of observations at latitudes higher than 60°. These data have been augmented by Hamilton (1980) and Ray (1998), with a subsequent fit of spherical harmonics for the semi-diurnal band presented in Ray (2001). Yet, the latter model does not account for the variation of the mean global pressure and also rests upon a sparse network of stations with the exception of North America and Europe as shown in Figure 4.6a. The currently most comprehensive pressure observations compilation has been created and analyzed by Dai & Wang (1999) on the basis of data from over 7500 weather stations, commercial ships, and ocean buoys during the period 1976–1997 as archived in synoptic (3-hourly) weather reports at NCAR (*National Center for Atmospheric Research*). While this dataset attains almost a perfect global coverage (Figure 4.6b), it is so large that the Fourier analysis at each station was performed completely by automated means. This strategy neglects the peculiarities of each individual time series and possibly severe errors in the harmonic fit (cf. Section 6.1), leading to large internal inconsistencies (Ray, 2001), which prohibit the use of the results by Dai & Wang (1999) for validation of AAM pressure term estimates. The present study thus requires its own extensive pressure data compilation from both surface stations and marine reports. Processing strategies, avoiding the previously mentioned problems, should ensure the best available global distribution and an accurate estimation of tidal harmonics.

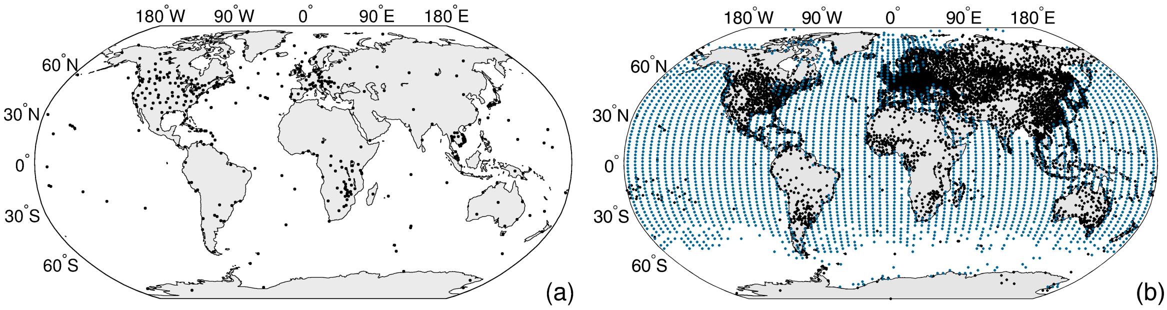

Figure 4.6: Locations of 'ground truth' stations where either S_1 or S_2 pressure tides have been determined from long time series of barometric observations: (a) 428 stations from Ray (2001), (b) compilation of Dai & Wang (1999) with 7553 land barometers depicted in black and 3073 ocean boxes shown in blue.

4.3.2 The International Surface Pressure Databank

The barometric data utilized in this work are a subset of version 2 of the *International Surface Pressure Databank* (ISPDv2), which is the world's largest compilation of surface and sea level pressure (SLP) observations provided for the time span 1768–2010. The databank has been assembled through extensive international collaboration under the auspices of the *Atmospheric Circulation Reconstructions over the Earth* (ACRE) initiative, and other working groups of the *Global Climate Observing System* (GCOS) and the *World Climate Research Program* (WCRP), see Compo *et al.* (2011). The three components of the ISPDv2 are pressure observations from land and ocean stations, marine reports, and so-called *tropical cyclone best-track* data, which originate from post-season reanalyses of tropical storm characteristics (Knapp *et al.*, 2010) and take into account all available cyclone tracking devices (ships, stations, satellites). However, pressure perturbations associated with severe storm events are anomalous signals with regard to the analysis of regular phenomena such as atmospheric tides and are thus not considered any further. The station portion of ISPDv2 represents a merger of numerous international collections, while the marine component is the current version of the *International Comprehensive Ocean Atmosphere Data Set* (ICOADS), see Compo (2013).

Overall, the chosen data archives largely coincide with that of Dai & Wang (1999) but profit from substantial improvements made over the last years such as ISPDv2's rigorous quality-control procedure in the context of a complete atmospheric reanalysis, which is version 2 of the *Twentieth Century Reanalysis Project* (20CRv2, Compo *et al.*, 2011) led by the *Earth System Research Laboratory* of NOAA (*National Oceanic and Atmospheric Administration*) and the CIRES (*Cooperative Institute for Research in Environmental Sciences*) *Climate Diagnostics Center* of the University of Colorado. The 20CRv2 has been chiefly motivated by the needs of climate research for reanalysis products spanning the entire 20th century, e.g. to validate climate model simulations and understand the statistics of extreme weather events. As such, it builds on surface pressure reports only and uses an Ensemble Kalman Filter assimilation system (Whitaker & Hamill, 2002), which produces 6-hourly analysis fields and also uncertainties for the state variables of the atmosphere. The quality control of each ISPD observation during the assimilation cycle comprises five steps: principal test of meteorological plausibility; test against the first guess of the Kalman filter ensemble; outlier detection based on the variability of neighboring stations; exclusion of observations with low impact in the assimilation; and correction of systematic differences to the time series of the local first guess (Compo *et al.*, 2011). The resulting distinction between assimilated and rejected observations constitutes a valuable information for the present study.

Nonetheless, the processing of in-situ observations remains less straightforward than that of gridded model fields and has to consider the subtleties of each individual time series, e.g. data gaps, non-equidistant sampling, or remaining systematic errors. Section 6.1 is in part devoted to those issues. Here, only the principal strategy shall be noted. All available surface and marine data of the ISPDv2 were downloaded via NCAR's *Data Support Section* from `http://rda.ucar.edu/datasets/ds132.0/` for the period 1990–2010. Longer time windows were allowed for in polar regions (1900–2010 north of $\theta = 20°$, and 1950–2010 south of $\theta = 138°$) to retain a sufficient number of stations also in sparsely sampled regions. The analysis should yield a globally well-distributed pool of accurate ground-truth tidal estimates, on the basis of which annual mean variations of $S_1(p_s)$ and $S_2(p_s)$ could be determined. Seasonal modulations of the pressure tides, as considered for instance by Dai & Wang (1999), were neglected for the sake of simplicity and the costs of the (partly non-automated) analysis. Unfortunately, this omission can introduce distortions of the mean tidal elements, particularly in those of the diurnal component, which is characterized by a strong seasonal and interannual variability (at about half the level of the mean annual amplitude, see Covey *et al.*, 2011; Ray, 1998). Those effects are minimized by using multi-year barometer series, preferably for an integral number of full calendar years (Ray & Ponte, 2003). Lastly, the sampling rates of the ISPDv2 data vary from one platform to another, with some stations observing every minute but others only at monthly intervals. The predominant sampling is at the eight synoptic hours (0, 3, 6, 9 UTC, etc.) and obviously sufficient to resolve harmonics with periods longer than 6 h. Harmonics above the semi-diurnal band (e.g. S_3) were neglected in the Fourier decomposition at each platform, but are small enough to engender only minor aliasing effects, typically below 10% (Cooper, 1984). More details on the handling of land and marine data are presented in Section 6.1.

Chapter 5

The balance of diurnal and semi-diurnal atmospheric angular momentum

Assessing the reliability of geophysical models with regard to their validity for predicting Earth rotation variations represents a valuable but less discussed complement to the plain quantification of excitation effects. At lower frequency bands model-based fluid excitation functions can be effectively verified by comparison to Earth rotation data, but such a strategy is less feasible at diurnal and sub-diurnal periodicities due to the dominance of the ocean tidal component over the effect of air tides. As an alternative approach, numerical verification of the AAM budget equation at frequencies of 1 and 2 cpd provides insight into the realism of atmospheric models by detecting inconsistencies between the AAM vector and the total atmospheric torque that portend systematic errors in short-range forecasts (Huang *et al.*, 1999), which in turn affect the accuracy of ERP estimates used for example in spacecraft navigation. This chapter details the balance of short period AAM from ERA-Interim, MERRA, and ECMWF DC over the period 2007–2011 in order to (1) assess the quality of state-of-the-art circulation/reanalysis models with regard to Earth rotation research; and (2) crosscheck torque and AAM estimates at S_1 and S_2. Those analyses shall provide the platform for using atmospheric interaction torques as complementary measures to the angular momentum approach. The considerations represent also a major update on the large quantitative AAM budget discrepancies observed by de Viron *et al.* (2005b).

5.1 Spectral analysis of angular momentum variations and torques

Examination of the torque and angular momentum contributions to their respective approaches at (sub-)diurnal periodicities is a useful preparation to the portrayal of the AAM balance. It testifies that the spectral characteristics of short period atmospheric torques, pressure and wind terms are much more multifaceted than the low frequency magnitude relationships documented

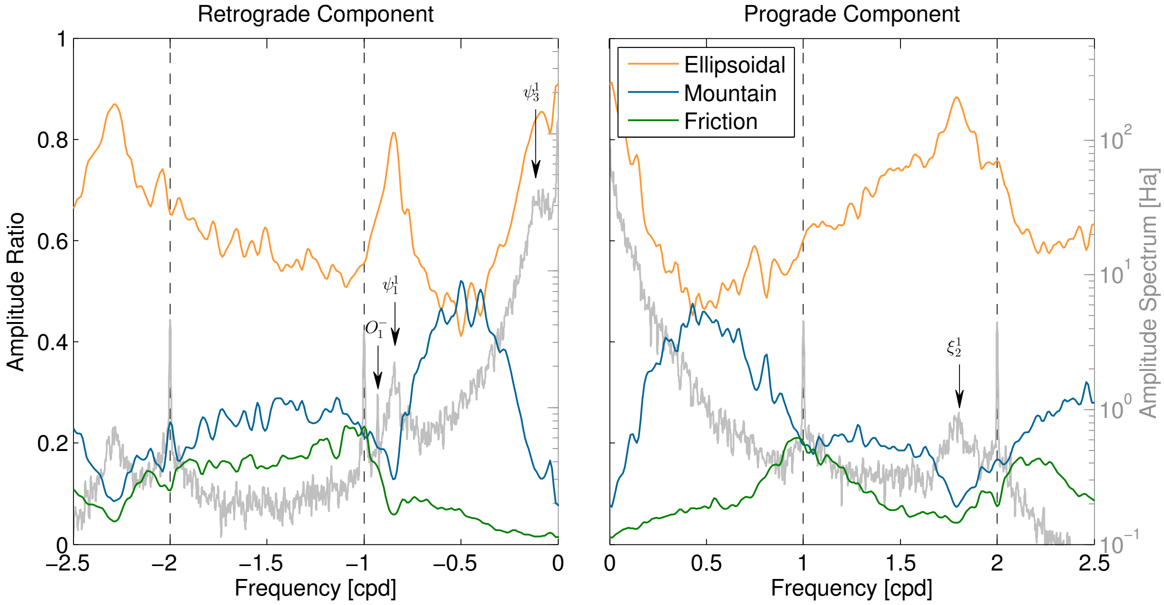

Figure 5.1: Amplitude spectrum (gray curve, scale on right) of the total equatorial torque from MERRA data (2007–2011), and frequency-dependent ratios (scale on left) of ellipsoidal torque (orange curve), mountain torque (blue curve), and friction torque (green curve) amplitudes relative to the sum of amplitudes of all three components.

by Gross *et al.* (2003, 2004) for angular momentum variations, Schindelegger *et al.* (2013c) for equatorial torques, and Iskenderian & Salstein (1998) for axial torques.

Equatorial torques

Figure 5.1 displays a smooth amplitude spectrum of the total equatorial torque $\hat{L}(t) = \hat{L}^e(t) + \hat{L}^m(t) + \hat{L}^f(t)$ from MERRA at pro- and retrograde frequencies. This approximate frequency domain representation was computed via the built-in MATLAB function *pwelch*, which implements the method of Welch (1967) of segmenting the input signal and averaging each section's periodogram to a PSD (*power spectral density*) curve of low variance. Here, each segment was windowed with a Hamming window of length 2^{11} and 50% overlap, while the length of the FFT (*Fast Fourier Transform*) and thus each periodogram was fixed to 2^{13} (approximately half the length of the input time series). A subsequent scale adaption of the PSD coefficients with respect to a standard FFT of $\hat{L}(t)$ yielded the final amplitude estimates. As apparent from Figure 5.1, the solar tidal forcing at the Earth's surface engenders distinct torque signals at $S_1^{\pm}$ and $S_2^{\pm}$ with prograde amplitudes (4.5 and 4.4 Ha, Hadleys, $1\text{Ha} = 10^{18}\text{kgm}^2\text{s}^{-2}$) being as large as the retrograde peaks (3.6 and 4.2 Ha). Alongside those oscillations, which will be scrutinized later, a few additional signals at nearby frequencies are worth noting. First, the gravitational lunar tide O_1^- is clearly visible close to the retrograde diurnal band. Second, a well-known subset of the so-called *atmospheric normal modes*, signified as ψ_1^1, ψ_3^1, and ξ_2^1 in Figure 5.1, do also couple with

Table 5.1: Period and mean amplitude of atmospheric normal modes in polar motion excitation as detected from the total torque amplitude spectrum in Figure 5.1.[a]

Normal Mode	Period [d]	Mean Amplitude	
		Torque [Ha]	Excitation [μas]
ψ_1^1	-1.2	2.2	3.0
ψ_3^1	-8.3	39	121.4
ξ_2^1	0.6	0.9	0.1

[a] The torque quantities were converted to AAM variations using Eq. (3.35), scaled to pressure term angular momentum functions and multiplied by the transfer coefficient of the respective frequency band.

polar motion, see Brzeziński *et al.* (2002) and references therein for a more detailed discussion of those phenomena. Their spectral peaks are much broader than those of tidal oscillations but basically centered at $\nu = -0.83$ cpd (ψ_1^1), $\nu = -0.12$ cpd (ψ_3^1), and $\nu = 1.67$ cpd (ξ_2^1), where $\nu = 86400\sigma/(2\pi)$. Table 5.1 summarizes their mean amplitudes in the spectrum of $\hat{L}(t)$ and also provides a rough estimate of the corresponding effects in polar motion.

The individual contributions of $\hat{L}^e$, $\hat{L}^m$ and $\hat{L}^f$ to the total Earth-atmosphere interaction torque in Figure 5.1 were computed in the manner of Schindelegger *et al.* (2013c) from the standard FFT of the three torque constituents (see Section 5.2 for some more details on the discrete spectral transform). Specifically, each Fourier coefficient series was dissected into overlapping spectral bins of distance 0.01 cpd and bandwidth ±0.03 cpd. After weighting the spectral content of each segment by a Hamming window placed on the central sampling frequency σ_i, average moduli $\left|\hat{L}^{e,m,f}(\sigma_i)\right|$ were obtained and expressed as *amplitude ratios* with respect to their sum $\left|\hat{L}^e(\sigma_i)\right| + \left|\hat{L}^m(\sigma_i)\right| + \left|\hat{L}^f(\sigma_i)\right|$. Note that this cumulative quantity is always larger than the total torque amplitude $\left|\hat{L}^e(\sigma_i) + \hat{L}^m(\sigma_i) + \hat{L}^f(\sigma_i)\right|$ of the considered bin. As anticipated from de Viron *et al.* (2005b), the ellipsoidal torque accounts for more than 50% of the cumulative amplitude ratio at short periods, reaching typical values of some two thirds at the frequencies of special interest, $S_1^\pm$ and $S_2^\pm$. Pronounced peaks of the bulge effect at the spectral locations of ψ_1^1, ψ_3^1 and ξ_2^1 suggest that atmospheric normal modes are well represented in the polar motion (degree 2, order 1) surface pressure pattern (Madden, 2000), but not in areas that are responsible for local torque signals. While the mountain torque magnitude ratio is interestingly high at periods of roughly 2 d, it drops to a level of approximately 10–30% at near-diurnal and sub-diurnal frequencies, thus being comparable to the friction component (de Viron *et al.*, 2001). The increased importance of $\hat{L}^f$ at S_1 and S_2 as opposed to longer time scales is one of the prominent characteristics of the torque method for the equatorial part of Earth rotation.

Equatorial AAM

An analogous analysis of the total equatorial AAM and its two constituents $\hat{H}^p$, $\hat{H}^w$ in Figure 5.2 unveils a clear asymmetry between the retrograde and prograde portions of the overall

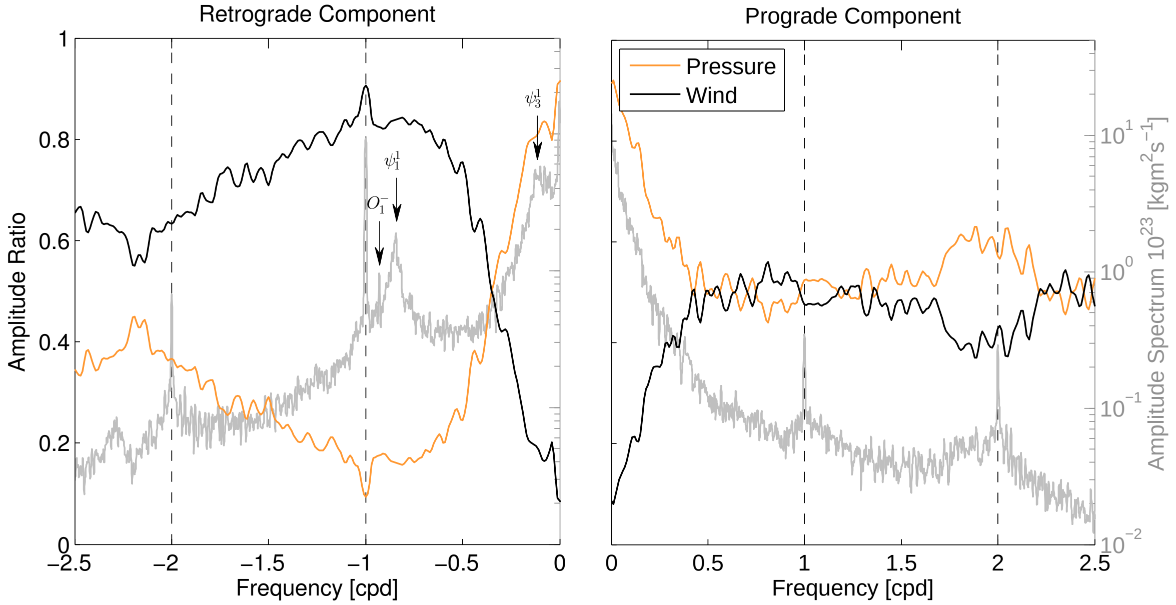

Figure 5.2: Amplitude spectrum (gray curve, scale on right) of the total equatorial AAM from MERRA, and frequency-dependent ratios (scale on left) of pressure term (orange curve) and wind term (black curve) amplitudes relative to the sum of amplitudes of all two components.

amplitude spectrum. While this finding relates to the existence of strong near-diurnal retrograde variations of the wind term (see Brzeziński *et al.*, 2002, and note the amplitude ratio of $\hat{H}^w$ above 80%), it can also be reasoned mathematically by recognizing that the symmetric torque spectrum in Figure 5.1 must be theoretically scaled with $-\mathrm{i}/(\sigma+\Omega)$ to obtain the corresponding AAM spectrum, cf. Eq. (3.35). The resonance of this transfer function at $\sigma=-\Omega$ implies an amplification of power near the diurnal band. However, a translation of the displayed magnitude relationships to excitation of nutation needs to take into account the second (physical) resonance effect of the FCN, which places a much stronger weight on the pressure term variability (Eq. 3.17). For the sake of completeness, the peak AAM amplitudes at diurnal and semi-diurnal frequencies shall be noted (in units of 10^{23} kgm^{2}s^{-1}): 9.2 (S_1^-), 0.3 (S_1^+), 0.7 (S_2^-), and 0.3 (S_2^+). Pressure and wind term contributions to the prograde part of the high frequency spectrum are approximately equal, which contrasts to the dominance of the inertia effect at intraseasonal and longer time scales (Gross *et al.*, 2003). Of the three normal modes listed in Table 5.1, ψ_1^1 and ψ_3^1 are readily apparent at retrograde frequencies, whereas the ξ_2^1 wave appears only as a slight increase of power at $\nu=1.67$ cpd, being probably subject to a counterbalance of pressure and wind terms.

Axial torques

The composition of both the (sub-)diurnal and long period axial torque spectrum has been portrayed in previous publications (e.g. Iskenderian & Salstein, 1998; Lott *et al.*, 2008). In essence, the amplitudes found at high frequencies match the spectral power at periods longer than 10–

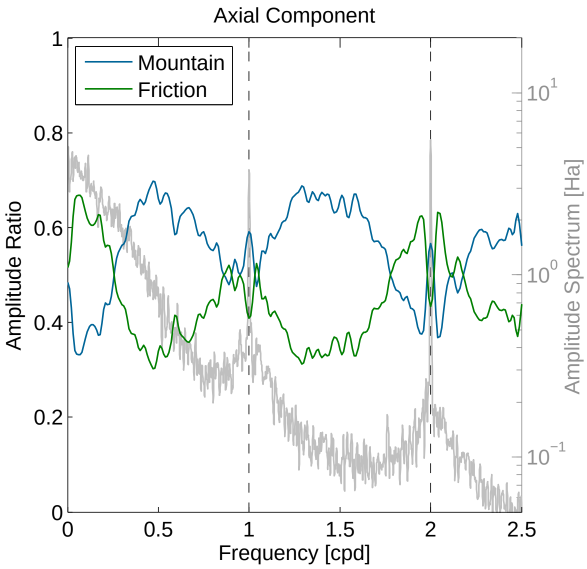

Figure 5.3: Amplitude spectrum (gray curve, scale on right) of the total axial torque from MERRA, and frequency-dependent ratios (scale on left) of mountain torque (blue curve) and friction torque (green curve) amplitudes relative to the sum of amplitudes of all two components.

15 d. Mountain and friction torques appear to contribute at about the same level at those tidal bands. When compared to the numerical results of Madden *et al.* (1998), the depicted values of 3.8 Ha (S_1) and 5.5 Ha (S_2) for the MERRA series in Figure 5.3 should be interpreted as more qualitative measures due to the smoothing of Welch's spectral estimator.

Axial AAM

The theoretical scaling factor translating the torque spectrum in Figure 5.3 to AAM variations is $-\mathrm{i}/\sigma$, and Figure 5.4 essentially confirms the resulting amplification of low frequency content. Contrary to the well-known dominance of relative angular momentum in the total AAM at periods longer than 25 d (Lott *et al.*, 2008), an equipartition between H_z^p and H_z^w occurs at shorter periods, including the diurnal and specifically the semi-diurnal band. While the individual S_2 pressure and wind term variations both feature peak-to-peak amplitudes of roughly $6 \cdot 10^{23}$ kgm^{2}s^{-1} (cf. their amplitude ratios of almost exactly 50%), their cumulative effect attains a remarkably small magnitude of only $0.5 \cdot 10^{23}$ kgm^{2}s^{-1}. This distinct cancellation of axial pressure and wind oscillations is reminiscent of the discussion inspired by Eq. (3.45) and has been addressed from a geometric point of view by Schindelegger *et al.* (2012), whereas a dynamical reasoning has been given by Lott *et al.* (2008). In brief, the latter study postulates that the semi-diurnal zonal mean of the meridional momentum per unit area (i.e. the integral of v-velocities over increments dλ and dp) drives a redistribution of masses from mid-latitudes to the tropics, which in turn produces variations in the pressure term (for instance a positive mass anomaly due to the accumulated high pressure at the equator). At the same time, these flow conditions trigger two extrema of the u-

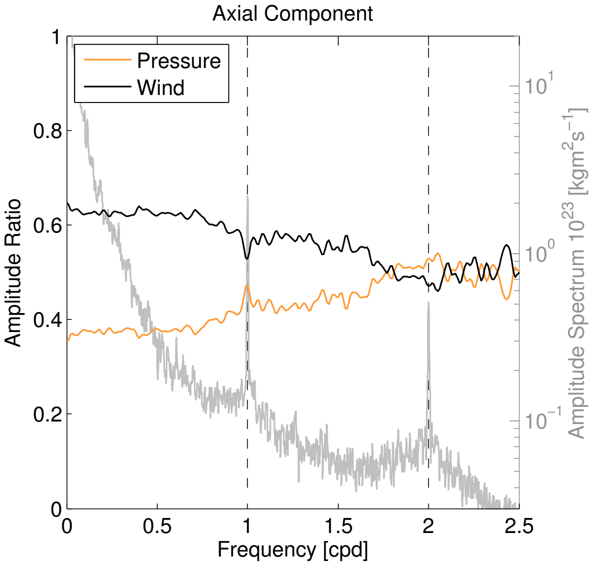

Figure 5.4: Amplitude spectrum (gray curve, scale on right) of the total axial AAM from MERRA, and frequency-dependent ratios (scale on left) of pressure term (orange curve) and wind term (black curve) amplitudes relative to the sum of amplitudes of all two components.

wind in mid-latitudes, resulting in variations of the motion term (a negative wind AAM anomaly in the above example as the transport of mass toward the equator is deflected to the west via the Coriolis force). Considering the numerical instability associated with such a pronounced compensation of mass and motion AAM, closing the axial AAM budget on diurnal and semi-diurnal time scales will be a difficult task.

5.2 AAM derivative versus Earth-atmosphere interaction torque

This section presents the sought-for numerical validation of the full AAM budget equation for ERA-Interim, MERRA, and ECMWF DC at short periods with an emphasis on atmospheric tidal bands. Perceived to supply a mean picture of the instantaneous AAM balance in 2007–2011, the spectral formulations in Eqs. (3.35) and (3.36) were tested similar to de Viron *et al.* (1999) by estimating correlation coefficients ρ and regression coefficients r at each frequency band. In the equatorial direction, the methodology utilized $\hat{H}(\sigma_e)$ and $\hat{L}(\sigma_e)$, i.e. the discrete, two-sided Fourier transforms (DFT) of equatorial AAM and the total Earth-atmosphere interaction torque of length n_f and sampling rate $\Delta t = 3$ h. The associated frequency vector reads

$$\sigma_e = 2\pi\nu_e = \frac{2\pi}{n_f \Delta t}\left[-n_f/2, -n_f/2+1, \ldots, n_f/2-1\right], \tag{5.1}$$

and a similar discretization can be given for the one-sided case σ_a or ν_a (Section 1.9 of Otnes & Enochson, 1978) allocated to the axial components $\hat{H}_z(\sigma_a)$ and $\hat{L}_z(\sigma_a)$. Multiplica-

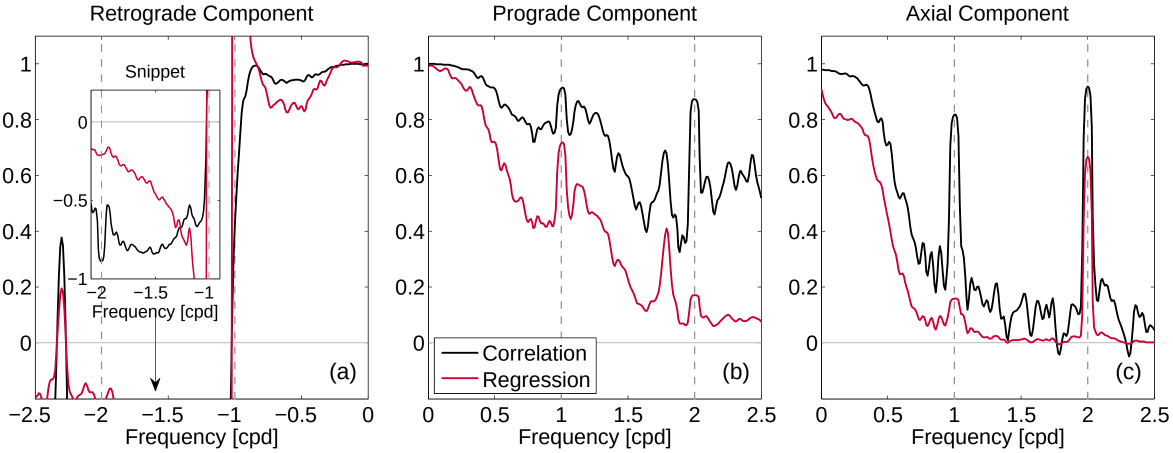

Figure 5.5: ERA-Interim: Frequency-dependent correlation (black curves) and regression coefficients (red curves) between the left- and right-hand side of the AAM budget equation in both the equatorial direction (a,b) and axial direction (c).

tion of the DFT vectors of equatorial (or axial) AAM with the corresponding transfer coefficients $\mathrm{i}\,(\sigma_e + \Omega)$ (or $\mathrm{i}\sigma_a$) yielded the AAM derivatives in inertial space (Eqs. 3.35 and 3.36). The Fourier coefficient series of the left- and right-hand side of each equation were subsequently split up into spectral bins of bandwidth ±0.05 cpd at steps of 0.01 cpd and weighted with a Hamming window, cf. Section 5.1. From the amplitude and phase information of the resulting segments, the sinusoids at each frequency were reconstructed in the time domain and superimposed to each other. (This procedure basically corresponds to the repeated application of a standard bandpass filter within a pure time domain approach, from which this study had to abstain due to the use of complex-valued series and the difficulties of numerical differentiation at high frequencies.) The final analysis step was to regress the residual time series of the torque against that of the AAM derivative and compute their correlation coefficient ρ.

Concerning the interpretation of results, ρ functions as a measure of the linear association between the two quantities of interest (say, L and H in a symbolic notation), whereas the regression coefficient r exactly measures the size of change in L when a unit change takes place in H (Draper & Smith, 1981). Hence, r can be conceived as a scale factor, related to the correlation coefficient via $r = \frac{s_L}{s_H}\rho$ (see also Draper & Smith, 1981), where s_L abd s_H are the ratio of spreads (standard deviations) inherent to the quantities L and H. A perfectly balanced budget, corresponding to an exact, positive linear dependency of the AAM derivative and the torque on the atmosphere, is thus indicated by $\{r, \rho\} = 1$. Strong negative linear dependency (out-of-phase behavior) supplies $\{r, \rho\} \approx -1$.

Figures 5.5 (ERA-Interim), 5.6 (MERRA), and 5.7 (ECMWF DC) show the correlation and regression results for each individual (re)analysis system at pro- and retrograde equatorial frequencies as well as for the axial component. At lower frequencies, specifically at $\{\nu_a, \nu_e\} < 0.5$ cpd, the three models unanimously report a well-closed AAM budget (Lejenäs *et al.*, 1997; Schindelegger

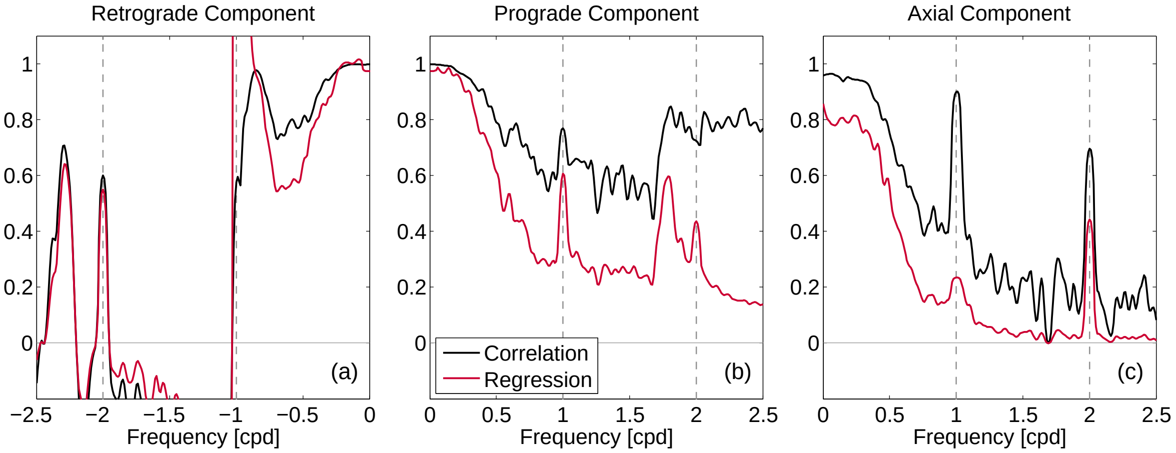

Figure 5.6: MERRA: Frequency-dependent correlation (black curves) and regression coefficients (red curves) between the left- and right-hand side of the AAM budget equation in both the equatorial direction (a,b) and axial direction (c).

et al., 2013c), with $r \approx 0.8$ being the one peculiarity in the axial component. Recall that due to the dominance of the ellipsoidal effect in both $\hat{L}$ and $\hat{H}$, the long period equatorial balance equation is easily satisfied. A similar conclusion can be drawn for other frequencies holding pronounced bulge torque signals, that are, $\nu_e = -2.30$ cpd, $\nu_e = -0.83$ cpd (ψ_1^1), and $\nu_e = 1.67$ cpd (ξ_2^1). Those bands are readily apparent in all three equatorial budget comparisons as enhanced peaks of correlation and regression, with a near-perfect validation achieved for the strongest mode (ψ_1^1) and a reduced agreement ($\rho, r = 0.2$–0.8) present for the low-power oscillations (< 1 Ha) at $\nu_e = -2.3$ cpd and $\nu_e = 1.67$ cpd.

Besides non-tidal effects, the most pronounced anomaly in the equatorial spectra of all models is the resonance curve-like change of coefficients at the frequency of exactly one retrograde cycle per sidereal day ($-\Omega$). The underlying ill-conditioned relationship between diurnal local torques and the ellipsoidal torque has been analytically examined in Section 3.3.3. It implies that very small (and probably erroneous) residuals need to be intercompared in the retrograde diurnal part of the AAM budget, and one should therefore not attach too much importance to the appearance of Figures 5.5–5.7 near $\sigma_e = -\Omega$. The separation into term-by-term phasors in the next section provides a clearer picture of the budget closure for the retrograde diurnal tide. Apart from this resonance feature, the numerical results at prograde frequencies are particularly encouraging. Although somewhat lower regression values have to be accepted, the correlation coefficients deduced for ERA-Interim ($\rho \approx 0.9$ at S_1^+ and S_2^+) and MERRA ($\rho \approx 0.8$ at S_1^+ and S_2^+) are indisputably higher than those indicated in earlier papers (de Viron & Dehant, 1999; de Viron *et al.*, 2005b). (Note that actual studies on the subject are limited in number, and none of these addresses the sub-daily AAM balance in such a comprehensiveness.) This partly successful budget verification at prograde frequencies represents a key result of the present chapter and also complements the excellent equatorial budget closure at intraseasonal periodicities from the same

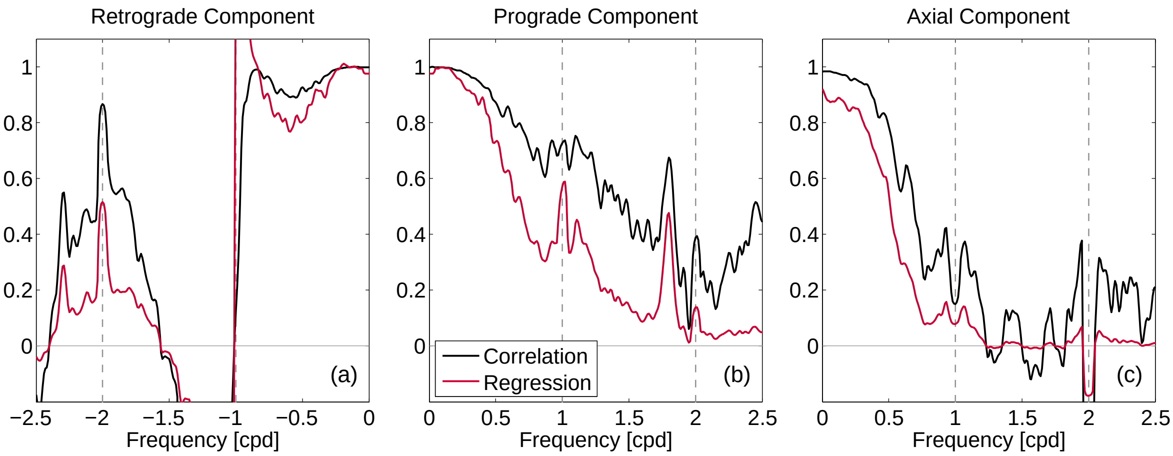

Figure 5.7: ECMWF DC: Frequency-dependent correlation (black curves) and regression coefficients (red curves) between the left- and right-hand side of the AAM budget equation in both the equatorial direction (a,b) and axial direction (c).

reanalysis data (Schindelegger *et al.*, 2013c).

A reasonably good agreement between AAM derivative and torques likewise appears at S_2^- for MERRA and ECMWF DC, whereas ERA-Interim reveals a strong inverse correlation ($\rho \approx -0.9$) and a degraded scale relationship ($r \approx -0.2$). In contrast, the ERA-Interim axial AAM budget is well closed at the semi-diurnal frequency, and to a lesser extent also for the MERRA system. Based on the unambiguous spectral resolution of the S_2 band with 3-hourly reanalysis fields, the decent axial AAM balance is another step forward with respect to previous attempts (Madden *et al.*, 1998). Admittedly, this successful verification is not universal, see e.g. the dismal axial correlation and regression results for the ECMWF DC operational analysis model (Figure 5.7c). In addition, a scale deficiency ($r \approx 0.2$) surfaces for each of the zonal S_1 solutions, refer to de Viron *et al.* (2001) and de Viron *et al.* (2005b) for similar findings.

5.3 AAM budget at diurnal and semi-diurnal frequencies

Probably the centerpiece of the present thesis, this section examines the balance of AAM within state-of-the-art atmospheric models/assimilation systems at frequencies of exactly 1 and 2 cpd. All numerical considerations are accomplished in the spectral domain, primarily for reasons of computational convenience and in order to avoid spurious high-frequency signals that might be introduced by differentiation of quickly-varying, discrete functions (Moritz & Müller, 1987). The much simpler axial part of the budget equation in the time domain (Eq. 3.34)

$$\frac{\mathrm{d}H_z^w}{\mathrm{d}t} + \frac{\mathrm{d}H_z^p}{\mathrm{d}t} = L_z^f + L_z^m \tag{5.2}$$

yields the following discrete frequency domain expression

$$\underline{\mathrm{i}\sigma_a \hat{H}_z^w(\sigma_a)} + \underline{\mathrm{i}\sigma_a \hat{H}_z^p(\sigma_a)} = \underline{\hat{L}_z^f(\sigma_a)} + \underline{\hat{L}_z^m(\sigma_a)}\,, \tag{5.3}$$

involving DFT vectors of both AAM terms and local torques at frequency samples σ_a. (The various underlinings conform to the color-code used in this section's figures.) For the equatorial component (Eq. 3.37), after abbreviating the wind term contributions as $\mathrm{d}\hat{H}^w/\mathrm{d}t + \mathrm{i}\Omega\hat{H}^w = \mathrm{D}\hat{H}^w/\mathrm{D}t$, one finds

$$\frac{\mathrm{D}\hat{H}^w}{\mathrm{D}t} + \frac{\mathrm{d}\hat{H}^p}{\mathrm{d}t} + \mathrm{i}\Omega\hat{H}^p = \hat{L}^f + \hat{L}^m + \hat{L}^e\,, \tag{5.4}$$

or, equivalently,

$$\underline{\mathrm{i}(\sigma_e + \Omega)\hat{H}^w(\sigma_e)} + \underline{\mathrm{i}\sigma_e\hat{H}^p(\sigma_e)} + \underline{\mathrm{i}\Omega\hat{H}^p(\sigma_e)} = \underline{\hat{L}^f(\sigma_e)} + \underline{\hat{L}^m(\sigma_e)} + \underline{\hat{L}^e(\sigma_e)}\,, \tag{5.5}$$

which also encompasses the formulation of the residual AAM budget by neglecting the ellipsoidal effect $\mathrm{i}\Omega\hat{H}^p = \hat{L}^e$ (orange underlining) on both sides of the equation. Given that the frequencies of interest $\nu_e = \{1, 2\}$ cycles per solar(!) day are virtually full integer multiples of the angular velocity of sidereal rotation Ω, the second and third term of Eq. (5.5) interrelate via a simple scale factor and their phasor equivalents in the complex plane must be parallel. At retrograde frequencies the bulge torque counterbalances the pressure term derivative (black underlining), specifically by 50% for S_2^- ($\sigma_e \approx -2\Omega$) and by (almost exactly) 100% for S_1^- ($\sigma_e \approx -\Omega$), see Section 3.3.3. At prograde frequencies both terms add up, either to $2\mathrm{i}\Omega\hat{H}^p$ ($S_1^+, \sigma_e \approx \Omega$) or to $3\mathrm{i}\Omega\hat{H}^p$ ($S_2^+, \sigma_e \approx 2\Omega$). Note that these analytical scale relationships are not exactly fulfilled in de Viron *et al.* (2005b, Figure 5). Nonetheless, their study attains a near-perfect closure of the (sub-)diurnal AAM budget from a GCM simulation run and therefore serves as a partial reference in the below comparisons.

Prograde diurnal component

Figures 5.8a (ERA), 5.9a (MERRA), and 5.10a (ECMWF DC) depict the superposition of Fourier coefficients extracted at $\nu_e = 1$ cpd from the DFT of all six equatorial AAM budget terms. Within this phasor representation, the agreement of the left-and right-hand sides of Eq. (5.5) can be assessed both with and without the ellipsoidal torque. In the latter case, the cumulative friction + mountain torque phasor needs to balance the sum of the wind term derivative $\mathrm{D}\hat{H}^w/\mathrm{D}t$ and the pressure term derivative $\mathrm{d}\hat{H}^p/\mathrm{d}t$ in the rotating frame . This requirement is fairly well met by ERA-Interim but less so by the other two models. However, the pronounced cancellation between prograde diurnal pressure and wind term derivatives (cf. also de Viron *et al.*, 2005b) impedes the verificiation of the residual AAM budget, and one should rather focus on the agreement after superposition of the ellipsoidal torque. Partly due to the dominance of $\hat{L}^e$ over local torques, the full AAM budget at S_1^+ is well closed within ERA-Interim and MERRA, which certainly represents a progress with respect to previous studies (de Viron *et al.*, 2001). ECMWF's operational DC model

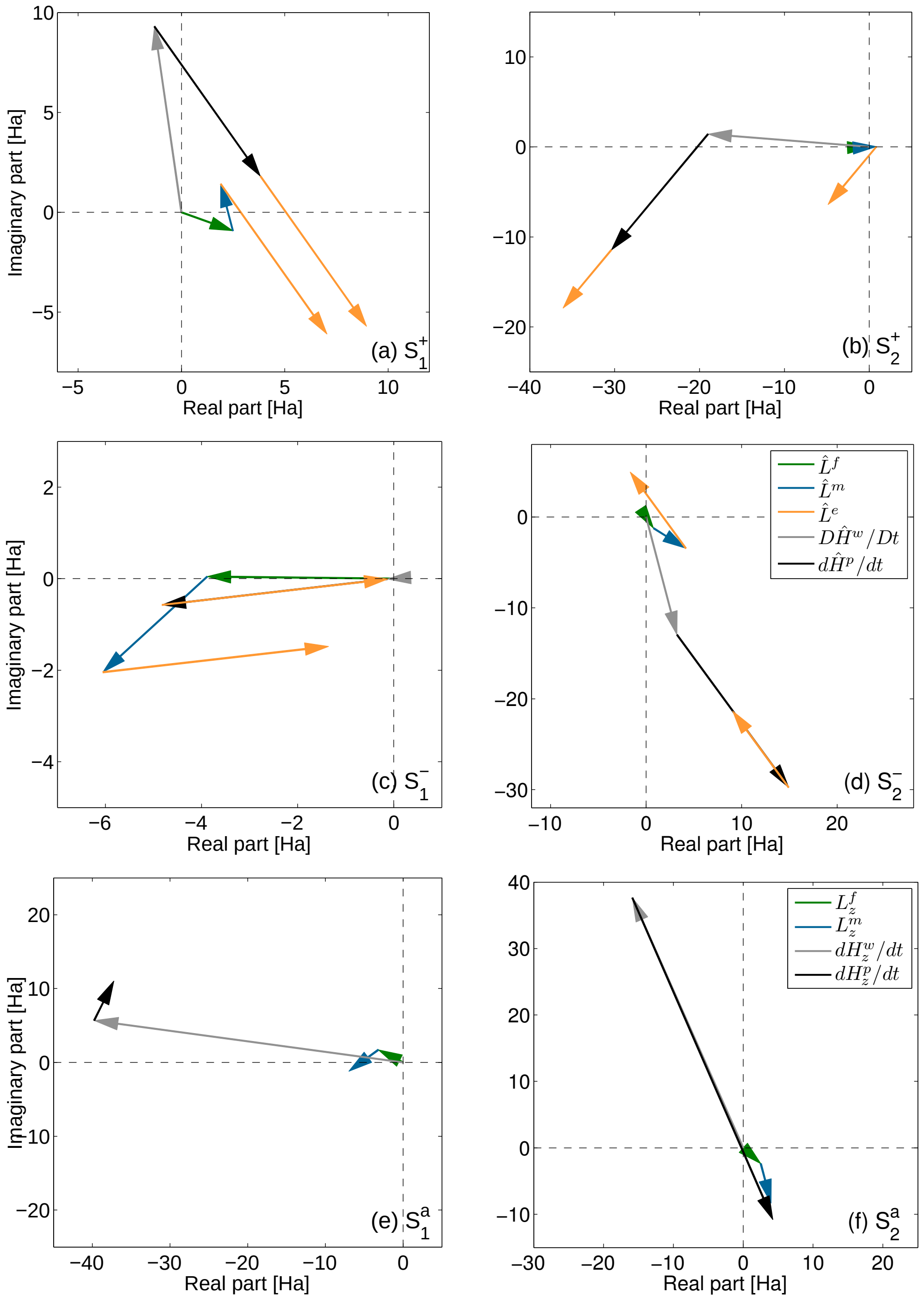

Figure 5.8: Phasor diagrams for the AAM budget verification within ERA-Interim (2007–2011): (a,b) Prograde diurnal and semi-diurnal equatorial components. (c,d) Retrograde diurnal and semi-diurnal equatorial components. (e,f) Diurnal and semi-diurnal axial components (superscript a). Closure of the residual AAM budget is indicated by the sum of friction torque (green arrow) + mountain torque (blue arrow) concurring with the sum of wind term derivative (gray arrow) + pressure term derivative (black arrow). Superposition of the ellipsoidal effect (orange arrow, only equatorial) on both the torque and AAM phasors leads to a test of the full budget equation (see text).

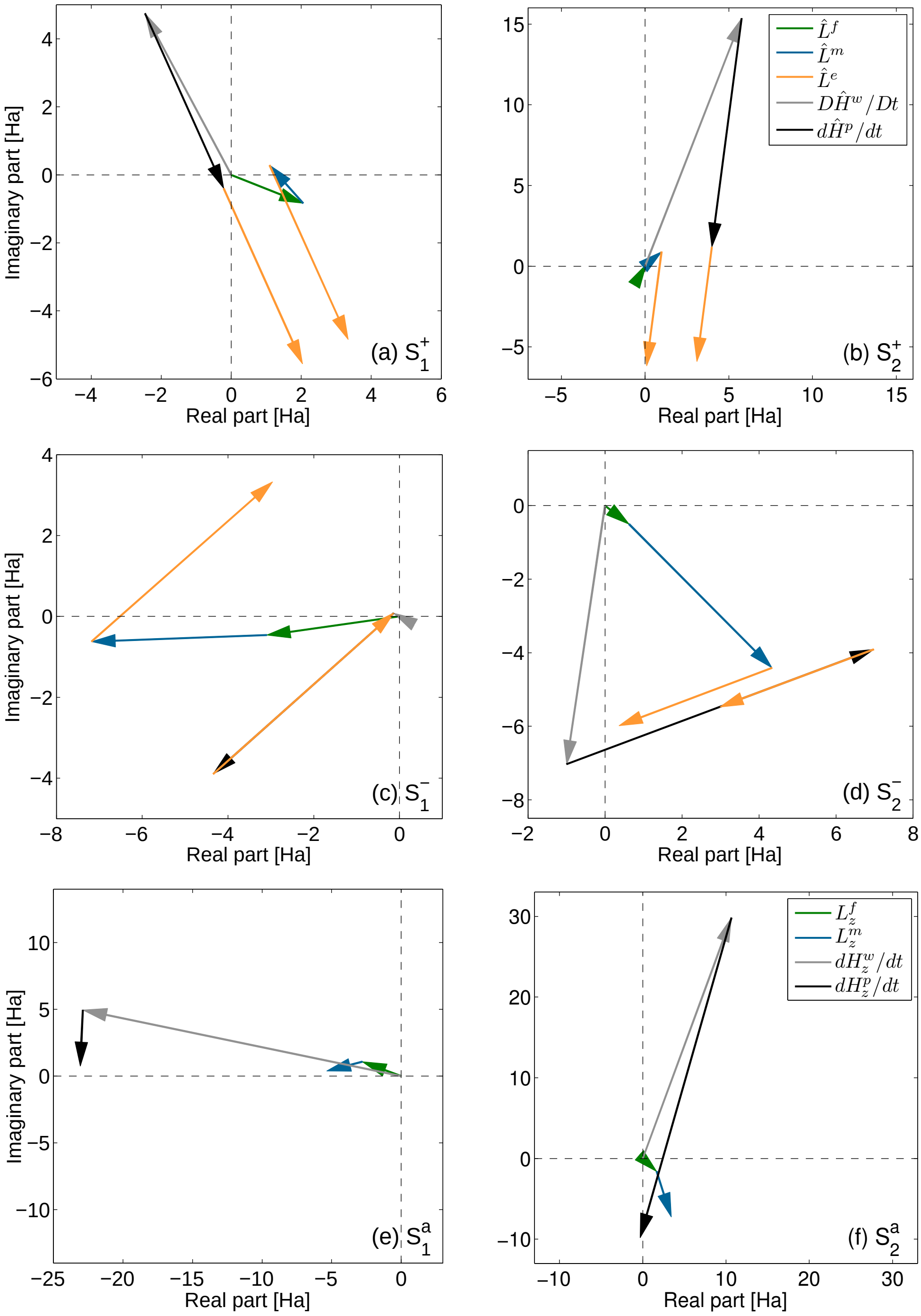

Figure 5.9: Phasor diagrams for the AAM budget verification within MERRA (2007–2011). Detailed description of the plot composition as in Figure 5.8.

produces a phase-shifted wind term derivative of large magnitude ($>$ 10 Ha), resulting in a 40° lead of the AAM tendency over the total torque (Figure 5.10a).

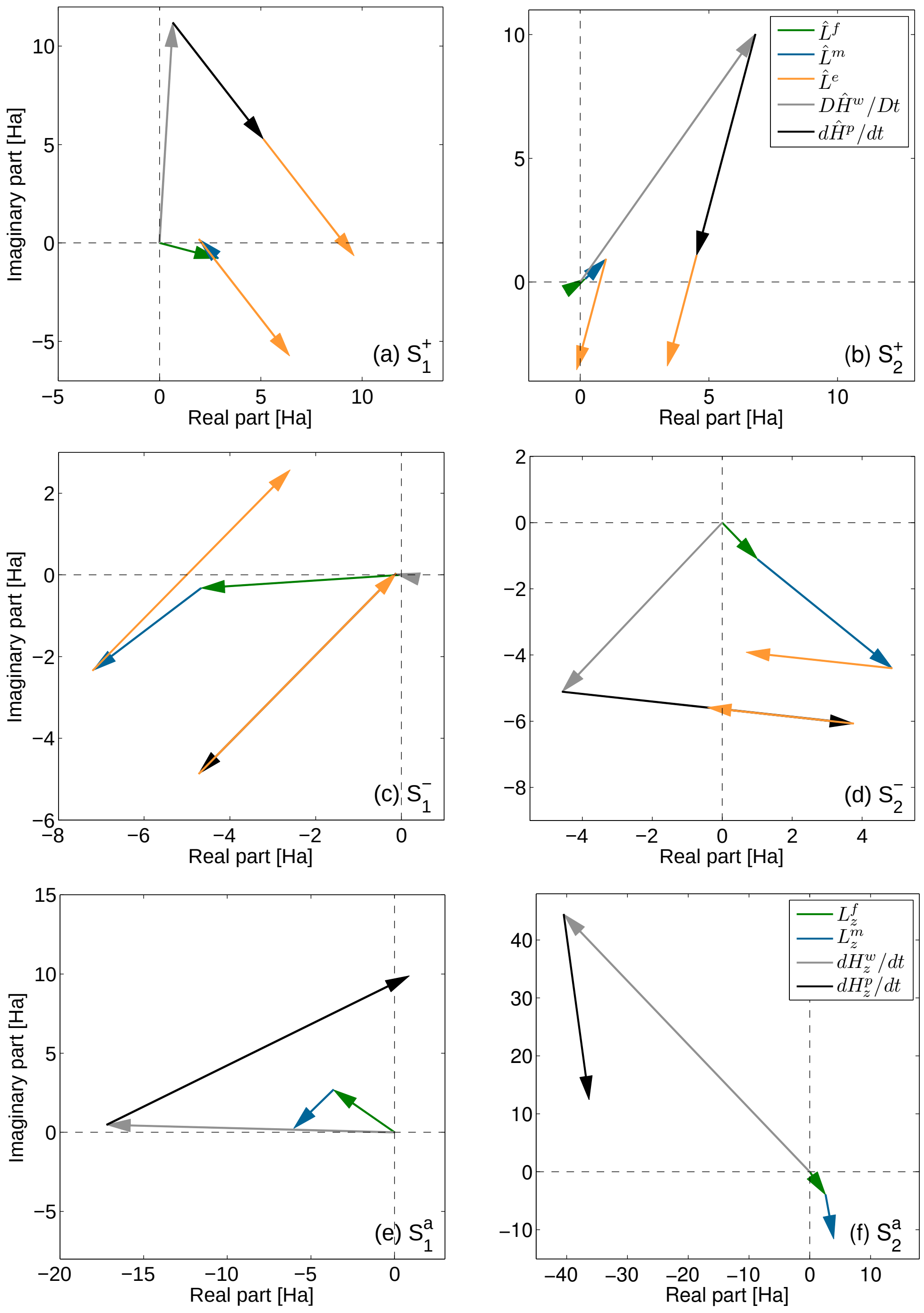

Figure 5.10: Phasor diagrams for the AAM budget verification within ECMWF DC (2007–2011). Detailed description of the plot composition as in Figure 5.8.

Prograde semi-diurnal component

In view of the small mountain and friction torque magnitudes (< 1 Ha) in Figures 5.8b, 5.9b, and 5.10b, validation of the AAM budget at S_2^+ solely depends on the quality of the wind term and the ellipsoidal torque/pressure term. Specifically, if $\hat{L}^f + \hat{L}^m \approx 0$, $\mathrm{d}\hat{H}^p/\mathrm{d}t$ must effectively compensate $\mathrm{D}\hat{H}^w/\mathrm{D}t$ to suffice Eq. (5.5). This requirement is indeed met within MERRA and to a lesser extent also within the DC analysis, where the constellation of phasors closely resembles that of de Viron *et al.* (2005b). For ERA-Interim, a clearly anomalous wind term of amplitude > 20 Ha and a phase disparity of about 120° corrupts the budget comparison and accounts for the markedly low semi-diurnal regression coefficient in Figure 5.5b.

Retrograde diurnal component

As reasoned in Section 3.3.3, the appearance of the AAM balance at S_1^- is characterized by a quasi-zero contribution from both pressure and wind terms. The resulting constraint of the bulge torque having to exactly balance the sum of local torques (Marcus *et al.*, 2004) can be assessed in Figures 5.8c, 5.9c, and 5.10c. In general, all three models tend to fulfill this requirement, as $\hat{L}^f + \hat{L}^m$ and $\hat{L}^e$ exhibit an out-of-phase behavior with respect to each other and their amplitudes of about 7 Ha closely match. For ERA-Interim, the magnitude of the total torque is reduced considerably, by a factor of 2.5 relative to the ellipsoidal torque. This result constitutes the hitherto best balance of retrograde diurnal angular momentum in any atmospheric reanalysis model. MERRA and ECMWF DC perform marginally worse due to torque amplitudes and phases ($\hat{L}^e$ in particular) being slightly different to that of ERA-Interim.

Retrograde semi-diurnal component

In contrast to the above-discussed components, the frequency band of the S_2^- tide accommodates AAM and torque variations of about the same magnitude (de Viron *et al.*, 2005b), enabling a clear crosscheck of both types of excitation measures. Figures 5.9d and 5.10d suggest a well-balanced budget equation for MERRA and ECMWF DC, with the contribution of the mountain torque close to that of $\mathrm{D}\hat{H}^w/\mathrm{D}t$ or $\mathrm{d}\hat{H}^p/\mathrm{d}t$ and even superseding that of the ellipsoidal torque. All AAM-based quantities from ECMWF DC appear to be rotated by approximately 25° with respect to the MERRA results, but otherwise the agreement of both phasor diagrams to that of de Viron *et al.* (2005b, Figure 5) is remarkable. For ERA-Interim (Figure 5.8d), the retrograde semi-diurnal AAM budget is highly deficient, though, cf. the previous assessment of Figure 5.5a. While also the wind term derivative differs from those of the other models, the largest anomaly can be ascribed to the pressure term derivative, of which the amplitude exceeds the MERRA/ECMWF DC predictions by at least a factor of two. This result definitely objects to the generally established opinion of the AAM pressure term being the most robust of all excitation measures (de Viron *et al.*, 2005a; Schindelegger *et al.*, 2013c) on all time scales.

Diurnal axial component

Verification of the axial AAM balance associated with the S_1 tide proves to be an abortive attempt in all three analysis systems (Figures 5.8e, 5.9e, and 5.10e) and one should question the realism of both torque and AAM terms. Some explicit observations to this effect can be made from intercomparing the available phasor diagrams. First, the wind term derivative solutions coincide in phase but differ considerably in their respective amplitudes (17 Ha for ECMWF DC as opposed to 40 Ha for MERRA). Second, even larger discrepancies are discerned for the pressure term derivative, suggesting that present circulation models for the atmosphere have great difficulty in reproducing the small surface pressure modes coupling to Earth's rotational rate, see Section 4.3.1. A possible reasoning for this finding might be twofold, as large, local non-migrating tidal effects complicate a proper representation of the global S_1 modes (Dai & Wang, 1999), and uncertainties in the diurnal hydrological cycle over equatorial landmasses affect the characterization of water vapor heating rates in the troposphere (Section 4.2.5). The sensitivity area of H_z^p is additionally centered above the equator, where conventional meteorological observations are rather sparse. Although the latter argument might also hold for local torques, ERA-Interim, MERRA, and ECMWF DC produce very similar mountain and friction phasors, which attain a cumulative magnitude of 5–7 Ha and agree well with comparative studies (de Viron *et al.*, 2001; Lott *et al.*, 2008). Overall, the ECMWF DC budget comes closest to the simulation results of de Viron *et al.* (2005b), who postulate a perfect counterbalance of pressure and wind term derivatives. This prerequisite represents another intricacy to the validation of the AAM budget equation at S_1.

Semi-diurnal axial component

Analogous to the diurnal band, the cancellation of mass and motion cycles (Section 5.1) has the potential to perturb the balance of semi-diurnal AAM. Notwithstanding this ill-conditioning, Figures 5.8f (ERA-Interim) and 5.9f (MERRA) reveal an excellent closure of the axial budget equation at 2 cpd. Magnitude differences aside, the ERA-Interim phasors in particular match the theoretically predicted AAM derivatives and torque values of Lott *et al.* (2008). With the exception of larger discrepancies for the ECMWF DC analysis (Figure 5.10f), the budget results at S_2 are much more positive than those at S_1, indicating that the semi-diurnal atmospheric circulation in equatorial regions can be better modeled than diurnal phenomena. In this context, the regular structure of the S_2 tide and the absence of strong non-migrating effects (Section 4.1.1) are certainly advantageous. On another note, the displayed mountain and friction torque estimates are consistent among all three models and the reported magnitude of 6 Ha in L_z^m conforms to the value found by Madden *et al.* (1998).

Intermediate Conclusion

Even though an all-around verification of the diurnal and semi-diurnal angular momentum budget has not been achieved, selected components yield an AAM balance that can be considered as unprecedented for atmospheric (re)analysis systems. Among those components are S_1^+ (ERA-Interim, MERRA), S_1^- (ERA-Interim), and S_2^- (MERRA, ECMWF DC) in the equatorial direction as well as S_2 (ERA-Interim, MERRA) in the axial direction. Some of those results are certainly a testament to the improvement of modern circulation models and assimilation systems for the atmosphere, but there is no denying the fact that many inadequacies remain, see for instance the large leakage effects at $S_2^{\pm}$ for ERA-Interim and S_1 (axial) in each of the datasets. Overall, the MERRA model performs best, yielding small residual vectors in all but one component, which in turn point to an acceptable reliability for predicting high-frequency ERP. The superiority of MERRA over the more frequently used ECMWF reanalysis (Brzeziński *et al.*, 2012) contrasts to the long period results of Schindelegger *et al.* (2013c) but might be to some extent a repercussion of GMAO's smooth predictor-corrector scheme IAU which avoids discontinuities between consecutive analysis cycles (as opposed to ERA-Interim and ECMWF DC, see Section 4.2.4). In a brief supplemental investigation to this section, the phasor constellations were also examined at yearly intervals (not shown), leading to a confirmation of the afore-mentioned statements.

5.4 Term-by-term comparison across atmospheric models

An intercomparison of the same types of excitation measures can also shed light on the validity of atmospheric circulation models in the frame of Earth rotation studies, see e.g. Yseboodt *et al.* (2002), de Viron & Dehant (2003), or Masaki (2008). Those studies exclusively focus on either AAM terms or atmospheric interaction torques, though, and if possible, a simultaneous inspection of consistently calculated AAM and torque series in the manner of Schindelegger *et al.* (2013c) should be envisaged. The analyses below present such thorough comparisons at diurnal and sub-diurnal periodicities.

5.4.1 Angular momentum components

The cross-spectral analysis of the three (re)analysis models in terms of AAM pressure and wind portions was conducted analogously to Section 5.2 through incremental extraction and superposition of Fourier coefficients. The resulting correlation coefficients ρ and regression values r at each sampled frequency are shown in Figures 5.11 and 5.12 for the model combinations MERRA/ERA-Interim and MERRA/ECMWF DC, respectively, where both ECMWF models were regressed against MERRA. Consistent with the findings of Schindelegger *et al.* (2013c), the pressure terms (i.e. ellipsoidal torques) display an impeccable agreement in both equatorial and axial directions outside the diurnal band, while the correlation and regression level of the equatorial wind terms is located at about 0.9. Below those periodicities, at $|\nu_e, \nu_a| > 0.3$ cpd, a marked decrease in agreement can be recognized for all components, as for most frequency bands only noise-related oscillations are present, recall Figures 5.2 and 5.4. Significant peaks in ρ and r relate either to radiational tides or to atmospheric normal modes $\left(\psi_1^1, \xi_2^1\right)$. In the tidal bands, the main observations from the phasor comparisons in the previous section reappear, most notably a deficient ERA-Interim pressure term at S_2^-, an out-of-phase behavior of the ERA-Interim wind term at S_2^+ $(\rho, r \approx -0.3)$, as well as a clear discord of all models with regard to the pressure term phasor and the wind term magnitude at 1 cpd in the axial direction. The agreement of the remaining components is, however, fairly acceptable, with correlation and regression values

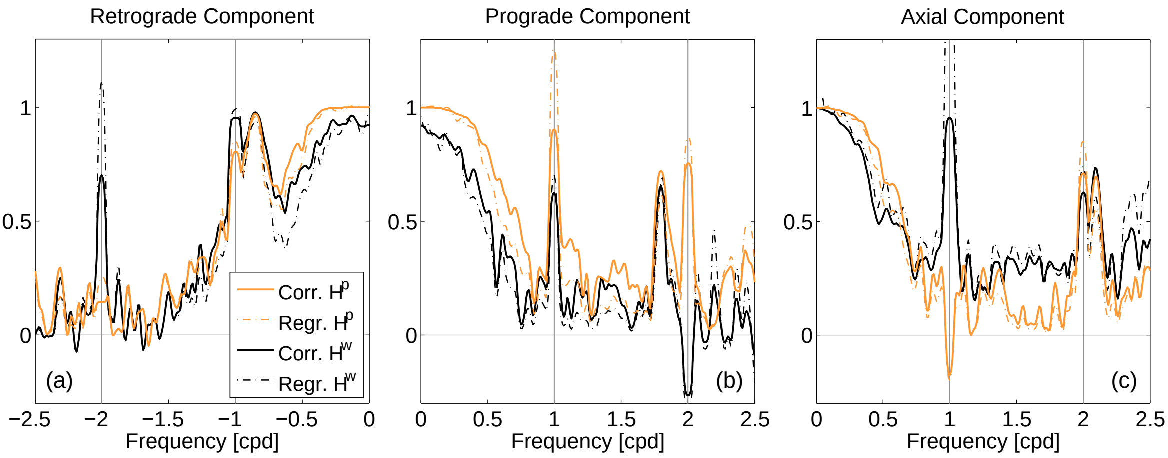

Figure 5.11: Frequency-dependent correlation coefficients (solid curves) and regression values (dashed curves) between MERRA and ERA-Interim in terms of the AAM pressure portion (orange curves) and AAM wind portion (black curves). Results shown for equatorial retrograde (a) and prograde (b) frequencies as well as the axial component (c).

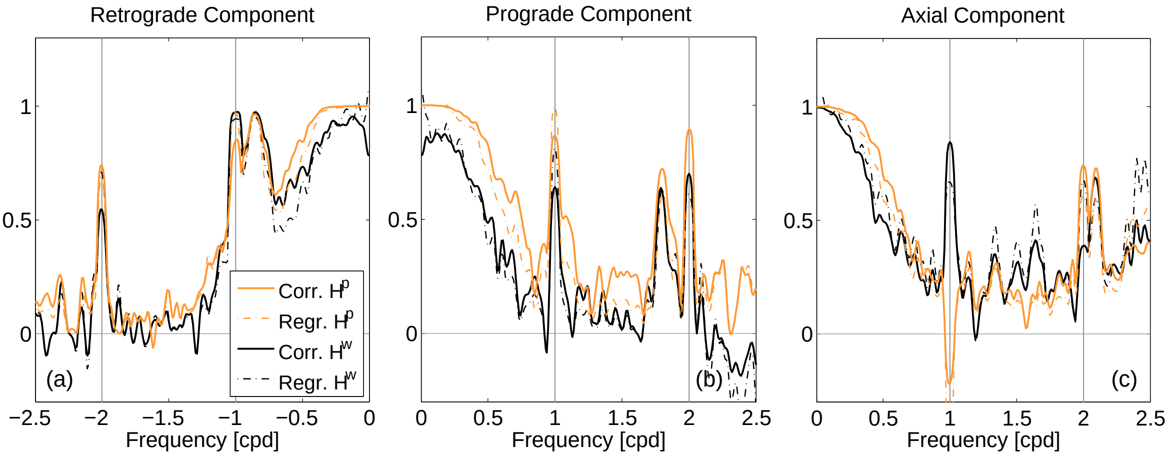

Figure 5.12: Frequency-dependent correlation coefficients (solid curves) and regression values (dashed curves) between MERRA and ECMWF DC in terms of the AAM pressure portion (orange curves) and AAM wind portion (black curves). Results shown for equatorial retrograde (a) and prograde (b) frequencies as well as the axial component (c).

generally located above 0.6 and approaching 1 in particular for the MERRA/ECMWF DC cross spectra, thus exceeding the match obtained by de Viron & Dehant (1999).

In order to underline some of those findings, Figure 5.13 juxtaposes the AAM phasors of all three models at selected frequencies ($S_2^{\pm}$ and S_1 axial), including both the mean values from 2007 to 2011 as well as yearly estimates of pressure and wind terms. The scatter of each component serves as an indication of the time variability of excitation measures, which is not specifically discussed in the present thesis. Larger-magnitude signals in either $\boldsymbol{H}^p$ or $\boldsymbol{H}^w$, such as the ERA-Interim phasors of the equatorial pressure term or the axial wind term, are generally equipped with a slightly smaller scatter of about 10° phase variability. Otherwise, the year-to-year changes of each component diverge from one model to the other, suggesting that they are rather expressions of the models' uncertainties than of any detectable physical phenomenon. Figure 5.13 also exposes the tendency of ERA-Interim to produce pressure and wind terms that differ either in phase or in magnitude from the other available solutions (at least in the frequency bands depicted).

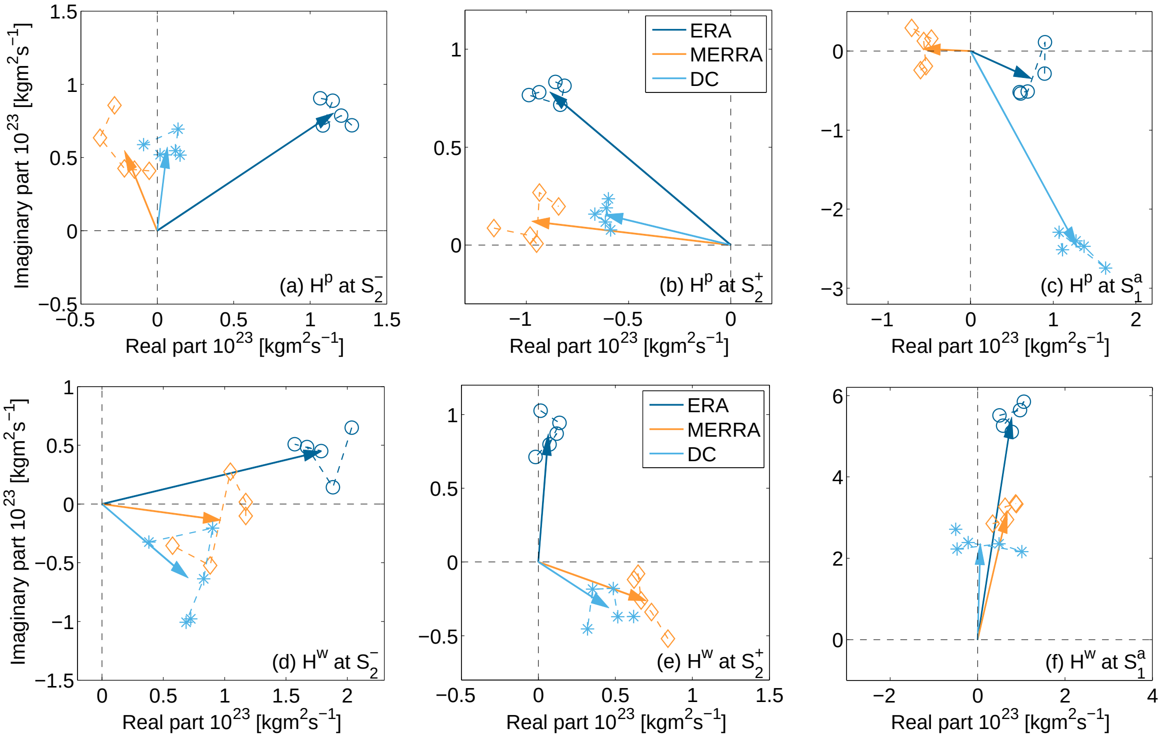

Figure 5.13: Phasor diagrams of pressure term (upper half) and wind term (lower half) estimates at S_2^- (a,d), S_2^+ (b,e), and S_1 in the axial direction (c,f). Results shown for ERA-Interim (blue arrows), MERRA (orange arrows), and ECMWF DC (turquoise arrows) both as averages from 2007 to 2011 (solid lines) as well as in yearly intervals (dashed lines and markers).

Parts of the inconsistencies between the utilized models are related to the smallness of the underlying geophysical signal. As argued by de Viron *et al.* (2005b) and also in Section 4.3.1, the predominant axial symmetry of S_1/S_2 pressure and wind effects does not favor AAM changes, and only small oscillations in the order of a few Pa and cm/s couple to variations in Earth rotation. To study the models' differences on this rather residual level, decompositions into spherical harmonics or wave numbers (Kadow *et al.*, 2012) are usually accomplished, but also analyses of the grid point-wise AAM contributions have been conducted (Masaki, 2008; Schindelegger *et al.*, 2012). Here, the latter approach is deployed using the example of the retrograde semi-diurnal mass term, which appears to be anomalous in the case of ERA-Interim.

In order to obtain a (mainly) qualitative illustration of how local and regional model differences in surface pressure account for the S_2^- phasor disagreement in Figure 5.13a, the semi-diurnal ($n = 2$) tidal components $\{a_2(\theta,\lambda), b_2(\theta,\lambda)\} = \{A_2\cos(\varphi_2), A_2\sin(\varphi_2)\}$ (Eq. 4.2) of each model were determined on a 1° grid from the respective surface pressure records in 2011, see also Section 4.2.5. Multiplication of those fields with the trigonometric weighting functions of equatorial pressure terms

$$\begin{pmatrix} W_x^p \\ W_y^p \end{pmatrix} = \begin{pmatrix} \cos\theta\sin^2\theta\cos\lambda \\ \cos\theta\sin^2\theta\sin\lambda \end{pmatrix} \tag{5.6}$$

corresponds to a separation into $\{x, y\}$-specific sin- and cos-components

$$\begin{pmatrix} x_2^c(\theta,\lambda) \\ y_2^c(\theta,\lambda) \end{pmatrix} = a_2(\theta,\lambda)\begin{pmatrix} W_x^p \\ W_y^p \end{pmatrix}, \quad \begin{pmatrix} x_2^s(\theta,\lambda) \\ y_2^s(\theta,\lambda) \end{pmatrix} = b_2(\theta,\lambda)\begin{pmatrix} W_x^p \\ W_y^p \end{pmatrix}, \tag{5.7}$$

from which grid point-wise phasors at pro- and retrograde terrestrial frequencies were deduced by means of Eq. (6.22). This analytical detour is admittedly unconventional but the resulting weighted surface pressure Fourier coefficients $\hat{p}_s(\theta,\lambda)$ at S_2^- directly relate to the mass term phasor of each model in Figure 5.13a. Specifically, $\hat{H}^p$ follows from global summation of the local phasors at increments $\mathrm{d}\theta, \mathrm{d}\lambda$ and a subsequent scaling to AAM values, cf. Eq. (3.18).

Figures 5.14a and 5.14c present the grid point-wise amplitude of residual signals in $\hat{p}_s(\theta,\lambda)$ for both ECMWF models with respect to the MERRA grid, which was subtracted on both occasions. At locations of differential magnitudes exceeding 3.5 Pa, the plots are augmented by a representation of the actual phasor deviations from the MERRA model. Besides the suppression of equatorial and polar mass distributions via $W_{x,y}^p$, the primary observation is that even the largest model differences are below a level of only 8 Pa. Consistent with the significant deviation of the ERA-Interim pressure term from the MERRA estimate at S_2^-, the local amplitude differences are markedly larger in Figure 5.14a (global mean at 1.6 Pa) than in Figure 5.14c (global mean at 1.1 Pa), with particular anomalies found over the northern hemispheric oceans, central and southeast Asia, as well as the coastal regions of Chile and South Africa. The allocated phasors mostly agree in phase and thus produce a considerable net effect for each latitude circle, as apparent from the zonal mean profile in Figure 5.14b. On the contrary, noticeable inconsistencies between ECMWF DC and MERRA are restricted to the northern Pacific and the Near East, for which the local phasors largely compensate each other. Their zonally averaged values (Figure 5.14d) are below 0.4 Pa, which is in stark contrast to the ERA-Interim results. Overall, the smallness of the involved effects elucidates the difficulties for current atmospheric (re)analysis models to produce coherent pressure term signals. A similar finding could be, in principle, obtained by extending the above analysis to the diurnal component in axial direction, which is sorely affected by the uncertainties in equatorial and non-migrating surface pressure oscillations, see Section 4.2.5.

5.4.2 Local torque components

With the bulge torque being equivalent to the AAM pressure term, only mountain and friction torques need to be crosschecked in the remainder of this section. The corresponding correlation

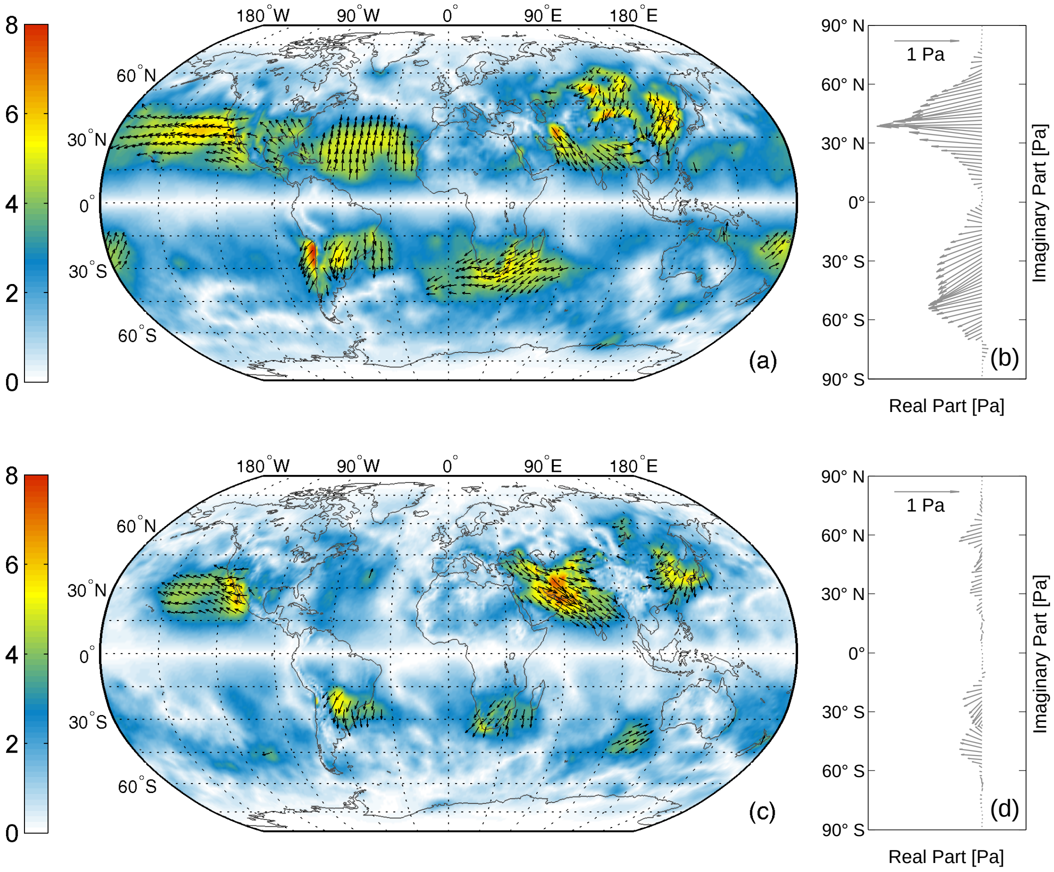

Figure 5.14: Differences between ERA-Interim and MERRA (a,b) as well as ECMWF DC and MERRA (c,d) in terms of surface pressure signals that couple to the retrograde semi-diurnal part of the equatorial matter term (see text). Amplitude of differences in units of Pa and residual phasors shown on a global map (a,c) and complemented by zonal mean phasor profiles (b,d).

and regression spectra for the two model combinations already utilized (ERA-Interim/MERRA and ECMWF DC/MERRA) are presented in Figures 5.15 and 5.16, showing a collectively good agreement between $\boldsymbol{L}^m$ and $\boldsymbol{L}^f$ from different sources. On a closer look, the results for the high-frequency mountain torque series are particularly remarkable. First, the drop from a correlation/regression level of practically 1.0 can be located at $|\nu_e, \nu_a| \approx 0.6$ cpd, i.e. at a frequency twice as high as in the AAM case (Figures 5.11 and 5.12). Second, with the exception of the equatorial ERA-Interim/MERRA cross spectra at S_2^+, values of ρ are above 0.7 at all tidal bands, and scale factors are limited to a range of $r \in [0.6; 1.4]$. Third, a close to perfect correlation is evident for two bands influenced by the semi-diurnal surface pressure tide: S_2^- (equatorial) and S_2 (axial), of which the phasor diagrams are depicted also in Figures 5.17b and 5.17c. This slight superiority above the diurnal band presumably relates to the smoother, zonally-symmetric wave pattern of the S_2 tide, which, as a first-order effect, is likely to be reproduced in the same manner by each (re)analysis model. In this respect, the small-scale variability of pressure signals

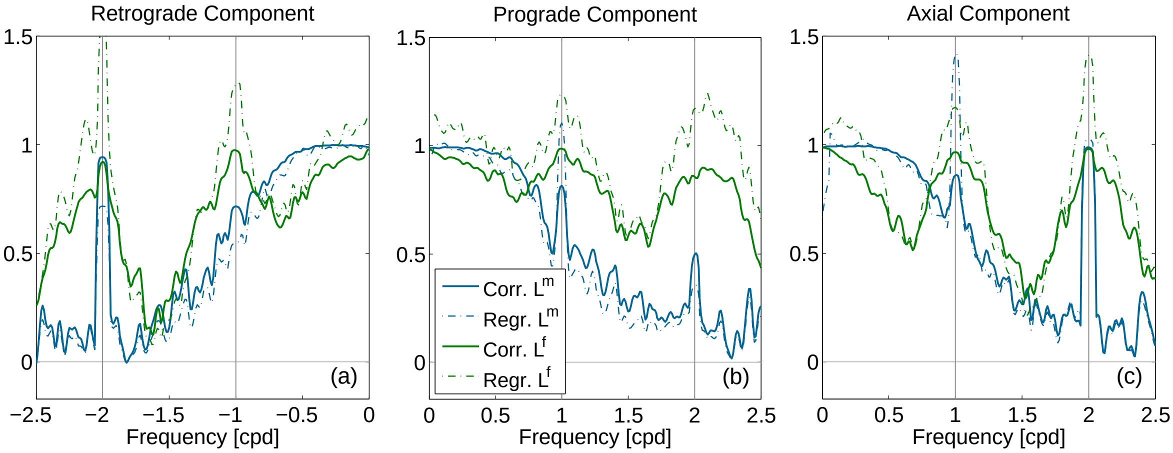

Figure 5.15: Frequency-dependent correlation coefficients (solid curves) and regression values (dashed curves) between MERRA and ERA-Interim with regard to mountain torques (blue curves) and friction torques (green curves). Results shown for equatorial retrograde (a) and prograde (b) frequencies as well as the axial component (c).

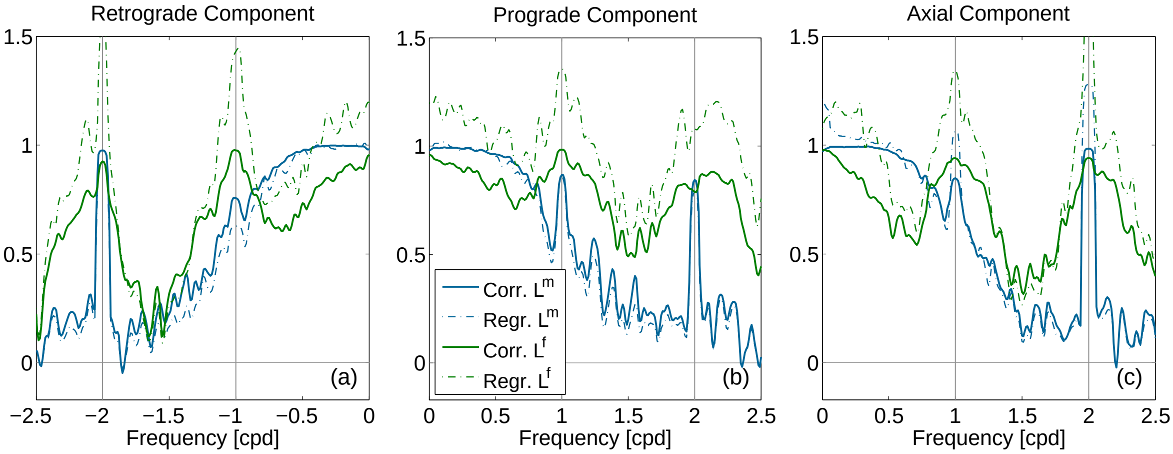

Figure 5.16: Frequency-dependent correlation coefficients (solid curves) and regression values (dashed curves) between MERRA and ECMWF DC with regard to mountain torques (blue curves) and friction torques (green curves). Results shown for equatorial retrograde (a) and prograde (b) frequencies as well as the axial component (c).

associated with non-migrating effects in S_1 has the potential to perturb the globally integrated mountain torque (de Viron & Dehant, 2003). However, Figures 5.15 and 5.16 do not confirm this conjecture, which is a very positive result, also in face of the different horizontal resolutions of ECMWF and MERRA surface pressure grids (0.5° and 1.25°, respectively). From a qualitative point of view, some of the above statements can also be reasoned by recalling the preliminary model comparison in Section 4.2.5. In Figure 4.4, the main disparities in surface pressure have been found in regions of rather flat terrain, e.g. Central Africa, Siberia or even over the oceans (S_2). Given that those differences in p_s must be weighted with the gradient of topography, the corresponding effect in $\boldsymbol{L}^m$ is naturally small. Yet, MERRA's diurnal tide across Peru and Bolivia differs from the ECMWF solutions by about 60 Pa, and that certainly transfers to both the zonal and meridional component of the mountain torque due to the vicinity of the Andes (de Viron *et al.*, 2001). The 40° phase lag of the MERRA phasor in Figure 5.17a and the reduced correlation coefficients in the retrograde diurnal band ($\rho = 0.72 - 0.76$) might be explained in this vein.

The intercomparison of the friction torque series in Figures 5.15 and 5.16 yields a high level of correlation above 0.9 for all diurnal and semi-diurnal frequencies except S_2^+. In contrast to all other excitation components, the spectral peaks are markedly broad, pointing to an increased signal-to-noise ratio in the proximity of tidal bands, cf. the axial torque spectrum in Figure 5.3. Similar to Schindelegger *et al.* (2013c), the regression results suppose that both ECMWF models tendentially produce larger friction torque amplitudes than MERRA by about 40–70% and mostly at semi-diurnal periods, see also the phasor plots in Figures 5.17d–5.17e. A comparison to the L_z^f values of Madden *et al.* (1998) favors the enhanced magnitude of the ECMWF solutions. However, definite conclusions—both on this scale issue as well as on the remarkably high correlation—need to acknowledge that any friction torque solution is less supported by direct observations of surface winds but instead mainly controlled by the implemented physical equations and the

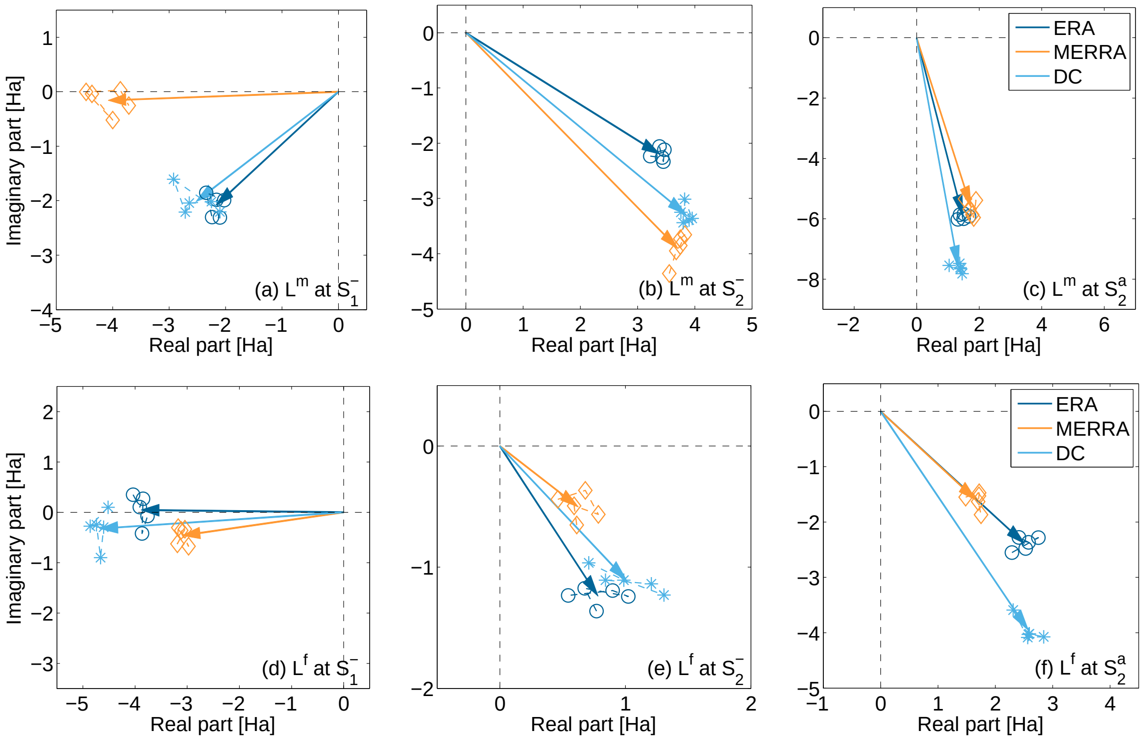

Figure 5.17: Phasor diagrams of mountain torque (upper half) and friction torque (lower half) estimates at S_1^- (a,d), S_2^- (b,e), and S_2 in the axial direction (c,f). Results shown for ERA-Interim (blue arrows), MERRA (orange arrows), and ECMWF DC (turquoise arrows) both as averages from 2007 to 2011 (solid lines) as well as in yearly intervals (dashed lines and markers).

model's parametrization scheme (Dee *et al.*, 2011).

Judging from the aggregate of numerical results, the bottom line of this section is an excellent agreement of present-day circulation models/assimilation systems in terms of diurnal and semi-diurnal local torques, surpassing the match in terms of consistently calculated AAM quantities or ellipsoidal torques, respectively. First and foremost, this finding testifies the ongoing convergence of atmospheric models even at the highest frequencies, but it also represents a partial rebuttal to the general scientific consensus of torque estimates being less stable and reliable than AAM terms. While such an assessment probably holds for longer period excitation processes, the particular weakness of the AAM approach at 1 and 2 cpd consists in matter and motion terms being insensitive to the first-order effect of migrating tidal components. Instead, only modes of significantly reduced magnitude are capable of producing a non-zero AAM net effect after global summation. On the contrary, local torques almost solely arise from the action of the primary migrating modes, either over the oceans (friction torque) or across steeply sloping terrain (mountain torque). Cancellation amongst the torque signals from different regions is potentially introduced via the geographical distribution of specific mountain ranges and/or water surfaces, but no evidence of such an effect has been obtained. On balance, the collected results certainly justify to utilize torques as complementary tools to the angular momentum method.

Chapter 6

An independent pressure term estimate from global barometric observations

Discrepancies in the diurnal and semi-diurnal pressure term estimates from various meteorological centers are well-documented in literature (Brzeziński *et al.*, 2002, 2004; Schindelegger *et al.*, 2011), and the preceding chapter has shown that even the currently most accurate reanalysis systems can disagree in terms of the exact amplitude and phase values of S_1 and S_2 in particular components of the AAM vector. It thus stands to reason to seek for auxiliary information which may be used to crosscheck model-based pressure terms. As anticipated from Section 4.3, such a validation can be conducted on the basis of harmonic analyses of long-term in-situ barometric measurements. The following chapter describes the technical details of the prerequisite data processing before placing the emphasis on the fit of spherical harmonics to the globally distributed tidal estimates.

6.1 Processing strategies for in-situ pressure data

The merits of having ISPDv2 as quality-controlled pressure data compilation have been introduced in Section 4.3.2. Both its land and marine component should be utilized to ensure the best possible global network of S_1 and S_2 tidal coefficients. However, barometric observations over the oceans originate from infrequent recordings of moving objects (ships and buoys), and are believed to yield pressure tide harmonics of low reliability (Ray, 2001). The handling of those data is thus separated from that of the conventional station-based measurements.

6.1.1 Station observations of surface pressure

Datasets

A unified analysis period from January 1990 to December 2010 was adopted across the globe but extended retrospectively for poorly sampled polar regions. Table 6.1 summarizes the main specifications of the resulting three ISPDv2 subsets.

Table 6.1: Specifications of the surface reports extracted from ISPDv2.

	Colatitude band	Temporal coverage	Data volume
Arctic	$\theta = 0°–20°$	1950–2010	1.8 GB
Mid-latitudes and tropics	$\theta = 20°–138°$	1990–2010	107.9 GB
Antarctic	$\theta = 138°–180°$	1900–2010	1.4 GB

The extracted data basically represent a listing of surface and sea level pressure observations in chronological order, with each entry noted together with the ID and location of the recording station as well as meta data coming from the assimilation and quality control procedures within the 20CRv2, see McColl *et al.* (2011). This includes quantities such as the ensemble mean analysis pressure or the interpolated pressure value at the model surface. Here, only the raw and unmodified observations were analyzed in order to construct a pressure tide model that is independent from any analysis system and the physics of general circulation. The one essential parameter retained from the meta data is called *usability check for reanalysis* and signifies whether the specific observation passed all 20CRv2 quality criteria except the process of data thinning. Anomalous pressure values, such as those introduced by severe storms or malfunctioning sensors, were thereby excluded from further processing steps. As an example, station *Alfred Faure*, one of the few islands in the southern Indian Ocean at $\theta \approx 136.4°/\lambda \approx 51.9°/h = 146$ m, has 2.2% of its observations during 1997–2004 rejected, nine of which are below 920 hPa and are thus indisputable outliers.

Selection of stations

The tedious task of allocating the pressure data to each individual station was solved by means of a station ID compilation available from Compo (2013). As this file contains more than 112,000 entries, an appropriate subset had to be chosen based on the requirement of at least 4 yr of observational coverage. (Note that the cited observation times are only indicative values of the actual coverage without any information on the data frequency at every site.) This criterion yielded 13,155 separate stations, according to which the pressure data files were dissected. Unfortunately, each single station ID within ISPDv2 is allowed to comprise several barometers with slightly different locations and/or observation types (surface or sea level pressure). The highest number of such subsets was 11, which occurred at *Yakutat State Airport*, Alaska. From this ensemble, the one barometer series providing the most reliable pressure tide signal was eventually selected during the harmonic analysis in the next steps.

Screening of time series

A range of tests and constraints was designed to check the principal usability of each barometer series for the estimation of diurnal and semi-diurnal signals:

1. No station observes continuously with invariant sampling, and therefore data gaps up to

a certain threshold had to be accepted. The maximum gap length was set to 20 d, which is still tenable with regard to the elimination of the seasonal pressure tide variability (cf. Section 4.3.2), and also permits stations in remote places with frequent operational breaks to contribute to an optimal global network.

2. Taking into account those gaps, each station should at least have 3 yr of data. This value is clearly sufficient to obtain representative annual averages of S_1 and S_2, see the case study of Mass *et al.* (1991) over the United States. Dai & Wang (1999) used a lower bound of 4 yr to accommodate also the seasonal modulations of the surface pressure tides.
3. The approximate data frequency was judged from the length of each time series. Stations with record lengths below 5000 (corresponding to an average sampling rate of roughly 6 h over 3 yr) were dropped.

Fourier decomposition

Non-uniform sampling intervals prohibit the use of standard methods (bandpass filtering or discrete Fourier transform) to extract diurnal and semi-diurnal pressure variations at each station. The chosen alternative procedure was to average the pressure values that occur at the same time of a day, thus ‘stacking’ the entire time series to a daily mean cycle. Such a data analysis is equivalent to a discrete Fourier transform for the case of evenly distributed observations and has been deployed in previous studies (Madden *et al.*, 1998; Mass *et al.*, 1991). Two final requirements were imposed on the mean day composite. First, only epochs that allocated a significant number of observations were retained in order to prevent infrequently sampled epochs to distort the subsequent fit of tidal harmonics. The chosen threshold was $n_e = 500$, which is about 50% of the highest possible amount of observations for any specific epoch over the course of 3 yr ($3 \cdot 365 = 1095$ samples). Second, at least six epochs, three of them each half-day, were required to come through all tests and form the observables for the least squares adjustment of diurnal and semi-diurnal harmonic coefficients $\{a_1, b_1, a_2, b_2\}$ in

$$p_s(t) = a_0 + S_1(p_s) + S_2(p_s) = a_0 + \sum_{n=1,2} a_n \cos(nt) + b_n \sin(nt) \ , \tag{6.1}$$

which is equivalent to Eq. (4.2) except for the inclusion of a daily mean pressure in a_0. Even though all pressure values were reduced by a cumulative mean over the length of the time series prior to stacking, other long-term artifacts, presumably related to data gaps or spurious monthly drifts (Mass *et al.*, 1991), have to be accounted for. Here, a_0 absorbs those effects and improves the fit of tidal harmonics, cf. also Dai & Wang (1999).

The proposed sets of minimum constraints in retrieving mean day composites is not universally applicable throughout the full station compilation and was in fact conceived to *a priori* eliminate records which are unsuitable for producing reliable pressure tide harmonics. At eligible stations, the constraints were allowed to be tightened so as to account for the characteristics of each barometer time series. Most of those changes concerned the minimum count of observa-

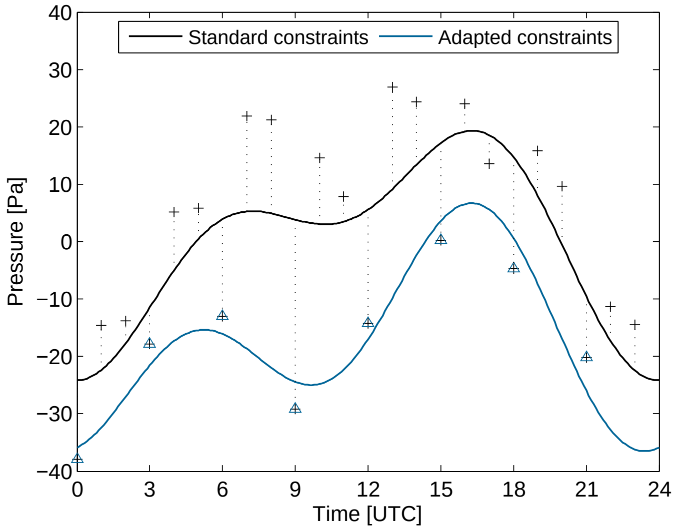

Figure 6.1: Fit of pressure tide harmonics at station *Fort Chipewyan*, Alberta, based on two different mean day composites: (1) that obtained from applying the standard constraints as given in the text, i.e. $n_e = 500$ observations (black crosses); (2) that obtained from setting n_e to 2000 (blue triangles). The offset of the second composite was adjusted so that common observables in (1) and (2) indeed coincide.

tions amassed for each epoch (n_e), an example of which is given in Figure 6.1 for station *Fort Chipewyan*, Alberta. The mean day composite based on standard constraints is markedly scattered and yields pressure tide harmonics of large uncertainty. Choosing $n_e = 2000$ retains only the statistically most significant averages at the eight synoptic hours (0, 3, 6, 9 UTC, etc.) and leads to a more reliable fit of Eq. (6.1). Overall, the correct choice of parameters at all sites can only be made manually, by plotting the observables, judging the first guess fit, and, if necessary, fine-tuning the initial constraints. This strategy is labor-intensive but it also makes the final station tide compilation far superior to that of Dai & Wang (1999).

Throughout the analysis, surface pressure observations were preferred to SLP reports, as bogus diurnal and semi-diurnal signals can be easily introduced when pressures are reduced to sea level by means of an imperfect temperature-averaging scheme (Mass *et al.*, 1991). Stations with SLP sensors only (common across the United Kingdom, India, Florida, or New Zealand) were examined for their elevation and rejected if located above 100 m. High-terrain surface pressure observations are typically included in a global analysis (Ray, 2001), what might appear obstructive to the idea of spherical harmonic expansion. However, there is no apparent systematic height dependence in the amplitude of pressure tides as represented by the ISPDv2 data.

Discussion of the surface station compilation

The retrieved network, implicitly shown in Figures 6.5 and 6.6 encompasses a total of 3565 continental and island barometers, with 286 sites located above 1000 m. While the coverage is

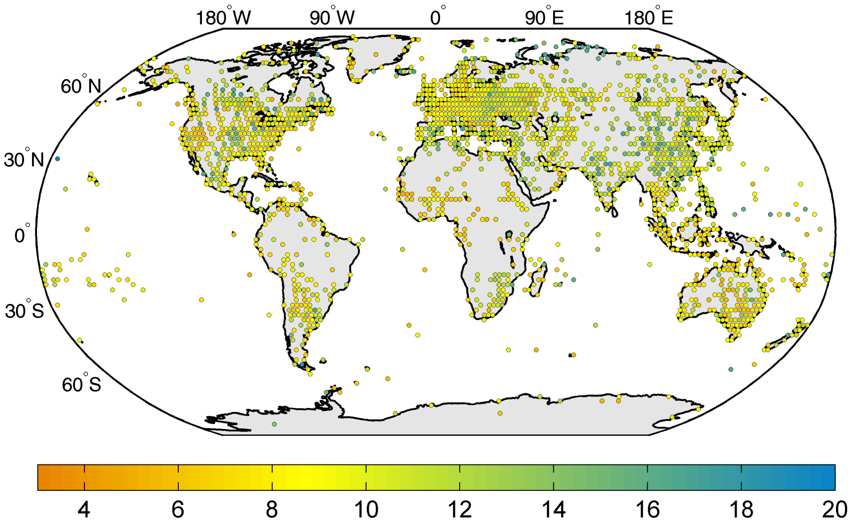

Figure 6.2: Length of time series in integral number of years, on the basis of which S_1 and S_2 pressure tide harmonics were determined for 3565 land stations. To support the comprehensibility of the plot, only average values in 2.0° × 2.0° cells are shown.

sparse over the Antarctic and other relevant regions such as the Amazon Basin or central Africa, the northern hemisphere holds clusters across Europe, southeast Asia, and the eastern United States, as one would expect. This imbalance is one of the main reasons for processing also marine observations in the subsequent section. Figure 6.2 illustrates the length of the analyzed barometer time series on a global map, with data in densely sampled areas averaged to 2.0° × 2.0° cells. The median time series length computed from all 3565 stations is 7 yr, the longest three records span 20 yr (station *Midway Islands*, north Pacific) and 18 yr (stations *Punta Arenas*, Chile, and *Svalbard*, Spitzbergen).

The internal consistency of the produced 'ground truth' tides is unprecedented in comparison to earlier compilations, as can be seen from computing the RMS differences of S_1 (or S_2) cycles at any two neighboring stations within a specified distance. Ray (2001) conducted such an analysis at the semi-diurnal frequency for his own dataset and that of Dai & Wang (1999), obtaining RMS differences of 12.9 Pa (200 km search radius) and 32.0 Pa (30 km search radius), respectively.

Table 6.2: Internal consistency of the station tide compilations from (1) Dai & Wang (1999), (2) Ray (2001), and (3) this study.[a]

Search radius	Dataset	$S_1(p_s)$	$S_2(p_s)$	Station pairs
30 km	This study	7.3	6.7	336
	Dai & Wang (1999)	-	32.0	2084
200 km	This study	10.9	6.5	13580
	Ray (2001)	-	12.9	176

[a] Judged on the basis of RMS differences [Pa] between neighboring stations.

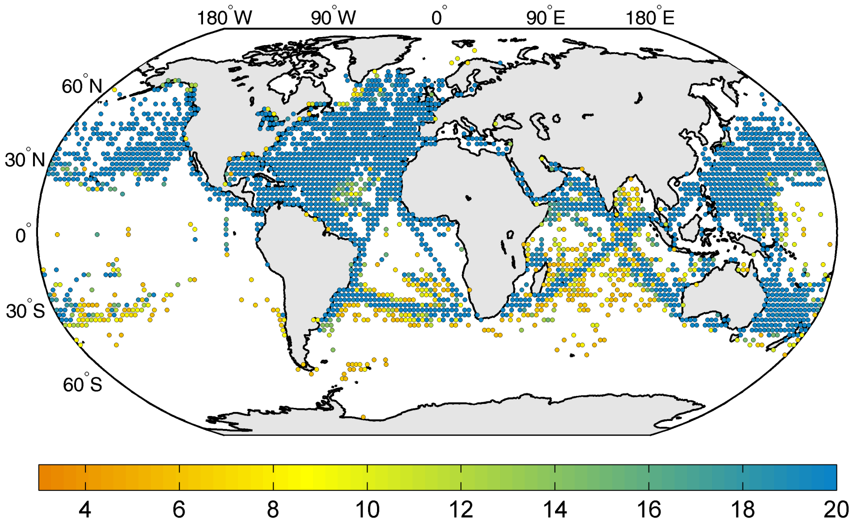

Figure 6.3: Length of time series in integral number of years, on the basis of which S_1 and S_2 pressure tide harmonics were determined for 2924 ocean boxes.

Table 6.2 summarizes these values and includes the results from an analogous analysis of the present S_1 and S_2 compilation, applying search radii of both 30 and 200 km. The RMS reduction down to a level of 6.5–6.7 Pa at S_2 is exceptional and encourages the use of the retrieved data for looking into the small tidal modes coupled to Earth rotation variations (recall Section 4.3.1). Slightly increased but generally comparable RMS differences are apparent at the diurnal cycle.

6.1.2 Marine observations of surface pressure

Test computations during the preparation of this study showed that an unambiguous determination of a climatological (time-invariant) pressure term vector is difficult to achieve from station tide estimates alone. Specifically, the imbalance in the density of observations between both hemispheres clearly impairs a well-conditioned expansion into spherical harmonics up to a certain degree and order. This deficiency can be partly rectified by inclusion of tidal harmonics estimated on the basis of marine observations.

Data processing

The handling of the ISPDv2 marine data for the period January 1990 to December 2010 accounts for both the sparseness of sub-daily pressure observations over the oceans and the fact that the reporting ships and buoys do not have fixed locations. Following Dai & Wang (1999), all observation files were screened sequentially and, by reference to the given latitude/longitude information, every entry was assigned to a cell of size 2.0° × 2.0°. (In retrospect, such an approach could have been also feasible for the barometric data from land stations.) Each ocean box thus assembles multiple pressure observations at individual epochs, with the accepted phase

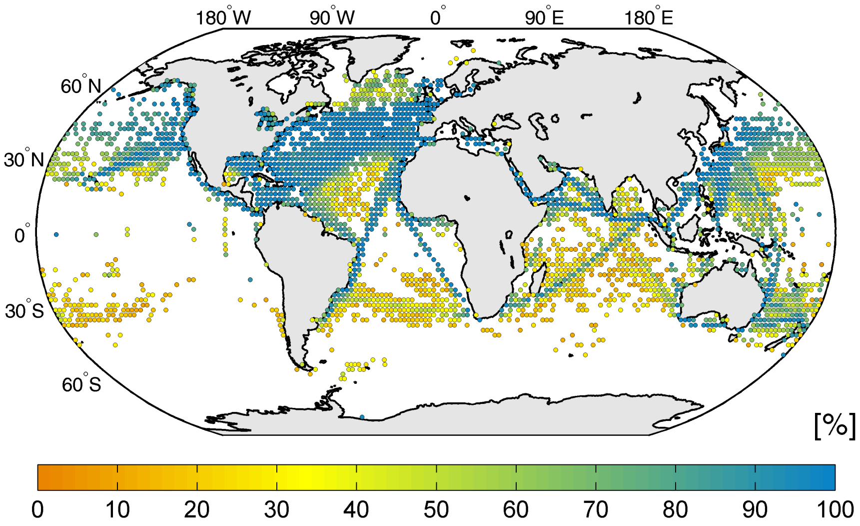

Figure 6.4: Total count of days containing sub-daily pressure observations for each of the 2924 ocean boxes. Numbers expressed as fraction of the observational time span as displayed in Figure 6.3 but converted to days.

differences (2.0°, corresponding to 16 min at 2 cpd) being markedly smaller than the uncertainty introduced by the sampling interval (±30 min for hourly sampling of S_2). As a second adaptation, the minimum constraints imposed on each pressure time series and its mean day composite were considerably loosened in an attempt to obtain tidal estimates even for remote areas with infrequent maritime traffic. Trial and error computations yielded a largest possible gap of 100 d and 500 pressure recordings over a minimum duration of 3 yr. The sample count per epoch is therefore $n_e = 50$ (cf. Section 6.1.1), which is a statistically far less significant value than that for the case of station data. S_1 and S_2 harmonics from ocean boxes are therefore indeed less reliable quantities (Ray, 2001), susceptible to the distortions from unresolved tidal time variability.

Discussion of the marine network of pressure tides

An otherwise analogous processing to Section 6.1.1—including the manual inspection of the harmonic fit at each 2.0° cell—resulted in a network of 2924 ocean boxes, see any of Figures 6.3, 6.4, or 6.5. The dependency on major ship routes is readily apparent (Woodruff *et al.*, 1987), leading to a good coverage of the entire Atlantic, the Indian Ocean, as well as the northern and westernmost regions of the Pacific. Almost no data points were retained in the Subantarctic and the east Pacific, with only 1057 of all boxes located on the southern hemisphere.

Figures 6.3 and 6.4 provide insight into the characteristics of the time series from which tidal harmonics were extracted. The largely loosened constraints in the above processing have two repercussions here. First, about 73% of the ocean box records span exactly 20 yr as a result of the large data gaps allowed (Figure 6.3). Second, the number of days containing sub-daily pressure observations, reckoned as fraction of the entire time series length, can drop to uncom-

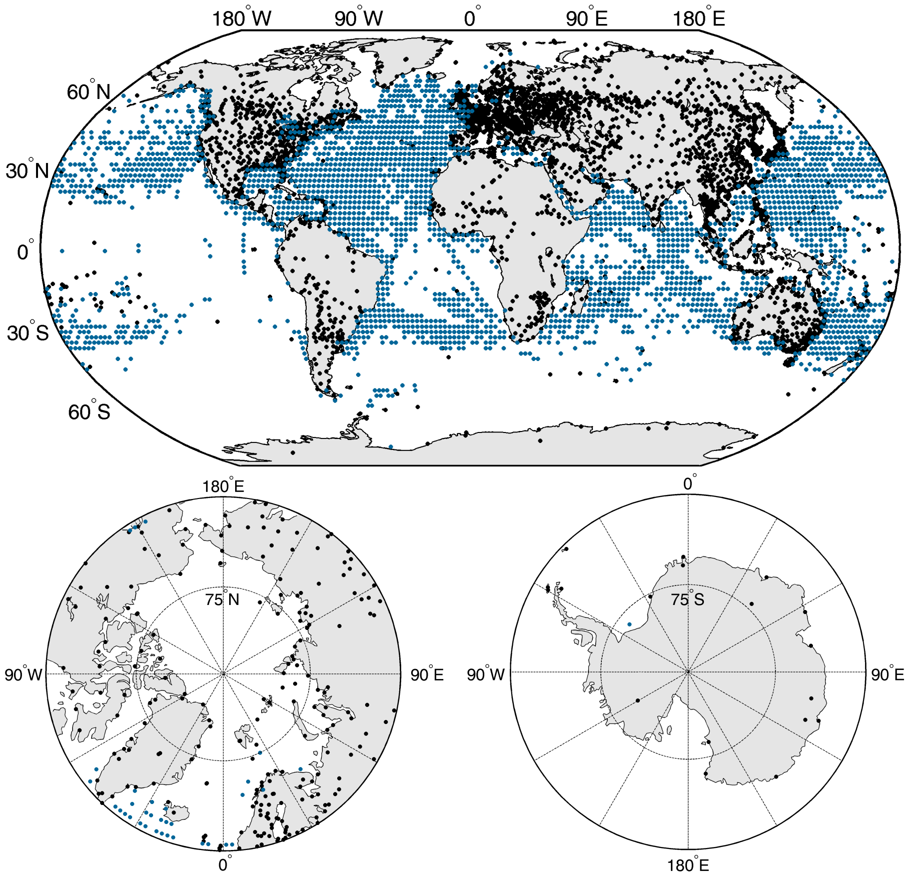

Figure 6.5: Different map projections of the station locations within dataset MA, where both S_1 or S_2 pressure tides were determined: 3565 continental and island stations (black dots); 2924 ocean boxes (blue dots).

fortably low levels (Figure 6.4). Specifically, 35% of the ocean boxes, mostly those on the southern hemisphere, 'operate' at only half of their observational time span, with an extremum of just 5% occurring at $\theta = 119^\circ/\lambda = 49^\circ$ in the Indian Ocean. Consequently, many of the acquired S_1 and S_2 estimates are unrepresentative of the true tides over the oceans, and it makes sense to consider two separate marine networks in the following. The first compilation comprises all ocean boxes without any restrictions. Its blend with the surface station data is denoted MA ('marine all') and shown in Figure 6.5 with an emphasis on the data density near the poles. Note that only 20 stations could be retained south of $\theta = 150^\circ$. The second merger MP ('marine partial') in Figure 6.6 combines all surface stations with only the more reliable estimates over the oceans based on the requirement of at least 50% of all possible days holding sub-daily pressure observations. As anticipated from Figure 6.4, this restriction sacrifices the majority of ocean boxes on the southern hemisphere.

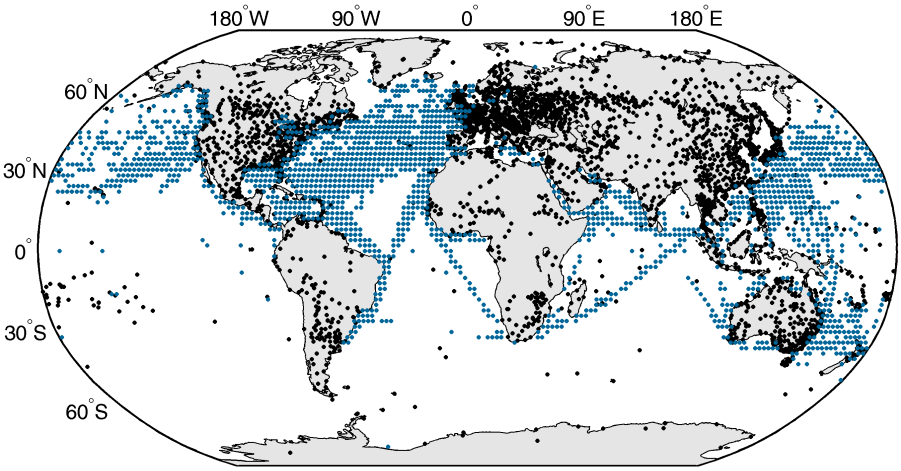

Figure 6.6: Station locations within dataset MP, where both S_1 or S_2 pressure tides were determined: 3565 continental and island stations (black dots); 1904 ocean boxes (blue dots), which form a subset of the ocean data in Figure 6.5 based on the requirement of at least 50% of all possible days holding sub-daily pressure observations.

6.1.3 Comparison with model data

It proves interesting to extract tidal harmonics from all three circulation models (ERA-Interim, MERRA, and ECMWF DC during 2007–2011) right at the surface and ocean box locations and compare them station by station to the S_1 and S_2 estimates of the in-situ scatter. The achieved levels of agreement are depicted in a qualitative manner in Figure 6.7, which regresses the blend of tidal components $\{A_n \cos(\varphi_n), A_n \sin(\varphi_n)\}$ (recall Eq. 4.2) from ERA-Interim against that of the land and ocean stations in dataset MA. Both diurnal and semi-diurnal point clouds are well condensed around the lines of slope 1, with the magnitude distribution of S_2 very uniform as a result of its dominating migrating wave. The main observation here is that the tidal components of the ocean boxes at S_2 are slightly more ill-assorted than that of the surface stations. Yet, for the diurnal tide (Figure 6.7a), both portions share virtually the same levels of scatter.

More quantitative comparisons of station and model tides at the locations of the MA dataset, presented in Table 6.3, confirm the graphical impressions from Figure 6.7. The three (re)analysis models show larger RMS differences with in-situ values at S_2 than at S_1, which is primarily a consequence of the weaker diurnal pressure signal at most locations. A considerable contribution to the deterioration of the S_2 results comes from the marine tidal components, as can be recognized from examining only the ocean subset of MA. This partition yields RMS differences at the level of 14.9–18.0 Pa across all three models as opposed to 11.9–14.7 Pa for the analysis of all stations, cf. similar conclusions reached by Ray (2001) based on his compilation of 428 data points. Moreover, and for the purposes of this study, the obtained values have to be assessed in light of the agreement of the three models amongst themselves at the locations of the MA dataset. Hence, Table 6.3 also includes the RMS differences between any two combinations out of ERA-

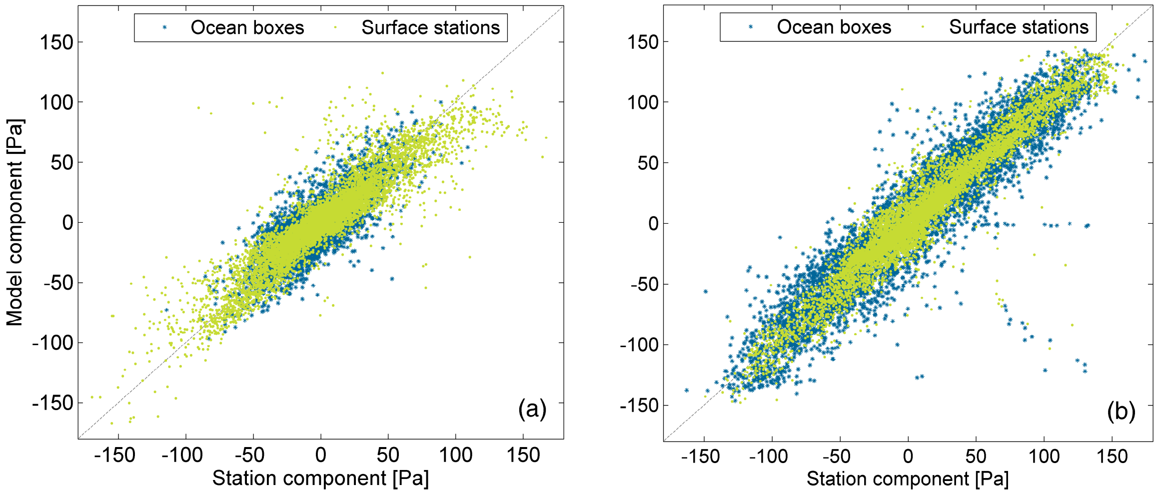

Figure 6.7: Regression diagrams comparing the blend of tidal components $\{A_n \cos(\varphi_n), A_n \sin(\varphi_n)\}$ for the ERA-Interim model against the tidal components of the MA dataset at (a) the diurnal cycle and (b) the semi-diurnal cycle.

Interim, MERRA, and ECMWF DC. At the diurnal cycle, model RMS values drop below 8.0 Pa and are thus significantly smaller than those obtained from the comparison with in-situ data (roughly 12.0 Pa). This is a major indication that from the network of S_1 estimates it is probably difficult to generate a mean AAM pressure term which is capable of validating the pressure term of an atmospheric circulation model. I suppose that artifacts from the harmonic fit of imperfect barometric time series as well as truly local (non-migrating) effects are accountable for the apparent discrepancies at the diurnal frequency. A much more positive conclusion can be drawn for the semi-diurnal tide, as the average RMS differences between the three models range from 10.7 to 15.2 Pa, what is basically the same level of agreement achieved in the comparison with in-situ data of S_2. Interestingly, out of all possible combinations, the seemingly most accurate sources, ERA-Interim and MERRA, differ the most, both for the full MA dataset (15.2 Pa) and the ocean partition (18.5 Pa), see also Figure 4.4. Results from the station tide comparison in the top half of Table 6.3 are below those thresholds throughout, testifying that the assembled S_2 estimates form a consistent and reliable dataset. The creation of an independent pressure term vector at the semi-diurnal frequency is thus a realistic prospect.

6.2 Derivation of pressure tide climatologies on a global grid

The determination of gridded surface pressure fields from a scatter of data points, as needed for the evaluation of AAM matter terms in Eqs. (3.18) and (3.19), can be approached as an interpolation or an approximation problem. Dai & Wang (1999) deployed a natural neighbor interpolation technique on a highly dense compilation of surface stations and ocean boxes, while Haurwitz & Cowley (1973) first gridded their much sparser network by hand contouring before

Table 6.3: RMS differences (Pa) of the diurnal and semi-diurnal tides from ERA-Interim, MERRA, ECMWF DC with the in-situ estimates of dataset MA.[a]

	$S_1(p_s)$		$S_2(p_s)$	
	All stations	Ocean boxes	All stations	Ocean boxes
In-situ / ERA	12.6	12.2	14.1	18.0
In-situ / MERRA	11.6	10.8	14.7	16.7
In-situ / DC	12.0	11.4	11.9	14.9
ERA / MERRA	8.0	7.6	15.2	18.5
ERA / DC	7.5	7.3	10.7	11.1
DC / MERRA	7.9	7.4	11.2	12.4

[a] The agreement of the models amongst themselves in terms of RMS differences is included as well

calculating spherical harmonic coefficients. Here, a direct fit of spherical harmonics to the station data is performed in the manner of Ray (2001). The clear advantage of this method consists in having variance and covariance charts that depend directly on the station data and can be propagated in tidal components as well as in AAM values. Such standard errors of excitation quantities have been rarely dealt with in literature (Ponte & Rosen, 2001) but represent precious information which is usually not provided by assimilation systems for (sub-)daily products.

6.2.1 Fit of spherical harmonics

Functional model

From a set of initial observations, least squares adjustment allows determining a unique solution for an unknown parameter vector in the sense that this solution minimizes the sum of squared residuals, i.e. the deviations of the adjusted observations from their measured values (Perović, 2005). If we strive for a spherical harmonic expansion of the pressure waves S_n at frequency $n = 1$ and 2 cpd, any available observations of cos- and sin-coefficients $\{l_a, l_b\} = \{a_n, b_n\}$ in Eq. (6.1) have to satisfy the following model

$$a_n(\theta,\lambda) = \sum_{l=0}^{l_{max}} \sum_{m=0}^{l} \left[\alpha_{n,lm}\cos(m\lambda) + \beta_{n,lm}\sin(m\lambda)\right] P_l^m(\cos\theta) \tag{6.2}$$

$$b_n(\theta,\lambda) = \sum_{l=0}^{l_{max}} \sum_{m=0}^{l} \left[\gamma_{n,lm}\cos(m\lambda) + \delta_{n,lm}\sin(m\lambda)\right] P_l^m(\cos\theta) \ , \tag{6.3}$$

where θ and λ denote the spherical coordinates of each data point, $\{l, m\}$ are the degree and order of each summand, and $P_l^m(\cos\theta)$ represent the associated Legendre functions in their fully normalized form as utilized also by Haurwitz & Cowley (1973). The chosen model is probably the simplest of pressure waves expansions but has the advantage of stating time dependence only implicitly in the combination of a_n and b_n. More sophisticated schemes, utilizing pro- and retrograde components or wavenumber distinctions, are readily accessible from the parameters estimated via Eqs. (6.2) and (6.3). Without loss of generality, the two sets of coefficients $\{\alpha_{n,lm}, \beta_{n,lm}\}$ and $\{\gamma_{n,lm}, \delta_{n,lm}\}$ were adjusted in separate steps on the basis of the two observation vectors

$$\boldsymbol{l}_a = \left(a_n^1 \dots a_n^{n_s}\right)^T , \quad \boldsymbol{l}_b = \left(b_n^1 \dots b_n^{n_s}\right)^T , \tag{6.4}$$

with $n_s = 6466$ entries in case of dataset MA. For both fits, a prior model, consisting either of the dominant migrating diurnal ($l = 1, m = 1$) or semi-diurnal ($l = 2, m = 2$) wave, can be subtracted from the observations (Ray, 2001). As those terms do not couple with variations in Earth rotation, such an adaptation has no impact on the eventual AAM results. It is also not needed from a numerical point of view, as the least squares system converges without any iteration step.

A much more vital role is assumed by the truncation level of the fit, i.e. the maximum degree of the expansion, l_{max}. Depending on the choice of this parameter, the final pressure term cycles can vary considerably. This problem arises from the fact that spherical harmonic coefficients cannot be determined independently of each other within the adjustment process in case of discrete observations (Fecher *et al.*, 2009). Moreover, degrees of expansion greater than 10 (wavelengths smaller than 4000 km) lead to somewhat ill-posed problems and require a regularization scheme to stabilize the solution (Shen & Xu, 2013). For the purpose of this study, there is no necessity for such a detailed expansion, though, and the largest considered value for l_{max} was set to 10. In contrast, low degrees of truncation are particularly prone to cut off errors and aliasing of high frequency content outside the parameter space (Jekeli, 1996). Here, l_{max} values down to degree 3 are investigated. The choice of the maximum degree controls the number of estimated parameters n_p, e.g. 121 for $l_{max} = 10$ and 16 for $l_{max} = 3$, leading to the following parameter vector $\boldsymbol{x}_a$ for the case of observations $\boldsymbol{l}_a$

$$\boldsymbol{x}_a = (\underbrace{\alpha_{00}}_{\text{l=0}}, \underbrace{\alpha_{10}, \alpha_{11}, \beta_{11}}_{\text{l=1}}, \underbrace{\alpha_{20}, \alpha_{21}, \beta_{21}, \alpha_{22}, \beta_{22}}_{\text{l=2}}, \underbrace{\alpha_{30}, \alpha_{31}, \beta_{31}, \alpha_{32}, \beta_{32}, \alpha_{33}, \beta_{33}}_{\text{l=3}})^T . \tag{6.5}$$

Linearization of the functional model is accomplished by building the partial derivatives of the n_s observation equations (any of Eqs. 6.2 or 6.3 for either diurnal or semi-diurnal pressure tide) with respect to the n_p unknown parameters in the design matrix $\boldsymbol{A} = \boldsymbol{A}_a = \boldsymbol{A}_b$

$$\boldsymbol{A} = \frac{\partial \boldsymbol{l}_a(\boldsymbol{x}_a)}{\partial \boldsymbol{x}_a} = \begin{pmatrix} \frac{\partial l_{a,1}(x_a)}{\partial x_{a,1}} & \cdots & \frac{\partial l_{a,1}(x_a)}{\partial x_{a,n_p}} \\ \vdots & \vdots & \vdots \\ \frac{\partial l_{a,n_s}(x_a)}{\partial x_{a,1}} & \cdots & \frac{\partial l_{a,n_s}(x_a)}{\partial x_{a,n_p}} \end{pmatrix} . \tag{6.6}$$

Stochastic model and inversion

As for most adjustment problems in geodesy, determination of the weight matrix $\boldsymbol{P}$ is a delicate task and ideally involves some prior knowledge about the accuracy of the utilized observations.

Here, this information is in principle available in form of standard errors as a by-product of the point-wise fit of harmonic coefficients in Section 6.1. However, the significance and reliability of those values should be disputed. Both at diurnal and semi-diurnal frequencies, the deduced errors of $\{a_n, b_n\}$ for continental stations possess median values in the vicinity of 2.4 Pa (4 Pa 'standard deviation'), which appears to be a far too optimistic measure. One the one hand, it is markedly smaller than the internal consistency RMS quoted in Table 6.3, and on the other hand it is also below the level of standard errors given by Ray (1998) for the thoroughly analyzed and highly accurate S_1 estimates at 25 island stations. Maximum and minimum standard errors (107 Pa at *Griffith Airport*, New South Wales, and 0.006(!) Pa at *Daneborg*, Greenland) within the land portion of dataset MA are additionally suspicious quantities. Utilizing these initial error estimates to determine the weights of observations can thus lead to singularities in the inversion explained below.

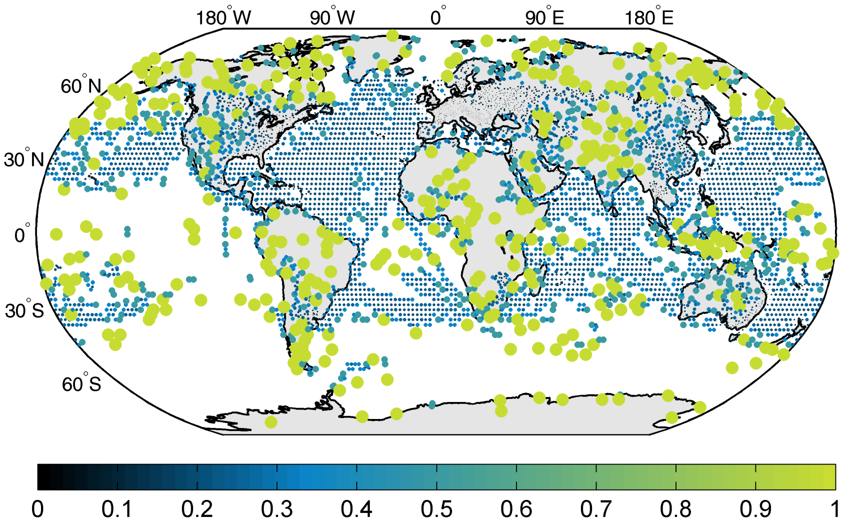

Figure 6.8: Illustration of the weights assigned to station and ocean box observations from dataset MA. The smallest value of 0.018 is occurring at four stations in the United Kingdom.

In fact, the primary issue that needs to be accounted for in $\boldsymbol{P}$ is the construction of a reasonable balance between sparsely and densely sampled regions of the globe. Without such an adaption, fitting directly to the station data overweights observational clusters (as evident for Europe and southeast Asia) and fuels both the ill-conditioning of the system and the negative effects of truncation. While Ray (2001) circuited these problems by regularization, such a strategy is too multi-layered and less objective for the present observational network. As a very effective remedy, one may form averages of the harmonic coefficients in cells of predefined size (R. Ray, personal communication), or, equivalently, define the weight of each observation based on the density of surrounding stations. Test computations with various schemes revealed that a stabilization of the AAM solutions over various values l_{max} and a vast improvement in the condition number of the normal equation matrix (see below) is achieved by counting the number of data points n_c

within 2° distance of each station and assigning to it a dimensionless weight of $p_i = \frac{1}{n_c}$. The sum of p_i in each observational cell of size 4.0° × 4.0° is thus approximately 1, which ensures a fine balance between various regions of the globe, see Figure 6.8 for a graphical illustration. The one probable harm caused by this concept consists in attributing highest weights to stations with not necessarily the best estimates of local tidal coefficients, e.g. those of isolated marine boxes in the southern hemisphere oceans (cf. Figure 6.4). Following Ray (2001), possible correlations of observations and the associated covariances were categorically neglected in the construction of $\boldsymbol{P}$. Despite reducing the computational costs to a bearable level, this measure is certainly a severe simplification for the semi-diurnal tide in face of its regular spatial wave pattern. Deduced standard errors of parameters and AAM terms are thus likely to be too optimistic.

Having defined both the linearized functional model and the weight matrix, the adjustment of the spherical harmonic coefficients $\boldsymbol{x}_a$ for observations $\boldsymbol{l}_a$ can be formulated as (Perović, 2005)

$$\boldsymbol{N} = \boldsymbol{A}^T \boldsymbol{P} \boldsymbol{A} \tag{6.7}$$

$$\boldsymbol{x}_a = \boldsymbol{N}^{-1} \boldsymbol{A}^T \boldsymbol{P} \boldsymbol{l}_a \tag{6.8}$$

$$\boldsymbol{v}_a = \boldsymbol{A} \boldsymbol{x}_a - \boldsymbol{l}_a \tag{6.9}$$

$$s_a^2 = \frac{\boldsymbol{v}_a^T \boldsymbol{P} \boldsymbol{v}_a}{n_s - n_p} \tag{6.10}$$

$$\boldsymbol{C}_{x_a} = s_a^2 \boldsymbol{N}^{-1} , \tag{6.11}$$

where $\boldsymbol{N}$ represents the normal equation matrix and $\boldsymbol{v}_a$ is the vector of residuals in the sense ‘model minus observation’. Diagonal and off-diagonal elements of the covariance matrix of estimated parameters $\boldsymbol{C}_{x_a}$ provide the variance and covariance information on $\boldsymbol{x}_a$. It is obtained by multiplying $\boldsymbol{N}^{-1}$ with the *a posteriori* variance of unit weight s_a^2 (Perović, 2005). Equations (6.8)–(6.11) can be analogously phrased for observations $\boldsymbol{l}_b$ and parameters $\boldsymbol{x}_b$.

6.2.2 Adjustment results

As a qualitative spot check of the spherical harmonic fit, global S_1 and S_2 amplitude and phase lag charts for the complete expansion up to degree and order 8 of dataset MA are shown in Figure 6.9. A close match to the tides from gridded analysis fields (Figure 4.1) is achieved in both frequency bands, in particular at S_2, with the station tide expansions providing somewhat smaller peak amplitudes over the tropics. In face of the sparseness of in-situ data over the Amazon rain forest and central Africa, as well as the smoothing associated with a low-degree harmonic expansion, this result should not be too surprising. It is also of little relevance for AAM terms in the following, as those quantities depend solely on the components of degree $l = \{0, 2\}$ and order $m = \{0, 1\}$. A more worrying disparity can be seen for the semi-diurnal phase behavior at the poles, where the fitted model predicts values about 50°–100° different to the results in Figure 4.1d. As non-zero tidal oscillations at the poles are purely zonal (Haurwitz & Cowley, 1973), one can expect those phase discrepancies being mapped into excitation of LOD. Furthermore, the

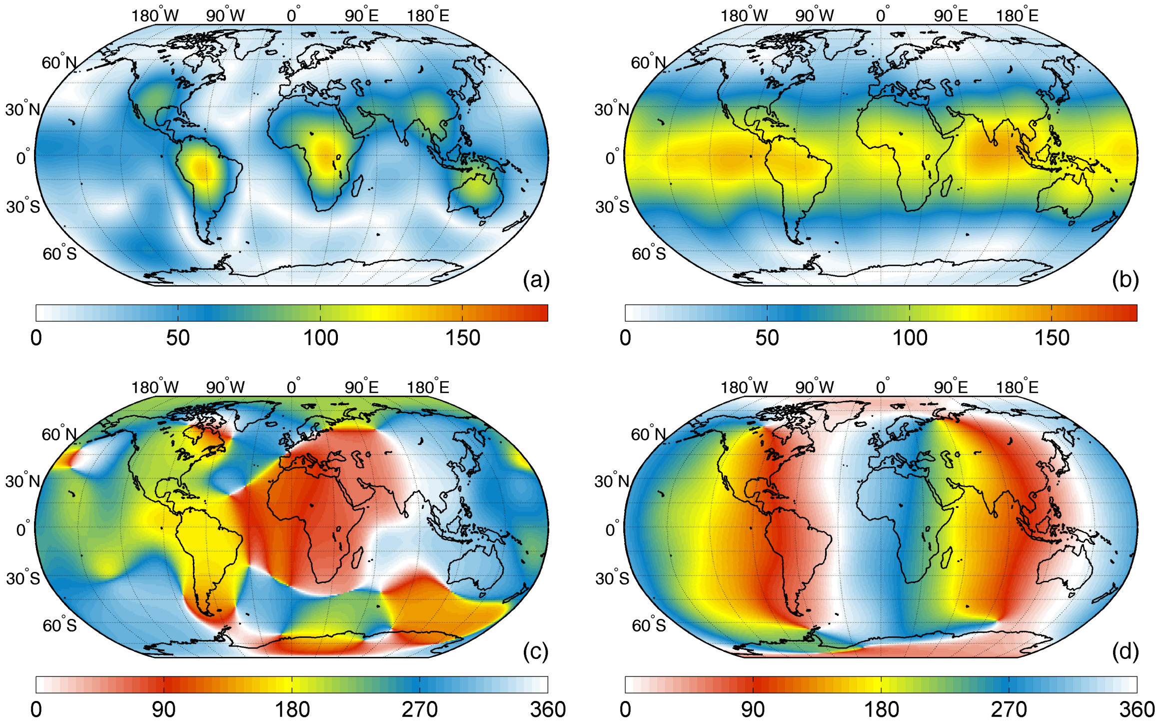

Figure 6.9: Diurnal (a) and semi-diurnal (b) surface pressure amplitudes [Pa], and the corresponding diurnal (c) and semi-diurnal (d) Greenwich phase lags [deg] as deduced from spherical harmonic expansion of dataset MA up to degree and order 8.

adjustment produces artificial tidal signals in the data-void regions of the southern Pacific Ocean, as evident in Figure 6.9a around 120°W. Throughout the tested expansions, this location always hosts the maximum of standard errors of tidal components—a fact demonstrated in Figure 6.10 on the basis of $s_{A(\theta,\lambda)}$, i.e. the error of the gridded amplitude of either S_1 or S_2

$$A_n(\theta,\lambda) = \sqrt{a_n^2(\theta,\lambda) + b_n^2(\theta,\lambda)}\,,\ n = 1,2. \tag{6.12}$$

Full variance and covariance propagation for linear functions (Mikhail & Ackermann, 1976) was applied to propagate the errors of estimated parameters in $\boldsymbol{C}_{x_a}$ into the tidal parameters $\{a_n, b_n\}$ discretized on a 1° grid, that is

$$\boldsymbol{C}_{a_n(\theta,\lambda)} = \boldsymbol{J}\boldsymbol{C}_{x_a}\boldsymbol{J}^T \tag{6.13}$$

$$\boldsymbol{C}_{b_n(\theta,\lambda)} = \boldsymbol{J}\boldsymbol{C}_{x_b}\boldsymbol{J}^T \tag{6.14}$$

$$\boldsymbol{J} = \frac{\partial a_n(\theta,\lambda)}{\partial \boldsymbol{x}_a}\,,$$

where $\boldsymbol{J}$ represents the Jacobian matrix of both $a_n(\theta,\lambda)$ and $b_n(\theta,\lambda)$ (as column vectors) with respect to the parameters $\boldsymbol{x}_a$ or $\boldsymbol{x}_b$, respectively (as row vectors). Simple variance propagation of the diagonal elements in $\boldsymbol{C}_{a_n(\theta,\lambda)}$ and $\boldsymbol{C}_{b_n(\theta,\lambda)}$ supplies the amplitude error grids in Figure 6.10.

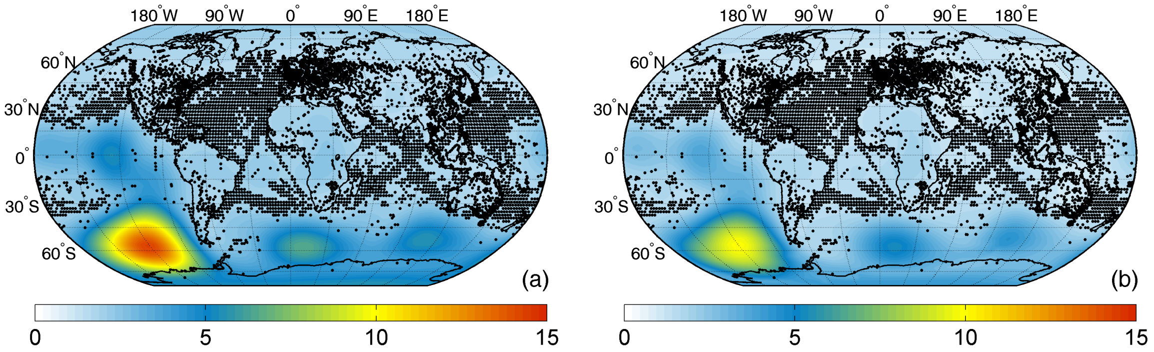

Figure 6.10: Standard errors [Pa] for the amplitudes of the diurnal (a) and semi-diurnal (b) pressure tides shown in Figure 6.9 for a spherical harmonic expansion up to degree and order 8.

Considerably smaller peak values of $s_{A(\theta,\lambda)}$ are obtained at 2 cpd, since the utilized model of low-degree spherical harmonics performs well in approximating the more regular wave structure of the S_2 tide, leading to a reduced variance of unit weight in Eq. (6.10).

Table 6.4 summarizes some of the numerical properties of the least squares system at S_1 and S_2 for the chosen values of truncation $l_{max} \in [3;10]$. Including smaller wavelengths with each step in l_{max} naturally deteriorates the condition number κ of the normal equation matrix $\boldsymbol{N}$ and results in large standard errors of the tidal amplitude. The value of κ does neither depend on the kind of observations nor on the frequency band (cf. Eqs. 6.2–6.3); it is solely determined by the capability of the station network to resolve all modes associated with l_{max}. Solutions with truncation degrees higher than 8 yield $\kappa > 300$ and produce suspicious amplitude errors > 15 Pa that are no more comparable with the error charts of Ray (2001). Hence, caution has to be

Table 6.4: Selected numerical properties of the adjustment of spherical harmonic coefficients to the station tide estimates within dataset MA.[a]

l_{max}	$\kappa(N)$	s_a [Pa]		max. $s_{A(\theta,\lambda)}$ [Pa]	
		$S_1(p_s)$	$S_2(p_s)$	$S_1(p_s)$	$S_2(p_s)$
3	8	11.6	6.9	2.4	1.7
4	11	10.4	6.1	2.9	2.0
5	20	9.8	6.0	4.6	3.0
6	36	9.1	5.9	6.4	4.5
7	73	8.6	5.8	9.4	6.5
8	158	8.3	5.7	14.4	10.0
9	310	8.1	5.6	20.5	17.1
10	633	8.0	5.6	30.5	25.2

[a] κ represents the condition number of the normal equation matrix, s_a the square root of the variance of unit weight, and $s_{A(\theta,\lambda)}$ denotes the maximum standard errors of the tidal amplitude at 1 and 2 cpd.

exercised if these expansions are converted to AAM pressure terms. Interestingly, the variances of unit weight for both S_1 and S_2 decrease with increasing l_{max} and converge to a level of 8.0 Pa and 5.6 Pa, respectively. This shows the benefit of having smaller wavelengths explaining the more detailed tidal variability, particularly that of the diurnal tide. Analogous to Table 6.4, numerical characteristics were retrieved also for the adjustment of the MP subset (not depicted). Here, the effects of an ill-posed least squares problem surface already at degree 7 to 8.

Closer examination of the modes that are determining for variations of polar motion and changes in LOD is achieved by rewriting the initial representation of S_n in Eqs. (6.1)–(6.3) in terms of prograde waves (superscript +, denoting westward propagation with the Sun[1]) and retrograde waves (superscript −) of surface pressure (Ray, 2001)

$$S_n(\theta,\lambda,t) = \sum_{l=0}^{l_{max}} \sum_{m=0}^{l} \left[D^+_{n,lm} \cos\left(nt + m\lambda - \psi^+_{n,lm}\right) + D^-_{n,lm} \cos\left(nt - m\lambda - \psi^-_{n,lm}\right) \right] P_l^m(cos\theta) \ . \tag{6.15}$$

Here, the amplitudes $D^{\pm}_{n,lm}$ and phase lags $\psi^{\pm}_{n,lm}$ are connected to the coefficients $\alpha_{n,lm}$, $\beta_{n,lm}$, $\gamma_{n,lm}$, and $\delta_{n,lm}$ via

$$D^{\pm}_{n,lm} \cos\psi^{\pm}_{n,lm} = \frac{1}{2}\left(\alpha_{n,lm} \mp \delta_{n,lm}\right) \tag{6.16}$$

$$D^{\pm}_{n,lm} \sin\psi^{\pm}_{n,lm} = \frac{1}{2}\left(\gamma_{n,lm} \pm \beta_{n,lm}\right) \ , \tag{6.17}$$

what can be recognized from phrasing Eq. (6.2) as real part and Eq. (6.3) as imaginary part of a two-dimensional oscillation in the complex plane. A complete set of diurnal and semi-diurnal pressure tide coefficients following the notation in Eq. (6.13) and truncated at degree 7 is included in Appendix A.3. From all spherical harmonics, only the terms associated with degree $l = 2$ and order $m = 1$ account for polar motion variability (de Viron *et al.*, 2002), i.e. the amplitude-phase pairs $\{D^+_{21}, \psi^+_{21}\}$ and $\{D^-_{lm}, \psi^-_{lm}\}$ for a chosen frequency n. As already noted in Section 4.3, two of the zonal terms, $\{D^+_{00}, \psi^+_{00}\} = \{D^-_{00}, \psi^-_{00}\}$ and $\{D^+_{20}, \psi^+_{20}\} = \{D^-_{20}, \psi^-_{20}\}$ couple to changes in LOD, and can be thought of as standing waves with an equal contribution from pro- and retrograde frequencies (as seen from evaluating Eq. 6.13 at $m = 0$). Amplitudes of the $l = 2$ zonal wave reach 8 Pa in the tropics and more than 12 Pa at the poles (Kadow *et al.*, 2012), thus being about 10% of the size of the main migrating waves.

The phase lags and fully normalized amplitudes of all introduced terms across the chosen degrees of truncation are displayed in Figures 6.11 (diurnal tide) and 6.12 (semi-diurnal tide) for the case of dataset MA. Truly encouraging results are achieved at S_2, for which amplitude and phase estimates are largely stable and independent of the degree of expansion. For instance, $\psi^{\pm}_{00}$ varies only about 15° (or 30 min) between the different solutions, which is an exceptional low level given the smallness of this component. Standard errors, obtained from propagating the

---

[1] As opposed to polar motion studies, tidal theory uses ‘prograde’ to signify westward motion in the direction of the tide-raising body.

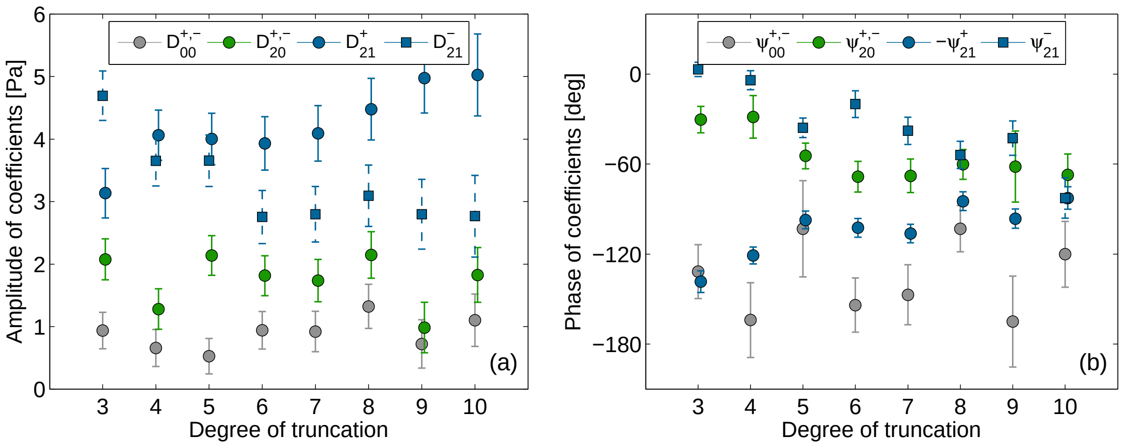

Figure 6.11: Amplitude (a) and phase values (b) of selected waves in the spherical harmonic expansion of the diurnal pressure tide based on dataset MA. Values and standard errors across various degrees of truncation are depicted for the following terms: $\{D^{\pm}_{00}, \psi^{\pm}_{00}\}$, $\{D^{\pm}_{20}, \psi^{\pm}_{20}\}$, $\{D^{\pm}_{21}, \psi^{\pm}_{21}\}$, with the pro- and retrograde waves of each zonal term being identical. For a better perception of the results, negative phase values (that of ψ^{+}_{21}) are mirrored to positive ones.

variances of estimated parameters in Eqs. (6.14)–(6.15), tend to grow with increasing l_{max} and peak either at degree 9 or 10. This finding, together with the ill-conditioning noted in Table 6.4 and the fact that the degree 9/10 solutions drop off with respect to lower degrees throughout all terms, leads to the omission of these expansions in the following. Moreover, the first expansion at degree 3 is probably too coarse for a proper representation of the small modes of interest (truncation errors) and is therefore also neglected. Any of the remaining solutions $l_{max} \in [4;8]$ appears be a good choice to be processed further toward an independent pressure term vector from barometric observations.

The analogous assessment of the diurnal tide in Figure 6.11 is however less positive. With the exception of solutions at degree 6 to 8, each of the different terms varies up to 50% in amplitude, which is a particular concern for the small zonal waves $D^{\pm}_{00}$ and $D^{\pm}_{20}$ that excite changes in LOD. None of the four terms possesses a stable phase level, and discrepancies in $\psi^{\pm}_{lm}$ are as large as 80° or 5.3 h between specific degrees of expansions. These erratic results partly originate from erroneous local S_1 cycles, which constitute much smaller signals than the semi-diurnal cycles at most locations and are therefore difficult to estimate. An even more severe problem consists in the nature of the diurnal pressure tide itself. Characterized by strong local, non-migrating effects and the dependence on the distribution of continents and oceans, S_1 is probably much less suited than S_2 for a decomposition into spherical harmonics. Such an inadequacy of the imposed model is likely to affect the representation of the small modes this study is concerned with.

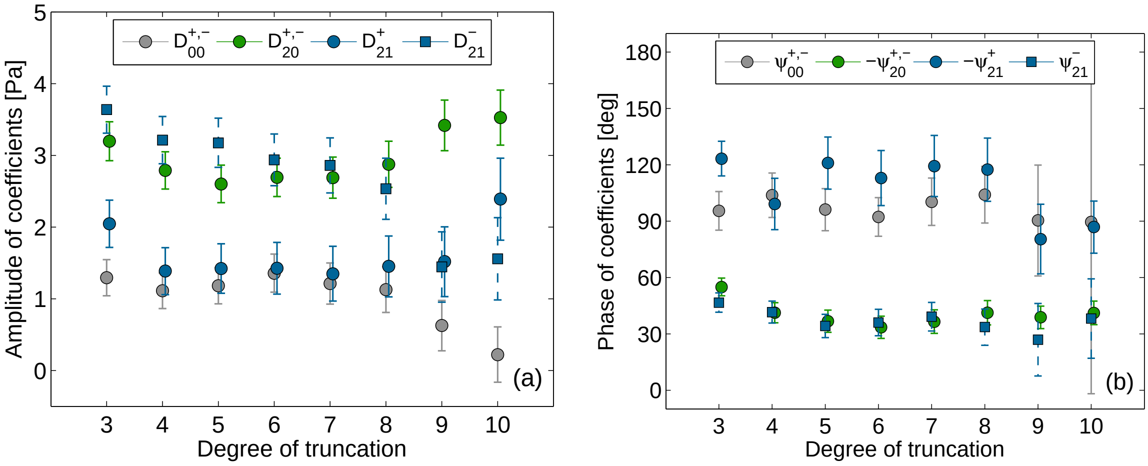

Figure 6.12: Amplitude (a) and phase values (b) of selected waves in the spherical harmonic expansion of the semi-diurnal pressure tide based on dataset MA. Values and standard errors across various degrees of truncation are depicted for the following terms: $\{D^{\pm}_{00}, \psi^{\pm}_{00}\}$, $\{D^{\pm}_{20}, \psi^{\pm}_{20}\}$, $\{D^{\pm}_{21}, \psi^{\pm}_{21}\}$, with the pro- and retrograde waves of each zonal term being identical. Negative phase values (that of $\psi^{\pm}_{20}$ and $\psi^{\pm}_{21}$) are mirrored to positive ones.

6.2.3 Comparison to pressure terms from atmospheric models

Any of the estimated sets of spherical harmonic coefficients can be converted to AAM pressure term quantities via the grid point-wise sinusoid expression for surface pressure in Eq. (6.1). At frequency n, the mean day cycles of $\boldsymbol{H}^p$ in x, y, z direction thus read

$$\begin{aligned} \begin{pmatrix} H^p_{x,n} \\ H^p_{y,n} \\ H^p_{z,n} \end{pmatrix} &= \begin{pmatrix} x^c_n \\ y^c_n \\ z^c_n \end{pmatrix} \cos(nt) + \begin{pmatrix} x^s_n \\ y^s_n \\ z^s_n \end{pmatrix} \sin(nt) = \\ &= \bar{c} \sum_{\theta} \sum_{\lambda} \left[a_n(\theta,\lambda)\cos(nt) + b_n(\theta,\lambda)\sin(nt) \right] \underbrace{\begin{pmatrix} -\cos\theta\sin\theta\cos\lambda \\ -\cos\theta\sin\theta\sin\lambda \\ \sin^2\theta \end{pmatrix}}_{\boldsymbol{W}^p} \sin\theta \qquad (6.18) \\ \bar{c} &= \Omega \frac{a^4}{g} \mathrm{d}\theta \mathrm{d}\lambda \, , \end{aligned}$$

where the weighting function composite has been abbreviated as $\boldsymbol{W}^p$. Equating coefficients in Eq. (6.18) yields

$$\begin{pmatrix} x^c_n \\ y^c_n \\ z^c_n \end{pmatrix} = \bar{c} \sum_{\theta} \sum_{\lambda} a_n(\theta,\lambda)\, \boldsymbol{W}^p \sin\theta, \quad \begin{pmatrix} x^s_n \\ y^s_n \\ z^s_n \end{pmatrix} = \bar{c} \sum_{\theta} \sum_{\lambda} b_n(\theta,\lambda)\, \boldsymbol{W}^p \sin\theta \, . \qquad (6.19)$$

Standard errors of those coefficients are obtained accordingly from the known variances and covariances of tidal components (Eqs. 6.13–6.14), e.g. for x_n^c via

$$\begin{aligned} \sigma^2_{x_n^c} &= \boldsymbol{J}_x \boldsymbol{C}_{a_n(\theta,\lambda)} \boldsymbol{J}_x^T \\ \boldsymbol{J}_x &= \frac{\partial x_n^c}{\partial a_n(\theta,\lambda)} = -\bar{c}\cos\theta\sin^2\theta\cos\lambda\,, \end{aligned} \tag{6.20}$$

with θ and λ representing the chosen 1° grid as reshaped column vectors. Below, the comparisons of model and station tide pressure terms are conducted by means of phasor plots in the axial and equatorial direction (both pro- and retrograde terms, reckoned in the usual way). The real and imaginary parts of those phasors ($\hat{H}_n^{p,\pm}$ and $\hat{H}_{z,n}^p$) follow from the notation as sin- and cos-coefficients (cf. Appendix A.1)

$$\hat{H}_n^{p,\pm} = \frac{1}{2}\left[\left(x_n^c \mp y_n^s\right) + \mathrm{i}\left(y_n^c \pm x_n^s\right)\right] \tag{6.21}$$

$$\hat{H}_{z,n}^p = z_n^c + \mathrm{i} z_n^s\,, \tag{6.22}$$

where the sin-coefficients need to be introduced with a negative sign to account for the fact that the Fourier coefficients (i.e. phasors) correspond to a sinusoid of type $A_n\cos(nt+\varphi_n)$ as opposed to the standard representation of harmonics $A_n\cos(nt-\varphi_n)$ in Eqs. (4.2) or (6.18).

Equatorial component

Figure 6.13 juxtaposes pro- and retrograde pressure term phasors from spherical harmonic expansion of the MA and MP compilations to the corresponding model pressure terms from ERA-Interim, MERRA, and ECMWF DC as averaged over the period 2007–2011. Two general observations can be noted:

- Both the scatter and standard errors of the MP solutions ($l_{max} \in [4;8]$) are considerably larger than that of the more comprehensive MA network. This finding illustrates that, despite their low reliability, southern hemisphere ocean box data stabilize the adjustment of the small polar motion modes $\{D_{21}^{\pm}, \psi_{21}^{\pm}\}$. The sensibility areas of those modes (analytically expressed by the first two components of $\boldsymbol{W}^p$) exactly coincide with the data gaps of the MP compilation (Figure 6.5) with respect to the full merger MA (Figure 6.6).
- As expected from the analysis conducted in Figure 6.12, semi-diurnal in-situ pressure term estimates from dataset MA are almost invariable across different degrees of expansion. Such an interagreement is only partly achieved at the diurnal band ±1 cpd and restricted to the solutions with truncation at $l_{max} \in [5;7]$.

Concentrating solely on the MA solutions, the station tide pressure terms at S_1^+, S_2^+, and S_2^- are sufficiently stable and close to the model phasors to be in line for a meaningful crosscheck. In Figure 6.13a, the prograde diurnal components of all models depict a perfect match in phase but differ up to 40% in amplitude. Here, the in-situ solutions at $l_{max} \in [5;7]$ give preference

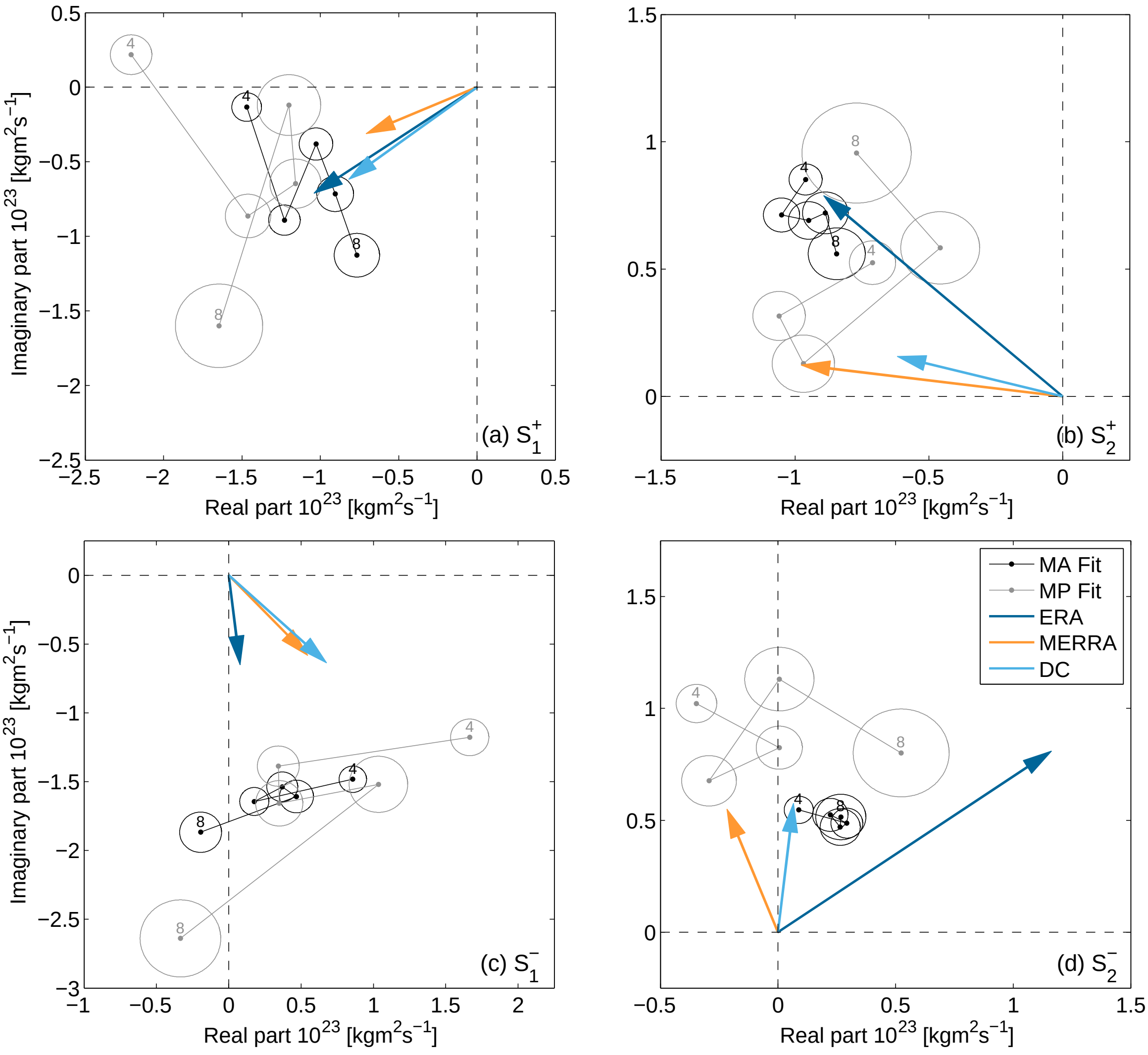

Figure 6.13: Equatorial in-situ pressure term estimates constructed from datasets MA and MP in comparison to the mean pressure term phasors (2007–2011) from ERA-Interim (blue arrows), MERRA (orange arrows), and ECMWF DC (turquoise arrows): (a,c) Pro- and retrograde diurnal component. (b,d) Pro- and retrograde semi-diurnal component. Results are plotted for spherical harmonic expansions with truncation at $l_{max} \in [4; 8]$ (see labels). The respective standard error of each pressure term solution is shown as an ellipse with semi-axis deduced from propagation of variances $\sigma^2_{x_n^{c,s}}$ and $\sigma^2_{y_n^{c,s}}$ according to Eq. (6.21).

to the larger magnitude of both ECMWF models. An even more distinct validation is possible at the prograde semi-diurnal frequency (Figure 6.13b), where the estimates from station tide data clearly approve the mean ERA-Interim pressure term. Both MERRA and ECMWF DC yield phase values that appear to be incorrect by about 30°. This situation is somehow reversed for the S_2^- component (Figure 6.13d), which features an ERA-Interim phasor that is markedly different from the MERRA and ECMWF DC estimates. The discrepancies in amplitude and phase have also been noted in the context of the AAM budget analysis in Section 5.3. With the aid of the station tide

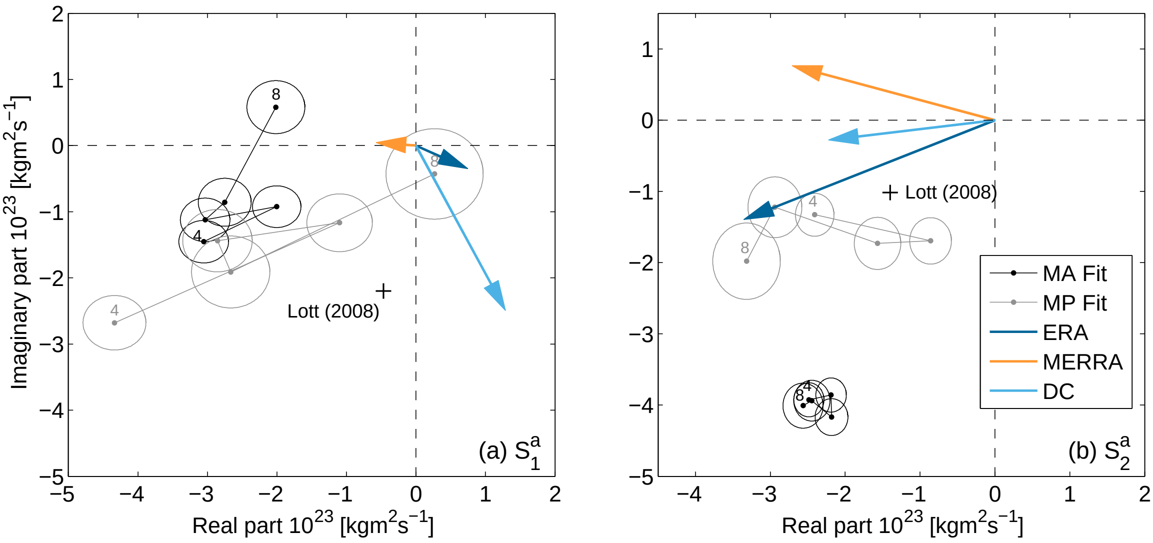

Figure 6.14: Axial in-situ pressure term estimates constructed from datasets MA and MP in comparison to the mean pressure term phasors (2007–2011) from ERA-Interim (blue arrows), MERRA (orange arrows), ECMWF DC (turquoise arrows), and Lott *et al.* (2008) (black crosses): (a) Diurnal and (b) semi-diurnal component. Results are plotted for spherical harmonic expansions with truncation at $l_{max} \in [4;8]$ (see labels). The respective standard error of each pressure term solution is shown as an ellipse with semi-axis deduced from propagation of variances $\sigma^2_{z^c_n}$ and $\sigma^2_{z^s_n}$ according to Eq. (6.22).

expansions, we are now able to identify the retrograde semi-diurnal pressure term of ERA-Interim as a definite anomaly. This is a remarkable result that rewards the efforts devoted to the analysis of surface station and ocean box time series.

Axial component

Analogous comparisons of $\hat{H}^p_{z,n}$ in Figure 6.14 confirm the two primary observations made for the equatorial component (little scatter of the MA solutions, particular good agreement of the semi-diurnal expansions), but are generally less satisfying. At the diurnal cycle, the model phasors are neither validated by the station tide solutions nor conform to the GCM simulation result of Lott *et al.* (2008)[1]. The disagreement of all depicted estimates, together with the deficiencies of the budget comparisons in Figures 5.8e, 5.9e, and 5.10e signals that the axial matter term at S_1 is probably the most uncertain excitation measure within short period Earth rotation studies. On the contrary, semi-diurnal pressure effects on LOD (Figure 6.14b) from ERA-Interim, MERRA, ECMWF DC, and Lott *et al.* (2008) are in good accordance with each other, disagreeing in amplitude by roughly 40%. The scatter of MA solutions is compact but also leading the model phasors as well as the MP solutions by approximately 40°, presumably due to the inclusion of S_2

---

[1] Values not tabulated but documented in graphical form.

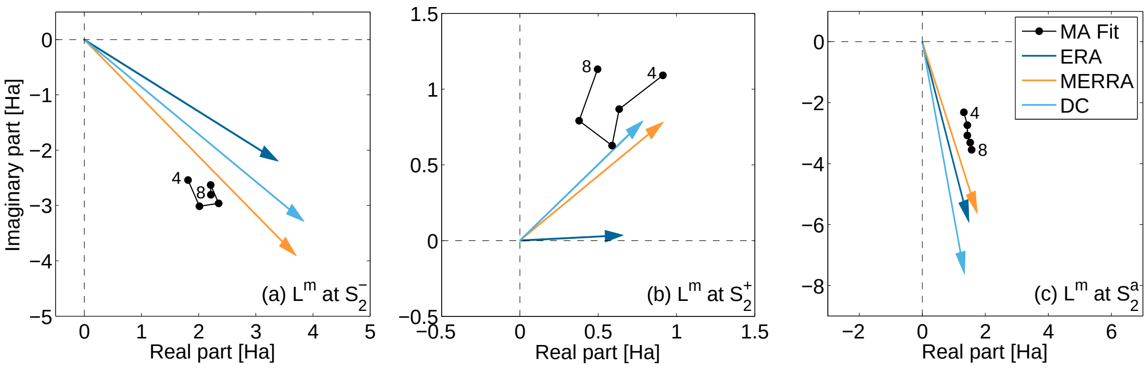

Figure 6.15: Semi-diurnal in-situ mountain torque estimates (black markers) constructed from dataset MA in comparison to the mean mountain torque phasors (2007–2011) from ERA-Interim (blue arrows), MERRA (orange arrows), and ECMWF DC (turquoise arrows). Both equatorial components (a,b) and the axial component (c) are shown, with results plotted for spherical harmonic expansions at $l_{max} \in [4; 8]$ (see labels).

data over the southern hemisphere oceans. This result, anticipated from the discussion of Figure 6.9d, prohibits a proper validation of the pressure term estimates from atmospheric models. Note that a large portion of the recognized difficulties in modeling the atmosphere-induced variations of LOD is inflicted by the smallness of the underlying modes $\{D_{00}^{\pm}, \psi_{00}^{\pm}\}$ and $\{D_{20}^{\pm}, \psi_{20}^{\pm}\}$. In particular, the exact amplitude and phase value of the $\{2, 0\}$-mode are exclusively determined by data in equatorial and polar regions, for which even the comprehensive MA network features very few reliable station tide harmonics.

6.2.4 Reconsideration of the atmospheric angular momentum balance

An interesting addition to this chapter is to depict how excitation measures from the ‘ground truth’ surface pressure tides blend in the AAM budget comparison of Section 5.3. One might especially seek to replace the obviously erroneous pressure term of ERA-Interim at S_2^- with one of the developed harmonic solutions. However, the model’s wind term at the same frequency is likewise suspicious in amplitude and phase (Figure 5.13d), making a reassessment of the AAM balance a futile endeavor. The same conclusion must be drawn at S_2^+ (Figure 5.13e) for ERA-Interim, while at diurnal periodicities the reliability of the station tide retrievals (such as $\boldsymbol{H}^p$) is *per se* questionable. Consequently, only the semi-diurnal band is addressed in the following, and either MERRA or ECMWF DC can be chosen. As MERRA displays a well-closed AAM budget in each semi-diurnal component (Figures 5.9b,d,f), the in-situ estimates are applied to the operational DC model.

Admittedly, using an externally created pressure term evokes inconsistencies with the remaining excitation measures. For instance, the zonal circulation pattern between meridional momentum and atmospheric mass (Section 5.1 or Lott *et al.*, 2008) is certainly violated. The one amendment mitigating this effect consists in constructing a mountain torque vector from the same surface pressure harmonics as the AAM matter term. In line with the previous section, the tidal

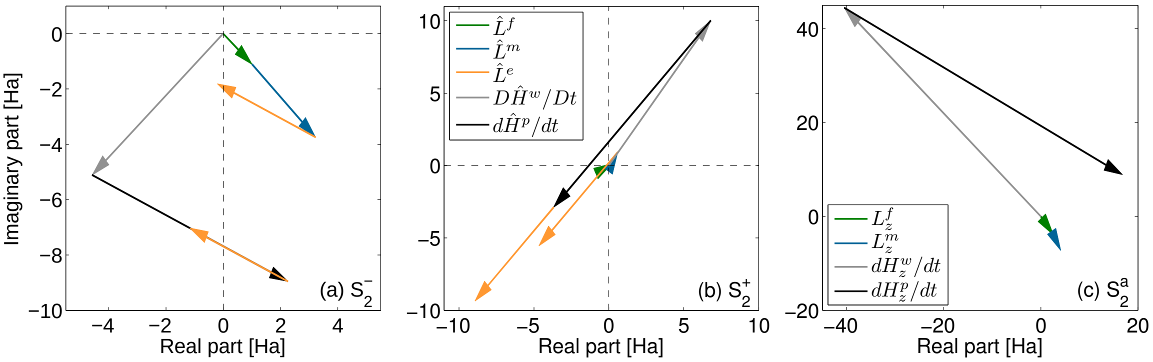

Figure 6.16: Phasor diagrams for the reconsidered semi-diurnal AAM budget within ECMWF DC (2007–2011) after replacing the pressure term derivatives, the ellipsoidal torque, and the mountain torque by their equivalents from surface pressure harmonics ($l_{max} = 7$) as developed on the basis of in-situ measurements. Both equatorial components (a,b) and the axial component (c) are shown.

components $\{a_2(\theta,\lambda), b_2(\theta,\lambda)\}$ on a 1° grid were extracted for $l_{max} \in [4;8]$ and inserted into the analytical expression for $\hat{L}^m$ as well as L_z^m. The more complex task of propagating standard errors in those estimates was disregarded. Figure 6.15 depicts the resulting semi-diurnal oscillations of equatorial and axial mountain torques alongside the corresponding model-based estimates in the complex plane. In each component, the five solutions for different degrees of truncation lie in close vicinity to each other, indicating that the underlying modes of surface pressure are stable, first-order effects in the tidal observations of dataset MA. Nonetheless, the amplitudes of both the retrograde and axial mountain torque phasors appear to be underestimated by about 30–50%, which is a repercussion of the attenuated $S_2(p_s)$ signal from spherical harmonic expansion (Figure 6.9b). Specifically, the sparse barometer coverage near mountainous areas (Andes, Himalaya) as well as the rather low degree of expansion complicate the determination of truly reliable values of $\boldsymbol{L}^m$ (Wahr & Oort, 1984). (This statement is particularly valid for the S_1 tide with its strong local component.) Hence, one should not understand Figure 6.15 as an attempt to verify the model-based mountain torques.

Considering the small variance between the different MA solutions in each of the semi-diurnal pressure terms and mountain torques, the AAM budget verification is largely independent of the choice of l_{max}. One might exclude the somewhat coarser expansion at degree 4 and likewise the slightly ill-conditioning solution at degree 8 (recall Table 6.4). From the remaining possibilities, $l_{max} = 7$ yields the highest level of detail, which is of benefit for the mountain torque representation. Thus, the semi-diurnal excitation quantities of $\boldsymbol{H}^p$ (ellipsoidal torque) and $\boldsymbol{L}^m$ based on surface pressure harmonics up to degree and order 7 were selected for combination with the wind term derivative and the friction torque of ECMWF DC in Figure 6.16. At S_2^-, the small phase deviation of the in-situ pressure term from the model's native pressure term (∼30°, see Figure 6.13b) acts to increase the discrepancy in the AAM balance from 2 Ha to about 5 Ha in magnitude. A more positive result is apparent for the prograde band S_2^+, whose budget closure solely depends on AAM quantities. Here, the in-situ pressure term meets the prerequisite out-of-phase behavior with respect to the wind term but slightly overcompensates its amplitude. Nonetheless, Figure 6.16b represent an improvement compared to the purely model-based balance in Figure 5.10b. The same conclusion can be drawn for the case of the S_2 budget in the axial direction, as the pressure term derivative from station tides reduces the leakage displayed in Figure 5.10f. Yet, in face of the uncertainty inherent to H_z^p from in-situ data (see previous section), one should not attach too much importance to this result.

Chapter 7

Comparison of atmosphere-ocean excitation signals and geodetic observations

After all the modeling efforts of the previous chapters, we are left with the effect of atmospheric fluid dynamics condensed to a few single scalars that can be compared to the global, integral Earth rotation indicators from space geodetic observations. This unpretentious approach might be unsatisfying from the viewpoint of a researcher eager to maintain the physical context of excitation results, but it is also a blessing in disguise regarding the comprehensibility of the final results. Via the torque method for the atmosphere, partial amends can be made in the former matter, but one must equally allow for the substantial contributions of the oceans to measured Earth rotation variability. Striving for a successful cross-verification of those observations and the associated excitation terms, this chapter is thus an interdisciplinary blend of diverse geophysical and geodetic data.

7.1 Short period oceanic angular momentum – gravitational and atmosphere-induced effects

Mass-field variability and currents related to tides in the global ocean constitute the paramount driving agents of wobbling motion and changes in LOD at distinct frequencies around one or more cycles per day. The regular, periodic nature of the ocean tidal signal in sea surface heights and velocities directly relates to the amplitude and phase of some periodic geophysical forcing, its dominant portion naturally attributed to spatially varying gravitational forces arising from the regular movements of the Earth-Moon and Earth-Sun systems (Pugh, 2001). Secondary excitation mechanisms have been labeled as *non-tidal* forces in Section 2.4 and basically encompass the oceans' response to regular meteorological cycles, most notably the pressure loading exerted by thermal tides in the atmosphere. These radiational contributions are virtually negligi-

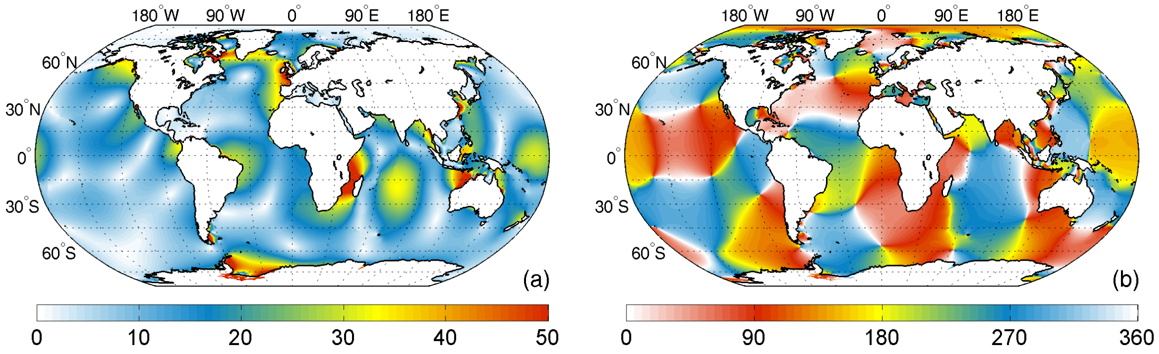

Figure 7.1: Tidal heights (a) and Greenwich phase lags (b) of the S_2 ocean tide as represented by the FES2012 model (Carrère *et al.*, 2012) produced under support of CNES (Centre National d'Études Spatiales) and distributed via `http://www.aviso.oceanobs.com/`. Heights given in units of cm and cotidal phases in degrees.

ble for most of the astronomical constituents (such as the K_1 and P_1 tides that coincide with the spectral lines of seasonal modulation in the diurnal solar heating cycle), but can reach several centimeters of elevation in the case of the main S_1 and S_2 waves (Lyard *et al.*, 2006). The relevance of both components in their respective frequency bands are markedly dissimilar, though, necessitating a somewhat different treatment of the oceanic S_1 and S_2 angular momentum in the compilation of Earth's high frequency excitation budget.

In order to aid the geophysical discussion of those effects in what follows, a brief categorization of the various types of ocean tide models shall be given. Forward tide or *hydrodynamic* models are conceived as mere solvers of the differential equations of fluid dynamics, driven solely by meteorological data. Augmentation of such models by manifold observational constraints in the form of sea level data from tide gauges or satellite altimetry yields so-called *assimilation* models, an early version of which (see Chao *et al.*, 1996, and references therein) still being the basis of predicted ocean tidal ERP variations in the IERS Conventions (Petit & Luzum, 2010, Chapter 8). The third species are purely *empirical* models, which do not invoke any physical equations but are instead derived from the direct analysis of observed sea surface changes (Lyard *et al.*, 2006).

7.1.1 The oceanic S_2 tide

As the second largest marine tide, S_2 is forced mainly by the gravitational potential and to a much lesser extent (by about one part in seven on the global average) by the semi-diurnal air pressure tide. After adjusting the radiational response in tidal heights for the 109° phase lag of the atmospheric forcing field with respect to the gravitational potential, the amplitude maps of both components are of great similarity, see Arbic (2005). Their cumulative effect, portrayed in Figure 7.1 by means of the newly published assimilation model FES2012 (*Finite Element Solution*, Carrère *et al.*, 2012), serves as a general illustration of the complex shape and temporal occurrence of ocean tides. Induced sea level variations are largely unrepresentative of the geometric forcing pattern, since their forming depends on a number of factors, such as the Coriolis force, the distribution of land masses, or energy dissipation over rough topography in the open ocean.

The mixed nature of the oceanic S_2 tide poses the question of how to optimally consider its excitation effect when juxtaposed to Earth rotation data. In principle, currently existing hydrodynamic models might be run with disjoint astronomical and meteorological forcing functions to produce separate gravitational and radiational solutions. The accuracy of purely gravitational S_2 simulations has been shown to be poor, though (Arbic, 2005), and the mere atmosphere-induced component is likely to be distorted by the insufficient standard sampling rate (6-hourly) of surface pressure analysis fields, see Brzeziński *et al.* (2004) or Lyard *et al.* (2006) but also Dobslaw & Thomas (2005) for a viable alternative employing 3-hourly forecasts. In addition, the success of atmosphere-driven hydrodynamic ocean models in predicting realistic meteorological tides relies much on solving the difficulties associated with the accurate characterization of the oceans' actual dynamic response to pressure forcing.

Assimilation models that constrain the full (gravitational + radiational) dynamical solution by ingesting satellite altimetry or potentially any in-situ or surface data therefore remain the most sensible choice for computing semi-diurnal ocean tidal angular momentum (OTAM) and thereupon ERP corrections. Given the dominance of those effects of up to two orders of magnitude over the faint atmospheric signals, a verification of geodetic observations solely by oceanic S_2 excitation values is warranted. Assembling OTAM estimates from various assimilation models might additionally convey a sense of the uncertainties inherent to those terms.

Two publicly available ocean tide models produced in the wake of more than a decade of multi-mission satellite altimetry data, TPXO7.2 (Egbert & Erofeeva, 2002) and HAMTIDE11a (Taguchi *et al.*, 2013), have been recently rendered to tidal ERP values by Böhm (2012). The present study replicates those efforts for the state-of-the-art FES2012 model by evaluating the global integrals of OTAM mass and motion terms at the frequencies of S_1 and S_2, see the short detour at the end of this section. Amongst the arsenal of earlier assimilation models, semi-diurnal OTAM harmonics are also accessible for the GOT99.2 solution of Ray (1999) via `http://bowie.gsfc.nasa.gov/ggfc/tides/mom_got99.html`. To produce a consistent blend of cos- and sin-amplitudes in ERP, i.e. $\{A^+, B^+\}$ for prograde polar motion, $\{A^-, B^-\}$ for retrograde polar motion, and $\{A^l, B^l\}$ for changes in LOD, the matter and motion terms of the S_2 components inherent to FES2012 and GOT99.2 were discretized over 1 yr, combined to complex-valued signals in the equatorial direction, and subject to a least squares fit of harmonic base functions[1]. The utilized parametrization adheres to that of Böhm (2012) (*ibid.*, Eqs. 6.1–6.3), which, in terms of single-frequency CIP perturbations $\delta\hat{p}(t)$ and LOD variations $\delta\mathrm{LOD}(t)$, reads

$$\delta\hat{p}(t) = \left(A^+ + \mathrm{i}B^+\right)\mathrm{e}^{\mathrm{i}\xi} + \left(A^- + \mathrm{i}B^-\right)\mathrm{e}^{-\mathrm{i}\xi} \tag{7.1}$$

$$\delta\mathrm{LOD}(t) = A^l\cos(\xi) + B^l\sin(\xi)\ , \tag{7.2}$$

---

[1] This detour via the time domain is introduced for didactic reasons regarding the next sections. It can be in principle replaced by a much shorter, direct conversion of OTAM harmonics to ERP harmonics.

Table 7.1: Semi-diurnal ocean tidal contributions (gravitational + radiational) to changes in LOD and polar motion as estimated from four hydrodynamic assimilation models. Perturbations in units of µs (µas) and termed as δLOD ($\delta\hat{p}$).[a] For each component, the mean value and the sample standard deviation (denominator $n-1$, see Section 2.2. of Otnes & Enochson, 1978) across $n = 4$ samples is quoted, too.

	δLOD, S_2		$\delta\hat{p}$, S_2^+		$\delta\hat{p}$, S_2^-	
Model	A^l	B^l	A^+	B^+	A^-	B^-
GOT99.2	92.2	-13.4	1.1	-28.8	-65.6	103.0
TPXO7.2	106.6	-3.4	1.6	-26.1	-70.0	110.6
HAMTIDE11a	106.3	-15.8	-1.2	-25.5	-64.4	112.8
FES2012	110.3	-4.8	6.3	-27.5	-61.6	112.6
sample mean	103.9 ± 8.0	-9.4 ± 6.2	2.0 ± 3.1	-27.0 ± 1.5	-65.4 ± 3.7	109.8 ± 4.6

[a] The phase inherent to the harmonic decomposition refers to the fundamental arguments of the S_2 tide (period exactly 0.5 d).

see Eqs. (A.1), (A.2), and (A.9) for the exact expressions of equatorial coefficients. With S_2 primarily being a gravitational phenomena, the argument $\xi = \xi(t)$ (frequency and phase) of the base functions was computed as a linear combination of six fundamental astronomical arguments by aid of pre-coded subroutines following the IERS Conventions (Petit & Luzum, 2010). Equations (3.15) and (3.17) translate the adjusted coefficients to the excitation values summarized in Table 7.1 together with respective estimates from TPXO7.2 and HAMTIDE11a, for which the cited UT1 amplitudes $\{A^u, B^u\}$ were converted to LOD amplitudes at $\sigma = 2$ cpd via the frequency domain differentiation scheme for ideal harmonics

$$A^l = -B^u \sigma \cdot 86400\,, \qquad B^l = A^u \sigma \cdot 86400\,. \tag{7.3}$$

As TPXO7.2, HAMTIDE11a, and FES2012 share much of the recently acquired altimetry data, one might expect them to agree well also on the level of Earth rotation variations. A tentative confirmation of this presumption is found only for the dominant in-phase component A^l in δLOD (∼106 µs) and the out-of-phase term B^- in $\delta\hat{p}$ (∼112 µas), for which the somewhat dated GOT99.2 model produces uncomfortably different results. The overall disparities confirm Brzeziński *et al.* (2004)'s assertion of the uncertainties in present semi-diurnal OTAM estimates being comparable to the size of the atmospheric excitation effect.

Computation of ocean tidal angular momentum

The tidal variables provided by FES2012 for 32 constituents at frequencies σ comprise sea height anomalies $\zeta(\sigma)$ as well as eastward and northward current velocities $u(\sigma), v(\sigma)$ at regular grids of 1/16° horizontal spacing. Assuming a flow that is uniform over the water column with undisturbed depth $D = D(\theta, \lambda)$ (available from the *General Bathymetric Chart of the Oceans* at `www.gebco.net`), the components of the OTAM vector, or rather its temporal variation, can be written as double integrals over the ocean surface (Chao & Ray, 1997)

$$\hat{H}^h = -\Omega a^4 \rho_w \iint_{ocean} \zeta(\sigma) \cos\theta \sin^2\theta e^{i\lambda} d\theta d\lambda \tag{7.4}$$

$$H_z^h = \Omega a^4 \rho_w \iint_{ocean} \zeta(\sigma) \sin^3\theta d\theta d\lambda \tag{7.5}$$

$$\hat{H}^c = -a^3 \rho_w \iint_{ocean} D(u(\sigma)\cos\theta + iv(\sigma)) \sin\theta e^{i\lambda} d\theta d\lambda \tag{7.6}$$

$$H_z^c = a^3 \rho_w \iint_{ocean} Du(\sigma) \sin^2\theta d\theta d\lambda \,. \tag{7.7}$$

Akin to the AAM formulae, the inertia effect in $\hat{H}$ and H_z has been separated from the motion term, and their respective superscripts are h (for *heights*) and c (for *currents*). The parameter ρ_w denotes the mean density of sea water. Tabulations of the S_1/S_2 mass and motion terms from FES2012 can be found in Appendix A.4.

7.1.2 The oceanic S_1 tide

The oceanic tide at the S_1 frequency represents an 'anomalous' phenomenon inasmuch as its gravitational excitation is minor as against the radiational effect in the form of the diurnal atmospheric tide. Ray & Egbert (2004) have recapitulated the likely generation mechanisms, finding that both thermal expansion in surficial water masses as well as wind stress forcing are negligible contributors compared to the pressure loading by the S_1 air tide. The complex spatial pattern of induced sea level oscillations, including large magnitude signals (> 15 mm) in the Gulf of Alaska, the Okhotsk Sea, the Arabian Sea, the eastern Indian Ocean, and especially the shallow Arafura Sea, is depicted in Figure 7.2. Qualitatively, the amplitude chart presages a sizable impact on rotational quantities, as tidal elevations of 2 cm equate to 200 Pa of water column height, which

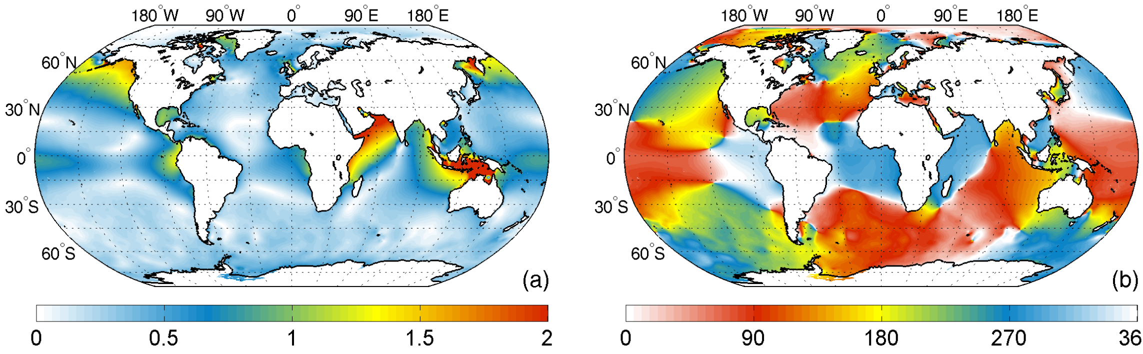

Figure 7.2: Tidal heights (a) and Greenwich phase lags (b) of the S_1 ocean tide as represented by the FES2012 model. Heights given in units of cm and cotidal phases [deg] reckoned relative to GMT = 0 in compliance with Figures 4.1, 4.2, and 6.9.

Table 7.2: Diurnal oceanic contributions to changes in LOD (and polar motion, respectively) in units of µs (µas) and termed as δLOD ($\delta\hat{p}$). Gravitational component from TPXO7.2 (Böhm, 2012) shown separately from the radiational part.[a]

	δLOD, S_1		$\delta\hat{p}$, S_1^+	
Source	A^l	B^l	A^+	B^+
Ray & Egbert (2004)	6.6	-0.8	-0.3	3.6
Brzeziński *et al.* (2012)	5.6	1.2	1.8	2.9
This study, FES2012	4.7	1.5	1.3	2.7
Böhm (2012), gravitational part	0.8	0.5	1.0	-0.7

[a] The phase inherent to the harmonic decomposition refers to the fundamental arguments of the gravitational S_1 tide (period 0.99999999 d), see explanations in the text.

is a definite match to the peak amplitudes of the diurnal air pressure tide (Figure 4.1a).

Reasonable accurate estimates of the radiational oceanic S_1 component originate from hydrodynamic time-stepping models on condition that the meteorological forcing data are themselves accurate (Lyard *et al.*, 2006). Both time-invariant surface pressure maps and 'real-time' analysis fields have been deployed for that purpose, with caveats on the negative effect of 6-hourly sampling usually being small (Brzeziński *et al.*, 2004). This thesis utilizes the angular momentum/excitation offspring of three present-day determinations of the S_1 ocean tide: the hydrodynamical solution of FES2012, which has been converted to OAM harmonics in the frame of this study (see Section 7.1.1 and Table A.3); Ray & Egbert (2004), whose result grounds on the time-stepping model of Egbert & Erofeeva (2002) under the constraint of a 13-year average of the diurnal barometric tide (Ray & Ponte, 2003); and Brzeziński *et al.* (2012), who analyzed consistently produced angular momentum series from a coupled atmosphere-ocean simulation covering 1990–2009. The oceanic component of this system is OMCT (*Ocean Model for Circulation and Tides*, Thomas, 2002), driven by 3-hourly forecast fields from ERA-Interim (Dobslaw & Thomas, 2005). Table 7.2 itemizes the ERP perturbations deduced from all three sources. In accordance with the results of Brzeziński *et al.* (2012), phase and frequency of the S_1 excitation values were referred to the fundamental arguments of nutation theory, implying a minute disparity from the radiation-bound frequency of exactly 1 cpd by $\sim$1/21000 cpy due to the apparent motion of the solar perigee. The spectral lines of the gravitational and radiational S_1 component thus coincide (period $T = 0.99999999$ d, cf. Chapter 8 of Petit & Luzum, 2010). More to the point, the astronomical phase convention was enforced upon the strictly diurnal OAM values from FES2012 and Ray & Egbert (2004) by discretizing them during 2007–2011 and adjusting harmonic coefficients in the usual manner, see Section 7.1.1.

Table 7.2 reveals a reasonably good agreement of the OAM excitation values from all sources, in particular in terms of LOD perturbations δLOD. The gravitational part of the oceanic S_1 tide produces ERP variations of subordinate amplitude, and the available models (IERS Conventions, TPXO7.2, and HAMTIDE11a, see Böhm, 2012) are concordant in this respect. Note that the elevations of minor astronomical tides such as S_1 usually derive from interpolation of the major tides' known admittances, i.e. smooth scaling functions relating the tide-generating potential to the associated sea level change. The conjuncture of having such a small gravitational influence at the diurnal frequency is definitely conducive to the verification of atmosphere-induced signals in polar motion and LOD against geodetic observations (Brzeziński *et al.*, 2004).

Validity issues

The superposition of oceanic and atmospheric excitation estimates entails a few inadequacies that have to be kept in mind. First, a dynamically coupled atmosphere-ocean model yielding consistent angular momentum and/or torque estimates from both fluids represents the route of choice in present-day considerations of geophysically-induced Earth rotation studies (e.g. Dobslaw *et al.*, 2010), but none of the utilized atmospheric (re)analysis systems is entirely consistent with the OAM values at hand. However, the ERA-Interim estimates should be reasonably consistent with the S_1 solution of Brzeziński *et al.* (2012), albeit the OMCT forcing extends over two decades instead of 2007–2011. A similar tentative coupling applies to the values from ECMWF DC and FES2012 as the meteorological constraints of the hydrodynamic ocean model are 10 yr of 3-hourly delayed cut-off forecasts (Carrère *et al.*, 2012). Ray & Egbert (2004)'s S_1 tide, based on ECMWF operational analysis data, also favors the excitation measures from ERA-Interim and DC forecasts. Yet, the results from MERRA do not need to be discounted in this regard, as a retrospective view of the pressure cycle RMS differences in Table 6.3 shows. MERRA seemingly matches the interagreement of both ECMWF models across the sea surface. Moreover, the generally low discrepancies between *all* three datasets (7.4 Pa global mean RMS differences in the diurnal band, with the average S_1 amplitude over the oceans being about 28 Pa) suggest that the pressure-induced oceanic currents and inertia effects might approximately be the same for varying forcing functions from different meteorological centers. Although analogous arguments can be brought forth for the S_2 tide, the influence of forcing field inconsistencies is positively below the level of uncertainties inherent to the dominant gravitational S_2 component, cf. Table 7.1.

As a second conceptual deficiency, the oversimplified assumption of time invariant geophysical phenomena has been invoked at numerous instances. While such an approach is in accordance with the strategy of this thesis or also with that of comparative studies like Brzeziński *et al.* (2012), one has to bear in mind that atmospheric tides and hence the forcing of hydrodynamic ocean models exhibit non-negligible temporal variations on seasonal and inter-annual time scales, cf. Ray & Ponte (2003) and also the phasor plots of excitation measures in Figures 5.13 and 5.17. Specifically, Ray & Egbert (2004) use a time invariant map of the S_1 barometric tide in driving their time-stepping model, implying that their estimate cannot reproduce the full pressure-induced tidal variability (Dobslaw & Thomas, 2005). These shortcomings might be acceptable for the purpose of the present work but certainly become more critical when instantaneous geophysical measures are employed for de-aliasing altimeter measurements (Lyard *et al.*, 2006) or gravity field estimations. Note also that combining time-averaged excitation values from different sources papers over the fact that the underlying observation periods generally disagree.

7.2 Compilation of geodetic S_1 and S_2 estimates

In recent years, numerous empirical models of short period ERP variations have been inferred from long-term space geodetic observations. Here, the S_1 and S_2 predictions of three different VLBI solutions and a stand-alone GPS reprocessing are utilized, cf. Table 7.3. Juxtaposing those models in terms of the differences and commonalities provides insight into their reliability and consistency (Artz *et al.*, 2011), and some of these features are to be touched upon in this thesis.

VLBI1 (Böhm *et al.*, 2012b): The collective tidal terms cited in the IERS Conventions (Chapter 8 of Petit & Luzum, 2010) were estimated as sinusoids by virtue of a standard time series approach applied on hourly (but not equidistant) ERP values. A two-step analysis of sessions covering the period 1984.0–2010.5 with VieVS (*Vienna VLBI Software*, Böhm *et al.*, 2012a) involved an initial determination of daily ERP and celestial pole offsets before fixing the latter in the second run, which produced the highly resolved polar motion and dUT1 series.

VLBI2 (Artz *et al.*, 2011): The coefficients of a poly-harmonic sub-daily ERP model were inferred from a global adjustment of accumulated normal equations after transforming them from a time domain representation to a spectral representation at tidal frequencies. This rigorous solution draws on 30 yr of observations and is believed to be slightly superior to the time series approach. Yet, their S_1/S_2 values (VLBI1 and VLBI2 in Table 7.3) largely agree, especially in the polar motion components.

VLBI3 (Gipson & Ray, 2009): Tidal ERP variations from this global adjustment of VLBI observations during 1979.8–2010.4 have been reported by Artz *et al.* (2011). Distinctions to the above models can be found in the set up of auxiliary parameters, such as tropospheric effects, and the treatment of geophysical influences in the computation of the theoretical delay. Specifically, no a priori ocean tidal model was taken into account as in the case of VLBI1 and VLBI2,

Table 7.3: Diurnal/semi-diurnal LOD and polar motion coefficients as observed by GPS (Steigenberger, 2009) and three different VLBI solutions: Böhm *et al.* (2012b) (VLBI1), Artz *et al.* (2011) (VLBI2) and Gipson & Ray (2009) (VLBI3). Coefficients in units of µs for δLOD and µas for polar motion perturbations $\delta\hat{p}$.

	δLOD, S_1		δLOD, S_2		$\delta\hat{p}$, S_1^+		$\delta\hat{p}$, S_2^+		$\delta\hat{p}$, S_2^-	
Acronym	A^l	B^l	A^l	B^l	A^+	B^+	A^+	B^+	A^-	B^-
VLBI1	3.6	-0.3	100.7	-8.6	10.6	11.2	-4.9	-33.9	-72.1	107.6
VLBI2	6.1	-1.0	92.2	-11.8	8.8	10.4	-1.2	-29.8	-74.7	105.2
VLBI3	3.5	0.8	95.3	-11.6	-3.9	5.5	-5.2	-21.0	-68.8	110.7
GPS	4.7	-2.5	94.6	-10.8	10.0	-3.6	3.5	-29.2	-63.6	111.7

whereas atmosphere-induced station displacements with seasonal and (semi-)diurnal frequencies were corrected for. Artz *et al.* (2011) suppose that these conceptual differences enforce much of the ERP discrepancies as apparent for δLOD (S_1) and $\delta\hat{p}$ (S_1^+, S_2^+) in Table 7.3.

GPS (Steigenberger, 2009): The reprocessing of global GPS measurements from 1994.1–2005.10 was accomplished by interlinking solutions at multiple stages (1 d, 3 d, 1 week), where the dense temporal availability of observations permitted the estimation of sub-daily ERP at 2-hourly, equidistant intervals. Appropriate initial values for dUT1 as well as tight constraints on the nutation parameters following the conventional model of Mathews *et al.* (2002) were incorporated. The geophysical modeling included a priori values for ocean tides but no loading corrections similar to VLBI1/VLBI2. Tidal harmonics of polar motion and dUT1 were extracted a posteriori, but are presumably subject to systematic effects as a result of their correlation to orbital biases. However, significant deviations from the VLBI solutions in Table 7.3 merely occur at S_1^+, though, larger differences have been reported by Artz *et al.* (2011) based on an updated version of Steigenberger (2009).

7.3 Cross-verification of geodetic observations and excitation terms

7.3.1 Determination and discussion of atmospheric excitation estimates

Pursuant to the thesis' emphasis on the torque approach, both angular momentum and torque quantities were deployed to obtain numerical values of the atmosphere's direct contribution to the excitation budget at the frequencies of S_1 and S_2. The prerequisite processing in the axial direction consisted of high-pass filtering (fifth-order Butterworth, cut-off frequency at 0.2 cpd) the time series of H_z^p, H_z^w, L_z^m, and L_z^f, before adjusting sin- and cos-amplitudes for each term by reference to the fundamental arguments of the S_1 and S_2 tidal constituents. Harmonic coefficients for $\delta\text{LOD}(t) = A^l \cos(\xi) + B^l \sin(\xi)$ were readily accessible via Eq. (3.15) for the angular momentum approach, while mountain and friction torque terms had to be integrated to AAM values by a reciprocal version of Eq. (7.3) ahead of the application in the hybrid torque scheme (Eq. 3.46, separate evaluation of sin- and cos-coefficients).

The computation of CIP perturbations from standard AAM series resembled the treatment of oceanic effects in Section 7.1.1 except for an initial high-pass filtering of $\hat{H}^p$ and $\hat{H}^w$. Harmonic amplitudes of pressure and wind components were adjusted separately, converted to pro- and retrograde terms following Eq. (A.9), and scaled to excitation values by means of the respective transfer coefficients in the broad-band Liouville equation (Gross, 1993). The modified torque approach suggested in Section 3.3.4 reduces to exactly the same strategy but draws on the torque-based wind term defined in Eq. (3.45). As demonstrated in Schindelegger *et al.* (2013c), this expression can be conveniently evaluated by aid of the two-sided DFT of equatorial torques and the attached discrete frequency vector σ_e (Eq. 5.1). In order to circuit any distortion of the resulting time series in the wake of resonance effects near $-\Omega$, the Fourier coefficients of $\hat{H}^w(\sigma)$ allocated to frequencies between -1.5 and -0.5 cpd were set to zero prior to performing the inverse

Table 7.4: Diurnal/semi-diurnal coefficients of atmospheric excitation signals in LOD and polar motion. ERA-Interim, MERRA, and ECMWF DC estimates deduced from both standard AAM series as well as the hybrid torque scheme introduced in Section 3.3.4. Gray numbers highlight components that are affected by seemingly erroneous wind terms and/or pressure terms (i.e. ellipsoidal torques) as judged from the AAM balance examination. Coefficients in units of μs for δLOD and μas for polar motion perturbations $\delta\hat{p}$.[a]

		δLOD, S_1		δLOD, S_2		$\delta\hat{p}$, S_1^+		$\delta\hat{p}$, S_2^+		$\delta\hat{p}$, S_2^-	
Method	Model	A^l	B^l	A^l	B^l	A^+	B^+	A^+	B^+	A^-	B^-
Angular momentum	ERA-Interim	-7.9	-4.1	0.1	-0.1	1.6	-0.8	-1.2	2.9	-5.4	-2.2
	MERRA	-5.0	-1.6	0.0	0.3	0.1	-0.8	0.0	-0.4	-1.6	-0.6
	ECMWF DC	-0.4	-1.9	2.3	-4.3	2.1	0.3	0.0	-0.4	-1.5	0.3
Torques	ERA-Interim	-1.8	0.2	0.4	-0.1	1.0	-0.8	-0.1	0.0	1.8	0.8
	MERRA	-1.1	-0.6	0.3	0.7	0.5	-0.7	-0.1	-0.1	-1.7	0.1
	ECMWF DC	-2.4	-0.1	-0.4	0.3	0.9	-0.9	0.0	-0.1	-1.1	0.0

[a] Corresponding phase values referred to the fundamental arguments of the S_1 and S_2 tidal constituents.

DFT on the torque-based wind term.

Table 7.4 summarizes the final harmonic coefficients of (semi-)diurnal atmospheric ERP signals, which may be compared to results of previous publications (e.g. Brzeziński *et al.*, 2002, 2012, see below) in case no correction for the static part of the oceans' response to air pressure fluctuations has been imposed on the estimates. Having investigated the balance of the full AAM vector in advance, it is now possible to point out components that are affected by probably erroneous AAM terms or ellipsoidal torques (NB: while local terms are certainly not void of deficiencies, the persistent agreement of mountain and friction effects from different sources supports their overall validity). Most of those caveats concern ERA-Interim, notably its excitation prediction for the S_2^- band in polar motion, which is corrupted both within the angular momentum and the torque approach by the anomalous pressure term identified already in Section 6.2.3. Judging by Figures 5.8e and 5.9e, the AAM-based estimates of diurnal changes in LOD from ERA-Interim and MERRA are equally lacking in credibility. By virtue of the loading correction ($-0.243H_z^p$) in Eq. (3.46), the problematic axial S_1 pressure term enters the torque method to some extent, even though the shading has been omitted at this place in Table 7.4.

In general, the deduced estimates are of very small magnitude (0–2 μs/μas) in accordance with recent determinations of ERP signals from hourly or 3-hourly AAM series (Brzeziński *et al.*, 2012; Schindelegger *et al.*, 2011). Larger discrepancies in comparison to the results from 6-hourly data (Brzeziński *et al.*, 2002) can be attributed to inadequacies of atmospheric models, aliasing effects, or different analysis strategies. With the exception of the equatorial S_2^- component, semi-diurnal excitation values appear to be especially minuscule owing to the distinct compensation of pressure and wind terms as anticipated in Sections 3.3.4 and 5.1. The S_2^+ band is a prime example in this regard, featuring almost negligible local torques (Figure 5.9b for instance), what in turn implies $\hat{H}^w(\sigma) \approx -\hat{H}^p(\sigma)$ as per Eq. (3.45), thus a near-perfect cancellation of pressure and wind excitation estimates of magnitude 1 µas apiece (not tabulated). In similar fashion, the S_1^+ bulge torque overwhelms mountain and friction effects (Figure 5.9a), and for the B^+ term this constellation implies that the wind excitation (1.8 µas for ECMWF DC) counters much of the pressure term contribution (−2.7 µas). Note also that the formal uncertainties of all adjusted coefficients (at the level of 0.1–0.2 µs/µas throughout) have not been maintained as they offer no particular asset in the following.

7.3.2 The semi-diurnal excitation budget

Section 7.1.1 already acknowledged the subordinate relevance of atmospheric effects compared to the oceanic S_2 tide in explaining semi-diurnal Earth rotation variability. Aiming at the presentation of some supplementary information to existing, largely successful cross-verifications (e.g. Böhm, 2012; Chao *et al.*, 1996), this study creates an approximate 'solution space' for the ERP residuals after removal of ocean tidal effects instead of explicitly citing their absolute values.

Equatorial component

In view of the considerable number of assembled geodetic ERP models and rotational predictions from hydrodynamic assimilation models, the residual semi-diurnal polar motion budget for each solution may be best visualized by subtracting only the mean OTAM correction (Table 7.1) and including the sample standard deviation from GOT99.2, TPXO7.2, HAMTIDE11a, and

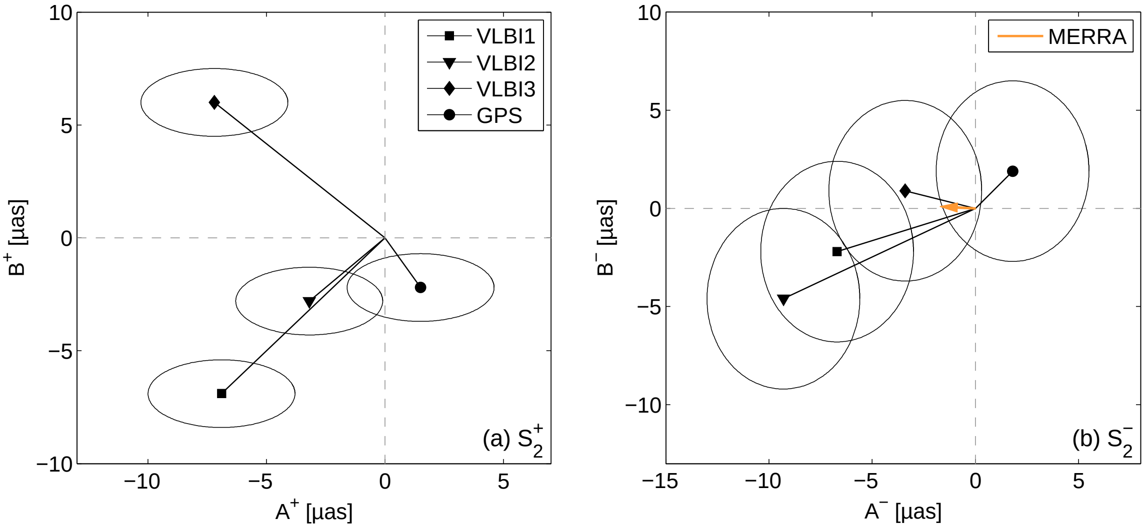

Figure 7.3: Residual polar motion excitation budget at semi-diurnal prograde (a) and retrograde (b) frequencies computed by subtracting the mean ocean tidal contributions (Table 7.1) from the four geodetic determinations of the S_2 tidal effect, see Section 7.2. The sample standard deviation of OTAM sin- and cos-coefficients has been attached to each estimate, and the direct atmospheric contribution to S_2^- from MERRA torque terms has been included in order to depict the different proportions of atmospheric and oceanic effects.

FES2012 as a proxy 'error ellipse'. Those curves do not represent error estimates *per se*, but are rather rough indicators of the variability that can be expected when utilizing present-day ocean tide models to explain Earth rotation observations. Specifically, they also showcase how the subtraction of ocean tidal terms from a single, arbitrarily chosen source can affect the interpretation of geodetic residuals.

The corresponding plots for the semi-diurnal polar motion bands in Figure 7.3 reveal budget deficiencies in the range of 2–10 µas, with the S_2^+ component being subject to a larger mismatch of the observed variations than in the case of S_2^-. Gipson & Ray (2009)'s VLBI3 solution for the prograde semi-diurnal component appears to be particularly offset with regard to all other models. Parts of this disparity are almost certainly repercussions of the different a priori treatment of geophysical fluid effects in the VLBI analysis, cf. Section 7.2, but then again, no such distortion can be observed for the VLBI3 phasor in the retrograde band. Moreover, the S_2^- budget is characterized by a relatively large (absolute) variability in its ocean tidal correction, presumably in consequence of the actual size of the effect ($B^+ \sim 110$ µas from Table 7.1, exceeding the B^- term by a factor of four, for instance). With the sample standard deviations in both sin- and cos-terms of oceanic excitation being at the level of 4 µas, an approximate verification of the atmospheric contribution to retrograde semi-diurnal polar motion (< 2 µas) does not stand to reason, yet. Geodetic residuals near zero, such as those emerging from the combinations VLBI2–GOT99.2 or GPS–GOT99.2 for S_2^+ and VLBI3–TPXO7.2 or GPS–HAMTIDE11a for S_2^- (not depicted in Figure 7.3), are rather fortuitous than of real physical significance.

Axial component

While the oceanic S_2 tide supplies the major point for discussion in the axial direction alike, it is imperative to account in advance for the influence of semi-diurnal spin libration following the conventional model of Petit & Luzum (2010) (*ibid.*, Table 5.1b). In terms of LOD variations, the suggested harmonic coefficients are $\{A^l, B^l\} = \{-9.5, -5.5\}$ µs at the exact frequency of S_2, and Böhm (2012) recently demonstrated how this correction and that of nearby tidal constituents improves the consistency of observed and modeled changes in LOD. As evident from Figure 7.4, the spread of geodetic residuals after reducing both libration and oceanic signals is uncomfortably high, amounting to about 8% of the full ocean tidal in-phase component A^l. On closer examination, this large sample standard deviation can be traced back to an apparent underestimation of the axial current term H_z^c within the GOT99.2 model by about $7 \cdot 10^{23}$kgm^{2}s^{-1} with respect to TPXO7.2, HAMTIDE11a, and FES2012, cf. the numerical values at `http://bowie.gsfc.nasa.gov/ggfc/tides/mom_got99.html` with Table A.3 (this study) and with Tables 6.1/6.2 of Böhm (2012). The geophysical signal governing the H_z^c prediction is an extraordinarily strong zonal volume transport across the equatorial Indian Ocean (see Figure C2 of Ray, 1999). A slightly deficient representation of this current within GOT99.2, which is based on a mere 6 yr of altimeter data, seems likely (R. Ray, personal communication), and one might exclude the corresponding correction in Figure 7.4. However, this modification does

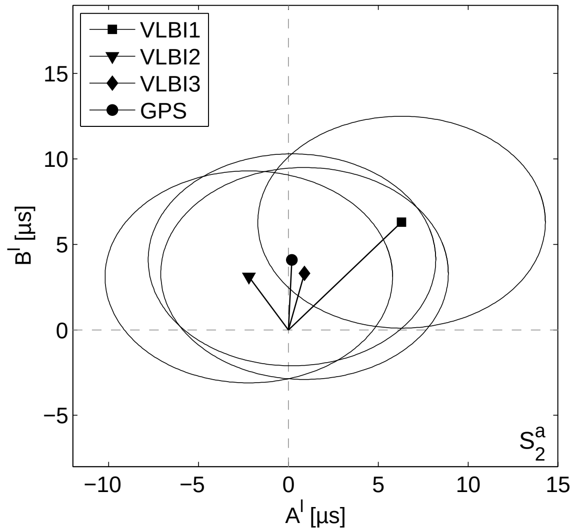

Figure 7.4: Residual excitation budget for semi-diurnal changes in LOD computed by subtracting the mean ocean tidal contributions (Table 7.1) and the effect of spin libration from the four geodetic determinations of the S_2 signal in the axial direction. The sample standard deviation of OTAM sin- and cos-coefficients has been attached to each estimate.

not conceal the fact that most of the VLBI/GPS–OTAM combinations yield randomly distributed remainders of 5–10 µs or even larger size.

7.3.3 The diurnal excitation budget

The smallness of the gravitationally-forced diurnal ocean tide allows for a truly meaningful cross-check of geodetic observations and the modeled atmospheric excitation signal—encompassing both the direct effect of atmospheric fluid dynamics on the angular momentum of the solid Earth as well as that portion engendered by the oceans' response to diurnal air pressure variations. Caveats on the validity when combining data from various sources have already been given in Section 7.1.2 and must be borne in mind in the following.

Equatorial component

Figure 7.5a provides a graphical assessment of the prograde diurnal polar motion budget, involving the torque-based atmospheric phasors from ERA-Interim and ECMWF DC superimposed on the radiational OAM signal as predicted by Ray & Egbert (2004) and Brzeziński *et al.* (2012). Further model pairings utilizing MERRA torque terms and FES2012 were omitted as no distinctly different information would have been supplied, see the agreement of harmonic coefficients at S_1^+ in Table 7.2 and Table 7.4, respectively. Also, standard AAM estimates could have been incorporated, even though their coherence is somewhat inferior to that of the torque terms. The verdict on the S_1^+ budget is disappointing in any case: neither do the Earth rotation observations offer a consensus on the most probable composition of the geodetic evidence, nor are the atmosphere-ocean excitation signals capable of explaining any of the S_1^+ determinations from GPS/VLBI, see also Brzeziński (2008). The mutual agreement of VLBI1 and VLBI2 probably owes much to their similarities in the modeling of the theoretical delay, while Gipson & Ray (2009)'s different handling of selected geophysical influences in the analysis also leads to different harmonic coefficients after the global adjustment. As mentioned earlier, the correlation with orbit errors impinges on the GPS-based ERP predictions in all likelihood and one should not lend too much credence to those values. In general, Figure 7.5a represents a step backward from a similar comparison in Böhm (2012), where the OAM+AAM results of Brzeziński *et al.* (2004) could account for at least 50% of the observed diurnal polar motion signal from VLBI. The size of this cumulative geophysical excitation is, however, debatable in light of the imperfect 6-hourly sampling of the underlying meteorological fields, and present-day determinations of the effect have led to a partial rebuttal (Brzeziński *et al.*, 2012). On the basis of this study's detailed investigations, the agreement of up-to-date models in terms of the geophysical fluid effect at S_1^+ is fairly acceptable, supported in particular by a reasonably well closed AAM budget (Chapter 5). Attempts of further advancing the agreement between geophysical and geodetic quantities should therefore primarily address the ERP artifacts introduced by measurement uncertainties and the parameter estimation strategy. Nevertheless, one has to acknowledge that an unambiguous detection of wobbling motion as small as 3 µas (i.e. 0.1 mm at the Earth's surface) might ultimately exceed the sensitivity of VLBI and global GPS networks.

Axial component

Verification of the diurnal excitation budget for changes in LOD proves to be the eventual flagship component of the present chapter. It is portrayed in Figure 7.5b and assembles estimates from basically the same sources as its S_1^+ counterpart above, including once again Ray & Egbert (2004)'s and Brzeziński *et al.* (2012)'s oceanic excitation values in the favor of FES2012. Caution has to be exercised when selecting appropriate estimates of the atmosphere's direct effect on LOD variations, predominantly due to the questionable reliability of pressure and wind terms as recognized from the AAM balance examinations in Section 5.3 and the model cross-check in Section 5.4. Brzeziński (2008) and Böhm (2012) document a clear degradation in the diurnal excitation budget when superimposing various AAM solutions on the rather coherent OAM phasors, and the comparison in Figure 7.5b would likewise go astray if it drew on the AAM signals of ERA-Interim or MERRA. Instead, an evasion to the alternative torque approach eventually produces an hitherto unmatched agreement between geodetic and geophysical quantities. The VLBI residuals are specifically well explained by any of the OAM–torque pairings, and the combination of phasors from Ray & Egbert (2004) and MERRA gives a near-perfect account of the S_1 coefficients as deduced by Artz *et al.* (2011) (VLBI2).

Yet, the application of the axial torque scheme (Eq. 3.46) is not without detriment. It involves the diurnal pressure term H_z^p as a very critical excitation measure (cf. Figures 5.8e, 5.9e, 5.10e,

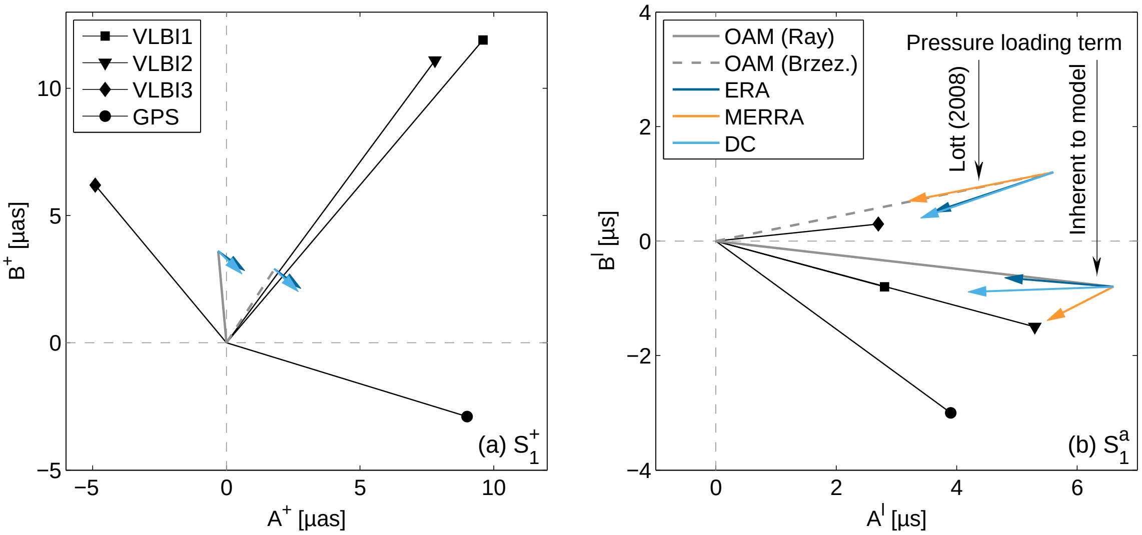

Figure 7.5: Diurnal excitation budget for prograde polar motion (a) and changes in LOD (b). The four geodetic determinations VLBI1, VLBI2, VLBI3, and GPS are given with respect to the small gravitational ocean tide contribution from TPXO7.2 and should balance the cumulative effect of pressure-forced OAM (two solutions from Table 7.2 depicted: Brzeziński *et al.*, 2012; Ray & Egbert, 2004) and atmospheric excitation from either ERA-Interim (blue arrows), MERRA (orange arrows), or ECMWF DC (turquoise arrows). All atmospheric phasors have been derived from torque quantities, with the pressure loading term in the axial direction conforming to that of Lott *et al.* (2008) for one selected solution, see labels.

5.13c), rendering the torque-based LOD predictions more incoherent than one might desire. Various determinations of the pressure loading correction ($-0.243H_z^p$) from the utilized models differ by nearly 1 μs in magnitude, with the ERA-Interim and MERRA versions being particularly vulnerable to deficiencies. Hence, the self-consistent atmospheric excitation estimates in Figure 7.5b are augmented by a makeshift solution, where the pressure loading effect has been inferred from an independent external source—in this case the simulation result of Lott *et al.* (2008). When superimposed on the OAM term of Brzeziński *et al.* (2012), these 'hybrid' atmospheric phasors produce an excellent match to the geodetic evidence from VLBI3. Notwithstanding that merging geophysical fluid effects from diverse sources somewhat restricts the validity of Figure 7.5b, the attained budget closure epitomizes a core result of this study, built on the benefits of a closely examined AAM balance and the mutual comparison of excitation measures. Considering that the approximate magnitude of the verified rotational perturbation is 4 μs in LOD, or equivalently 0.3 mm at the equator, the achieved agreement testifies also the prowess of state-of-the-art space geodetic techniques.

Chapter 8

Summary and conclusions

Diurnal and semi-diurnal radiational tides in the atmosphere elicit changes in LOD and polar motion on a level that is generally perceptible by modern space geodetic techniques. Significant signal components issue from both the direct influence of atmosphere dynamics on the solid Earth as well as oceanic mass-field variability and currents driven by air pressure variations. Detailed investigations of those phenomena foster the understanding of Earth system dynamics but also contribute to improving selected bands of high-frequency Earth rotation models, which are deployed in the analysis of space geodetic observations and the prediction of ERP. Two equivalent modeling approaches, utilizing either AAM quantities or Earth-atmosphere interaction torques, have been proposed for quantifying in particular the direct portion of the atmospheric effect, but standard estimates from AAM series are markedly inconclusive on the most probable harmonic coefficients of induced ERP perturbations. The central objective of the present thesis is to remedy this uncertainty by assessing the reliability of (semi-)diurnal torque and AAM terms from present-day atmospheric analysis and reanalysis systems. The acquired insight into the validity of excitation measures stimulates a reconsideration of Earth's short period rotational budget as another major research aim. On a more fundamental level, existing torque approach formalisms must be reconciled with the challenges posed by Earth rotation studies at the highest frequencies. A compilation and discussion of the prime findings concerning these three issues is presented below.

8.1 Have the set objectives been mastered?

The narrative of this study first provides the basis on which ellipsoidal, mountain, and friction torques can be interrelated with reported Earth rotation quantities at (semi-)diurnal periodicities. This mathematical framework is required to include FCN resonance effects and simultaneously avoid inconsistencies when combining torque terms for the atmosphere and angular momentum terms for the oceans. Following Schindelegger *et al.* (2013c), the standard torque formalism is therefore replaced by a hybrid solution in the spectral domain, where total equatorial and axial torques are translated to AAM changes and subsequently inserted in the established angular momentum excitation schemes. These AAM surrogates appear to be particularly beneficial in the axial component, where the standard angular momentum route is numerically impaired by a compensation constraint between large but nearly opposite pressure and wind term phasors (Lott *et al.*, 2008). Similar constellations are apparent for selected polar motion components that accommodate dominant bulge effects (prograde S_1 and S_2 bands), and in these cases the 'hybrid' torque approach almost solely depends on the quality of the ellipsoidal torque. Overall, by evading possibly erroneous AAM wind and/or pressure terms, the investigated torque scheme represents a viable alternative to the routinely used pure angular momentum approach.

Based upon the 3-hourly forecast and assimilation fields of ERA-Interim, MERRA, and ECMWF DC for 2007–2011, an expansive survey on the validity of consistently calculated atmospheric torque and angular momentum terms at the exact frequencies of 1 and 2 cpd is accomplished. In the first place, the experiment resorts to a complete breakdown and verification of the AAM balance equation, leading to a significant betterment of previously published comparisons. Occasional deficiencies persist, but the overall similarities of the budget among all models as well as effective verifications in specific cases (MERRA) positively warrant a torque-based view of short period ERP signals. The mutual agreement of atmospheric models in terms of mountain and friction torques—considerably exceeding the match achievable for AAM quantities—even substantiates this proposition. Partly, the seeming superiority of the use of local torque terms might be attributed to the convergence of atmospheric (re)analysis systems, but then again, one must not lose sight of the fact that (semi-)diurnal mountain and friction torques relate to the whole magnitude spectrum of atmospheric surface tides whereas pressure and wind terms are sensitive to small secondary modes only.

Several S_1 and S_2 mass components are particularly suspicious and need to be further validated by external pressure term solutions constructed on the basis of long-term, high-resolution barometer recordings from continental stations and marine reports. The imposed functional model draws on a low-degree spherical harmonic decomposition, which proves to be an appropriate analytical mean for the smooth S_2 tide but fails to echo the local, non-migrating nature of the S_1 tide. Accordingly, a reasonable verification of AAM signals is mostly confined to the semi-diurnal band, resulting in a clear rejection of the retrograde S_2 pressure term from ERA-Interim. The underlying processing route from point observations to climatological AAM phasors is admittedly tedious and cannot be accomplished in a fully automated way.

In the context of Earth's short period excitation budget, the semi-diurnal direct atmospheric contributions to polar motion and changes in LOD are virtually irrelevant, with perturbations larger than 2 µas or 2 µs suspicious of being artifacts as a result of AAM balance defects. Ascribing the apparent leakage of up to 10 µas or 10 µs in the semi-diurnal excitation budget to uncertainties in the atmospheric component is therefore not justified and a discussion of the remaining errors in both the geodetic determinations and ocean tidal angular momentum should be held instead. Altimetry-based solutions of the latter, oceanic effect include a large 'meteorological' component due to pressure forcing, and in this regard, novel OMCT and FES2012 hydrodynamic simulations using 3-hourly atmospheric forecast fields represent a definite advancement.

The cross-check of observed ERP and atmosphere-induced signals becomes truly insightful at the frequency of S_1. For polar motion, different model combinations of OAM and AAM (or their torque replacements) are in reasonable agreement with each other, thus demonstrating an improvement over earlier studies. However, a successful validation of the effect still founders on its small magnitude (0.1 mm at the Earth's surface) which cannot be unequivocally detected by means of VLBI or GPS solutions. On the contrary, the geophysical fluid perturbation in axial direction is large enough to produce a systematic remainder in space geodetic dUT1/LOD determinations. Non-gravitational OAM accounts for the majority of this signal but a simple superposition of standard AAM values corrupts the agreement. The conducted reliability investigations make a strong case for withdrawing AAM values in favor of torque-based solutions, and that route eventually yields a sufficiently closed excitation budget. This essential statement is obtained under the reservation that the combined atmospheric and oceanic excitation quantities derive from somewhat inconsistent geophysical models and that their respective averaging periods are not congruent, either. Moreover, all results are tentative inasmuch as they represent snapshots of three selected atmospheric models condensed to a time-invariant picture over 5 yr. Extension to a decadal analysis window stands to reason as does the incorporation of another reanalysis system, such as the current CFSR (*Climate Forecast System Reanalysis*, Saha *et al.*, 2010) version of NCEP.

8.2 Implications and recommendations for future research

In light of the reduced credibility of (semi-)diurnal AAM estimates in this study and the discrepancies of comparative determinations in previous publications, I genuinely advocate for an inspection of the associated AAM balance prior to actually juxtaposing geodetic and geophysical excitation terms. Built upon a thorough selection of surface and vertical level data, the cross-examination of angular momentum derivatives and torque phasors constitutes the platform on which different model solutions might be discarded or approved. The underlying temporal discretization of meteorological and/or oceanic data should allow for an unambiguous resolution of semi-diurnal effects, as possible for instance by use of 3-hourly short-term forecasts. The rationale behind this suggestion is not to obtain reasonable semi-diurnal ERP predictions (which are minute in any case) but rather to avoid possible distortions of grid point-wise S_1 cycles by undersampling of the usually stronger, migrating S_2 constituents. Such aliasing influences are likely to engender spurious AAM signals after global integration.

A similar stance on the necessary temporal discretization must be adopted when shifting the focus to geophysical excitation of nutation. Atmospheric tides with terrestrial frequencies near the retrograde diurnal band (i.e. the principal S_1 component and its side lobes K_1, P_1, ψ_1, π_1) induce seasonal nutation contributions of occasionally more than 100 µas as aggregated from both their direct and indirect (oceanic) influence on the rotation of the solid Earth. Recent determinations of the effect display an encouraging agreement (Koot & de Viron, 2011), but a reconsideration on the basis of 3-hourly angular momentum data from second-generation atmospheric reanalysis models (MERRA, CFSR, and also ERA-Interim as in Brzeziński *et al.*, 2012) emerges as a definite recommendation from this study. Supplemental reliability investigations by virtue of the AAM balance are entirely limited to the pressure term in the form of the ellipsoidal torque, since the AAM derivative contribution to the budget equation is effectively scaled to zero. Term-by-term comparisons across different models are worthwhile, though, and should span all diurnal tidal bands, especially S_1, K_1, and P_1, which accommodate substantial excitation signals due to wind variability. In this vein, progress toward an update of existing models for non-rigid Earth nutation in terms of mean harmonic and/or time-variable atmospheric contributions comes into range.

Another challenging extension of the presented work might address torque quantities for the oceans, which—given the relative success of the OAM approach in providing reliable ERP corrections—have what one can call an “under-realized" history. Standard caveats against the use of oceanic torques ground on the uncertainties of both pressure and friction forcing fields at the bathymetry as well as numerical instabilities in case the ocean mass-field variability is mainly triggered by atmospheric winds at the sea surface (de Viron *et al.*, 2005a). On (sub-)diurnal time scales, however, water height changes are almost solely driven by the air pressure (cf. Section 7.1), the frictional solid Earth-ocean coupling is virtually irrelevant (Seiler, 1991), and the ocean dynamics itself can be adequately modeled by a two-dimensional (depth-independent) approach. These mitigations reduce the required local interaction forces to rather well-known quantities, that is to say, pressure values and water heights at the sea surface for considerations of the purely radiational portions of the oceanic S_1 and S_2 tides, as well as gradients of the tidal potential for any kind of gravitationally-driven tide, see Seiler (1991). Provided that OAM series and all major torque terms acting on the oceans are calculated in a consistent manner from a coupled atmosphere-ocean model, a successful validation of the OAM balance at different diurnal and semi-diurnal bands should be possible and may warrant the subsequent use of oceanic torques in the context of Earth rotation. Analogous to the atmosphere, integration of ellipsoidal and local torques in the equatorial direction grants access to an alternative estimate of the OAM motion term and its excitation effect at the level of polar motion. Moreover, the availability of all relevant torque quantities in a three-component system (Earth-atmosphere-ocean) would allow for an unambiguous localization of angular momentum exchanges and an illuminating analysis of the actual physical interaction processes.

On a final note, the attained agreement between observed changes in LOD and the atmosphere-ocean excitation signal in the diurnal band stimulates a discussion on the feasibility of proposing a time-invariant a priori model of the effect for use in the analysis of space geodetic data. While such a measure is in principle possible based on the study’s numerical torque results, a few loopholes with regard to the underlying data still need to be closed. The prime issue consists in aligning atmospheric and oceanic model components to a coupled system over a period considerably longer than the 5 yr window investigated here. FES2012 and ECMWF DC, albeit prone to changes in the atmospheric analysis system, represent one version of such a consistent blend. Reanalysis models are equivalent contenders, but irrespective of the final combination, the prerequisite of an approximately valid AAM pressure term must be fulfilled if the LOD prediction is to be accurate and self-consistent. An AAM budget inquiry or the comparison to external mass term determinations (e.g. from simulation studies or an extended, dedicated compilation of barometric in-situ observations) supply suitable verification options.

Both prospects of an advanced understanding of Earth system dynamics and the advent of novel models for selected components of Earth's rotary motion, as presaged above, embody the optimistic legacy of this thesis. Even though the improvement within the analysis of space geodetic observations will be marginal, it is beyond dispute that the sum of such small amendments eventually promotes the quality and accuracy of resultant parameters as well as real-time predictions of Earth rotation variability.

Appendix A

Auxiliary Material

A.1 Pro- and retrograde harmonic coefficients

A (two-dimensional) polar motion excitation signal $\hat{s}(t) = x(t) + \mathrm{i}y(t)$ composed of real-valued sinusoids depending on the angle argument ξ

$$x(t) = x^c \cos(\xi) + x^s \sin(\xi) \tag{A.1}$$

$$y(t) = y^c \cos(\xi) + y^s \sin(\xi) \tag{A.2}$$

can be phrased as sum of two circular (pro- and retrograde) motions of opposite direction but common frequency $\mathrm{d}\xi/\mathrm{d}t$

$$\begin{aligned}\hat{s}(t) &= \frac{x^c}{2}\left(\mathrm{e}^{\mathrm{i}\xi} + \mathrm{e}^{-\mathrm{i}\xi}\right) - \mathrm{i}\frac{x^s}{2}\left(\mathrm{e}^{\mathrm{i}\xi} - \mathrm{e}^{-\mathrm{i}\xi}\right) + \mathrm{i}\frac{y^c}{2}\left(\mathrm{e}^{\mathrm{i}\xi} + \mathrm{e}^{-\mathrm{i}\xi}\right) + \frac{y^s}{2}\left(\mathrm{e}^{\mathrm{i}\xi} - \mathrm{e}^{-\mathrm{i}\xi}\right) && \text{(A.3)}\\ &= \underbrace{\left(\frac{x^c + y^s}{2}\right)}_{A^+}\mathrm{e}^{\mathrm{i}\xi} + \underbrace{\left(\frac{-x^s + y^c}{2}\right)}_{B^+}\mathrm{i}\mathrm{e}^{\mathrm{i}\xi} + \underbrace{\left(\frac{x^c - y^s}{2}\right)}_{A^-}\mathrm{e}^{-\mathrm{i}\xi} + \underbrace{\left(\frac{x^s + y^c}{2}\right)}_{B^-}\mathrm{i}\mathrm{e}^{-\mathrm{i}\xi} && \text{(A.4)}\\ &= \left(A^+ + \mathrm{i}B^+\right)\mathrm{e}^{\mathrm{i}\xi} + \left(A^- + \mathrm{i}B^-\right)\mathrm{e}^{-\mathrm{i}\xi}\,. && \text{(A.5)}\end{aligned}$$

$\{A^+, B^+, A^-, B^-\}$ represent legitimate versions of the sin- and cos-coefficients of geophysically-induced pro- and retrograde polar motion, but they must be adapted to comply with the preset parametrization of the utilized comparative studies (Artz *et al.*, 2011; Böhm *et al.*, 2012b). Estimated harmonics of observed polar motion $\hat{p}(t) = x_p(t) - \mathrm{i}y_p(t)$ derive from (cf. Eq. 6.1 of Böhm, 2012)

$$x_p(t) = \underbrace{\left(-A^+ - A^-\right)}_{x^c}\cos(\xi) + \underbrace{\left(B^+ - B^-\right)}_{x^s}\sin(\xi) \tag{A.6}$$

$$y_p(t) = \underbrace{\left(B^+ + B^-\right)}_{y^c}\cos(\xi) + \underbrace{\left(A^+ - A^-\right)}_{y^s}\sin(\xi)\ , \tag{A.7}$$

which, after some algebra in the fashion of Eq. (A.3), translates to

$$\hat{p}(t) = -\left(A^{+} + \mathrm{i}B^{+}\right)\mathrm{e}^{\mathrm{i}\xi} - \left(A^{-} + \mathrm{i}B^{-}\right)\mathrm{e}^{-\mathrm{i}\xi} \,. \tag{A.8}$$

Hence, if the geophysical excitation signal $\hat{s}(t)$ is to be juxtaposed to observation-based harmonics, the correct formulation of pro- and retrograde coefficients in Eq. (A.5) reads

$$A^{\pm} = -\frac{1}{2}\left(x^{c} \mp y^{s}\right) \,, \qquad B^{\pm} = -\frac{1}{2}\left(y^{c} \pm x^{s}\right) \,. \tag{A.9}$$

A.2 Discrete angular momentum and torque formulae

Pressure and wind terms: The summation over the vertical is performed from the uppermost layer ($k = 1$) to the lowermost pressure level above the topography ($k = n_p$) in each column.

$$\hat{H}^{p} \approx -\frac{\Omega a^{4}}{g}\sum_{\lambda}\sum_{\theta} p_{s}(\theta,\lambda)(\cos\lambda + \mathrm{i}\sin\lambda)\cos\theta\,\sin^{2}\theta\,\mathrm{d}\theta\mathrm{d}\lambda \tag{A.10}$$

$$H_{z}^{p} \approx \frac{\Omega a^{4}}{g}\sum_{\lambda}\sum_{\theta} p_{s}(\theta,\lambda)\sin^{3}\theta\,\mathrm{d}\theta\mathrm{d}\lambda \tag{A.11}$$

$$\begin{aligned}\hat{H}^{w} \approx -\frac{a^{3}}{g}\sum_{\lambda}\sum_{\theta}\sum_{k=1}^{n_p}\frac{p_{k+1}-p_{k}}{2}(\cos\lambda + \mathrm{i}\sin\lambda)\left[(u_{k}(\theta,\lambda) + u_{k+1}(\theta,\lambda))\cos\theta + \right.\\ \left. + \,\mathrm{i}(v_{k}(\theta,\lambda) + v_{k+1}(\theta,\lambda))\right]\sin\theta\,\mathrm{d}\theta\mathrm{d}\lambda\end{aligned} \tag{A.12}$$

$$H_{z}^{w} \approx \frac{a^{3}}{g}\sum_{\lambda}\sum_{\theta}\sum_{k=1}^{n_p}\frac{p_{k+1}-p_{k}}{2}(u_{k}(\theta,\lambda) + u_{k+1}(\theta,\lambda))\sin^{2}\theta\,\mathrm{d}\theta\mathrm{d}\lambda \tag{A.13}$$

Mountain and friction torques: The central difference scheme for topographic gradients utilizes i as longitudinal and j as co-latitudinal index.

$$\hat{L}^{f} \approx -a^{3}\sum_{\lambda}\sum_{\theta}(\cos\lambda + \mathrm{i}\sin\lambda)(-\tau_{\lambda}(\theta,\lambda)\cos\theta + \mathrm{i}\tau_{\theta}(\theta,\lambda))\sin\theta\,\mathrm{d}\theta\mathrm{d}\lambda \tag{A.14}$$

$$L_{z}^{f} \approx -a^{3}\sum_{\lambda}\sum_{\theta}\tau_{\lambda}(\theta,\lambda)\sin^{2}\theta\,\mathrm{d}\theta\mathrm{d}\lambda \tag{A.15}$$

$$\hat{L}^{m} \approx a^{2}\sum_{\lambda}\sum_{\theta}p_{s}(\theta,\lambda)(\cos\lambda + \mathrm{i}\sin\lambda)\left(dh^{\lambda}(\theta,\lambda)\cos\theta - \mathrm{i}dh^{\theta}(\theta,\lambda)\sin\theta\right)\mathrm{d}\theta\mathrm{d}\lambda \tag{A.16}$$

$$L_{z}^{m} \approx -a^{2}\sum_{\lambda}\sum_{\theta}p_{s}(\theta,\lambda)\,dh^{\lambda}(\theta,\lambda)\sin\theta\,\mathrm{d}\theta\mathrm{d}\lambda \tag{A.17}$$

$$\left(\frac{\partial h}{\partial\lambda}\right)_{i} \approx dh_{i}^{\lambda}(\theta,\lambda) = \frac{1}{2\mathrm{d}\lambda}\left(h_{i+1}(\theta,\lambda) - h_{i-1}(\theta,\lambda)\right) \tag{A.18}$$

$$\left(\frac{\partial h}{\partial\theta}\right)_{j} \approx dh_{j}^{\theta}(\theta,\lambda) = \frac{1}{2\mathrm{d}\theta}\left(h_{j+1}(\theta,\lambda) - h_{j-1}(\theta,\lambda)\right) \tag{A.19}$$

A.3 Tidal spherical harmonic coefficients

Table A.1: Spherical harmonic coefficients of the diurnal surface pressure tide following the wave representation in Eq. (6.15) with truncation at $l_{max} = 7$. Amplitudes in units of Pa and phase values in degrees.

l	m	D^+_{lm}	ψ^+_{lm}	D^-_{lm}	ψ^-_{lm}
0	0	0.9 ± 0.3	-147.1 ± 20.0	0.9 ± 0.3	-147.1 ± 20.0
1	0	0.5 ± 0.4	-23.5 ± 40.0	0.5 ± 0.4	-23.5 ± 40.0
	1	23.0 ± 0.4	91.7 ± 1.0	1.9 ± 0.4	-34.1 ± 12.4
2	0	1.7 ± 0.3	-67.9 ± 11.2	1.7 ± 0.3	-67.9 ± 11.2
	1	4.1 ± 0.4	106.3 ± 6.2	2.8 ± 0.4	-37.8 ± 9.1
	2	5.7 ± 0.4	146.2 ± 3.9	5.0 ± 0.4	23.2 ± 4.4
3	0	1.6 ± 0.3	-106.7 ± 10.7	1.6 ± 0.3	-106.7 ± 10.7
	1	9.2 ± 0.5	-93.4 ± 2.9	0.3 ± 0.5	-48.6 ± 104.3
	2	2.9 ± 0.4	178.6 ± 8.0	2.6 ± 0.4	89.7 ± 9.0
	3	1.6 ± 0.4	-74.3 ± 13.4	5.2 ± 0.4	2.6 ± 4.1
4	0	1.2 ± 0.3	156.7 ± 14.6	1.2 ± 0.3	156.7 ± 14.6
	1	0.5 ± 0.5	14.3 ± 51.0	3.0 ± 0.5	-176.0 ± 8.7
	2	3.0 ± 0.4	-61.1 ± 8.6	1.2 ± 0.4	-115.9 ± 21.4
	3	5.3 ± 0.4	-129.3 ± 3.9	3.6 ± 0.4	131.1 ± 5.7
	4	2.9 ± 0.4	178.2 ± 7.3	1.8 ± 0.4	40.6 ± 11.6
5	0	1.4 ± 0.3	129.7 ± 13.0	1.4 ± 0.3	129.7 ± 13.0
	1	2.1 ± 0.4	21.0 ± 11.3	1.3 ± 0.4	105.7 ± 19.1
	2	1.1 ± 0.4	117.3 ± 24.1	1.4 ± 0.4	-1.3 ± 18.1
	3	2.8 ± 0.4	-80.4 ± 8.2	2.1 ± 0.4	-149.7 ± 11.2
	4	2.3 ± 0.3	64.1 ± 8.4	3.0 ± 0.3	-126.8 ± 6.4
	5	4.8 ± 0.4	-167.9 ± 4.4	0.9 ± 0.4	98.0 ± 22.7
6	0	1.8 ± 0.3	-15.9 ± 9.9	1.8 ± 0.3	-15.9 ± 9.9
	1	1.7 ± 0.4	-74.6 ± 13.6	2.1 ± 0.4	84.1 ± 10.7
	2	1.8 ± 0.4	-35.4 ± 13.3	0.5 ± 0.4	-38.9 ± 46.5
	3	2.3 ± 0.4	-29.9 ± 10.3	1.9 ± 0.4	-42.9 ± 12.5
	4	1.0 ± 0.4	135.9 ± 21.4	0.1 ± 0.4	85.0 ± 161.5
	5	4.2 ± 0.3	58.8 ± 4.5	2.0 ± 0.3	-132.0 ± 9.3
	6	1.3 ± 0.4	179.6 ± 15.3	2.3 ± 0.4	-152.1 ± 8.8
7	0	1.2 ± 0.3	-154.1 ± 13.8	1.2 ± 0.3	-154.1 ± 13.8
	1	1.5 ± 0.4	159.5 ± 14.5	0.5 ± 0.4	-0.8 ± 43.8
	2	1.1 ± 0.4	-132.0 ± 19.9	0.8 ± 0.4	-142.6 ± 26.3
	3	1.1 ± 0.4	130.0 ± 19.5	1.3 ± 0.4	8.9 ± 16.5
	4	1.3 ± 0.4	157.4 ± 15.6	0.5 ± 0.4	-107.0 ± 43.2
	5	0.9 ± 0.3	51.8 ± 21.1	1.1 ± 0.3	56.5 ± 17.9
	6	1.8 ± 0.3	-87.6 ± 10.5	3.2 ± 0.3	61.7 ± 5.8
	7	1.1 ± 0.3	160.2 ± 18.9	1.7 ± 0.3	-99.1 ± 11.8

Table A.2: Spherical harmonic coefficients of the semi-diurnal surface pressure tide following the wave representation in Eq. (6.15) with truncation at $l_{max} = 7$. Amplitudes in units of Pa and phase values in degrees.

l	m	D^+_{lm}	ψ^+_{lm}	D^-_{lm}	ψ^-_{lm}
0	0	1.2 ± 0.3	100.3 ± 12.6	1.2 ± 0.3	100.3 ± 12.6
1	0	0.8 ± 0.3	-58.0 ± 20.5	0.8 ± 0.3	-58.0 ± 20.5
	1	3.6 ± 0.3	49.6 ± 5.6	1.8 ± 0.3	-53.0 ± 11.0
2	0	2.7 ± 0.3	-36.5 ± 6.3	2.7 ± 0.3	-36.5 ± 6.3
	1	1.3 ± 0.4	-119.4 ± 16.3	2.9 ± 0.4	39.1 ± 7.7
	2	58.1 ± 0.3	-67.9 ± 0.3	3.2 ± 0.3	-33.1 ± 5.9
3	0	1.2 ± 0.3	46.8 ± 12.6	1.2 ± 0.3	46.8 ± 12.6
	1	1.1 ± 0.4	-85.7 ± 21.1	0.2 ± 0.4	-161.3 ± 98.0
	2	3.0 ± 0.3	38.6 ± 6.6	1.1 ± 0.3	-70.9 ± 18.4
	3	3.8 ± 0.3	16.1 ± 4.8	2.5 ± 0.3	-110.6 ± 7.5
4	0	1.0 ± 0.3	141.9 ± 14.6	1.0 ± 0.3	141.9 ± 14.6
	1	0.5 ± 0.4	96.7 ± 41.6	1.4 ± 0.4	166.4 ± 15.4
	2	6.8 ± 0.4	123.0 ± 3.2	1.1 ± 0.4	122.3 ± 20.7
	3	1.2 ± 0.3	87.4 ± 15.3	1.1 ± 0.3	57.7 ± 16.1
	4	0.8 ± 0.3	-163.1 ± 22.1	0.5 ± 0.3	-39.8 ± 36.3
5	0	0.3 ± 0.3	-176.9 ± 59.3	0.3 ± 0.3	-176.9 ± 59.3
	1	1.0 ± 0.4	90.8 ± 19.8	0.6 ± 0.4	5.3 ± 32.8
	2	0.7 ± 0.4	-154.4 ± 29.9	0.9 ± 0.4	-173.9 ± 24.1
	3	1.4 ± 0.3	112.3 ± 13.8	0.9 ± 0.3	62.2 ± 20.8
	4	2.2 ± 0.3	120.8 ± 7.7	0.8 ± 0.3	-7.1 ± 20.4
	5	1.3 ± 0.3	87.4 ± 13.9	0.3 ± 0.3	137.3 ± 65.6
6	0	0.9 ± 0.3	-34.6 ± 16.9	0.9 ± 0.3	-34.6 ± 16.9
	1	0.7 ± 0.3	-68.7 ± 26.7	0.6 ± 0.3	3.3 ± 34.7
	2	0.5 ± 0.4	35.3 ± 38.0	0.3 ± 0.4	-45.5 ± 70.3
	3	0.9 ± 0.4	-89.3 ± 21.5	0.6 ± 0.3	1.3 ± 35.2
	4	1.2 ± 0.3	115.8 ± 15.0	0.5 ± 0.3	-36.7 ± 37.9
	5	1.6 ± 0.3	12.4 ± 10.5	0.5 ± 0.3	-140.2 ± 31.3
	6	0.8 ± 0.3	81.6 ± 22.7	0.1 ± 0.3	-107.4 ± 240.0
7	0	0.3 ± 0.2	172.0 ± 52.3	0.3 ± 0.2	172.0 ± 52.3
	1	0.6 ± 0.3	177.3 ± 30.6	1.0 ± 0.3	161.5 ± 18.2
	2	0.4 ± 0.3	-174.4 ± 42.3	0.6 ± 0.3	67.1 ± 33.4
	3	0.4 ± 0.3	-123.3 ± 53.0	0.8 ± 0.3	-159.5 ± 24.4
	4	0.2 ± 0.3	25.7 ± 89.2	0.4 ± 0.3	-165.9 ± 44.9
	5	0.7 ± 0.3	-123.8 ± 22.5	0.4 ± 0.3	-16.7 ± 44.5
	6	1.6 ± 0.3	-58.6 ± 10.2	0.2 ± 0.3	-143.5 ± 100.6
	7	0.8 ± 0.3	110.5 ± 22.4	0.7 ± 0.3	71.7 ± 24.8

A.4 Ocean tidal angular momentum terms

Table A.3: Global angular momentum integrals of the S_1 and S_2 ocean tides as deduced from FES2012. Amplitudes in units of $10^{23}\mathrm{kgm}^2\mathrm{s}^{-1}$ and cotidal phases in degrees; diurnal estimates relative to Greenwich noon, cf. Ray & Egbert (2004).

		Heights		Currents	
Tide		Amplitude	Phase Lag	Amplitude	Phase Lag
	x	0.84	141.9	1.39	-25.3
S_1	y	1.87	-41.3	1.63	-123.7
	z	2.05	-137.5	2.33	-53.9
	x	10.77	39.4	56.63	-60.5
S_2	y	27.99	8.5	97.12	-161.6
	z	25.25	128.7	80.37	-12.8

A.5 Numerical constants and parameters

Table A.4: Numerical values of the utilized parameters following Gross (2007) and references therein. Sources other than Gross (2007) are indicated on the right.

Parameter	Value	Source
Ω	$7.292115 \cdot 10^{-5}$ rad/s	
G	$6.67259 \cdot 10^{-11}$ m^3/kg·s^2	
a	6371.0 km	
A'	$8.0102 \cdot 10^{37}$ kg·m^2	
C	$8.0365 \cdot 10^{37}$ kg·m^2	
C_m	$7.1236 \cdot 10^{37}$ kg·m^2	
k_2	0.30097	Dickman (2005)
α_2	0.886	Dickman (2005)
k_2'	-0.305	
α_3	0.792	
T_c	433.1 d	Vicente & Wilson (1997)
Q_c	179	Vicente & Wilson (1997)
T_f'	-430.2 d	Mathews *et al.* (2002)
Q_f	20000	Mathews *et al.* (2002)
g	9.80665 m/s^2	Taylor & Thompson (2008)
ρ_w	1035 kg/m^3	Gill (1982)
R_g[a]	8.3143 J/K·mol	Böhm *et al.* (2013)
M_d[a]	28.965 g/mol	Böhm *et al.* (2013)

[a] Universal gas constant R_g and molecular weight of dry air M_d were used for extrapolating pressure values.

List of Figures

List of Tables

Acronyms

20CRv2	Twentieth Century Reanalysis Project
AAM	Atmospheric Angular Momentum
ACRE	Atmospheric Circulation Reconstructions over the Earth
BIH	Bureau International de l'Heure
CFSR	Climate Forecast System Reanalysis
CIP	Celestial Intermediate Pole
CIRES	Cooperative Institute for Research in Environmental Sciences
CNES	Centre National d'Études Spatiales
COSMIC	Constellation Observing System for Meteorology, Ionsosphere, and Climate
CRF	Celestial Reference Frame
CW	Chandler Wobble
DC	Delayed Cut-off
DFT	Discrete Fourier Transform
DORIS	Doppler Orbitography Radiopositioning Integrated by Satellite
ECMWF	European Centre for Medium-Range Weather Forecasts
EOP	Earth Orientation Parameters
ERA-Interim	ECMWF Reanalysis Interim
ERP	Earth Rotation Parameters
FCN	Free Core Nutation
FFT	Fast Fourier Transform
GCM	General Circulation Model
GCOS	Global Climate Observing System
GCRS	Geocentric Celestial Reference System
GEBCO	General Bathymetric Chart of the Oceans
GEOS	Goddard Earth Observing System Model
GLONASS	Global'naya Navigatsionnaya Sputnikowaya Sistema
GMAO	Global Modeling and Assimilation Office
GNSS	Global Navigation Satellite Systems
GPS	Global Positioning System
IAU	Incremental Analysis Update
IAU	International Astronomical Union

ICOADS	International Comprehensive Ocean Atmosphere Data Set
ICRF	International Celestial Reference Frame
ICRS	International Celestial Reference System
IERS	International Earth Rotation and Reference Systems Service
IFS	Integrated Forecast System
ISPD	International Surface Pressure Databank
ITRS	International Terrestrial Reference System
IUGG	International Union of Geodesy and Geophysics
JMA	Japan Meteorological Agency
LOD	Length of Day
MERRA	Modern Era-Retrospective Analysis for Research and Applications
NASA	National Aeronautics and Space Administration
NCAR	National Center for Atmospheric Research
NCEP	National Centers for Environmental Prediction
NOAA	National Oceanic and Atmospheric Administration
OAM	Oceanic Angular Momentum
OMCT	Ocean Model for Circulation and Tides
OTAM	Ocean Tidal Angular Momentum
PSD	Power Spectral Density
SLP	Sea Level Pressure
SLR	Satellite Laser Ranging
TRF	Terrestrial Reference Frame
UT1	Universal Time 1
UTC	Universal Time Coordinated
VieVS	Vienna VLBI Software
VLBI	Very Long Baseline Interferometry
WCRP	World Climate Research Program

Bibliography

Altamimi, Z., Sillard, P. and Boucher, C. (2003). The impact of a no-net-rotation condition on ITRF2000. *Geophys. Res. Lett.*, 30, 1064, doi:10.1029/2002GL016279.

Altamimi, Z., Collilieux, X. and Métivier, L. (2011). ITRF2008: an improved solution of the international terrestrial reference frame. *J. Geod.*, 85, 457–473.

Arbic, B. (2005). Atmospheric forcing of the oceanic semidiurnal tide. *Geophys. Res. Lett.*, 32, L02610, doi:10.1029/2004GL021668.

Arias, E., Charlot, P., Feissel, M. and Lestrade, J.F. (1995). The extragalactic reference system of the International Earth Rotation Service, ICRS. *Astron. Astrophys.*, 303, 604–608.

Artz, T., Tesmer née Böckmann, S. and Nothnagel, A. (2011). Assessment of periodic subdiurnal Earth rotation variations at tidal frequencies through transformation of VLBI normal equation systems. *J. Geod.*, 85, 565–584, doi:10.1007/s00190–011–0457–z.

Artz, T., Bernhard, L., Nothnagel, A., Steigenberger, P. and Tesmer, S. (2012). Methodology for the combination of sub-daily Earth rotation from GPS and VLBI observations. *J. Geod.*, 86, 221–239, doi:10.1007/s00190–011–0512–9.

Barnes, R., Hide, R., White, A. and Wilson, C. (1983). Atmospheric angular momentum fluctuations, length-of-day changes and polar motion. *Proc. R. Soc. Lond.*, A 387, 31–73.

Bloom, S., Takacs, L., DaSilva, A. and Ledvina, D. (1996). Data assimilation using incremental analysis updates. *Mon. Weather Rev.*, 24, 1256–1271.

Blumen, W. (1972). Geostrophic adjustment. *Rev. Geophys.*, 10, 485–528, doi:10.1029/RG010i002p00485.

Boer, G. (1990). Earth-atmosphere exchange of angular momentum simulated in a general circulation model and implications for the length of day. *J. Geophys. Res.*, 95, 5511–5531, doi:10.1029/JD095iD05p05511.

Böhm, J., Böhm, S., Nilsson, T., Pany, A., Plank, L., Spicakova, H., Teke, K. and Schuh, H. (2012a). The new Vienna VLBI software VieVS. In S. Kenyon, M. Pacino and U. Marti, eds., *Proceedings of IAG Scientific Assembly 2009, International Association of Geodesy Symposia Series*, Vol. 136, 1007–1077, doi:10.1007/978–3–642–20338–1_126.

Böhm, J., Salstein, D., Alizadeh, M. and Wijaya, D. (2013). Geodetic and atmospheric background. In J. Böhm and H. Schuh, eds., *Atmospheric Effects in Space Geodesy*, 1–33, doi:10.1007/978–3–642–36932–2_1, Springer.

Böhm, S. (2012). Tidal excitation of Earth rotation observed by VLBI and GNSS. *Geowissenschaftliche Mitteilungen*, Schriftenreihe der Studienrichtung Vermessung und Geoinformation, Heft Nr. 90.

Böhm, S., Brzeziński, A. and Schuh, H. (2012b). Complex demodulation in VLBI estimation of high frequency Earth rotation components. *J. Geodyn.*, 62, 56–68, doi:10.1016/j.jog.2011.10.002.

Brzeziński, A. (1994). Polar motion excitation by variations of the effective angular momentum function, II: extended-model. *Manuscr. Geodaet.*, 19, 157–171.

Brzeziński, A. (2008). On the influence of diurnal atmospheric tides on Earth rotation. In N. Capitaine, ed., *Proc. Journées Systèmes de Référence Spatio-Temporels 2007*, 180–183, Observatoire de Paris.

Brzeziński, A., Bizouard, C. and Petrov, S. (2002). Influence of the atmosphere on Earth rotation: What new can be learned from the recent atmospheric angular momentum estimates? *Surv. Geophys.*, 23, 33–69, doi:10.1023/A:1014847319391.

Brzeziński, A., Ponte, R. and Ali, A. (2004). Nontidal oceanic excitation of nutation and diurnal/semidiurnal polar motion revisited. *J. Geophys. Res.*, 109, B11407, doi:10.1029/2004JB003054.

Brzeziński, A., Dobslaw, H., Thomas, M. and Ślusarczyk, Ł. (2012). Subdiurnal atmospheric and oceanic excitation of Earth rotation estimated from 3-hourly AAM and OAM data. *Geophys. Res. Abstracts*, 14, poster presentation at EGU General Assembly 2012, EGU2012-10530.

Butler, S. and Small, K. (1963). The excitation of atmospheric oscillations. *P. Roy. Soc. Lond. A Mat.*, 274, 91–121.

Carrère, L., Lyard, F., Cancet, M., Guillot, A. and Roblou, L. (2012). FES2012: A new global tidal model taking taking advantage of nearly 20 years of altimetry. In *Proc. 20 Years of Progress in Radar Altimetry Symposium*, in preparation.

Chao, B. and Ray, R. (1997). Ocean tidal angular momentum and Earth's rotation variations. *Prog. Oceanogr.*, 40, 399–421.

CHAO, B., RAY, R., GIPSON, J., EGBERT, G. AND MA, C. (1996). Diurnal/semidiurnal polar motion excited by oceanic tidal angular momentum. *J. Geophys. Res.*, 101, 20151–20163, doi:10.1029/96JB01649.

CHAPMAN, S. AND LINDZEN, R. (1970). *Atmospheric Tides*. Gordan and Breach, New York.

CHEN, W., RAY, J., LI, J., HUANG, C. AND SHEN, W. (2013). Polar motion excitations for an Earth model with frequency-dependent responses: 1. A refined theory with insight into the Earth's rheology and core-mantle coupling. *J. Geophys. Res.*, 118, 4975–4994, doi:10.1002/jgrb.50314.

COMPO, G. (2013). Reanalysis intercomparison and observations: The International Surface Pressure Databank. http://reanalyses.org/observations/international-surface-pressure-databank, as at April 2013.

COMPO, G. *et al.* (2011). The Twentieth Century Reanalysis Project. *Q. J. R. Meteorol. Soc.*, 137, 1–28, doi:10.1002/qj.776.

COOPER, N. (1984). Errors in atmospheric tidal determination from surface pressure observations. *Q. J. R. Meteorol. Soc.*, 110, 1053–1059, doi:10.1002/qj.49711046615.

COVEY, C., DAI, A., MARSH, D. AND LINDZEN, R. (2011). The surface-pressure signature of amospheric tides in modern climate models. *J. Atmos. Sci.*, 68, 495–514, doi:10.1175/2010JAS3560.1.

DAHLEN, F. (1976). The passive influence of the oceans upon the rotation of the Earth. *Geophys. J. R. Astron. Soc.*, 46, 363–406.

DAI, A. AND DESER, C. (1999). Diurnal and semidiurnal variations in global surface wind and divergence fields. *J. Geophys. Res.*, 104, 31109–31125, doi:10.1029/1999JD900927.

DAI, A. AND WANG, J. (1999). Diurnal and semidiurnal tides in global surface pressure fields. *J. Atmos. Sci.*, 56, 3874–3891.

DE VIRON, O. AND DEHANT, V. (1999). Earth's rotation and high frequency equatorial angular momentum budget of the atmosphere. *Surv. Geophys.*, 20, 441–462, doi:10.1023/A:1006723924421.

DE VIRON, O. AND DEHANT, V. (2003). Tests on the validity of atmospheric torques on Earth computed from atmospheric model outputs. *J. Geophys. Res.*, 108, B22068, doi:10.1029/2001JB001196.

DE VIRON, O., BIZOUARD, C., SALSTEIN, D. AND DEHANT, V. (1999). Atmospheric torque on the Earth and comparison with atmospheric angular momentum variations. *J. Geophys. Res.*, 104, 4861–4875, doi:10.1029/1998JB900063.

DE VIRON, O., MARCUS, S. AND DICKEY, J. (2001). Diurnal angular momentum budget of the atmosphere and its consequences for Earth's nutation. *J. Geophys. Res.*, 106, 26747–26759, doi:10.1029/2000JB000098.

DE VIRON, O., PONTE, R. AND DEHANT, V. (2001a). Indirect effect of the atmosphere through the oceans on the Earth nutation using the torque approach. *J. Geophys. Res.*, 106, 8841–8851, doi:10.1029/2000JB900387.

DE VIRON, O., DICKEY, J. AND MARCUS, S. (2002). Annual atmospheric torques: Processes and regional contributions. *Geophys. Res. Lett.*, 29, doi:10.1029/2001GL013859.

DE VIRON, O., KOOT, L. AND DEHANT, V. (2005a). Polar motion models: the torque approach. In H. Plag, B. Chao, R. Gross and T. van Dam, eds., *Forcing of Polar Motion in the Chandler Frequency Band: A Contribution to Understanding Interannual Climate Change*, Vol. 24, 9–14, Cahiers du Centre Européen de Géodynamique et du Séismologie, Luxembourg.

DE VIRON, O., SCHWARZBAUM, G., LOTT, F. AND DEHANT, V. (2005b). Diurnal and subdiurnal effects of the atmosphere on the Earth rotation and geocenter motion. *J. Geophys. Res.*, 110, B11404, doi:10.1029/2005JB003761.

DEE, D. *et al.* (2011). The ERA-Interim reanalysis: configuration and performance of the data assimilation system. *Q. J. R. Meteorol. Soc.*, 137, 553–597, doi:10.1002/qj.828.

DICKMAN, S. (1993). Dynamic ocean-tide effects on Earth's rotation. *Geophys. J. Int.*, 112, 448–470.

DICKMAN, S. (2003). Evaluation of 'effective angular momentum functions' formulations with respect to core-mantle coupling. *J. Geophys. Res.*, 108, 2150, doi:10.1029/2001JB001603.

DICKMAN, S. (2005). Rotationally consistent Love numbers. *Geophys. J. Int.*, 161, 31–40, doi:10.1111/j.1365–246X.2005.02574.x.

DICKMAN, S. AND GROSS, R. (2010). Rotational evaluation of a long-period spherical harmonic ocean tide model. *J. Geod.*, 84, 457–464, doi:10.1007/s00190–010–0383–5.

DOBSLAW, H. (2007). Modellierung der allgemeinen ozeanischen Dynamik zur Korrektur und Interpretation von Satellitendaten. *Scientific Technical Report*, GeoForschungsZentrum Potsdam, doi:10.2312/GFZ.b103-07103.

DOBSLAW, H. AND THOMAS, M. (2005). Atmospheric induced oceanic tides from ECMWF forecasts. *Geophys. Res. Lett.*, 32, L10615, doi:10.1029/2005GL022990.

DOBSLAW, H., DILL, R., GRÖTZSCH, A., BRZEZIŃSKI, A. AND THOMAS, M. (2010). Seasonal polar motion excitation from numerical models of atmosphere, ocean, and continental hydrosphere. *J. Geophys. Res.*, 115, B10406, doi:10.1029/2009JB007127.

DRAPER, N. AND SMITH, H. (1981). *Applied Regression Analysis*. John Wiley and Sons, New York, 2nd edn.

EGBERT, G. AND EROFEEVA, S. (2002). Efficient inverse modeling of barotropic ocean tides. *J. Atmos. Ocean. Technol.*, 19, 183–204.

EGGER, J. AND HOINKA, K. (2002). Equatorial components of global atmospheric angular momentum: Covariance functions. *Q. J. R. Meteorol. Soc.*, 128, 1137–1157.

EUBANKS, T. (1993). Variations of the orientation of the Earth. In D. Smith and D. Turcotte, eds., *Contributions of Space Geodesy to Geodynamics: Earth Dynamics*, Vol. 24, 1–54, American Geophysical Union, Washington.

FARRELL, W. (1972). Deformation of the Earth by surface loads. *Rev. Geophys.*, 10, 761–797, doi:10.1029/RG010i003p00761.

FECHER, T., GRUBER, T. AND RUMMEL, R. (2009). Truncation of spherical harmonic series and its influence on gravity field modelling. *Geophys. Res. Abstracts*, 11, poster presentation at EGU General Assembly 2009, EGU2009-6072.

FEY, A., GORDON, D. AND JACOBS, C. (2009). The Second Realization of the International Celestial Reference Frame by Very Long Baseline Interferometry, IERS Technical Note No. 35, Verlag des Bundesamtes für Kartographie und Geodäsie, Frankfurt am Main.

FORBES, J. AND GARRETT, H. (1978). Thermal excitation of atmospheric tides due to insolation absorption by O_3 and H_2O. *Geophys. Res. Lett.*, 5, 1013–1016, doi:10.1029/GL005i012p01013.

FORBES, J. AND GARRETT, H. (1979). Theoretical studies of atmospheric tides. *Rev. Geophys.*, 17, 1951–1984, doi:10.1029/RG017i008p01951.

FUJITA, M., CHAO, B., SANCHEZ, B. AND JOHNSON, T. (2002). Oceanic torques on solid Earth and their effects on Earth rotation. *J. Geophys. Res.*, 107, B8, doi:10.1029/2001JB000339.

GARRATT, J. (1977). Review of drag coefficients over oceans and continents. *Mon. Wea. Rev.*, 105, 915–929.

GEGOUT, P., HINDERER, J., LEGROS, H., GREFF, M. AND DEHANT, V. (1998). Influence of atmospheric pressure on the Free Core Nutation, precession and some forced nutational motions of the Earth. *Phys. Earth Planet. Inter.*, 106, 337–351.

GILL, A. (1982). Atmosphere-ocean dynamics. In *International Geophysics*, Vol. 30, Academic Press.

GIPSON, J. AND RAY, R. (2009). A new model of tidal EOP variations from VLBI data spanning 30 years. *Geophys. Res. Abstracts*, 11, oral presentation at EGU General Assembly 2009, EGU2009-13096.

GIWA, F. AND HUSSAIN, L. (1978). A theory of atmospheric tides generated by the differential heating between land and sea. *Pure Appl. Geophys.*, 116, 56–65.

GROSS, R. (1992). Correspondence between theory and observations of polar motion. *Geophys. J. Int.*, 109, 162–170.

GROSS, R. (1993). The effect of ocean tides on the Earth's rotation as predicted by the results of an ocean tide model. *Geophys. Res. Lett.*, 20, 293–296, doi:10.1029/93GL00297.

GROSS, R. (2000). The excitation of the Chandler wobble. *Geophys. Res. Lett.*, 27, 2329–2332, doi:10.1029/2000GL011450.

GROSS, R. (2007). Earth rotation variations – long period. In T. Herring, ed., *Treatise on Geophysics*, Vol. 3, Geodesy, 239–294, Elsevier.

GROSS, R., FUKUMORI, I. AND MENEMENLIS, D. (2003). Atmospheric and oceanic excitation of the Earth's wobbles during 1980–2000. *J. Geophys. Res.*, 108, 2370, doi:10.1029/2002JB002143.

GROSS, R., FUKUMORI, I., MENEMENLIS, D. AND GEGOUT, P. (2004). Atmospheric and oceanic excitation of length-of-day variations during 1980–2000. *J. Geophys. Res.*, 109, B01406, doi:10.1029/2003JB002432.

HAGAN, M., FORBES, J. AND RICHMOND, A. (2003). Atmospheric tides. In J. Holton, J. Pyle and J. Curry, eds., *Encyclopedia of Atmospheric Sciences*, 159–165, Academic Press, 1st edn.

HAMILTON, K. (1980). The geographical distribution of the solar semidiurnal surface pressure oscillation. *J. Geophys. Res.*, 85, 1945–1949, doi:10.1029/JC085iC04p01945.

HAURWITZ, B. AND COWLEY, A. (1970). The lunar barometric tide, its globe distribution and annual variation. *Pure Appl. Geophys.*, 75, 122–150.

HAURWITZ, B. AND COWLEY, A. (1973). The diurnal and semidiurnal barometric oscillations, global distribution and annual variation. *Pure Appl. Geophys.*, 102, 193–222.

HOBIGER, T. *et al.* (2012). Consistent height transformations between geodetic and meteorologic reference systems. Abstract G11A-0904, presented at 2012 Fall Meeting, AGU, San Francisco, 3–7 December.

HSU, H. AND HOSKINS, B. (1989). Tidal fluctuations as seen in ECMWF data. *Q. J. R. Meteorol. Soc.*, 115, 247–264.

HUANG, H. AND WEICKMANN, K. (2008). On the computation of the mountain torque from gridded global datasets. *Mon. Weather Rev.*, 136, 4005–4009, doi:10.1175/2008MWR2359.1.

HUANG, H., SARDESHMUKH, P. AND WEICKMANN, K. (1999). The balance of global angular momentum in a long-term atmospheric data set. *J. Geophys. Res.*, 104, 2031–2040, doi:10.1029/1998JD200068.

HUGHES, C. (2002). Torques exerted by a shallow fluid on a non-spherical, rotating planet. *Tellus A*, 54, 56–62, doi:10.1034/j.1600–0870.2002.00326.x.

HUNT, B. AND MANABE, S. (1968). An investigation of thermal tidal oscillations in the Earth's atmosphere using a general circulation model. *Mon. Weather Rev.*, 96, 753–766.

ISKENDERIAN, H. AND SALSTEIN, D. (1998). Regional sources of mountain torque variability and high-frequency fluctuations in atmospheric angular momentum. *Mon. Wea. Rev.*, 126, 1681–1694.

JACKSON, A. (1997). Time-dependency of tangentially geostrophic core surface motions. *Phys. Earth Planet. Int.*, 103, 293–311, doi:10.1016/S0031–9201(97)00039–3.

JEKELI, C. (1996). Spherical harmonic analysis, aliasing, and filtering. *J. Geod.*, 70, 214–223, doi:10.1007/BF00873702.

JENKINS, G. AND WATTS, D. (1968). *Spectral Analysis and its Applications*. Holden-Day, San Francisco.

KADOW, C., DOBSLAW, H., MATTHES, K. AND THOMAS, M. (2012). Impact of atmospheric tides simulated in a chemistry-climate model on sub-diurnal variations in UT1. In H. Schuh, S. Böhm, T. Nilsson and N. Capitaine, eds., *Proceedings of the Journées 2011 Systèmes de Référence Spatio-Temporels*, 144–147, Vienna University of Technology and Observatoire de Paris.

KNAPP, K., KRUK, M., LEVINSON, D., DIAMOND, H. AND NEUMANN, C. (2010). The International Best Track Archive for Climate Stewardship (IBTrACS): Unifying tropical cyclone best track data. *Bull. Amer. Meteorol. Soc.*, 9, 363–376, doi:10.1175/2009BAMS2755.1.

KOOT, L. AND DE VIRON, O. (2011). Atmospheric contributions to nutations and implications for the estimation of deep Earth's properties from nutation observations. *Geophys. J. Int.*, 185, 1255–1265, doi:10.1111/j.1365–246X.2011.05026.x.

KURSINSKI, E., HAJJ, G., SCHOFIELD, R., LINFIELD, P. AND HARDY, K. (1997). Observing Earth's atmosphere with radio occultation measurements using the Global Positioning System. *J. Geophys. Res.*, 102, 23,429–23,465, doi:10.1029/97JD01569.

LAMBECK, K. (1980). *The Earth's Variable Rotation: Geophysical Causes and Consequences*. Cambridge University Press, New York.

LEJENÄS, H., MADDEN, R. AND HACK, J. (1997). Global atmospheric angular momentum and Earth-atmosphere exchange of angular momentum in a general circulation model. *J. Geophys. Res.*, 102, 1931–1941, doi:10.1029/96JD03264.

LINDZEN, R. (1979). Atmospheric tides. *Ann. Rev. Earth Planet. Sci.*, 7, 199–225.

LINDZEN, R. (1990). *Dynamics in Atmospheric Physics*. Cambridge University Press, New York.

LOTT, F., DE VIRON, O., VITERBO, P. AND VIAL, F. (2008). Axial atmospheric angular momentum budget at diurnal and subdiurnal periodicities. *J. Atmos. Sci.*, 65, 156–171, doi:10.1175/2007JAS2178.1.

LUCCHESI, R. (2012). File Specifications for MERRA Products, GMAO Office Note No. 1 (Version 2.3), 82 pp, available from http://gmao.gsfc.nasa.gov/pubs/office_notes.

LYARD, F., LEFEVRE, F., LETELLIER, T. AND FRANCIS, O. (2006). Modelling the global ocean tides: Modern insights from FES2004. *Ocean Dynam.*, 56, 394–415.

MADDEN, R. (2000). Large-scale, free Rossby waves in the atmosphere–an update. *Tellus A*, 59, 571–590, doi:10.1111/j.1600–0870.2007.00257.x.

MADDEN, R., LEIJNÄS, H. AND HACK, J. (1998). Semidiurnal variations in the budget of angular momentum in a general circulation model and in the real atmosphere. *J. Atmos. Sci.*, 55, 2561–2575.

MARCUS, S., DE VIRON, O. AND DICKEY, J. (2004). Atmospheric contributions to Earth nutation: Geodetic constraints and limitations of the torque approach. *J. Atmos. Sci.*, 61, 352–356.

MASAKI, Y. (2008). Wind field differences between three meteorological reanalysis data sets detected by evaluating atmospheric excitation of Earth rotation. *J. Geophys. Res.*, 113, D07110, doi:10.1029/2007JD008893.

MASS, C., STEENBURGH, W. AND SHULTZ, D. (1991). Diurnal surface-pressure variations over the continental United States and the influence of sea level reduction. *Mon. Weather Rev.*, 119, 2814–2830.

MATHEWS, P., HERRING, T. AND BUFFETT, B. (2002). Modeling of nutation and precession: New nutation series for nonrigid Earth and insights into the Earth's interior. *J. Geophys. Res.*, 104, 2068, doi:10.1029/2001JB000390.

MCCOLL, C., MATSUI, N. AND COMPO, G. (2011). HDF5 format for International Surface Pressure Data Bank v10.11. http://rda.ucar.edu/datasets/ds132.0/#docs, as at August 2011.

MIKHAIL, E. AND ACKERMANN, F. (1976). *Observations and Least Squares*. IEP–A Dun-Donnelley Publisher, New York.

MORITZ, H. AND MÜLLER, I. (1987). *Earth Rotation: Theory and Observation*. Ungar, New York.

MORRISON, L. AND STEPHENSON, F. (2001). Historical eclipses and the variability of the Earth's rotation. *J. Geodyn.*, 32, 247–265, doi:10.1016/S0264–3707(01)00024–2.

MUNK, W. AND GROVES, G. (1952). The effect of winds and ocean currents on the annual variation in latitude. *J. Meteor.*, 9, 385–396.

MUNK, W. AND MACDONALD, G. (1960). *The Rotation of the Earth: A Geophysical Discussion*. Cambridge University Press, NewYork.

NAFISI, V. *et al.* (2012). Comparison of ray-tracing packages for troposphere delays. *IEEE Trans. Geosci. Remote Sens.*, 50, 469–480.

NASTULA, J. AND SALSTEIN, D. (1999). Regional atmospheric angular momentum contributions to polar motion excitation. *J. Geophys. Res.*, 104, 7347–7358, doi:10.1029/1998JB900077.

NEWTON, I. (1687). *Philosophiae Naturalis Principia Mathematica*.

OTNES, R. AND ENOCHSON, L. (1978). *Applied Time Series Analysis: Volume 1, Basic Techniques*. John Wiley and Sons, New York.

PANCHEVA, D., MIYOSHI, Y., MUKHTAROV, P., JIN, H., SHINAGAWA, H. AND FUJIWARA, H. (2012). Global response of the ionosphere to atmospheric tides forced from below: Comparison between COSMIC measurements and simulations by atmosphere-ionosphere coupled model GAIA. *J. Geophys. Res.*, 117, A07319, doi:10.1029/2011JA017452.

PEIXOTO, J. AND OORT, A. (1992). *Physics of Climate*. Springer, New York.

PEROVIĆ, G. (2005). *Least Squares*. University of Belgrade, Faculty of Civil Engineering.

PERSSON, A. (2011). User guide to ECMWF forecast products. http://ecmwf.int/products/forecasts/guide/, as at October 2011.

PETIT, G. AND LUZUM, B. (2010). IERS Conventions 2010, IERS Technical Note No. 36, Verlag des Bundesamtes für Kartographie und Geodäsie, Frankfurt am Main.

PIRSCHER, B., FOELSCHE, U., BORSCHE, M., KIRCHENGAST, G. AND KUO, Y.H. (2010). Analysis of migrating diurnal tides detected in FORMOSAT-3/COSMIC temperature data. *J. Geophys. Res.*, 115, D14108, doi:10.1029/2009JD013008.

PONTE, R. AND ROSEN, R. (2001). Atmospheric torques on land and ocean and implications for Earth's angular momentum budget. *J. Geophys. Res.*, 106, 11793–11799, doi:10.1029/2001JD900028.

PUGH, D. (2001). Tides. In J. Steele, ed., *Encyclopedia of Ocean Sciences*, 2961–2968, Academic Press.

RANDALL, D. (2007). The Laplace tidal equations and atmospheric tides, Selected Notes of David A. Randall, pages 277-305, Department of Atmospheric Science, Colorado State University.

RAY, R. (1998). Diurnal oscillations in atmospheric pressure at twenty-five small oceanic islands. *Geophys. Res. Lett.*, 25, 3851–3854, doi:10.1029/1998GL900039.

Ray, R. (1999). A global ocean tide model from Topex/Poseidon altimetry: GOT99.2. NASA Tech. Memo. 209478.

Ray, R. (2001). Comparisons of global analyses and station observations of the S_2 barometric tide. *J. Atmos. Sol.-Terr. Phy.*, 63, 1085–1097.

Ray, R. and Egbert, G. (2004). The global S_1 tide. *J. Phys. Oceanogr.*, 34, 1922–1935.

Ray, R. and Ponte, R. (2003). Barometric tides from ECMWF operational analyses. *Ann. Geophys.*, 21, 1897–1910.

Ray, R., Steinberg, D., Chao, B. and Cartwright, D. (1994). Diurnal and semidiurnal variations in the Earth's rotation rate induced by oceanic tides. *Science*, 264, 830–832, doi:10.1126/science.264.5160.830.

Rienecker, M. *et al.* (2008). The GEOS-5 Data Assimilation System–Documentation of Versions 5.0.1, 5.1.0, and 5.2.0. *Technical Report Series on Global Modeling and Data Assimilation*, 27.

Rienecker, M. *et al.* (2011). MERRA: NASA's Modern-Era Retrospective Analysis for Research and Applications. *J. Climate*, 24, 3624–3648.

Rothacher, M., Beutler, G., Herring, T. and Weber, R. (1999). Estimation of nutation using the Global Positioning System. *J. Geophys. Res.*, 104, 4835–4859, doi:10.1029/1998JB900078.

Saha, S. *et al.* (2010). The NCEP climate forecast system reanalysis. *Bull. Amer. Meteor. Soc.*, 91, 1015–1057.

Sasao, T. and Wahr, J. (1981). An excitation mechanism for the free 'core nutation'. *Geophys. J. R. Astron. Soc.*, 64, 729–746.

Schindelegger, M., Böhm, J., Salstein, D. and Schuh, H. (2011). High-resolution atmospheric angular momentum functions related to Earth rotation parameters during CONT08. *J. Geod.*, 8, 425–433, doi:10.1007/s00190–011–0458–y.

Schindelegger, M., Böhm, J., Schuh, H. and Salstein, D. (2012). The signature of atmospheric tides in sub-daily variations of Earth rotation as unveiled by globally-gridded atmospheric angular momentum functions. In H. Schuh, S. Böhm, T. Nilsson and N. Capitaine, eds., *Proc. Journées Systèmes de Référence Spatio-Temporels 2011*, 140–143, Vienna University of Technology and Observatoire de Paris.

Schindelegger, M., Böhm, J. and Salstein, D. (2013a). Seasonal and intraseasonal polar motion variability as deduced from atmospheric torques. *J. Geod. Geoinf.*, 1, 89–95, doi:10.9733/jgg.231112.1.

Schindelegger, M., Böhm, S., Böhm, J. and Schuh, H. (2013b). Atmospheric effects on Earth rotation. In J. Böhm and H. Schuh, eds., *Atmospheric Effects in Space Geodesy*, 181–231, doi:10.1007/978–3–642–36932–2_6, Springer.

SCHINDELEGGER, M., SALSTEIN, D. AND BÖHM, J. (2013c). Recent estimates of Earth-atmosphere interaction torques and their use in studying polar motion variability. *J. Geophys. Res.*, 118, 4586–4598, doi:10.1002/jgrb.50322.

SCHLÜTER, W. AND BEHREND, D. (2007). The International VLBI Service for Geodesy and Astrometry (IVS): current capabilities and future prospects. *J. Geod.*, 81, 379–387, doi:10.1007/s00190–006–0131–z.

SCHUH, H. AND BEHREND, D. (2012). VLBI: A fascinating technique for geodesy and astrometry. *J. Geodyn.*, 61, 68–80.

SCHUH, H. AND BÖHM, J. (2013). Very Long Baseline Interferometry for geodesy and astrometry. In G. Xu, ed., *Sciences of Geodesy - II: Innovations and Future Developments*, 339–376, Springer.

SCHUH, H., NAGEL, S. AND SEITZ, T. (2001). Linear drift and periodic variations observed in long time series of polar motion. *J. Geod.*, 74, 701–710, doi:10.1007/s001900000133.

SEEBER, G. (2003). *Satellite Geodesy*. Walter de Gruyter, Berlin, 2nd edn.

SEILER, U. (1991). Periodic changes of the angular momentum budget due to the tides of the World Ocean. *J. Geophys. Res.*, 96, 10287–10300, doi:10.1029/91JB00219.

SEITZ, F. AND SCHMIDT, M. (2005). Atmospheric and oceanic contributions to Chandler wobble excitation determined by wavelet filtering. *J. Geophys. Res.*, 110, B11406, doi:10.1029/2005JB003826.

SEITZ, F. AND SCHUH, H. (2010). Earth rotation. In G. Xu, ed., *Science of Geodesy - I: Advances and Future Directions*, 185–227, Springer.

SHEN, Y. AND XU, G. (2013). Regularization and Adjustment. In G. Xu, ed., *Sciences of Geodesy - II: Innovations and Future Developments*, 293–337, Springer.

SIEBERT, M. (1961). Atmospheric tides. In *Advances in Geophysics*, Vol. 7, 105–182, Academic Press, New York.

SMITH, M. AND DAHLEN, F. (1981). The period and Q of the Chandler wobble. *Geophys. J. R. Astron. Soc.*, 64, 223–281.

SOVERS, O., FANSELOW, J. AND JACOBS, C. (1998). Astrometry and geodesy with radio interferometry: experiments, models, results. *Rev. Mod. Phys.*, 70, 1393–1454, doi:10.1103/RevModPhys.70.1393.

STARR, V. (1948). An essay on the general circulation of the Earth's atmosphere. *J. Meteor.*, 5, 39–43.

STEIGENBERGER, P. (2009). Reprocessing of a global GPS network. *DKG, Reihe C*, Heft 640, Verlag der Bayerischen Akademie der Wissenschaften.

SWINBANK, R. (1985). The global atmospheric angular momentum balance inferred from analyses made during FGGE. *Q. J. R. Meteorol. Soc.*, 111, 977–992.

TAGUCHI, E., STAMMER, D. AND ZAHEL, W. (2013). Estimation of deep ocean tidal energy dissipation based on the high-resolution data-assimilative HAMTIDE model, in preparation.

TAYLOR, B. AND THOMPSON, A. (2008). The International System of Units (SI), NIST Special Pulication 330, National Institute of Standards and Technology, Gaithersburg.

THOMAS, I., KING, M. AND CLARKE, P. (2007). A comparison of GPS, VLBI and model estimates of ocean tide loading displacements. *J. Geod.*, 81, 359–368, doi:10.1007/s00190–006–0118–9.

THOMAS, M. (2002). *Ocean induced variations of Earth's rotation - Results from a simultaneous model of global circulation and tides*. Ph.D. thesis, Univ. of Hamburg, Germany.

TISSERAND, F. (1891). Théorie de la figure des corps célestes et de leur mouvement de rotation. In *Traité de mécanique céleste*, Vol. II, Paris: Gauthier-Villars et Fils.

UPPALA, S. *et al.* (2005). The ERA-40 re-analysis. *Q. J. R. Meteorol. Soc.*, 131, 2961–3012.

VICENTE, R. AND WILSON, C. (1997). On the variability of the Chandler frequency. *J. Geophys. Res.*, 102, 20439–20445, doi:10.1029/97JB01275.

WAHR, J. (1982). The effects of the atmosphere and oceans on the Earth's wobble - I. Theory. *Geophys. J. R. Astron. Soc.*, 70, 349–372.

WAHR, J. AND OORT, A. (1984). Friction- and mountain-torque estimates from global atmospheric data. *J. Atm. Sci.*, 41, 190–204.

WELCH, P. (1967). The use of fast Fourier transform for the estimation of power spectra: A method based on time-averaging over short, modified periodograms. *IEEE Trans. Audio and Electroacoustics*, 15, 70–73.

WHITAKER, J. AND HAMILL, T. (2002). Ensemble data assimilation without perturbed observations. *Mon. Wea. Rev.*, 130, 1913–1924.

WHITEMAN, C. AND BIAN, X. (1996). Solar semidiurnal tides in the troposphere: Detection by radar profilers. *B. Am. Meteorol. Soc.*, 77, 529–542.

WOLF, W. AND SMITH, R. (1987). Length-of-day changes and mountain torques during El Niño. *J. Atm. Sci.*, 44, 3656–3660.

WOODRUFF, S., SLUTZ, R., JENNE, R. AND STEURER, P. (1987). A comprehensive ocean-atmosphere data set. *Bull. Amer. Meteor. Soc.*, 68, 1239–1250.

YSEBOODT, M., DE VIRON, O., CHIN, T. AND DEHANT, M. (2002). Atmospheric excitation of the Earth's nutation: Comparison of different atmospheric models. *J. Geophys. Res.*, 107, 2036, doi:10.1029/2000JB000042.

Curriculum vitae

Michael Schindelegger, Dipl.-Ing., Univ. Ass.

Vienna University of Technology
Department of Geodesy and Geoinformation
Gusshausstraße 27-29, 1040 Vienna
E-mail: michael.schindelegger@tuwien.ac.at
Tel.: +43 1 58801 12828

Date of birth:	November 3, 1984
Place of birth:	Scheibbs, Austria
Marital status:	married

University and Education

11/2009 – 01/2014	Doctoral Program in Technical Sciences – Surveying and Geoinformation, Vienna University of Technology
10/2009	Dipl.-Ing. Degree (M.Sc.) from the Vienna University of Technology. Thesis Title: *Modeling atmospheric influences on the Earth's rotation on different time scales*. Supervisors: Prof. H. Schuh and Dr. J. Böhm
10/2004 – 10/2009	Master Program in Surveying and Geoinformation – Geodesy and Geophysics, Vienna University of Technology
09/1995 – 06/2003	Grammar School (Bundesrealgymnasium), Wieselburg

Employment Record

01/2013 – present	University assistant at the Vienna University of Technology, Department of Geodesy and Geoinformation, Advanced Geodesy
10/2009 – 12/2012	Scientific research assistant at the Vienna University of Technology, Department of Geodesy and Geoinformation, Advanced Geodesy
08/2005 – 09/2005	Employee of surveying company 'Angst Vermessung', Vienna

Areas of Scientific Interest

Earth rotation and its geophysical excitation, mass transports within near-surface fluids, atmospheric circulation, mathematical methods for geosciences

GEOWISSENSCHAFTLICHE MITTEILUNGEN

Bisher erschienen:

Heft 1 Kolloquium der Assistenten der Studienrichtung Vermessungswesen. 1970 - 1973, Dezember 1973.

Heft 2 EGGER-PERDICH-PLACH-WAGENSOMMERER, Taschenrechner HP 45 und HP 65, Programme und Anwendungen im Vermessungswesen. 1. Auflage, März 1974, Special Edition in English, Juli 1974, 2. verbesserte Auflage, November 1974.

Heft 3 Kolloquium der Assistenten der Studienrichtung Vermessungswesen 1973 - 1974, September 1974.

Heft 4 EGGER-PALFINGER-PERDICH-PLACH-WAGENSOMMERER, Tektronix-Tischrechner TEK 31, Programmbibliothek für den Einsatz im Vermessungswesen, November 1974.

Heft 5 K. LEDERSTEGER, Die horizontale Isostasie und das isostatische Geoid, Februar 1975.

Heft 6 F. REINHART, Katalog von FK4 Horrebow-Paaren für Breiten von +30 bis +60, Oktober 1975.

Heft 7 Arbeiten aus dem Institut für Höhere Geodäsie, Wien, Dezember 1975.

Heft 8 Veröffentlichungen des Instituts für Photogrammetrie zum XIII. Internationalen Kongreß für Photogrammetrie in Helsinki 1976, Wien, Juli 1976.

Heft 9 W. PILLEWIZER, Felsdarstellung aus Orthophotos, Wien, Juni 1976.

Heft 10 PERDICH-PLACH-WAGENSOMMERER, Der Einsatz des programmierbaren Taschenrechners Texas Instruments SR-52 mit Drucker PC100 in ingenieurgeodätischen Rechentechnik, Wien, Mai 1976.

Heft 11 Kolloquium der Assistenten der Studienrichtung Vermessungswesen 1974 - 1976, November 1976.

Heft 12 Kartographische Vorträge der Geodätischen Informationstage 1976, Wien, Mai 1977.

Heft 13 Veröffentlichung des Instituts für Photogrammetrie anläßlich des 80. Geburtstages von Prof. Dr.h.c. K. Neumaier, Wien, Januar 1978.

Heft 14 L. MOLNAR, Self Checking Analytical Relative Orientation and Strip Formation, Wien, Dezember 1978.

Heft 15 Veröffentlichung des Instituts für Landesvermessung anläßlich des 80. Geburtstages von Prof. Dr. Alois Bavir, Wien, Januar 1979.

Heft 16 Kolloquium der Assistenten der Studienrichtung Vermessungswesen 1976 - 1978, Wien, November 1979.

Heft 17 E. VOZIKIS, Die photographische Differentialumbildung gekrümmter Flächen mit Beispielen aus der Architekturbildmessung, Wien, Dezember 1979.

Heft 18 Veröffentlichung des Instituts für Allgemeine Geodäsie anläßlich des 75. Geburtstages von Prof. Dipl.-Ing. Dr. F. Hauer, Die Höhe des Großglockners, Wien, 1981.

Heft 19 H. KAGER, Bündeltriangulation mit indirekt beobachteten Kreiszentren, Wien, April 1981.

Heft 20 Kartographische Vorträge der Geodätischen Informationstage 1980, Wien, Mai 1982.

Heft 21 Veröffentlichung des Instituts für Kartographie anläßlich des 70. Geburtstages von Prof. Dr. Wolfgang Pillewizer: Glaziologie und Kartographie, Wien, Dezember 1982.

Heft 22 K. TEMPFLI, Genauigkeitsschätzung digitaler Höhenmodelle mittels Spektralanalyse, Wien, Mai 1982.

Heft 23 E. CSAPLOVICS, Interpretation von Farbinfrarotbildern, Wien, November 1982.

Heft 24 J. JANSA, Rektifizierung von Multispektral-Scanneraufnahmen - Entwicklung und Erprobung eines EDV-Programms, Wien, Mai 1983.

Heft 25 Zusammenfassung der Diplomarbeiten, Dissertationen und Habilitationen an den geodätischen Instituten der TU Wien, Wien, November 1984.

Heft 26 T. WUNDERLICH, Die voraussetzungsfreie Bestimmung von Refraktionswinkeln, Wien, August 1985.

Heft 27 G. GERSTBACH (Hrsg.), Geowissenschaftliche/geotechnische Daten in Landinformationssystemen - Bedarf und Möglichkeiten in Österreich, Juni 1986.

Heft 28 K. NOVAK, Orientierung von Amateuraufnahmen ohne Paßpunkte, Wien, August 1986.

Heft 29 Veröffentlichung des Instituts für Landesvermessung und Ingenieurgeodäsie, Abt. Ingenieurgeodäsie, anläßlich des 80. Geburtstages von Prof. Dipl.-Ing. Dr. F. Hauer, Wien, Oktober 1986.

Heft 30 K.-H. ROCH, Über die Bedeutung dynamisch ermittelter Parameter für die Bestimmung von Gesteins- und Gebirgseigenschaften, Wien, Februar 1987.

Heft 31 G. HE, Bildverbesserung mittels digitaler Filterung, Wien, April 1989.

Heft 32 F. SCHLÖGELHOFER, Qualitäts- und Wirtschaftlichkeitsmodelle für die Ingenieurphotogrammetrie, Wien, April 1989.

Heft 33 G. GERSTBACH (Hrsg.), Geowissenschaftliche/geotechnische Daten in Landinformationssystemen - Datenbestände und Datenaustausch in Österreich, Wien, Juni 1989.

Heft 34 F. HOCHSTÖGER, Ein Beitrag zur Anwendung und Visualisierung digitaler Geländemodelle, Wien, Dezember 1989.

Heft 35 R. WEBER, Lokale Schwerefeldmodellierung unter Berücksichtigung spektraler Methoden zur Geländereduktion, Wien, April 1990.

Heft 36 o.Prof. Dr. Hans Schmid zum 70. Geburtstag. Veröffentlichung der Abteilung für Landesvermessung, Wien, Oktober 1990.

Heft 37 G. GERSTBACH, H. P. HÖLLRIEGL und R. WEBER, Geowissenschaftliche Informationsbörse - Eine Nachlese zu GeoLIS II, Wien, Oktober 1990.

Heft 38 R. ECKER, Rastergraphische Visualisierungen mittels digitaler Geländemodelle, Wien, August 1991.

Heft 39 Kartographische Forschungen und Anwendungsorientierte Entwicklungen, herausgegeben von W. Stams und F. Kelnhofer zum 80. Geburtstag von Prof. Dr. W. Pillewizer, Wien, Juli 1991.

Heft 39a W. RIEGER, Hydrologische Anwendungen des digitalen Geländemodelles, Wien, Juli 1992.
Heft 40 K. STEINNOCHER, Methodische Erweiterungen der Landnutzungsklassifikation und Implementierung auf einem Transputernetzwerk, Wien, Juli 1994.

Heft 41 G. FORKERT, Die Lösung photogrammetrischer Orientierungs- und Rekonstruktionsaufgaben mittels allgemeiner kurvenförmiger Elemente, Wien, Juli 1994.

Heft 42 M. SCHÖNER, W. SCHÖNER, Photogrammetrische und glaziologische Untersuchungen am Gàsbre (Ergebnisse der Spitzbergenexpedition 1991), Wien, Mai 1996.

Heft 43 M. ROIC. Erfassung von nicht signalisierten 3D-Strukturen mit Videotheodoliten, Wien, April 1996.

Heft 44 G. RETSCHER, 3D-Gleiserfassung mit einem Multisensorsystem und linearen Filterverfahren, Wien, April 1996.

Heft 45 W. DAXINGER, Astrogravimetrische Geoidbestimmung für Ingenieurprojekte, Wien, Juli 1996.

Heft 46 M. PLONER, CCD-Astrometrie von Objekten des geostationären Ringes, Wien, November 1996.

Heft 47 Zum Gedenken an Karl Killian "Ingenieur" und "Geodät" 1903-1991, Veröffentlichung der Fachgruppe Geowissenschaften, Wien, Februar 1997.

Heft 48 A. SINDHUBER, Ergänzung und Fortführung eines digitalen Landschaftsmodelles mit multispektralen und hochauflösenden Fernerkundungsaufnahmen, Wien, Mai 1998.

Heft 49 W. WAGNER, Soil Moisture Retrieval from ERS Scatterometer Data, Wien, Dezember 1998.

Heft 50 R. WEBER, E. FRAGNER (Editoren),Prof. Bretterbauer, Festschrift zum 70. Geburtstag, Wien, Juli 1999.

Heft 51 Ch. ÖHRENEDER, A Similarity Measure for Global Image Matching Based on The Forward Modeling Principle, Wien, April 1999.

Heft 52 M. LECHTHALER, G. GARTNER, Per Aspera ad Astra, Festschrift für Fritz Kelnhofer zum 60. Geburtstag, Wien, Jänner 2000.

Heft 53 F. KELNHOFER, M. LECHTHALER, Interaktive Karten (Atlanten) und Multimedia – Applikationen, Wien, März 2000.

Heft 54 A. MISCHKE, Entwicklung eines Videotheodlit-Meßsystems zur automatischen Richtungsmessung von nicht signalisierten Objektpunkten, Wien, Mai 2000.

Heft 55 Veröffentlichung des I.P.F. anlässlich der Emeritierung von Prof. Dr. Peter Waldhäusl, Wien.

Heft 56 F. ROTTENSTEINER, Semi-automatic Extraction of Buildings Based on Hybrid Adjustment Using 3D Surface Models and Management of Building Data in a TIS, Wien, Juni 2001.

Heft 57 D. LEGENSTEIN, Objektrekonstruktion aus perspektiven Bildern unter Einbeziehung von Umrisslinien, Wien, Mai 2001.

Heft 58 F. KELNHOFER, M. LECHTHALER und K. BRUNNER (Hrsg.), Telekartographie und Location Based Services, Wien, Jänner 2002.

Heft 59 K. BRETTERBAUER, Die runde Erde eben dargestellt: Abbildungslehre und sphärische Kartennetzentwürfe, Wien, 2002.

Heft 60 G. GARTNER, Maps and the Internet 2002, Wien 2002.

Heft 61 L. DORFFNER, Erzeugung von qualitativ hochwertigen 3D Photomodellen für Internetbasierte Anwendungen mit besonderem Augenmerk auf Objekte der Nahbereichsphotogrammetrie, Wien, Jänner 2002.

Heft 62 K. CHMELINA, Wissensbasierte Analyse von Verschiebungsdaten im Tunnelbau, Wien 2002.

Heft 63 A. NIESSNER, Qualitative Deformationsanalase unter Ausnutzung der Farbinformation, Wien 2002.

Heft 64 K. BRETTERBAUER, R. WEBER, A Primer of Geodesy for GIS-Users, Wien 2003.

Heft 65 N. PFEIFER, 3D Terrain Models on the basis of a triangulation, Wien, Jänner 2002.

Heft 66 G. GARTNER (Hrsg), Lacation Based Services & Telecartography, Wien 2004.

Heft 67 I. KABASHI, Gleichzeitig-gegenseitige Zenitwinkelmessung über größere Entfernungen mit automatischen Zielsystemen, Wien 2004.

Heft 68 J. BÖHM, Troposphärische Laufzeitverzögerungen in der VLBI, Wien 2004.

Heft 69 R. WEBER, W. SCHLÜTER, U. SCHREIBER, O. TITOV Evolving Space Geodesy Techniques (EGS XXVII General Assembly, Nice, France, 2002), Wien 2004.

Heft 70 G. WEINWURM, Amalthea's Gravity Field and its Impact on a Spacecraft Trajectory, Wien 2004.

Heft 71 Forschungsgruppe Ingenieurgeodäsie, Festschrift anlässlich des 65. Geburtstages von Herrn o.Univ. Prof. Dr.-Ing. Heribert Kahmen, Wien 2005.

Heft 72 A. REITERER, A Knowledge-Based Decision System for an On-Line Video-Theodolite-Based Multisensor System, Wien 2005.

Heft 73 M. HABERLER, Einsatz von Fuzzy Methoden zur Detektion konsistenter Punktbewegungen, Wien 2005.

Heft 74 G. GARTNER, Location Based Services & Telecartography, Proceedings of the Symposium 2005, Wien 2005.

Heft 75 Th. HOBIGER, VLBI as a tool to probe the ionosphere, Wien 2006.

Heft 76 E. KLAFFENBÖCK, Troposphärische Laufzeitverzögerung von GNSS-Signalen – Nutzen aktiver Referenzstationsnetze für die Meteorologie, Wien 2006.

Heft 76a P. J. MENDES-CERVEIRA, Tidal and non-tidal contributions to surface loading processes on station coordinates, Wien 2006.

Heft 78 G. KOSTOV, G. BOURDA, L. FERNANDEZ, T. KONDO, Research Projects at IGG Reports, Wien 2007.

Heft 79 J. BÖHM, A. PANY, H. SCHUH (Editors), Proceedings of the 18th European VLBI for Geodesy and Astrometry Working Meeting, 12-13 April 2007, Wien 2007.

Heft 80 J. BÖHM, Tropospheric Delay Modelling at Radio Wavelengths for Space Geodetic Techniques, Wien 2007.

Heft 81 G. Retscher, Mobile Multi-sensor Systems for Personal Navigation and Location-based Services, Wien 2007.

Heft 82 R. HEINKELMANN, Bestimmung des atmosphärischen Wasserdampfes mittels VLBI als Beitrag zur Klimaforschung, Wien 2008.

Heft 83 F. ROTTENSTEINER, Automatic extraction of buildings from airborne laserscanner data and aerial images, Wien 2008.

Heft 84 S. TODOROVA, Kombination geodätischer Weltraumverfahren für globale Karten der Ionosphäre, Wien 2009.

Heft 85 J. WRESNIK, Simulationen für die neue Generation von VLBI-Systemen, Wien 2009.

Heft 86 A. KARABATIC, Precise Point Positioning (PPP). An alternative technique for ground based GNSS troposphere monitoring, Wien 2011.

Heft 87 K. TEKE, Sub-daily Parameter Estimation in VLBI Data Analysis, Wien 2011.

Heft 88 G. THALER, Echtzeit Bahn- und Uhrberechnung der GPS-Satellitenkonstellation basierend auf Beobachtungsdaten des RTIGS-Stationsnetzwerkes, Wien.

Heft 89 P. SWATSCHINA, Dynamic and Reduced-Dynamic Precise Orbit Determination of Satellites in Low Earth Orbits, Wien 2012.

Heft 90 S. BÖHM, Tidal excitation of Earth rotation observed by VLBI and GNSS, Wien 2012.

Heft 91 H. KRÁSNÁ, Estimation of solid Earth tidal parameters and FCN with VLBI, Wien 2013.

Heft 92 J. SUN, VLBI scheduling strategies with respect to VLBI2010, Wien 2013.

Heft 93 M.M. ALIZADEH ELIZEI, Multi-Dimensional modeling of the ionospheric parameters, using space geodetic techniques, Wien 2013.

Heft 94 M. KARBON, Atmospheric effects on measurements of the Earth gravity field, Wien 2013.

Heft 95 L. PLANK, VLBI satellite tracking for the realization of frame ties, Wien 2014.

Heft 96 M. SCHINDELEGGER, Atmosphere-induced short period variations of Earth rotation, Wien 2014.